Size-Selective Separation and Process Analytical Technology for the Purification of Non-Viral Vectors

—

Lipid Nanoparticles and Virus-Like Particles

Zur Erlangung des akademischen Grades einer
Doktorin der Ingenieurwissenschaften (Dr.-Ing.)

von der KIT-Fakultät für Chemieingenieurwesen und Verfahrenstechnik des
Karlsruher Instituts für Technologie (KIT)
genehmigte

Dissertation

von
M. Sc. Annabelle Dietrich
aus Lörrach

Tag der mündlichen Prüfung: 17.11.2025

Erstgutachter: Prof. Dr. Jürgen Hubbuch
Zweitgutachter: Prof. Dr. Alois Jungbauer

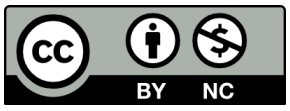

„Going viral with non-viral vectors“

Unknown

Acknowledgements

Während meiner Promotion durfte ich von der Begleitung, Inspiration und dem Beitrag vieler Menschen profitieren.

Mein besonderer Dank gilt Prof. Dr. Jürgen Hubbuch für die Möglichkeit der Promotion am Institut für Molekulare Aufarbeitung von Bioprodukten (MAB). Die gelungene Balance aus wissenschaftlicher Freiheit und verlässlicher Unterstützung ermöglichte mir fachliches und persönliches Wachstum. Außerdem danke ich Prof. Dr. Alois Jungbauer für das Interesse an meiner Arbeit und die Übernahme des Koreferats.

Besonderen Dank richte ich auch an Nicole Beckert und Robin Schiemer für die wissenschaftliche Zusammenarbeit im Rahmen mehrerer Projekte, die in gemeinsamen Publikationen mündeten. Diese Kooperationen zeichneten sich insbesondere durch tiefgehende und konstruktive Diskussionen aus, die mir neue Perspektiven aufzeigten und zu spürbaren synergetischen Effekten führten.

Für die tatkräftige Unterstützung bei der Durchführung dieser Projekte danke ich meinen Studierenden Luca Heim, Jasper Kurmann und Shiqi Zhang. Neben der außerordentlich gewissenhaften und zuverlässigen Arbeit hat auch das Einbringen neuer Ideen maßgeblich zum Erfolg dieser Projekte beigetragen.

Außerdem möchte ich allen aktuellen und ehemaligen MABlern für die stets angenehme Arbeitsatmosphäre und das ausgeprägte kollegiale Miteinander danken. Ich schätze den wertvollen Austausch und die Bereicherung des Arbeitsalltags, sei es in wissenschaftlichen Kontexten wie Seminarfahrten und Konferenzen oder in den gemeinsamen Mittags- und Kaffeepausen sowie bei Feierlichkeiten.

Zuletzt möchte ich mich bei meinen Freunden und meiner Familie bedanken, die meine Freizeit durch gemeinsame Aktivitäten wie Sport, Spieleabende und Urlaube wesentlich bereichert haben.

Abstract

As modern medicines, biopharmaceuticals are characterized by high functional specificity and offer innovative solutions for the prevention or treatment of complex diseases, including autoimmune, infectious, genetic diseases, and cancer. The functionality of biopharmaceuticals is rooted in the product's structure, whereby its quality attributes are intrinsically linked to the production process, making process understanding the key to ensuring product quality. Thus, the overarching objective of biopharmaceutical process development is to enhance process understanding through methodological and systematic approaches.

Beyond monoclonal antibodies representing the core platform in the biopharmaceutical industry, vector technologies have emerged as versatile nanocarrier platforms, particularly for vaccines and gene therapeutics. Nowadays, the leading non-viral vector classes comprise lipid nanoparticles (LNPs) and virus-like particles (VLPs), which are associated with lower safety concerns in comparison to viral vectors. LNPs are utilized for the protected delivery of nucleic acids and are composed of a defined ratio of distinct lipid types. In contrast, VLPs are formed through the spontaneous assembly of recombinant capsid proteins, thereby mimicking the structure of the native virus. VLPs can be used to present heterologous surface proteins or for the protected delivery of a post-inserted payload. As VLPs are recombinantly produced, a cascade of downstream processing (DSP) steps is required for their purification, involving the removal of process- and product-related impurities. However, the nanocarriers' overall larger size compared to monoclonal antibodies, as well as their structural diversity within and between those non-viral vector classes, pose new challenges in the development of purification processes and analytics.

Recent advancements in nanocarrier purification promise a broader application of size-selective separation techniques and elevate the potential of precipitation and cross-flow filtration (CFF) for standardized purification processes. In contrast to size exclusion chromatography, precipitation and CFF offer universal applicability alongside fundamental process requirements covering reproducibility, scalability, and efficiency, but without being restricted by limited loading capacities. Presumably due to the recent emergence of the LNP technology, CFF process development for LNPs has not yet reached a mature state. The present limitations in process understanding are to be addressed through dedicated process parameter studies and analysis of process intermediates. In contrast, CFF is well established for VLP purification and has recently been explored for the processing of VLP precipitates, as selective precipitation is commonly employed to capture VLPs from clarified lysate. Consequently, ongoing efforts in process development for VLPs are already directed towards

process integration, intensification, and standardization, with the objective of streamlining their DSP.

Beyond standard analytics, the concept of process analytical technology (PAT) enables real-time monitoring and control of critical process parameters and quality attributes by combining advanced sensor technologies and chemometrics. As with the DSP development, the maturity of sensor-based PAT tool development for monitoring varies across different separation techniques and biopharmaceuticals. PAT tools relying on ultraviolet-visible (UV/Vis) spectroscopy are leading for monitoring chromatographic purification of monoclonal antibodies, with the approach undergoing expansion to encompass filtration processes, including those for VLPs. Shortcomings persist in the development of PAT tools for the monitoring of precipitation processes, including VLP precipitation, as well as LNP purification in general. These shortcomings are accompanied by considerable challenges, requiring the utilization of alternative sensor technologies. In the field of optical spectroscopy, scattering-based sensor technologies such as Raman and dynamic light scattering (DLS) hold promise in addressing the individual challenges associated with the monitoring of VLP precipitation and LNP purification, respectively.

Supported by references, Chapter 1 provides a more detailed introduction that summarizes the theoretical background, recent advancements, and remaining research gaps in the field. As outlined in Chapter 2, the objective of this thesis was to advance the primary purification of the non-viral vector classes LNPs and VLPs through (I) size-selective separation and (II) sensor-based analytics and PAT tools. Aiming for standardized, scalable, size-selective processing, innovations in primary purification were driven through the integration of CFF. In order to obtain further insights into these purification processes and thereby enhance process understanding, tailored analytics and PAT tools were developed based on charged aerosol detection (CAD), DLS, and Raman spectroscopy. As demonstrated in diverse, consecutive studies, the integration of CFF enabled efficient processing. Moreover, analytics and the implementation of process monitoring tools yielded valuable insights into these processes.

For LNPs, standard analytical procedures are primarily applied to the microfluidic mixing step and typically cover particle size, surface charge, and encapsulation efficiency. Although lipid composition directly affects the aforementioned LNP attributes, the quantification of lipids remains an uncommon practice. Reversed-phase (RP)-high performance liquid chromatography (HPLC) in conjunction with CAD previously demonstrated a high degree of selectivity and sensitivity for lipids. Thus, a RP-HPLC-CAD method was developed to quantify lipids in LNP process intermediates (Chapter 3). The method enabled precise lipid quantification of former LNPs, providing the lipid molar ratio as an additional LNP attribute and the lipid recovery at each process step as a key process performance parameter. The method's applicability and its benefits were demonstrated in a process parameter study involving microfluidic mixing and dialysis, with variations in the mixing total flow rate (TFR). LNP size exhibited a TFR-dependency, which is in accordance with the results of previous studies, whereas all novel findings derived from lipid analytics were TFR-independent. The lipid concentrations showed a batch and process step dependency, while the lipid molar ratio was batch-independent and constant throughout the processing. Another batch-dependency was found for the performance of the dialysis step, with lipid loss-associated decreases in lipid recovery. In summary, utilizing lipid analytics supports the characterization of LNPs and processes. To contribute to new perspectives on process development for LNPs and to enhance process understanding, LNP purification by CFF may also benefit from its application.

Although CFF offers a scalable, time- and cost-efficient alternative to dialysis for buffer exchange to remove residual solvent and raise the pH, with seamless, integrated LNP concentration through volume reduction, CFF-based LNP purification remains unexplored. This includes the effects of membrane characteristics and CFF process parameters on LNP attributes, as well as CFF monitoring. Thus, a CFF parameter study was performed, with at-line monitoring of the LNP size using DLS (Chapter 4). Four experiments were conducted, in which LNPs were purified by dialysis and CFF for side-by-side comparison, with the latter as constant-volume diafiltration (DF) followed by ultrafiltration (UF). No consistent impact on LNP attributes was observed from the systematic variations of distinct membrane characteristics and CFF process parameters. This included persistent lipid molar ratios and lipid recoveries, as revealed by the developed RP-HPLC-CAD method (cf. Chapter 3). However, time-resolved analysis supported by at-line monitoring using DLS revealed a linear dependency of LNP size on CFF processing time. Differences in particle size alternation between dialyzed and CFF-purified LNPs led to the hypothesis of an interplay among pump-induced shear forces, LNP fusion, and LNP equilibrium size. In summary, this study provides novel insights into LNP purification by CFF. Alongside the underlying mechanisms driving these increasing particle sizes, which still need to be explored, these findings point towards future size-controlled CFF-based LNP purification.

With respect to the size-selectivity of CFF, precipitation also exploits the size difference between the product and impurities. For the primary purification of VLPs from clarified lysate, the conjunction of selective precipitation and CFF-based microfiltration (MF) for precipitate processing previously demonstrated improvements in productivity, purity, and yield compared to VLP recovery by centrifugation, thereby addressing scalability, process integration, and intensification. Specifically, two consecutive constant-volume DF steps on one CFF unit enable precipitate washing to remove soluble impurities, followed by VLP re-dissolution. During the latter step, the VLPs pass through the MF membrane and are thereby separated from the irreversibly precipitated species. However, VLP concentration is constrained by DF-induced permeate dilution, and purity is limited by the presence of residual precipitant. To improve VLP concentration and purity through process integration, a novel dual-stage CFF set-up was developed for the integrated, seamless recovery of VLP precipitates (Chapter 5). The dual-stage CFF set-up was equipped with a MF/UF membrane configuration. With this set-up, DF-based VLP recovery involved VLP re-dissolution and their isolation through the simultaneous depletion of residual precipitant under constant volume in the second membrane stage, and their subsequent concentration using an integrated UF step. Alongside precipitant depletion, the dual-stage CFF set-up allowed for the effective removal of co-redissolved impurities. In summary, the dual-stage CFF setup with the MF/UF membrane configuration establishes a foundation for standardized precipitate processing and has promising future applications for diverse VLPs and biopharmaceuticals, as well as potential transferability to crystallization processes.

Next to the high impurity levels in primary purification processes, selective precipitation inherently yields particulate precipitates and turbidity through the addition of precipitant, rendering direct quantification of the precipitated product impossible and posing distinct challenges for developing sensor-based PAT tools. In such environments, widely applied monitoring tools based on UV/Vis spectroscopy and chemometrics reach their limits, while Raman spectroscopy represents a promising sensor alternative. However, in general, in-depth insights into data generation and spectral preprocessing for the knowledge-driven development of Raman-based PAT tools remain relatively rare. Thus, a systematic approach was pursued for the development of a Raman-based PAT tool for VLP precipitation monitoring (Chapter 6). To ensure data diversification, batch and fed-batch

precipitation experiments were conducted using conditioned lysate, resulting in variations in the precipitation dynamics and background composition. A systematic combination of spectral preprocessing operations and spectral feature analysis was used to evaluate the effectiveness in eliminating differences in spectral backgrounds as well as interferences caused by the presence of precipitates and turbidity. The concentration of precipitated VLPs was predicted with preprocessed Raman spectral data and partial least squares (PLS) regression, and effects of individual preprocessing operations on PLS model performances were evaluated. In summary, Raman-based PAT enables VLP precipitation monitoring in particulate, turbid lysate. The gained insights through a deliberately systematic development approach underscore the importance of data diversification and targeted spectral preprocessing for future PAT tool development.

Compared to the controlled addition of precipitant in batch and fed-batch precipitation processes, precipitant depletion in dynamic processes should be monitored through precipitant quantification, such as during the filtration-based VLP recovery using the presented dual-stage CFF set-up (cf. Chapter 5). Furthermore, the quantification of the re-dissolved VLPs accumulated in the second membrane stage is of particular interest; however, sampling during the DF process leads to product loss and perturbs its dynamics. PAT tool development for monitoring two components simultaneously from the same acquired spectral data clearly benefits from a systematic development approach, such as the one presented for VLP precipitation monitoring (cf. Chapter 6). However, a limitation observed was the transfer from batch precipitation-derived Raman-based PAT tools for monitoring fed-batch precipitation, which, however, might be more straightforward in the processes where fewer spectral interferences are expected. Under the scope of model transfer, Raman-based PAT tools were developed from stock solutions of pure components for simultaneous monitoring of VLP accumulation and precipitant depletion in the filtration-based VLP recovery step (Chapter 7). Investigating spectral contributions of VLPs and precipitant using pure component spectra revealed attribute-specific spectral features as well as a higher inherent sensor sensitivity towards the precipitant than VLPs. Accordingly, attribute-specific preprocessing operations were selected to account for these differences as well as for detector saturation effects, and several regression models were built with preprocessed spectral data from pure component solutions. Concurrently, the dual-stage CFF set-up was equipped with a Raman spectrometer within an on-line monitoring loop in the second membrane stage, and process spectral data were acquired from three diversified CFF experiments. From these CFF-derived spectral data, VLP and precipitant concentrations were predicted by application of the transferred models. The fact that the final prediction accuracy was higher for the precipitant than VLPs despite attribute-specific selections of preprocessing operations and models unraveled the importance of attribute-specific sensor selection. In summary, model transfer is demonstrated through the systematic development of Raman-based PAT tools, thereby emphasizing the critical role of attribute-specific sensor selection for future PAT tool development.

This thesis presents advances in DSP development through the integration of size-selective separation techniques and sensor-based PAT tools, tailored to the primary purification of the current leading non-viral vector classes, namely LNPs and VLPs. Despite the differences in developmental maturity between LNP and VLP process development, the tailored integration of CFF enabled efficient processing, and analytics and process monitoring tools provided valuable insights into these processes. Overall, the methodological and systematic approaches presented demonstrate the potential to be transferred to other biopharmaceuticals or processes. Collectively, these advances highlight the potential of size-selective purification and scattering-based sensor technologies to address the specific challenges associated with novel vector technologies, while ultimately supporting the overarching goal

of enhancing process understanding in biopharmaceutical process development. Such developments lay the foundation for future standardized and controlled DSP of vectors in the biopharmaceutical industry.

Zusammenfassung

Als moderne Medikamente zeichnen sich Biopharmazeutika durch eine hohe funktionelle Spezifität aus und bieten innovative Lösungen zur Vorbeugung und Behandlung komplexer Krankheiten, darunter Autoimmunerkrankungen, Infektionskrankheiten, genetische Erkrankungen und Krebs. Die Funktionalität von Biopharmazeutika ist dabei abhängig von der Produktstruktur, wobei die Qualitätsattribute des Produkts untrennbar mit dem Produktionsprozess verbunden sind. Das Prozessverständnis ist somit von entscheidender Bedeutung für die Gewährleistung der Produktqualität. Das übergeordnete Ziel in der biopharmazeutischen Prozessentwicklung besteht demnach in der Steigerung des Prozessverständnisses durch methodische und systematische Ansätze.

Monoklonale Antikörper stellen die zentrale Plattform der biopharmazeutischen Industrie dar, doch darüber hinaus haben sich Vektortechnologien als vielseitige Nanotransporter-Plattformen hervorgetan, die insbesondere als Impfstoffe und in der Gentherapie Anwendung finden. Zu den führenden nicht-viralen Vektorklassen zählen Lipidnanopartikel (LNPs) und Virus-ähnliche Partikel (VLPs), welche im Gegensatz zu viralen Vektoren mit einem geringeren Sicherheitsbedenken einhergehen. LNPs finden Anwendung für den geschützten Transport von Nukleinsäuren und bestehen aus einem definierten Verhältnis verschiedener Lipidtypen. Demgegenüber bestehen VLPs aus assemblierten, rekombinant hergestellten Kapsidproteinen, wodurch sie die Struktur des nativen Virus nachahmen. VLPs finden Anwendung als Nanotransporter für einen nachträglich eingefügten Wirkstoff oder zur Präsentation heterologer Oberflächenproteine. Da VLPs rekombinant hergestellt werden, ist die anschließende Entfernung von prozess- und produktbezogenen Verunreinigungen notwendig, welche in der Regel über eine Abfolge mehrerer Aufreinigungsschritte erfolgt. Die größere Partikelgröße der Nanotransporter im Vergleich zu monoklonalen Antikörpern sowie ihre strukturelle Vielfalt innerhalb und zwischen den Vektorklassen resultieren jedoch in neuen Herausforderungen bei der Entwicklung von Aufreinigungsprozessen und Analysemethoden.

Jüngste Fortschritte in der Aufreinigung von Nanotransportern orientieren sich verstärkt an Trennverfahren, die auf Größenselektion basieren. In diesem Zusammenhang bieten insbesondere die Präzipitation und die Querstromfiltration ein hohes Potenzial für die Standardisierung von Aufreinigungsprozessen. Im Gegensatz zur Größenausschlusschromatographie sind Präzipitation und Querstromfiltration universeller anwendbar und erfüllen die grundlegenden Prozessanforderungen wie Reproduzierbarkeit, Skalierbarkeit und Effizienz, ohne jedoch von einer begrenzten Beladungskapazität limitiert zu sein. Die Prozessentwicklung für LNPs basierend auf Querstromfiltration ist

bisher noch nicht ausgereift, was vermutlich auf den erst jüngsten Durchbruch der LNP-Technologie zurückzuführen ist. Das derzeit fehlende Prozessverständnis könnte durch gezielte Prozessparameterstudien und Analyse von Prozesszwischenprodukten erlangt werden. Demgegenüber ist der Einsatz der Querstromfiltration zur Aufreinigung der VLPs bereits gut etabliert und wurde jüngst auch für die Weiterverarbeitung von VLP-Präzipitaten untersucht, da selektive Präzipitation bereits als initialer Aufreinigungsschritt dient, um VLPs aus geklärtem Lysat zu isolieren. Infolgedessen fokussieren sich gegenwärtige Bestrebungen in der Prozessentwicklung für VLPs auf die Integration, Intensivierung und Standardisierung von Prozessen, mit dem Ziel, deren Aufreinigungsprozesse zu optimieren.

Über die Standardanalytik hinaus ermöglicht das Konzept von Prozessanalytischer Technologie (PAT) die Echtzeitüberwachung und -steuerung kritischer Prozessparameter und Qualitätsattribute. Dies wird durch die Kombination fortschrittlicher Sensortechnologien und Chemometrie ermöglicht. Der gegenwärtige Entwicklungsstand von sensorbasierten PAT-Tools variiert, ebenso wie die Entwicklung von Aufreinigungsprozessen, je nach Trennverfahren und Biopharmazeutika. PAT-Tools basierend auf UV/Vis-Spektroskopie sind führend, um chromatographische Aufreinigungsschritte monoklonaler Antikörper zu überwachen, wobei diese Tools bereits auch auf Filtrationsprozesse, einschließlich solcher für VLPs, übertragen wurden. Doch die Entwicklung von PAT-Tools zur Überwachung von Präzipitationsprozessen, einschließlich der Präzipitation von VLPs, sowie für die LNP-Aufreinigung befindet sich noch in einem frühen Stadium und erfordert den Einsatz alternativer Sensortechnologien. Im Bereich der optischen Spektroskopie bieten streuungsbasierte Sensortechnologien wie die Raman-Spektroskopie und die dynamische Lichtstreuung (DLS) das Potenzial, die individuellen Herausforderungen in diesem Zusammenhang anzugehen.

Eine detailliertere Einleitung in das Forschungsfeld mit Verweisen auf die Literatur ist in Kapitel 1 dargelegt. Sie umfasst den theoretischen Hintergrund sowie die jüngsten Fortschritte und die bestehenden Wissenslücken. Wie in Kapitel 2 dargelegt, verfolgte diese Arbeit das Ziel, die Prozessentwicklung für die nicht-viralen Vektorklassen LNPs und VLPs durch (I) Trennverfahren auf Basis der Größenselektion sowie durch (II) sensorbasierte Analytik und PAT-Tools voranzutreiben. Mit dem Ziel standardisierter, skalierbarer und größenselektiver Aufreinigungsprozesse wurden Innovationen im jeweils initialen Aufreinigungsschritt durch die Integration von Querstromfiltration realisiert. Um zusätzliche Einblicke in die Prozesse zu gewinnen und damit das Prozessverständnis zu verbessern, wurden maßgeschneiderte Analytik- und PAT-Tools auf der Grundlage von Charged Aerosol Detection (CAD), DLS und Raman-Spektroskopie entwickelt. Die nachfolgend beschriebenen, aufeinander aufbauenden Studien zeigen, dass die Integration der Querstromfiltration eine effiziente Aufreinigung ermöglicht und dass die Analytik und PAT-Tools wertvolle Einblicke in diese Prozesse gewähren.

Für LNPs wird primär der mikrofluidische Mischschritt unter Anwendung von Standardanalyseverfahren zur Bestimmung der Partikelgröße, der Oberflächenladung und der Verkapselungseffizienz untersucht. Obwohl die Lipidzusammensetzung diese LNP-Attribute direkt beeinflusst, werden Lipide selten quantifiziert. Analysemethoden basierend auf der Umkehrphasen-Hochleistungsflüssigkeitschromatographie (RP-HPLC) in Kombination mit einem CAD zeigen eine hohe Selektivität und Sensitivität für Lipide. Daher wurde eine RP-HPLC-CAD-Methode entwickelt, um Lipide in LNPs entlang der Prozesskette zu quantifizieren (Kapitel 3). Die Methode ermöglichte eine genaue Lipidquantifizierung und lieferte das Lipidmolverhältnis als zusätzliches LNP-Attribut und die Lipidausbeute zu jedem Prozessschritt als wichtigen Parameter der Prozessleistung. Die Anwend-

barkeit und die Vorteile der Methode wurden anhand einer Prozessparameterstudie gezeigt, in der Variationen der Flussrate des mikrofluidischen Mischers gefolgt von einem Dialyseschritt untersucht wurden. Die Partikelgröße der LNPs zeigte in Übereinstimmung mit früheren Studien eine Flussratenabhängigkeit, während alle neuen Erkenntnisse aus der Lipidanalytik keine Flussratenabhängigkeit aufwiesen. Die Lipidkonzentrationen wiesen Abhängigkeiten bezüglich des Batchs und des Prozessschritts auf, während das Lipidmolverhältnis als konstant und batchunabhängig identifiziert wurde. Eine weitere Batchabhängigkeit wurde für die Lipidausbeute des Dialyseschritts festgestellt, welche in Verbindung mit Lipidverlusten steht. Die Lipidanalytik stellt folglich einen integralen Aspekt in der Prozessentwicklung zur Charakterisierung der LNPs und der Prozesse dar. Um neue Perspektiven für die Prozessentwicklung für LNPs zu eröffnen und das Prozessverständnis zu verbessern, kann die Lipidanalytik auch für den LNP-Aufreinigungsschritt mittels Querstromfiltration genutzt werden.

Obwohl die Querstromfiltration eine skalierbare, zeit- und kosteneffiziente Alternative zur Dialyse darstellt, um durch Pufferaustausch Restlösemittel zu entfernen und den pH-Wert einzustellen, ist die LNP-Aufreinigung mittels Querstromfiltration mit potentiell nachgelagerter, integrierter LNP-Aufkonzentrierung noch unerforscht. Dazu gehören die Einflüsse der Membraneigenschaften und der Prozessparameter auf die LNP-Attribute sowie die Echtzeitüberwachung des Prozesses. Dementsprechend wurde eine Parameterstudie durchgeführt, bei der zusätzlich die Partikelgröße der LNPs während der Querstromfiltration mittels DLS at-line überwacht wurde (Kapitel 4). In vier Experimenten wurden LNPs mittels Dialyse und Querstromfiltration zur direkten Vergleichbarkeit aufgereinigt, wobei die Querstromfiltration als Diafiltration mit konstantem Volumen gefolgt von Ultrafiltration durchgeführt wurde. Trotz systematischer Variation bestimmter Membraneigenschaften und Prozessparameter konnte kein konsistenter Einfluss auf die LNP-Attribute festgestellt werden. Auch die entwickelte RP-HPLC-CAD-Methode (vgl. Kapitel 3) ermittelte konstante Lipidmolverhältnisse und Lipidausbeuten. Allerdings wurde eine lineare Abhängigkeit der Partikelgröße der LNPs von der Prozesszeit der Querstromfiltration festgestellt, die durch die Überwachung mittels at-line DLS in Quasi-Echtzeit bestätigt wurde. Die Unterschiede in der Partikelgrößenveränderung zwischen den mit der Dialyse oder der Querstromfiltration aufgereinigten LNPs führten zur Aufstellung einer Hypothese, die auf Wechselwirkungen zwischen pumpeninduzierten Scherkräften, Fusion und Gleichgewichtsgröße der LNPs basiert. In dieser Studie wurden somit neue Erkenntnisse zur LNP-Aufreinigung mittels Querstromfiltration gewonnen. Neben den noch zu klärenden Mechanismen der Partikelgrößenzunahme deuten diese Erkenntnisse auf eine zukünftige größenregulierte LNP-Aufreinigung mittels Querstromfiltration hin.

In Bezug auf die Größenselektivität der Querstromfiltration nutzt auch die Präzipitation den Größenunterschied zwischen Produkt und Verunreinigungen. Für den initialen VLP-Aufreinigungsschritt aus geklärtem Lysat hat sich die Kombination aus selektiver Präzipitation und querstrombasierter Mikrofiltration (MF) für die Weiterverarbeitung des Präzipitats als vorteilhaft erwiesen. Die filtrationsbasierte Weiterverarbeitung adressiert die Skalierbarkeit, Integration und Intensivierung dieses Prozesses und führt zu einer gesteigerten Produktivität, Reinheit und Ausbeute im Vergleich zur VLP-Rückgewinnung mittels Zentrifugation. Hierbei werden in derselben Querstromfiltrationseinheit zwei aufeinanderfolgende Dialfiltrationsschritte durchgeführt. Zunächst wird das Präzipitat gewaschen, um Verunreinigungen zu entfernen. Anschließend werden die VLPs zurückgelöst, sodass diese die MF-Membran passieren und somit von zurückgehaltenen Verunreinigungen getrennt werden. Allerdings weist das Permeat Einschränkungen bezüglich der VLP-Konzentration und der Reinheit auf, die auf die diafiltrationsinduzierte Verdünnung sowie das Vorhandensein von restlichem Fällungsmittel zurückzuführen sind. Zur Optimierung der VLP-Konzentration und der Reinheit durch

Prozessintegration wurde ein neuer zweistufiger Filtrationsaufbau für die integrierte, nahtlose Rückgewinnung von VLP-Präzipitat entwickelt (Kapitel 5). Die erste Querstromfiltrationseinheit wurde mit einer zweiten Einheit verbunden, welche mit einer Ultrafiltrationsmembran (UF-Membran) ausgestattet wurde. Der zweistufige Filtrationsaufbau unter Einsatz der MF/UF-Membrankombination ermöglichte während der VLP-Rücklösung die Isolation der VLPs in der zweiten Membranstufe. Die VLPs wurden hierbei an der UF-Membran zurückgehalten, während das restliche Fällungsmittel diese passierte. Neben der Entfernung des Fällungsmittels wurden auch rückgelöste Verunreinigungen entfernt. Der zweistufige Filtrationsaufbau unter Verwendung einer MF/UF-Membrankonfiguration bildet somit die Grundlage für eine standardisierte Weiterverarbeitung von Präzipitat. Darüber hinaus sind vielversprechende zukünftige Anwendungen für verschiedene VLPs und Biopharmazeutika sowie eine potenzielle Übertragbarkeit auf Kristallisationsprozesse gegeben.

Die ohnehin signifikant hohe Verunreinigungslast in initialen Aufreinigungsprozessen wird durch selektive Präzipitation naturgemäß durch die Zugabe eines Fällungsmittels ergänzt. Dies hat die Entstehung von partikulären Präzipitaten und Trübung zur Folge, wodurch eine direkte Quantifizierung des Produkts unmöglich wird. Dies resultiert in besonderen Herausforderungen für die Entwicklung sensorbasierter PAT-Tools. In solchen Umgebungen stoßen die weit verbreiteten PAT-Tools basierend auf UV/Vis-Spektroskopie und Chemometrie an ihre Grenzen, während die Raman-Spektroskopie eine vielversprechende Sensoralternative darstellt. Allerdings sind tiefgreifende Einblicke in die Datengenerierung und spektrale Datenverarbeitung für die wissensbasierte Entwicklung von Raman-basierten PAT-Tools nach wie vor relativ selten. Daher wurde ein systematischer Ansatz für die Entwicklung eines Raman-basierten PAT-Tools verfolgt, um die VLP-Präzipitation zu überwachen (Kapitel 6). Um eine Diversifizierung der Daten zu gewährleisten, wurden Batch- und Fed-Batch-Präzipitationsexperimente mit konditioniertem Lysat durchgeführt. Dies resultierte in gezielten Variationen in der Präzipitationsdynamik und der Hintergrundzusammensetzung. Mittels einer systematischen Kombination von Operationen für Spektraldatenverarbeitung und der Analyse spektraler Merkmale wurde die Wirksamkeit dieser Operationen bei der Beseitigung von Unterschieden im spektralen Hintergrund sowie von Störungen durch das Vorhandensein von Präzipitat und Trübungen bewertet. Die Konzentration der VLP-Präzipitate wurde mithilfe verarbeiteter Raman-Spektraldaten und einer Partielle Kleinste-Quadrate (PLS)-Regression vorhergesagt. Zudem wurde die Modellleistung unter Berücksichtigung der Auswirkungen einzelner Datenverarbeitungsoperationen bewertet. Raman-basiertes PAT ermöglicht somit die Überwachung der VLP-Konzentration während der Präzipitation in partikulärem, trübem Lysat. Die im Rahmen des bewusst systematischen Entwicklungsansatzes gewonnenen Erkenntnisse betonen die Relevanz der Datendiversifizierung und der gezielten spektralen Datenverarbeitung auch für zukünftige Entwicklungen von Raman-basierten PAT-Tools.

Im Vergleich zur kontrollierten Zugabe eines Fällungsmittels in Batch- und Fed-Batch-Präzipitationsprozessen sollte die Abreicherung an Fällungsmittel in dynamischen Prozessen durch Fällungsmittelquantifizierung überwacht werden, beispielsweise während der filtrationsbasierten VLP-Rückgewinnung unter Verwendung des vorgestellten zweistufigen Filterationsaufbaus (vgl. Kapitel 5). Darüber hinaus ist die Quantifizierung der sich akkumulierenden rückgelösten VLPs von besonderem Interesse. Allerdings führt die Probenahme während des Diafiltrationsprozesses zu Produktverlusten und stört dessen Dynamik. Die Entwicklung von PAT-Tools zur gleichzeitigen Überwachung von zwei Komponenten aus denselben erfassten Spektraldaten profitiert eindeutig von einem solchen systematischen Entwicklungsansatz, wie er für die Überwachung der VLP-Präzipitation vorgestellt wurde (vgl. Kapitel 6). Eine Einschränkung, die in diesem Zusammenhang beobachtet wurde, betraf

die Übertragbarkeit von Raman-basierten PAT-Tools, die aus den Batch-Experimenten abgeleitet wurden, auf die Überwachung der Fed-Batch-Experimente. In Prozessen, in denen weniger spektrale Interferenzen zu erwarten sind, könnte die Modellübertragung jedoch gelingen. Im Rahmen der Modellübertragung wurden Raman-basierte PAT-Tools aus Stammlösungen reiner Komponenten für die gleichzeitige Überwachung der VLP-Akkumulation und der Fällungsmittel-Abreicherung im filtrierungsbasierten VLP-Rückgewinnungsschritt entwickelt (Kapitel 7). Die Untersuchung der spektralen Beiträge der VLPs und des Fällungsmittels unter Verwendung von Spektren reiner Komponenten ergab attributspezifische spektrale Merkmale sowie eine höhere inhärente Sensorempfindlichkeit gegenüber dem Fällungsmittel im Vergleich zu den VLPs. Dementsprechend wurden attributspezifische Datenverarbeitungsoperationen ausgewählt, um diese Unterschiede sowie auch Detektorsättigungseffekte zu berücksichtigen, und es wurden mehrere Regressionsmodelle mit verarbeiteten Spektraldaten erstellt. Gleichzeitig wurde der zweistufige Querstromfiltrationsaufbau mit einem Raman-Spektrometer innerhalb einer On-line-Überwachungsschleife in der zweiten Membranstufe ausgestattet, und Prozessspektraldaten wurden aus drei diversifizierten Filtrationsexperimenten erfasst. Aus den erfassten Spektraldaten wurden die Konzentrationen von VLP und Fällungsmittel unter Anwendung der übertragenen Modelle vorhergesagt. Die Tatsache, dass die endgültige Vorhersagegenauigkeit für das Fällungsmittel höher war als für die VLPs, trotz attributspezifischer Auswahl der Datenverarbeitungsoperationen und Modelle, verdeutlichte die Relevanz einer attributspezifischen Sensorauswahl. In dieser Studie wurde die Modellübertragung durch die systematische Entwicklung von Raman-basierten PAT-Tools demonstriert, wodurch die entscheidende Rolle der attributspezifischen Sensorauswahl für die zukünftige Entwicklung von PAT-Tools hervorgehoben wird.

In der vorliegenden Arbeit wurden Fortschritte in der Entwicklung von Aufreinigungsprozessen durch die Integration von Trennverfahren basierend auf Größenselektivität und sensorbasierten PAT-Tools präsentiert, die speziell auf den jeweiligen initialen Aufreinigungsschritt der derzeit führenden nicht-viralen Vektorklassen LNPs und VLPs zugeschnitten sind. Trotz der Unterschiede im Entwicklungsstand zwischen der Prozessentwicklung für LNPs und VLPs ermöglichte die maßgeschneiderte Integration der Querstromfiltration eine effiziente Aufreinigung, und Analyse- und Prozessüberwachungswerkzeuge lieferten wertvolle Einblicke in den Prozess. Die vorgestellten methodischen und systematischen Ansätze weisen insgesamt das Potenzial auf, auf andere Biopharmazeutika oder Prozesse übertragen zu werden. Zusammenfassend betonen diese Fortschritte das Potenzial der größenselektiven Aufreinigung und der streuungsbasierten Sensortechnologien, um die spezifischen Herausforderungen im Zusammenhang mit neuartigen Vektortechnologien zu bewältigen und gleichzeitig das übergeordnete Ziel der Verbesserung des Prozessverständnisses in der biopharmazeutischen Prozessentwicklung zu unterstützen. Solche Entwicklungen legen den Grundstein für eine künftig standardisierte und geregelte Aufreinigung von Vektoren in der biopharmazeutischen Industrie.

Contents

1

Introduction

Biologics classified as biopharmaceuticals have transformed modern medicine by addressing unmet medical needs and will continue to shape its future, as they have laid the groundwork for further innovations. As biopharmaceuticals possess considerably higher structural and functional complexity compared to conventional pharmaceuticals, they pave the way for the prevention or targeted treatment of complex, previously untreatable diseases, most notably autoimmune, infectious, and genetic diseases, as well as cancer. To date, a broad spectrum of platform technologies has emerged beyond the use of recombinant proteins and naked nucleic acids, as further exemplified by the significant advances in vaccine technology.

While traditional vaccines have relied on live-attenuated, inactivated, or isolated subunits of pathogens, genetically engineered vaccines have rapidly expanded the vaccine portfolio during the last 40 years [1]. Genetically engineered vaccines deliver either a protein or its genetic code to trigger an immune response. In 1986, the first genetically engineered vaccine targeting hepatitis B was approved [1], which was developed through the recombinant expression of its surface proteins [2]. These spontaneously assemble into virus-like particles (VLPs) that mimic the native virus structure. Since then, extensive research has led to the approval of several other VLP-based vaccines targeting hepatitis B, cervical cancer, and hepatitis E [3]. Promising developments have also been reported towards future applications as nanocarriers for nucleic acid delivery [4]. In contrast, viral vectors use harmless viruses to deliver the genetic code of the protein as a transgene. While viral vector technology has been under investigation for decades, its use in vaccines did not emerge until the 2010s, with prominent examples targeting Ebola and SARS-CoV-2 [5]. Most recently, the lipid nanoparticle (LNP)-based messenger RNA (mRNA) technology has emerged with vaccines against SARS-CoV-2 [6], which enable the protected delivery of the mRNA encoding the protein.

As such, the high flexibility of genetic engineering has given rise to a variety of vector technologies for protected delivery. With significantly lower safety concerns than viral vectors [7–9], VLPs and LNPs as leading non-viral vectors represent versatile platform technologies with promising

applications as vaccines and in gene therapy [3, 4, 10]. These nanocarriers are larger in size and exhibit greater structural complexity and diversity compared to traditional biopharmaceuticals such as monoclonal antibodies, creating an urgent demand for alternative processing techniques. Although the downstream processing (DSP) requirements of VLPs and LNPs vary fundamentally due to the differences in their structure and production processes, separation is still the core objective. The recombinant production of VLPs necessitates a cascade of DSP steps to remove both process- and product-related impurities and, if required, to encapsulate the payload prior to formulation [11]. The DSP of the synthesized, loaded LNPs primarily aims to remove residual organic solvent in addition to formulation [12]. Beyond meeting fundamental process requirements such as reproducibility, scalability, and efficiency, size-selective separation techniques particularly accommodate the large size of nanocarriers, thereby facilitating universal processing and laying the groundwork for standardization across their structural diversity. For VLPs and viral vectors, size-selective separation techniques include tailored chromatographic methods based on size exclusion, steric exclusion, or multimodal size exclusion [13]. However, chromatography faces the challenge of limited loading capacities [11]. Complementary, precipitation and filtration represent non-chromatographic, size-selective separation techniques, with cross-flow filtration (CFF) being explored for the processing of both VLPs and LNPs as protein-based and lipid-based vectors, respectively. However, CFF process development for LNPs is still in its early stages, and process understanding remains far from complete, which could be significantly improved through dedicated development studies and in-process analytics. Moreover, process integration and intensification hold strong potential to streamline DSP of VLPs.

Since the process is closely linked to the quality attributes of a biopharmaceutical, process understanding is key to ensuring consistent product quality. Within the framework of process analytical technology (PAT) [14], the development of sensor-based PAT tools enables real-time monitoring and control of critical process parameters and quality attributes. The maturity of sensor-based PAT tool development for DSP monitoring varies across different separation techniques and biopharmaceuticals, with ultraviolet-visible (UV/Vis) spectroscopy-based PAT tools for chromatographic separation of monoclonal antibodies being by far at the forefront [15]. The principle of UV/Vis-based PAT can indeed be transferred to VLPs due to their protein structure and has already been applied for filtration processes [16, 17]; however, UV/Vis spectroscopy is not applicable for particulates such as precipitates. Scattering-based Raman spectroscopy has been reported for monitoring of protein precipitation [18] or filtration [19, 20], but deeper insights into the spectral data and their preprocessing by chemometrics are generally rare. Compared to VLPs, LNPs require an alternative analytical approach due to their non-chromophoric, lipid-based structure, with dynamic light scattering (DLS) being the standard analysis for particle size. Accordingly, the development of scattering-based PAT tools for monitoring non-chromatographic, size-selective separation processes of non-viral vectors holds potential to enhance process understanding.

The following subchapters provide the theoretical background, recent advancements, and remaining research gaps in the field, and cover LNPs and VLPs as non-viral vectors (Chapter 1.1), precipitation and CFF as non-chromatographic, size-selective separation techniques for biopharmaceutical DSP (Chapter 1.2), and sensor-based analytics and PAT tools for process monitoring (Chapter 1.3).

1.1 Non-Viral Vectors

1.1.1 Lipid Nanoparticles

LNPs represent a lipid-based vector technology, characterized by an inverted micellar structure exhibiting non-continuous lipid bilayers and an electron-dense core [12, 21]. With these characteristics, they are distinguished from liposomes, which consist of a continuous lipid bilayer enclosing an aqueous core [12]. The progression in lipid-based technology from liposomes to LNPs was driven by the objective to encapsulate nucleic acids for protected delivery. Encapsulation of nucleic acids in LNPs is achieved through charge interactions with cationic or ionizable lipids [21], which can constitute up to 50% of certain formulations. Onpattro® (patisiran) was the first approved LNP-based technology for small interfering RNA (siRNA)-mediated gene silencing, followed by the technology transfer to the mRNA vaccines, Comirnaty® and Spikevax®, accelerated by the COVID-19 pandemic [6]. To date, about 30 other LNP-based vector technologies for both prophylactic and therapeutic purposes have already progressed beyond Phase I clinical trials [10].

In general, structural functionality is driven by their structural components, and hence lipid selection and lipid molar ratio [22]. Next to nucleic acid encapsulation, the selection of cationic or ionizable lipids has been shown to influence particle size [23] and potency [24–26]. The ratio of nitrogen from the cationic or ionizable lipids to phosphate from the nucleic acid backbone is known as the N/P ratio, and variations have been shown to influence particle structures and encapsulation efficiencies [27–29]. The primary functions of the other lipid components are stability provided by the helper lipid [21, 30], lipid packing facilitated by cholesterol [30], and shielding and particle size control by the polyethylene glycol (PEG)ylated lipid [28, 31, 32]. Given the impact of particle size on LNP pharmacokinetics [33], LNP production and processing should aim to ensure precise control of particle size.

Conventional production methods, such as ethanol injection or thin-film hydration followed by size reduction methods, are similar to those used for liposomes, but suffer from limitations in reproducibility and scalability [12]. Improved strategies based on microfluidic mixing of a lipid-containing organic phase with an acidic, nucleic acid-containing aqueous phase have since been introduced [12], with direct impacts of the phase [23, 29, 34] and mixing process characteristics [23, 29, 34, 35] on the particle size of LNPs, with the latter including the total flow rate (TFR) and flow rate ratio (FRR). Although dialysis is routinely applied on laboratory scale to raise the pH and remove residual organic solvent, its specific impact on particle characteristics remains poorly investigated, aside from studies focusing on the influence of buffer pH [34]. In contrast to diffusion-driven dialysis, pressure-driven processing by CFF offers scalability, improved resource efficiency, and integrated product concentration [36]. As outlined in Section 1.2.2, specific CFF process parameters and their associated phenomena may impact LNP characteristics, which, aside from two recent studies [37, 38], remain largely unexplored.

1.1.2 Virus-Like Particles

VLPs are virus-mimicking structures formed by viral subunit proteins with an inherent property to self-assemble, but without any genetic material, rendering them non-replicative and non-infectious [39]. The highly ordered repetitive structures confer higher immunogenicity than the soluble subunit proteins [39, 40]. Functional versatility of the VLPs is driven by their structural diversity, with classifications into enveloped and non-enveloped VLPs, each composed of single or multiple

subunit proteins and layers [3]. In the following, 'VLPs' refers to non-enveloped capsids formed by a single type of subunit protein, serving as a protein-based vector technology. VLP vaccines against the native virus rely on its unmodified viral subunit protein [41], such as Gardasil®, Gardasil9®, and Cervarix® against human papillomavirus-induced cervical cancer and genital warts [42, 43]. Chimeric and packaged VLPs are promising delivery systems for both prophylactic and therapeutic purposes. Chimeric VLPs are defined as VLPs that use the virus-mimicking structure as a scaffold to present heterologous epitopes or antigens on their surface [4], which have been either introduced through genetic fusion [44] or post-translational conjugation [45]. Furthermore, VLPs can act as nanocarrier for targeted delivery by encapsulating proteins or nucleic acids [4], with the latter having potential future applications in gene therapy.

Several viruses can serve as a scaffold for VLPs, including the hepatitis B virus, which has a nucleocapsid composed of Hepatitis B core Antigen (HBcAg) proteins. HBcAg VLPs represent the earliest VLP technology [46, 47], with capsid proteins expressed in *Escherichia coli* (*E. coli*). They are characterized by an icosahedral capsid symmetry with typically 180 or 240 assembled HBcAg proteins, resulting in a particle size of 30 nm or 34 nm, respectively [48]. Over the years, various modifications of the wild-type HBcAg have been explored, including terminal truncations or extensions [49–52], as well as internal insertions [53–55], to tailor the functionality of the HBcAg VLPs. Compared to other expression systems, recombinant expression of capsid proteins in *E. coli* offers several advantages, as *E. coli* represents a cost-efficient, well-characterized expression system that provides high scalability, productivity, and yields [40, 56]. However, due to the absence of a secretion mechanism, a cell lysis step is required to release the self-assembled, intracellularly accumulated VLPs. The resulting high impurity burden after initial clarification, combined with the vast diversity of VLPs, significantly compromises the establishment of standardized platform processes in DSP [57].

To remove process-related impurities, purification is either performed with the capsid proteins or the assembled VLPs [58]. Capsid protein purification may require additives such as reducing or chaotropic agents to prevent premature assembly, followed by *in vitro* assembly [59, 60]. For assembled VLP purification, however, the application of conventional protein purification techniques is limited due to their large size [57]. With size-selective separation techniques, their considerably larger size compared to process-related impurities can be exploited, thereby extending applicability to various modalities and replacing traditional density gradient centrifugation, which is known for its limitations in scalability, automation, and productivity [11, 57]. Although tailored chromatographic methods based on size exclusion, steric exclusion, or multimodal size exclusion exist [13], precipitation has emerged as a broadly applicable, non-chromatographic, size-selective separation technique for universal VLP capture (cf. Section 1.2.1), with integrated CFF-based precipitate processing and recovery (cf. Section 1.2.2).

Depending on the application, the removal of product-related and encapsulated process-related impurities requires further polishing steps beyond chromatography [11]. By altering environmental conditions, *in vitro* VLP disassembly and reassembly can be achieved, which has already been performed using CFF [16, 17, 61]. In addition to increasing purity, the latter steps contribute to improved structural homogeneity, stability, and enhanced immunogenicity [62, 63]. Furthermore, prior encapsulated process-related impurities can be removed [64–66], thereby making binding sites accessible when they exist, to enable the subsequent encapsulation of the payload [65, 67, 68], such as nucleic acids, for delivery.

1.2 Size-Selective Separation in Biopharmaceutical Downstream Processing

Size-selective separation techniques are highly versatile for applications in biopharmaceutical DSP, especially for the universal processing of large molecules, such as viral and non-viral vectors. Processing with these techniques addresses one or more of the objectives: product purification, buffer exchange, and product concentration. Tailored chromatographic techniques based on size exclusion, steric exclusion, or multimodal size exclusion are employed for the purification of protein-based vectors [13]. Precipitation and filtration represent non-chromatographic, size-selective separation techniques, with filtration being explored for the processing of both protein-based and lipid-based vectors. The following sections focus on the principles and applications of precipitation (Section 1.2.1) and CFF (Section 1.2.2) in biopharmaceutical DSP.

1.2.1 Precipitation

Protein precipitation is classified as a solubility-driven separation technique, in which exceeding the solubility limit leads to the formation of disordered amorphous precipitates.

The solubility of proteins in solutions depends on protein-solvent and protein-protein interactions, with predominant solubility-promoting repulsive forces between proteins [69]. These interactions depend on protein characteristics, such as size, surface charge, and surface hydrophobicity, protein concentration, and external factors, including temperature, pH, ionic strength, and additives [70–73]. The addition of precipitants, such as polymers and salts, creates a supersaturation state and directly affects protein-protein interactions [69]. Supersaturation drives both controlled crystallization and spontaneous, fast precipitation. At very high supersaturation, the critical nucleus size required for sustained crystal growth of highly ordered crystal structures is smaller than the smallest structural unit, and disordered amorphous precipitates form instead [69]. Polymers such as PEG initiate protein precipitation by volume exclusion [74], with its fundamentals, latest advancements, and future directions comprehensively reviewed by Pons Royo et al. [75]. Salts in higher concentrations reduce the solubility of proteins (salting out) by competing for water molecules and disrupting their hydration layers, thereby exposing their hydrophobic surfaces [76, 77]. Salt ions differ in their ability to stabilize (kosmotropic) or destabilize (chaotropic) native protein structures, as reflected in the Hofmeister series [78, 79]. Since the native protein structure should be preserved during protein precipitation, salts containing kosmotropic ions are selected, such as ammonium sulfate (AMS) [80].

Precipitation is a cost-effective, scalable separation technique that can be implemented in continuous mode. In biopharmaceutical processing, selective precipitation has emerged as an alternative separation technique for capturing the target protein from clarified lysate. The considerable size difference between VLPs and host-cell impurities favors their selective precipitation, as larger proteins are more susceptible to precipitation [70]. Next to PEG-induced precipitation of Ty-VLPs [81] and norovirus VLPs [82], selective precipitation by AMS has been reported for human papillomavirus VLPs [83, 84], different HBcAg VLPs [51, 52, 85, 86], and other VLPs derived from plant viruses or bacteriophages [87]. To optimize the design of a precipitation step with regard to purity and yield, precipitation curves are generated by screening additive concentrations. The gradual addition of the precipitant is recommended to minimize concentration spikes, which affect precipitate formation and co-precipitation, and hence purity [75]. The impact of protein surface characteristics on VLP precipitation is highlighted by Valentic et al. [52], who reported a

comparable precipitation behavior for HBcAg VLPs differing in the lengths of their internally located nucleic acid binding regions and bound nucleic acids, which distinctly differs from the behavior of a chimeric HBcAg VLP [88]. Spiking studies are particularly useful for identifying factors that affect precipitation behavior, such as the reported composition of contaminants, which influences the purity and yield of monoclonal antibody precipitation [89]. Such screening studies often rely on systematic high-throughput experiments, but require the separate analysis of each individual species in the precipitate-free supernatant. An analytical, model-based approach has been introduced by coupling a calibration-free, chemometric model with spectral data to predict individual species concentrations, which was applied, among others, for HBcAg VLP precipitation [90]. For in-silico process design, machine learning approaches have been developed based on hydrophobicity scales and amino acid sequences to predict the solubility of various chimeric HBcAg VLPs [91] and the required ammonium sulfate concentration for their precipitation [92].

Traditional precipitate recovery involves centrifugation and manual resuspension of the pellet, suffering from high batch-to-batch variation and low productivity. Recent advancements have been made in precipitate processing and recovery by CFF, thereby addressing process scalability, integration, and intensification, as outlined in Section 1.2.2.

1.2.2 Cross-Flow Filtration

CFF is classified as a membrane filtration technique and operates in a tangential flow configuration, with a feed flow tangentially directed along the membrane surface.

According to Darcy's law [93], the permeate flux J is proportional to the transmembrane pressure (TMP), which represents the primary driving force in CFF, and is given by

$$J = L_\mathrm{p} \Delta p_\mathrm{Mem} = \frac{\Delta p_\mathrm{Mem}}{\eta R_\mathrm{h}}, \tag{1.1}$$

with L_p denoting the membrane permeability, η denoting the dynamic viscosity, and R_h denoting the intrinsic membrane resistance. The TMP is defined as the average pressure difference across the membrane according to

$$\Delta p_\mathrm{Mem} = \frac{p_\mathrm{Feed} + p_\mathrm{Ret}}{2} - p_\mathrm{Per}. \tag{1.2}$$

The pressures of feed, retentate, and permeate are denoted as p_Feed, p_Ret, and p_Per, respectively. The effective permeate flux is calculated by dividing the volumetric flow rate of the permeate stream by the membrane surface area, as the presence of solutes in the solvent introduces behavioral changes.

Using conventional CFF, where the retentate stream containing the retained target molecule is recycled, the target molecule is concentrated by volume reduction, and buffer exchange can be achieved through sequential volume reduction and dilution [36]. By contrast, the process configuration of constant-volume diafiltration (DF) enables seamless processing by replacing the permeate passed through the membrane with an equal volume of diluent. The progress of buffer exchange is stated in diafiltration volumes (DVs), with one DV corresponding to the addition of a diluent volume equal to the initial retentate volume. During solute separation by constant-volume DF, the solute concentration in the retentate c_Ret decreases according to

$$c_\mathrm{Ret} = c_0 \exp\left(-n_\mathrm{DV} S\right), \tag{1.3}$$

with initial retentate concentration c_0, the amount of DV n_{DV}, and the intrinsic sieving coefficient S. The intrinsic sieving coefficient relates to the solute concentrations in the permeate and on the membrane surface, providing information on the solute-specific permeability of the membrane, which is influenced by both the solute and membrane characteristics [94]. Recent advancements have been made in model development to account for non-ideality phenomena such as the Gibbs–Donnan effect and volume exclusion, as such effects lead to measurable deviations in solute concentrations and pH under practical conditions [95–97].

Since CFF productivity relies on permeate flux, it is directly influenced by TMP and membrane permeability (Equation 1.1). Membrane permeability is primarily affected by fouling, which is aimed to be mitigated by a high ratio of feed to permeate flow rate [98]. A high feed flow rate further reduces concentration polarization, which also poses a risk of fouling; however, it must be balanced against shear-induced product degradation. Concentration polarization describes the formation of a concentration boundary layer at the membrane surface, which further increases the osmotic backpressure counteracting the TMP, and hence reduces the permeate flux [99]. Beyond its direct impact on osmotic backpressure, concentration polarization can, upon reaching the gel concentration, cause gel layer formation, which constitutes an additional resistance to permeate flux. Such phenomena must be taken into account when mathematically describing the permeate flux, which has led to various modeling approaches, as thoroughly reviewed by Quezada et al. [100].

The CFF membrane is selected according to the separation objective. Microfiltration (MF) membranes with pore sizes between 0.05 µm and 10 µm are used for solid-liquid separations, with CFF-based MF providing a efficient and scalable alternative to centrifugation [36] while offering process integration and intensification. For clarification of crude lysate, CFF-based MF offers single-use compatibility [101] and provides integrated sterile filtration of the product-containing permeate stream if using a 0.2 µm cut-off [36]. For precipitation-based capture, several advancements have been reported for the processing and recovery of precipitates. If using CFF-based MF for washing of precipitates, the precipitates remain in the retentate while the impurities pass the membrane, allowing the removal of additional contaminants that would otherwise remain in the interstitial pellet liquid due to compaction by centrifugation [102–104]. In addition to higher purity, the dilution-based re-dissolution to recover the product exhibits much faster kinetics compared to the resuspension of a compacted pellet. Continuous precipitate washing has been achieved using serial MF configurations [105, 106], with further advancements in wash efficiency through countercurrent washing [107, 108]. Precipitate processing with a vibration-assisted single-pass CFF has been recently investigated, demonstrating potential for higher CFF productivity in continuous washing and concentration of precipitates [109]. To overcome precipitate re-dissolution by dilution, Hillebrandt et al. [88] performed an integrated DF step on the MF-equipped CFF unit, employing a re-dissolution buffer as diluent. As the re-dissolved product passes through the MF membrane and is thereby separated from irreversibly precipitated species, product purity has been improved; however, limitations remain regarding product concentration and residual precipitant. In summary, CFF-based MF has been applied in early DSP for VLPs to clarify crude lysate [101] and recover precipitated VLPs [88], replacing centrifugation-based solid-liquid separation.

For solute separations, ultrafiltration (UF) membranes with pore sizes ranging from 1 nm to 20 nm are used, with a molecular weight cut-off (MWCO) corresponding to a 90% retention of a molecule at that molecular weight [36]. As the target molecule is retained, UF membranes are widely employed across biopharmaceutical DSP, mostly for product concentration or buffer exchange, with the

latter replacing size exclusion chromatography [110]. For buffer exchange, CFF-based DF offers significant advantages over diffusion-driven dialysis, including reduced buffer consumption, shorter processing times, scalability [36], and seamless integration of volume reduction while maintaining high productivity. Although CFF-based UF would therefore be highly suitable for LNPs to remove the solvent, exchange the buffer, and concentrate the particles, studies on CFF process development are limited. Geng et al. [37] employed a two-step CFF process for initial ethanol removal prior to buffer exchange and found improved mRNA-LNP characteristics. Wu et al. [38] varied CFF membrane and process parameters for mRNA-LNP processing and compared process performances. Given the commonly reported shear sensitivity of lipid-based particles, the effects of desired CFF membrane and process parameters on LNP characteristics remain poorly understood.

In solute separation, solutes refer to solvents, buffer components, and salts, but may also include other excipients or impurities. For VLPs, CFF-based UF has also been used for impurity removal during capture and purification, employing a two-step approach [111], or to induce protein structural changes during polishing steps. The latter includes studies on the disassembly of VLP capsids into subunits [17, 61] and VLP reassembly [16], with CFF-based UF representing an alternative to dilution or resource-consuming dialysis. Further, the assembly of purified VLP subunits and VLP formulation has been integrated using CFF-based UF [59].

For process monitoring and control, the CFF unit is equipped with flow and pressure sensors, since CFF processes are typically operated under constant TMP or permeate flux. However, insights into CFF-based processes beyond these standard process parameters typically require manual sampling for off-line sample analysis. To overcome product loss, prevent time delays, and enhance process understanding, implementing additional sensors is advised by the FDA [14].

1.3 Process Analytical Technology

PAT was introduced as a regulatory initiative by the FDA in 2004 [14], providing a framework for designing, analyzing, and controlling pharmaceutical manufacturing processes to ensure consistent product quality. To build quality into products, the integration of PAT tools is advised to enhance process understanding, among others, by first identifying the relationships between product and process variables and critical quality attributes [14]. Sensor-based PAT tools enable real-time monitoring and control of critical process parameters and quality attributes, achieved through at-line, on-line, or in-line implementation of process analyzers [112, 113]. For at-line measurement, a process sample is manually taken and immediately analyzed next to the process itself. For on-line or in-line measurements, the process analyzer is implemented into a temporarily divided product stream or directly into the product stream, respectively. With on-line or in-line integration, higher measurement frequencies can be realized, and process intervention and product loss are avoided [112, 113].

The maturity of sensor-based PAT tool development for process monitoring varies across different biopharmaceuticals. While substantial progress has already been made for protein-based biopharmaceuticals [15, 114], the development of sensor-based PAT tools for LNP process monitoring has received limited attention so far. The differences in developmental maturity of sensor-based PAT tools may be attributed, at least in part, to the relatively recent emergence of the LNP technology. Comparing the analytical strategies employed for lipid-based and protein-based non-viral vectors, exclusively focusing on the characterization of the carrier (lipids and proteins), they differ sub-

stantially according to the carrier structure. While LNPs are characterized as particle systems consisting of individual lipid components, VLPs are characterized across structural levels of primary, secondary, tertiary, and quaternary protein structure, accessible by optical spectroscopy.

1.3.1 From HPLC-Based Analysis to Optical Spectroscopy

High performance liquid chromatography (HPLC) is regarded as a versatile and powerful technique for quantitative analysis, supporting the automated analysis of minimal sample volumes with high accuracy and reproducibility. As a broad range of analytical chromatography columns can be coupled with detectors, it offers the flexibility to optimize selectivity and sensitivity towards the analytes of interest.

UV/Vis detectors are used for proteins as proteins contain several so-called chromophores, such as aromatic amino acids within their primary structure [115]. UV/Vis spectroscopy is based on the absorption of light, providing characteristic absorbance spectra with the absorption intensity over the wavelengths [115]. The phenomenon of light absorption describes an electronic transition, as valence electrons from the molecule are promoted from the ground state to an excited state. The absorbance $A_{\lambda,i}$ of a pure component i at a wavelength λ is logarithmically correlated to the light transmission I_0/I, with the measured initial and final intensities, I_0 and I, respectively. The absorbance $A_{\lambda,i}$ is linearly correlated with the component concentration c_i according to the Beer-Lambert law [116]. As proteins exhibit a mean absorbance maximum at 280 nm, $A_{280,i}$ is used for quantification of the prior separated components [115]. Compared to proteins, several lipids lack chromophores, which is why aerosol-based detectors are employed for universal, quantitative HPLC analysis of lipids, independent of their spectral or physicochemical characteristics.

Charged aerosol detection (CAD) is based on mass detection, and, similar to evaporative light scattering detection (ELSD), the volatile liquid phase is nebulized into aerosol particles and evaporated to detect the dried particles [117]. For CAD, the dried particles are charged by ionized nitrogen, and the charge is subsequently measured by an electrometer [117, 118]. Compared to ELSD, CAD is less sensitive to particle size, and hence provides a higher sensitivity, higher precision, and wider linearity range [119]. CAD has already been used for HPLC-based quantification of lipids in LNP formulations [120–124]. As a destructive technique, however, HPLC-CAD analytics is limited to off-line or at-line measurements.

Far more employed is the development of sensor-based PAT tools for (near) real-time monitoring based on optical spectroscopy [15, 114] without the need for prior HPLC-based separation of the components, thereby effectively eliminating time delays. Optical spectroscopy implies various non-destructive techniques, hence supporting on-line or in-line integration. In optical spectroscopy, the interaction between electromagnetic radiation and matter, or light and molecules, is studied by measuring the physical processes of absorption, emission, or scattering of light [125]. UV/Vis, near-infrared (IR), and mid-IR spectroscopy are based on absorption of light, excited by a broadband light source. Contrarily, fluorescence spectroscopy relies on the subsequent emission of monochromatic laser light. The following sections focus on DLS (Section 1.3.2) and Raman spectroscopy (Section 1.3.3), which are based on elastic and inelastic light scattering, respectively.

1.3.2 Dynamic Light Scattering

DLS is based on elastic light scattering, providing the hydrodynamic particle size and size distribution by measuring the intensity fluctuations of the scattered light over time [126].

The phenomenon of elastic light scattering describes the scattering of light in which the scattered photons retain the same energy as the incident photons. Rayleigh scattering predominates for particle systems with particle sizes much smaller than the wavelength of the incident light. The Brownian motion of the particles causes intensity fluctuations of the scattered light over time [126]. By autocorrelating these intensity fluctuations, a mean diffusion coefficient D is determined, which is used to calculate the hydrodynamic radius r_{H} using the Stokes-Einstein equation [127]:

$$D = \frac{k_{\mathrm{B}}T}{6\pi\eta r_{\mathrm{H}}}, \tag{1.4}$$

with k_B denoting the Boltzmann constant, T denoting the temperature, and η denoting the dynamic viscosity of the solution. The hydrodynamic radius r_{H} is an intensity-weighted harmonic mean, and its corresponding diameter d_{H} is referred to as z-average [128]. For polydisperse particles in solution, the size distribution is reconstructed by inverting the intensity autocorrelation function to extract a distribution of diffusion coefficients, which are subsequently converted into hydrodynamic radii. Assuming Rayleigh scattering, the scattering intensity scales with the sixth power of the particle diameter [126], thereby biasing the observed intensity fluctuations towards larger particles in polydisperse systems.

Besides its use for off-line analysis of LNP particle size, PAT tools developed based on DLS have been rarely reported. In biopharmaceutical processing, DLS has been implemented for on-line size monitoring during CFF-based processing, providing insights into the aggregation tendency of proteins [19], disassembly of VLP capsids into subunits [17], and VLP reassembly [16]. Whereas DLS provides information on the quaternary structure of proteins, Raman spectroscopy is sensitive towards the primary, secondary, and tertiary structures of proteins.

1.3.3 Raman Spectroscopy

Raman spectroscopy is a vibrational spectroscopic technique based on inelastic light scattering, providing unique spectral fingerprints due to molecular vibrations [129].

The phenomenon of inelastic scattering describes the energy transfer between an incident photon and a molecule, resulting in a change in the vibrational mode of the molecule and a corresponding scattered photon with an energy different from that of the incident photon [129]. In Stokes scattering, the molecule is excited to a higher vibrational state, and the scattered photon has lower energy than the incident photon. Contrarily, Anti-Stokes scattering describes the relaxation of a molecule in an already excited vibrational state, resulting in the scattered photon having more energy than the incident photon. Those differences in energy correspond to Raman shifts. A Raman spectrum encodes the intensity of inelastic scattering as a function of the Raman shifts expressed in wavenumbers. Wavenumber ranges that exhibit strong vibrational signals from specific molecular bonds are referred to as Raman bands [129]. The Raman bands observed in the Raman spectra of an aqueous solution containing proteins arise from molecular vibrations of characteristic functional groups and bonds. Functional groups with high polarizability, such as C=O in the peptide backbone, or C=C in aromatic rings of tyrosine (Tyr), tryptophan (Trp), and phenylalanine (Phe), strongly

contribute to distinct Raman bands [130]. Although less intense, the Raman spectrum also exhibits distinct bands arising from vibrations of disulfide bridges as well as C–N, N–H, C–C, and C–O bonds [131, 132]. As a result, Raman bands reflect information related to the primary, secondary, and tertiary structure of proteins.

When developing sensor-based PAT tools for biopharmaceutical process monitoring, Raman spectroscopy offers significant advantages over other spectroscopic techniques. Raman spectroscopy is, compared to UV/Vis spectroscopy, suitable for analyzing particulate-containing solutions, such as applied during the production of rabies VLPs [133–135], protein precipitation [18], or protein crystallization [136], and shows significantly less water interference than near-IR or mid-IR spectroscopy [129]. Among others, it has already been applied for monitoring biopharmaceutical CFF processes [20, 137], or for the simultaneous monitoring of protein and excipient concentrations [137, 138]. However, Raman scattering is inherently weak, with only approximately one in 10^{10} photons undergoing inelastic scattering [129], and spectral features can be obscured by spectral interferences, including fluorescence. To overcome partially obscured spectral features, spectral data are processed by chemometrics [139, 140].

1.3.4 Chemometrics for Spectral Data

Chemometrics provides a set of tools to extract relevant information from spectral data.

Raw spectral data contain noise-induced variability that can obscure the relevant information to be extracted. Depending on the spectroscopic technique and its sensitivity towards the target components, appropriate preprocessing operations can be applied. To remove uncorrelated or background noise and extract relevant spectral features, signal correction techniques are employed, among others, normalization, baseline correction, background correction, and derivative filtering [139–141]. Further, to address dimensionality reduction while focusing on the relevant spectral data, variable selection techniques are used [142]. However, it is essential to carefully consider the choice, parameters, number, and order of preprocessing operations to avoid losing too much relevant information [19]. Preprocessed spectral data can further be standardized by centering and scaling before being used for multivariate regression.

Among statistical methods for quantitative prediction, partial least squares (PLS) regression is the most frequently applied multivariate regression method. PLS regression extends (i) linear regression by considering multiple predictor variables, (ii) multiple linear regression (MLR) by further reducing dimensionality through decomposition, and (iii) principal component regression (PCR) by selecting predictors based on their relevance to one or multiple response variables [143]. More precisely, PLS algorithms identify latent variables that maximize the covariance between the predictor and response variables [144].

In biopharmaceutical processing, spectral data are typically used for predicting component concentrations. Stored in the spectral data matrix $\mathbf{X}$, predictor variables $\mathbf{x}_i$ represent the spectral signal intensities at the spectral variable i. The response variables $\mathbf{y}_j$ of component j are stored in the concentration data $\mathbf{Y}$. Both variables (column vectors) are variable-wise stacked in the respective data matrix, with each row corresponding to an individual measurement.

According to Wold et al. [144], the linear correlation between the spectral data $\mathbf{X}$ and concentration data $\mathbf{Y}$ is given by

$$\mathbf{Y} = \mathbf{XB} + \mathbf{E}, \tag{1.5}$$

with **B** denoting the regression coefficient matrix and **E** denoting the residual error matrix. The key difference between the multivariate regression models lies in the estimation method for the regression coefficient matrix **B**. MLR estimates **B** by directly minimizing squared **E**, PCR estimates **B** by regressing **Y** on principal components that maximize the variance in **X**, and PLS estimates **B** by extracting latent variables that maximize the covariance between **X** and **Y**.

In PLS regression, latent variables, so-called X-scores **T**, are calculated according to

$$\mathbf{T} = \mathbf{XW}, \tag{1.6}$$

with **W** denoting the weighting matrix. A similar projection is done for **Y**, yielding the Y-scores **U**. **X** and **Y** are reconstructed by

$$\mathbf{X} = \mathbf{TP}^\top + \mathbf{E}_X, \tag{1.7}$$

$$\mathbf{Y} = \mathbf{UQ}^\top + \mathbf{E}_Y, \tag{1.8}$$

with X-loadings **P**, Y-loadings **Q**, and the respective residuals $\mathbf{E_X}$ and $\mathbf{E_Y}$.

PLS regression effectively handles multicollinearity by reducing the dimensionality of the predictors and accounts for their relevance [144], ensuring the extracted information is most relevant for the predictions. Since PLS regression is a linear statistical method, its applicability may be limited when dealing with spectral data exhibiting non-linear spectral effects, in which case non-linear models may be more appropriate.

Chapter References

[1] S. Plotkin. „History of vaccination“. In: *Proceedings of the National Academy of Sciences of the United States of America* 111.34 (2014), pp. 12283–12287. DOI: 10.1073/pnas.1400472111.

[2] W. J. McAleer, E. B. Buynak, R. Z. Maigetter, D. E. Wampler, W. J. Miller, and M. R. Hilleman. „Human hepatitis B vaccine from recombinant yeast“. In: *Nature* 307.5947 (1984), pp. 178–180. DOI: 10.1038/307178a0.

[3] L. H. Lua, N. K. Connors, F. Sainsbury, Y. P. Chuan, N. Wibowo, and A. P. Middelberg. „Bioengineering virus-like particles as vaccines“. In: *Biotechnology and Bioengineering* 111.3 (2014), pp. 425–440. DOI: 10.1002/bit.25159.

[4] Y. H. Chung, H. Cai, and N. F. Steinmetz. „Viral nanoparticles for drug delivery, imaging, immunotherapy, and theranostic applications“. In: *Advanced Drug Delivery Reviews* 156 (2020), pp. 214–235. DOI: 10.1016/j.addr.2020.06.024.

[5] N. McCann, D. O'Connor, T. Lambe, and A. J. Pollard. „Viral vector vaccines“. In: *Current Opinion in Immunology* 77 (2022), p. 102210. DOI: 10.1016/j.coi.2022.102210.

[6] L. Schoenmaker et al. „mRNA-lipid nanoparticle COVID-19 vaccines: Structure and stability“. In: *International Journal of Pharmaceutics* 601 (2021), p. 120586. DOI: 10.1016/j.ijpharm.2021.120586.

[7] C. Wang et al. „Emerging non-viral vectors for gene delivery“. In: *Journal of Nanobiotechnology* 21.1 (2023), p. 272. DOI: 10.1186/s12951-023-02044-5.

[8] J. Gu et al. „Building a Better Silver Bullet: Current Status and Perspectives of Non-Viral Vectors for mRNA Vaccines“. In: *Advanced Healthcare Materials* 13.3 (2024), pp. 444–456. DOI: 10.1002/adhm.202302409.

[9] M. F. Bachmann, P. van Damme, F. Lienert, and T. F. Schwarz. „Virus-like particles: a versatile and effective vaccine platform“. In: *Expert Review of Vaccines* 24.1 (2025), pp. 444–456. DOI: 10.1080/14760584.2025.2508517.

[10] P. R. Cullis and P. L. Felgner. „The 60-year evolution of lipid nanoparticles for nucleic acid delivery“. In: *Nature Reviews Drug Discovery* 23.9 (2024), pp. 709–722. DOI: 10.1038/s41573-024-00977-6.

[11] C. L. Effio and J. Hubbuch. „Next generation vaccines and vectors: Designing downstream processes for recombinant protein-based virus-like particles“. In: *Biotechnology Journal* 10.5 (2015), pp. 715–727. DOI: 10.1002/biot.201400392.

[12] M. J. W. Evers, J. A. Kulkarni, R. van der Meel, P. R. Cullis, P. Vader, and R. M. Schiffelers. „State-of-the-Art Design and Rapid-Mixing Production Techniques of Lipid Nanoparticles for Nucleic Acid Delivery“. In: *Small Methods* 2.9 (2018), p. 1700375. DOI: 10.1002/smtd.201700375.

[13] N. Hillebrandt and J. Hubbuch. „Size-selective downstream processing of virus particles and non-enveloped virus-like particles“. In: *Frontiers in Bioengineering and Biotechnology* 11 (2023). DOI: 10.3389/fbioe.2023.1192050.

[14] FDA. *Guidance for Industry: PAT—a framework for innovative pharmaceutical development, manufacturing, and quality assurance*. 2004.

[15] M. Rüdt, T. Briskot, and J. Hubbuch. „Advances in downstream processing of biologics – Spectroscopy: An emerging process analytical technology“. In: *Journal of Chromatography A* 1490 (2017), pp. 2–9. DOI: 10.1016/j.chroma.2016.11.010.

[16] M. Rüdt, P. Vormittag, N. Hillebrandt, and J. Hubbuch. „Process monitoring of virus-like particle reassembly by diafiltration with UV/Vis spectroscopy and light scattering“. In: *Biotechnology and Bioengineering* 116.6 (2019), pp. 1366–1379. DOI: 10.1002/bit.26935.

[17] N. Hillebrandt, P. Vormittag, A. Dietrich, and J. Hubbuch. „Process monitoring framework for cross-flow diafiltration-based virus-like particle disassembly: Tracing product properties and filtration performance“. In: *Biotechnology and Bioengineering* 119.6 (2022), pp. 1522–1538. DOI: 10.1002/bit.28063.

[18] L. J. Lohmann and J. Strube. „Process analytical technology for precipitation process integration into biologics manufacturing towards autonomous operation—mab case study“. In: *Processes* 9.3 (2021). DOI: 10.3390/pr9030488.

[19] L. Rolinger et al. „Multi-attribute PAT for UF/DF of Proteins—Monitoring Concentration, particle sizes, and Buffer Exchange“. In: *Analytical and Bioanalytical Chemistry* 412.9 (2020), pp. 2123–2136. DOI: 10.1007/s00216-019-02318-8.

[20] D. Vaskó et al. „Raman and NIR spectroscopy-based real-time monitoring of the membrane filtration process of a recombinant protein for the diagnosis of SARS-CoV-2“. In: *International Journal of Pharmaceutics* 660 (2024), p. 124251. DOI: 10.1016/j.ijpharm.2024.124251.

[21] A. K. Leung et al. „Lipid nanoparticles containing siRNA synthesized by microfluidic mixing exhibit an electron-dense nanostructured core“. In: *Journal of Physical Chemistry C* 116.34 (2012), pp. 18440–18450. DOI: 10.1021/jp303267y.

[22] C. H. Albertsen, J. A. Kulkarni, D. Witzigmann, M. Lind, K. Petersson, and J. B. Simonsen. „The role of lipid components in lipid nanoparticles for vaccines and gene therapy“. In: *Advanced Drug Delivery Reviews* 188 (2022), p. 114416. DOI: 10.1016/j.addr.2022.114416.

[23] C. B. Roces et al. „Manufacturing considerations for the development of lipid nanoparticles using microfluidics“. In: *Pharmaceutics* 12.11 (2020), pp. 1–19. DOI: 10.3390/pharmaceutics12111095.

[24] S. C. Semple et al. „Rational design of cationic lipids for siRNA delivery“. In: *Nature Biotechnology* 28.2 (2010), pp. 172–176. DOI: 10.1038/nbt.1602.

[25] K. T. Love et al. „Lipid-like materials for low-dose, in vivo gene silencing“. In: *Proceedings of the National Academy of Sciences of the United States of America* 107.5 (2010), pp. 1864–1869. DOI: 10.1073/pnas.0910603106.

[26] M. Jayaraman et al. „Maximizing the potency of siRNA lipid nanoparticles for hepatic gene silencing in vivo“. In: *Angewandte Chemie - International Edition* 51.34 (2012), pp. 8529–8533. DOI: 10.1002/anie.201203263.

[27] J. A. Kulkarni et al. „On the Formation and Morphology of Lipid Nanoparticles Containing Ionizable Cationic Lipids and siRNA“. In: *ACS Nano* 12.5 (2018), pp. 4787–4795. DOI: 10.1021/acsnano.8b01516.

[28] Y. Fan et al. „Automated high-throughput preparation and characterization of oligonucleotide-loaded lipid nanoparticles“. In: *International Journal of Pharmaceutics* 599 (2021). DOI: 10.1016/j.ijpharm.2021.120392.

[29] K. Okuda et al. „On the size-regulation of RNA-loaded lipid nanoparticles synthesized by microfluidic device“. In: *Journal of Controlled Release* 348 (2022), pp. 648–659. DOI: 10.1016/j.jconrel.2022.06.017.

[30] A. K. Leung, Y. Y. C. Tam, S. Chen, I. M. Hafez, and P. R. Cullis. „Microfluidic Mixing: A General Method for Encapsulating Macromolecules in Lipid Nanoparticle Systems“. In: *Journal of Physical Chemistry B* 119.28 (2015), pp. 8698–8706. DOI: 10.1021/acs.jpcb.5b02891.

[31] J. A. Kulkarni, D. Witzigmann, J. Leung, Y. Y. C. Tam, and P. R. Cullis. „On the role of helper lipids in lipid nanoparticle formulations of siRNA“. In: *Nanoscale* 11.45 (2019), pp. 21733–21739. DOI: 10.1039/c9nr09347h.

[32] J. A. Kulkarni et al. „Fusion-dependent formation of lipid nanoparticles containing macromolecular payloads“. In: *Nanoscale* 11.18 (2019), pp. 9023–9031. DOI: 10.1039/C9NR02004G.

[33] R. A. Petros and J. M. DeSimone. „Strategies in the design of nanoparticles for therapeutic applications“. In: *Nature Reviews Drug Discovery* 9.8 (2010), pp. 615–627. DOI: 10.1038/nrd2591.

[34] T. Terada et al. „Characterization of Lipid Nanoparticles Containing Ionizable Cationic Lipids Using Design-of-Experiments Approach“. In: *Langmuir* 37.3 (2021), pp. 1120–1128. DOI: 10.1021/acs.langmuir.0c03039.

[35] R. Vargas et al. „Dialysis is a key factor modulating interactions between critical process parameters during the microfluidic preparation of lipid nanoparticles“. In: *Colloids and Interface Science Communications* 54 (2023). DOI: 10.1016/j.colcom.2023.100709.

[36] R. van Reis and A. Zydney. „Bioprocess membrane technology“. In: *Journal of Membrane Science* 297.1-2 (2007), pp. 16–50. DOI: 10.1016/j.memsci.2007.02.045.

[37] C. Geng et al. „A preparation method for mRNA-LNPs with improved properties“. In: *Journal of Controlled Release* 364 (2023), pp. 632–643. DOI: 10.1016/j.jconrel.2023.11.017.

[38] W. Wu et al. „Process development of tangential flow filtration and sterile filtration for manufacturing of mRNA-lipid nanoparticles: A study on membrane performance and filtration modeling“. In: *International Journal of Pharmaceutics* 675 (2025). DOI: 10.1016/j.ijpharm.2025.125520.

[39] B. Chackerian. „Virus-like particles: Flexible platforms for vaccine development“. In: *Expert Review of Vaccines* 6.3 (2007), pp. 381–390. DOI: 10.1586/14760584.6.3.381.

[40] N. Kushnir, S. J. Streatfield, and V. Yusibov. „Virus-like particles as a highly efficient vaccine platform: Diversity of targets and production systems and advances in clinical development“. In: *Vaccine* 31.1 (2012), pp. 58–83. DOI: 10.1016/j.vaccine.2012.10.083.

[41] H. Tariq, S. Batool, S. Asif, M. Ali, and B. H. Abbasi. „Virus-Like Particles: Revolutionary Platforms for Developing Vaccines Against Emerging Infectious Diseases“. In: *Frontiers in Microbiology* 12 (2022). DOI: 10.3389/fmicb.2021.790121.

[42] Y. Liu, M. Pietzsch, and J. Ulrich. „Determination of the phase diagram for the crystallization of L-asparaginase II by a turbidity technique“. In: *Crystal Research and Technology* 49.4 (2014), pp. 262–268. DOI: 10.1002/crat.201300402.

[43] S. Nooraei et al. „Virus-like particles: preparation, immunogenicity and their roles as nanovaccines and drug nanocarriers“. In: *Journal of Nanobiotechnology* 19.1 (2021), p. 59. DOI: 10.1186/s12951-021-00806-7.

[44] B. E. Clarke et al. „Improved immunogenicity of a peptide epitope after fusion to hepatitis B core protein“. In: *Nature* 330.6146 (1987), pp. 381–384. DOI: 10.1038/330381a0.

[45] M. Peacey, S. Wilson, M. A. Baird, and V. K. Ward. „Versatile RHDV virus-like particles: Incorporation of antigens by genetic modification and chemical conjugation“. In: *Biotechnology and Bioengineering* 98.5 (2007), pp. 968–977. DOI: 10.1002/bit.21518.

[46] C. J. Burrell, P. Mackay, P. J. Greenaway, P. H. Hofschneider, and K. Murray. „Expression in Escherichia coli of hepatitis B virus DNA sequences cloned in plasmid pBR322“. In: *Nature* 279.5708 (1979), pp. 43–47. DOI: 10.1038/279043a0.

[47] S. Stahl, P. MacKay, M. Magazin, S. A. Bruce, and K. Murray. „Hepatitis B virus core antigen: Synthesis in Escherichia coli and application in diagnosis“. In: *Proceedings of the National Academy of Sciences of the United States of America* 79.5 (1982), pp. 1606–1610. DOI: 10.1073/pnas.79.5.1606.

[48] F. A. Crowther et al. „Three-Dimensional Structure of Hepatitis B Virus Core Particles Determined by Electron Cryomicroscopy“. In: *Cell* 77 (1994), pp. 943–950. DOI: 10.1016/0092-8674(94)90142-2.

[49] A. Zlotnick et al. „Dimorphism of Hepatitis B Virus Capsids Is Strongly Influenced by the C-Terminus of the Capsid Protein“. In: *Biochemistry* 35.23 (1996), pp. 7412–7421. DOI: 10.1021/bi9604800.

[50] R. McGonigle et al. „An N-terminal extension to the hepatitis B virus core protein forms a poorly ordered trimeric spike in assembled virus-like particles“. In: *Journal of Structural Biology* 189.2 (2015), pp. 73–80. DOI: 10.1016/j.jsb.2014.12.006.

[51] J. Schumacher et al. „Enhanced stability of a chimeric hepatitis B core antigen virus-like-particle (HBcAg-VLP) by a C-terminal linker-hexahistidine-peptide“. In: *Journal of Nanobiotechnology* 16.1 (2018), p. 39. DOI: 10.1186/s12951-018-0363-0.

[52] A. Valentic, J. Müller, and J. Hubbuch. „Effects of Different Lengths of a Nucleic Acid Binding Region and Bound Nucleic Acids on the Phase Behavior and Purification Process of HBcAg Virus-Like Particles“. In: *Frontiers in Bioengineering and Biotechnology* 10 (2022). DOI: 10.3389/fbioe.2022.929243.

[53] T. Klamp et al. „Highly Specific Auto-Antibodies against Claudin-18 Isoform 2 Induced by a Chimeric HBcAg Virus-Like Particle Vaccine Kill Tumor Cells and Inhibit the Growth of Lung Metastases“. In: *Cancer Research* 71.2 (2011), pp. 516–527. DOI: 10.1158/0008-5472.CAN-10-2292.

[54] M. Moradi Vahdat et al. „Hepatitis B core-based virus-like particles: A platform for vaccine development in plants“. In: *Biotechnology Reports* 29 (2021), e00605. DOI: 10.1016/j.btre.2021.e00605.

[55] A. M. Hassebroek et al. „A hepatitis B virus core antigen-based virus-like particle vaccine expressing SARS-CoV-2 B and T cell epitopes induces epitope-specific humoral and cell-mediated immune responses but confers limited protection against SARS-CoV-2 infection“. In: *Journal of Medical Virology* 95.2 (2023). DOI: 10.1002/jmv.28503.

[56] A. Zeltins. „Construction and Characterization of Virus-Like Particles: A Review“. In: *Molecular Biotechnology* 53.1 (2013), pp. 92–107. DOI: 10.1007/s12033-012-9598-4.

[57] M. G. Moleirinho, R. J. Silva, P. M. Alves, M. J. T. Carrondo, and C. Peixoto. „Current challenges in biotherapeutic particles manufacturing“. In: *Expert Opinion on Biological Therapy* 20.5 (2020), pp. 451–465. DOI: 10.1080/14712598.2020.1693541.

[58] L. K. Pattenden, A. P. Middelberg, M. Niebert, and D. I. Lipin. „Towards the preparative and large-scale precision manufacture of virus-like particles“. In: *Trends in Biotechnology* 23.10 (2005), pp. 523–529. DOI: 10.1016/j.tibtech.2005.07.011.

[59] M. W. Liew, Y. P. Chuan, and A. P. Middelberg. „Reactive diafiltration for assembly and formulation of virus-like particles“. In: *Biochemical Engineering Journal* 68 (2012), pp. 120–128. DOI: 10.1016/j.bej.2012.07.009.

[60] L. Gerstweiler, J. Billakanti, J. Bi, and A. Middelberg. „Comparative evaluation of integrated purification pathways for bacterial modular polyomavirus major capsid protein VP1 to produce virus-like particles using high throughput process technologies“. In: *Journal of Chromatography A* 1639 (2021), p. 461924. DOI: 10.1016/j.chroma.2021.461924.

[61] N. Hillebrandt, P. Vormittag, A. Dietrich, C. H. Wegner, and J. Hubbuch. „Process development for cross-flow diafiltration-based VLP disassembly: A novel high-throughput screening approach“. In: *Biotechnology and Bioengineering* 118.10 (2021), pp. 3926–3940. DOI: 10.1002/bit.27868.

[62] H. Mach et al. „Disassembly and reassembly of yeast-derived recombinant human papillomavirus virus-like particles (HPV VLPs)“. In: *Journal of Pharmaceutical Sciences* 95.10 (2006), pp. 2195–2206. DOI: 10.1002/jps.20696.

[63] Q. Zhao et al. „Disassembly and reassembly of human papillomavirus virus-like particles produces more virion-like antibody reactivity“. In: *Virology Journal* 9 (2012). DOI: 10.1186/1743-422X-9-52.

[64] A. Strods et al. „Preparation by alkaline treatment and detailed characterisation of empty hepatitis B virus core particles for vaccine and gene therapy applications“. In: *Scientific Reports* 5 (2015), pp. 1–16. DOI: 10.1038/srep11639.

[65] I. Petrovskis et al. „Production of the HBc Protein from Different HBV Genotypes in E. coli. Use of Reassociated HBc VLPs for Packaging of ss- and dsRNA“. In: *Microorganisms* 9.2 (2021), p. 283. DOI: 10.3390/microorganisms9020283.

[66] A. Valentic and J. Hubbuch. „Effective removal of host cell-derived nucleic acids bound to hepatitis B core antigen virus-like particles by heparin chromatography“. In: *Frontiers in Bioengineering and Biotechnology* 12 (2024), pp. 1–15. DOI: 10.3389/fbioe.2024.1475918.

[67] A. Cooper and Y. Shaul. „Recombinant viral capsids as an efficient vehicle of oligonucleotide delivery into cells“. In: *Biochemical and Biophysical Research Communications* 327.4 (2005), pp. 1094–1099. DOI: 10.1016/j.bbrc.2004.12.118.

[68] J. Z. Porterfield, M. S. Dhason, D. D. Loeb, M. Nassal, S. J. Stray, and A. Zlotnick. „Full-Length Hepatitis B Virus Core Protein Packages Viral and Heterologous RNA with Similarly High Levels of Cooperativity“. In: *Journal of Virology* 84.14 (2010), pp. 7174–7184. DOI: 10.1128/JVI.00586-10.

[69] S. D. Durbin and G. Feher. „Protein Crystallization“. In: *Annual Review of Physical Chemistry* 47.1 (1996), pp. 171–204. DOI: 10.1146/annurev.physchem.47.1.171.

[70] F. Rothstein. „Differential precipitation of proteins“. In: *Protein purification process engineering*. Ed. by R. G. Harrison. New York, 1994, pp. 115–208.

[71] E. Y. Chi, S. Krishnan, T. W. Randolph, and J. F. Carpenter. „Physical stability of proteins in aqueous solution: Mechanism and driving forces in nonnative protein aggregation“. In: *Pharmaceutical Research* 20.9 (2003), pp. 1325–1336. DOI: 10.1023/a:1025771421906.

[72] M. Boström, F. Tavares, S. Finet, F. Skouri-Panet, A. Tardieu, and B. Ninham. „Why forces between proteins follow different Hofmeister series for pH above and below pI“. In: *Biophysical Chemistry* 117.3 (2005), pp. 217–224. DOI: 10.1016/j.bpc.2005.05.010.

[73] E. O. Watanabe, E. Popova, E. A. Miranda, G. Maurer, and P. d. A. P. Filho. „Phase equilibria for salt-induced lysozyme precipitation: Effect of salt type and temperature“. In: *Fluid Phase Equilibria* 281.1 (2009), pp. 32–39. DOI: 10.1016/j.fluid.2009.03.021.

[74] H. Mahadevan and C. K. Hall. „Experimental analysis of protein precipitation by polyethylene glycol and comparison with theory“. In: *Fluid Phase Equilibria* 78.C (1992), pp. 297–321. DOI: 10.1016/0378-3812(92)87043-M.

[75] M. d. C. Pons Royo, J. L. Beulay, E. Valery, A. Jungbauer, and P. Satzer. „Mode and dosage time in polyethylene glycol precipitation process influences protein precipitate size and filterability“. In: *Process Biochemistry* 114 (2022), pp. 77–85. DOI: 10.1016/j.procbio.2022.01.017.

[76] Y.-C. Shih, J. M. Prausnitz, and H. W. Blanch. „Some characteristics of protein precipitation by salts“. In: *Biotechnology and Bioengineering* 40.10 (1992), pp. 1155–1164. DOI: 10.1002/bit.260401004.

[77] R. A. Curtis, J. M. Prausnitz, and H. W. Blanch. „Protein-protein and protein-salt interactions in aqueous protein solutions containing concentrated electrolytes“. In: *Biotechnology and Bioengineering* 57.1 (1998), pp. 11–21. DOI: 10.1002/(SICI)1097-0290(19980105)57:1<11::AID-BIT2>3.0.CO;2-Y.

[78] W. Kunz, J. Henle, and B. Ninham. „‘Zur Lehre von der Wirkung der Salze’ (about the science of the effect of salts): Franz Hofmeister’s historical papers“. In: *Current Opinion in Colloid & Interface Science* 9.1-2 (2004), pp. 19–37. DOI: 10.1016/j.cocis.2004.05.005.

[79] B. Kang, H. Tang, Z. Zhao, and S. Song. „Hofmeister Series: Insights of Ion Specificity from Amphiphilic Assembly and Interface Property“. In: *ACS Omega* 5.12 (2020), pp. 6229–6239. DOI: 10.1021/acsomega.0c00237.

[80] P. Wingfield. „Protein Precipitation Using Ammonium Sulfate“. In: *Current Protocols in Protein Science* 13.1 (1998), pp. 1–8. DOI: 10.1002/0471140864.psa03fs13.

[81] S. Tsoka, O. C. Ciniawskyj, O. R. T. Thomas, N. J. Titchener-Hooker, and M. Hoare. „Selective Flocculation and Precipitation for the Improvement of Virus-Like Particle Recovery from Yeast Homogenate“. In: *Biotechnology Progress* 16.4 (2000), pp. 661–667. DOI: 10.1021/bp0000407.

[82] T. Koho et al. „Purification of norovirus-like particles (VLPs) by ion exchange chromatography“. In: *Journal of Virological Methods* 181.1 (2012), pp. 6–11. DOI: 10.1016/j.jviromet.2012.01.003.

[83] H. J. Kim, S. Y. Kim, S. J. Lim, J. Y. Kim, S. J. Lee, and H. J. Kim. „One-step chromatographic purification of human papillomavirus type 16 L1 protein from Saccharomyces cerevisiae“. In: *Protein Expression and Purification* 70.1 (2010), pp. 68–74. DOI: 10.1016/j.pep.2009.08.005.

[84] M. Zahin et al. „Scalable production of HPV16 L1 protein and VLPs from tobacco leaves“. In: *PLoS ONE* 11.8 (2016), pp. 1–16. DOI: 10.1371/journal.pone.0160995.

[85] A. Kazaks et al. „Production and purification of chimeric HBc virus-like particles carrying influenza virus LAH domain as vaccine candidates“. In: *BMC Biotechnology* 17.1 (2017), pp. 1–11. DOI: 10.1186/s12896-017-0396-8.

[86] Y. Zhang et al. „In vitro preparation of uniform and nucleic acid free hepatitis B core particles through an optimized disassembly-purification-reassembly process“. In: *Protein Expression and Purification* 178 (2021). DOI: 10.1016/j.pep.2020.105747.

[87] J. Yang, L. Zhang, C. Zhang, and Y. Lu. „Exploration on the expression and assembly of virus-like particles“. In: *Biotechnology Notes* 2 (2021), pp. 51–58. DOI: 10.1016/j.biotno.2021.08.003.

[88] N. Hillebrandt, P. Vormittag, N. Bluthardt, A. Dietrich, and J. Hubbuch. „Integrated Process for Capture and Purification of Virus-Like Particles: Enhancing Process Performance by Cross-Flow Filtration“. In: *Frontiers in Bioengineering and Biotechnology* 8 (2020). DOI: 10.3389/fbioe.2020.00489.

[89] S. Großhans, S. Suhm, and J. Hubbuch. „Precipitation of complex antibody solutions: influence of contaminant composition and cell culture medium on the precipitation behavior“. In: *Bioprocess and Biosystems Engineering* (2019). DOI: 10.1007/s00449-019-02103-y.

[90] C. H. Wegner and J. Hubbuch. „Calibration-free PAT: Locating selective crystallization or precipitation sweet spot in screenings with multi-way PARAFAC models“. In: *Frontiers in Bioengineering and Biotechnology* 10 (2022), pp. 1–18. DOI: 10.3389/fbioe.2022.1051129.

[91] P. Vormittag, T. Klamp, and J. Hubbuch. „Ensembles of Hydrophobicity Scales as Potent Classifiers for Chimeric Virus-Like Particle Solubility – An Amino Acid Sequence-Based Machine Learning Approach“. In: *Frontiers in Bioengineering and Biotechnology* 8 (2020). DOI: 10.3389/fbioe.2020.00395.

[92] P. Vormittag, T. Klamp, and J. Hubbuch. „Optimization of a Soft Ensemble Vote Classifier for the Prediction of Chimeric Virus-Like Particle Solubility and Other Biophysical Properties“. In: *Frontiers in Bioengineering and Biotechnology* 8 (2020), pp. 1–17. DOI: 10.3389/fbioe.2020.00881.

[93] A.-S. Jönsson and G. Trägårdh. „Fundamental principles of ultrafiltration“. In: *Chemical Engineering and Processing: Process Intensification* 27.2 (1990), pp. 67–81. DOI: 10.1016/0255-2701(90)85011-R.

[94] R. Van Reis and S. Saksena. „Optimization diagram for membrane separations“. In: *Journal of Membrane Science* 129.1 (1997), pp. 19–29. DOI: 10.1016/S0376-7388(96)00319-5.

[95] J. E. Ladwig, X. X. Zhu, P. Rolandi, R. Hart, J. Robinson, and A. Rydholm. „Mechanistic model of pH and excipient concentration during ultrafiltration and diafiltration processes of therapeutic antibodies“. In: *Biotechnology Progress* 36.5 (2020), pp. 1–19. DOI: 10.1002/btpr.2993.

[96] R. Ambrožič, D. Arzenšek, and A. Podgornik. „Designing scalable ultrafiltration/diafiltration process of monoclonal antibodies via mathematical modeling by coupling mass balances and Poisson–Boltzmann equation“. In: *Biotechnology and Bioengineering* 118.2 (2021), pp. 633–646. DOI: 10.1002/bit.27598.

[97] T. Briskot et al. „Modeling the Gibbs-Donnan effect during ultrafiltration and diafiltration processes using the Poisson–Boltzmann theory in combination with a basic Stern model“. In: *Journal of Membrane Science* 648 (2022), p. 120333. DOI: 10.1016/j.memsci.2022.120333.

[98] A. D. Marshall, P. A. Munro, and G. Trägårdh. „The effect of protein fouling in microfiltration and ultrafiltration on permeate flux, protein retention and selectivity: A literature review“. In: *Desalination* 91.1 (1993), pp. 65–108. DOI: 10.1016/0011-9164(93)80047-Q.

[99] W. F. Blatt, A. Dravid, A. S. Michaels, and L. Nelsen. „Solute Polarization and Cake Formation in Membrane Ultrafiltration: Causes, Consequences, and Control Techniques“. In: *Membrane Science and Technology: Industrial, Biological, and Waste Treatment Processes*. Ed. by J. E. Flinn. Boston, MA: Springer US, 1970, pp. 47–97. DOI: 10.1007/978-1-4684-1851-4_4.

[100] C. Quezada, H. Estay, A. Cassano, E. Troncoso, and R. Ruby-Figueroa. „Prediction of permeate flux in ultrafiltration processes: A review of modeling approaches“. In: *Membranes* 11.5 (2021). DOI: 10.3390/membranes11050368.

[101] T. Vicente, S. Burri, S. Wellnitz, K. Walsh, S. Rothe, and J. Liderfelt. „Fully aseptic single-use cross flow filtration system for clarification and concentration of cytomegalovirus-like particles“. In: *Engineering in Life Sciences* 14.3 (2014), pp. 318–326. DOI: 10.1002/elsc.201300093.

[102] A. Venkiteshwaran, P. Heider, L. Teysseyre, and G. Belfort. „Selective precipitation-assisted recovery of immunoglobulins from bovine serum using controlled-fouling crossflow membrane microfiltration“. In: *Biotechnology and Bioengineering* 101.5 (2008), pp. 957–966. DOI: 10.1002/bit.21964.

[103] M. Kuczewski, E. Schirmer, B. Lain, and G. Zarbis-Papastoitsis. „A single-use purification process for the production of a monoclonal antibody produced in a PER.C6 human cell line“. In: *Biotechnology Journal* 6.1 (2011), pp. 56–65. DOI: 10.1002/biot.201000292.

[104] N. Hammerschmidt, S. Hobiger, and A. Jungbauer. „Continuous polyethylene glycol precipitation of recombinant antibodies: Sequential precipitation and resolubilization“. In: *Process Biochemistry* 51.2 (2016), pp. 325–332. DOI: 10.1016/j.procbio.2015.11.032.

[105] D. Burgstaller, A. Jungbauer, and P. Satzer. „Continuous integrated antibody precipitation with two-stage tangential flow microfiltration enables constant mass flow“. In: *Biotechnology and Bioengineering* 116.5 (2019), pp. 1053–1065. DOI: 10.1002/bit.26922.

[106] G. Recanati et al. „Integration of a perfusion reactor and continuous precipitation in an entirely membrane-based process for antibody capture“. In: *Engineering in Life Sciences* 23.10 (2023), pp. 1–14. DOI: 10.1002/elsc.202300219.

[107] Z. Li, Q. Gu, J. L. Coffman, T. Przybycien, and A. L. Zydney. „Continuous precipitation for monoclonal antibody capture using countercurrent washing by microfiltration“. In: *Biotechnology Progress* 35.6 (2019), pp. 1–8. DOI: 10.1002/btpr.2886.

[108] M. Minervini et al. „Continuous precipitation-filtration process for initial capture of a monoclonal antibody product using a four-stage countercurrent hollow fiber membrane washing step“. In: *Biotechnology and Bioengineering* 121.8 (2024), pp. 2258–2268. DOI: 10.1002/bit.28525.

[109] K. P. S. Piash, C. MacElroy, Z. Wang, and A. L. Zydney. „Vibration-Assisted Single-Pass tangential flow filtration for processing precipitated proteins“. In: *Separation and Purification Technology* 376.P3 (2025), p. 134136. DOI: 10.1016/j.seppur.2025.134136.

[110] R. T. Kurnik et al. „Buffer exchange using size exclusion chromatography, countercurrent dialysis, and tangential flow filtration: Models, development, and industrial application“. In: *Biotechnology and Bioengineering* 45.2 (1995), pp. 149–157. DOI: 10.1002/bit.260450209.

[111] S. B. Carvalho et al. „Membrane-Based Approach for the Downstream Processing of Influenza Virus-Like Particles“. In: *Biotechnology Journal* 14.8 (2019). DOI: 10.1002/biot.201800570.

[112] A. S. Rathore, R. Bhambure, and V. Ghare. „Process analytical technology (PAT) for biopharmaceutical products“. In: *Analytical and Bioanalytical Chemistry* 398.1 (2010), pp. 137–154. DOI: 10.1007/s00216-010-3781-x.

[113] J. Glassey et al. „Process analytical technology (PAT) for biopharmaceuticals“. In: *Biotechnology Journal* 6.4 (2011), pp. 369–377. DOI: 10.1002/biot.201000356.

[114] L. Rolinger, M. Rüdt, and J. Hubbuch. „A critical review of recent trends, and a future perspective of optical spectroscopy as PAT in biopharmaceutical downstream processing“. In: *Analytical and Bioanalytical Chemistry* 412.9 (2020), pp. 2047–2064. DOI: 10.1007/s00216-020-02407-z.

[115] M. S. H. Akash and K. Rehman. „Ultraviolet-Visible (UV-VIS) Spectroscopy“. In: *Essentials of Pharmaceutical Analysis*. Singapore: Springer Nature Singapore, 2020, pp. 1–222. DOI: 10.1007/978-981-15-1547-7.

[116] D. F. Swinehart. „The Beer-Lambert Law“. In: *Journal of Chemical Education* 39.7 (1962), p. 333. DOI: 10.1021/ed039p333.

[117] P. H. Gamache et al. „HPLC analysis of nonvolatile analytes using charged aerosol detection“. In: *LC-GC Europe* 18.6 (2005), pp. 345–354.

[118] P. H. Gamache and S. L. Kaufman. *Principles of Charged Aerosol Detection*. John Wiley & Sons, Ltd, 2017, pp. 1–65. DOI: 10.1002/9781119390725.ch1.

[119] R. A. Moreau. „The analysis of lipids via HPLC with a charged aerosol detector“. In: *Lipids* 41.7 (2006), pp. 727–734. DOI: 10.1007/s11745-006-5024-7.

[120] L. Li, J. P. Foley, and R. Helmy. „Simultaneous separation of small interfering RNA and lipids using ion-pair reversed-phase liquid chromatography“. In: *Journal of Chromatography A* 1601 (2019), pp. 145–154. DOI: 10.1016/j.chroma.2019.04.061.

[121] C. Kinsey et al. „Determination of lipid content and stability in lipid nanoparticles using ultra high-performance liquid chromatography in combination with a Corona Charged Aerosol Detector“. In: *Electrophoresis* 43.9-10 (2022), pp. 1091–1100. DOI: 10.1002/elps.202100244.

[122] K. H. Kim et al. „Optimization of HPLC–CAD method for simultaneous analysis of different lipids in lipid nanoparticles with analytical QbD“. In: *Journal of Chromatography A* 1709 (2023), p. 464375. DOI: 10.1016/j.chroma.2023.464375.

[123] V. Bender, L. Fuchs, and R. Süss. „RP-HPLC-CAD method for the rapid analysis of lipids used in lipid nanoparticles derived from dual centrifugation“. In: *International Journal of Pharmaceutics: X* 7 (2024), p. 100255. DOI: 10.1016/j.ijpx.2024.100255.

[124] X. Yu et al. „Validation of an HPLC-CAD Method for Determination of Lipid Content in LNP-Encapsulated COVID-19 mRNA Vaccines“. In: *Vaccines* 11.5 (2023). DOI: 10.3390/vaccines11050937.

[125] M. Hof and R. Macháň. „Basics of Optical Spectroscopy“. In: *Handbook of Spectroscopy*. Ed. by G. Gauglitz and D. Moore. John Wiley & Sons, Ltd, 2014, pp. 31–38. DOI: https://doi.org/10.1002/9783527654703.ch3.

[126] J. Stetefeld, S. A. McKenna, and T. R. Patel. „Dynamic light scattering: a practical guide and applications in biomedical sciences“. In: *Biophysical Reviews* 8.4 (2016), pp. 409–427. DOI: 10.1007/s12551-016-0218-6.

[127] A. Einstein. „Zur Theorie der Brownschen Bewegung“. In: *Annalen der Physik* 324.2 (1906), pp. 371–381. DOI: 10.1002/andp.19063240208.

[128] J. C. Thomas. „The determination of log normal particle size distributions by dynamic light scattering“. In: *Journal of Colloid and Interface Science* 117.1 (1987), pp. 187–192. DOI: 10.1016/0021-9797(87)90182-2.

[129] R. L. McCreery. *Raman Spectroscopy for Chemical Analysis*. New York: John Wiley & Sons, 2005.

[130] K. A. Bakeev. *Process Analytical Technology: Spectroscopic Tools and Implementation Strategies for the Chemical and Pharmaceutical Industries*. Ed. by K. A. Bakeev. John Wiley & Sons, 2010. DOI: 10.1002/9780470689592.

[131] N. C. Maiti, M. M. Apetri, M. G. Zagorski, P. R. Carey, and V. E. Anderson. „Raman Spectroscopic Characterization of Secondary Structure in Natively Unfolded Proteins: α-Synuclein“. In: *Journal of the American Chemical Society* 126.8 (2004), pp. 2399–2408. DOI: 10.1021/ja0356176.

[132] A. Rygula, K. Majzner, K. M. Marzec, A. Kaczor, M. Pilarczyk, and M. Baranska. „Raman spectroscopy of proteins: A review“. In: *Journal of Raman Spectroscopy* 44.8 (2013), pp. 1061–1076. DOI: 10.1002/jrs.4335.

[133] L. G. d. O. Guardalini et al. „Comparison of chemometric models using Raman spectroscopy for offline biochemical monitoring throughout the VLP-making upstream process“. In: *Biochemical Engineering Journal* 198 (2023), p. 109013. DOI: 10.1016/j.bej.2023.109013.

[134] L. G. d. O. Guardalini et al. „Biochemical monitoring throughout all stages of rabies virus-like particles production by Raman spectroscopy using global models“. In: *Journal of Biotechnology* 363 (2023), pp. 19–31. DOI: 10.1016/j.jbiotec.2022.12.009.

[135] L. G. d. O. Guardalini et al. „Monitoring by Raman spectroscopy of rabies virus-like particles production since the initial development stages“. In: *Journal of Chemical Technology & Biotechnology* 99 (2023), pp. 658–673. DOI: 10.1002/jctb.7571.

[136] C. H. Wegner, S. M. Eming, B. Walla, D. Bischoff, D. Weuster-Botz, and J. Hubbuch. „Spectroscopic insights into multi-phase protein crystallization in complex lysate using Raman spectroscopy and a particle-free bypass“. In: *Frontiers in Bioengineering and Biotechnology* 12 (2024), pp. 1–16. DOI: 10.3389/fbioe.2024.1397465.

[137] L. Rolinger, J. Hubbuch, and M. Rüdt. „Monitoring of ultra- and diafiltration processes by Kalman-filtered Raman measurements“. In: *Analytical and Bioanalytical Chemistry* 415.5 (2023), pp. 841–854. DOI: 10.1007/s00216-022-04477-7.

[138] D. Weber and J. Hubbuch. „Raman spectroscopy as a process analytical technology to investigate biopharmaceutical freeze concentration processes“. In: *Biotechnology and Bioengineering* 118.12 (2021), pp. 4708–4719. DOI: 10.1002/bit.27936.

[139] Å. Rinnan, L. Nørgaard, F. V. D. Berg, J. Thygesen, R. Bro, and S. B. Engelsen. „Data Pre-processing“. In: *Infrared Spectroscopy for Food Quality Analysis and Control*. Vol. 3. Academic Press, 2009. Chap. 2, pp. 29–50.

[140] R. Gautam, S. Vanga, F. Ariese, and S. Umapathy. „Review of multidimensional data processing approaches for Raman and infrared spectroscopy“. In: *EPJ Techniques and Instrumentation* 2.1 (2015). DOI: 10.1140/epjti/s40485-015-0018-6.

[141] T. Bocklitz, A. Walter, K. Hartmann, P. Rösch, and J. Popp. „How to pre-process Raman spectra for reliable and stable models?“ In: *Analytica Chimica Acta* 704.1-2 (2011), pp. 47–56. DOI: 10.1016/j.aca.2011.06.043.

[142] T. Mehmood, K. H. Liland, L. Snipen, and S. Sæbø. „A review of variable selection methods in Partial Least Squares Regression“. In: *Chemometrics and Intelligent Laboratory Systems* 118 (2012), pp. 62–69. DOI: 10.1016/j.chemolab.2012.07.010.

[143] W. Kessler. „Multivariate Regressionsmethoden“. In: *Multivariate Datenanalyse*. Wiley, 2006, pp. 89–152. DOI: 10.1002/9783527610037.ch3.

[144] S. Wold, M. Sjöström, and L. Eriksson. „PLS-regression: a basic tool of chemometrics“. In: *Chemometrics and Intelligent Laboratory Systems* 58.2 (2001), pp. 109–130. DOI: 10.1016/S0169-7439(01)00155-1.

2

Thesis Outline

2.1 Research Proposal

Biopharmaceuticals offer new opportunities for the targeted prevention and treatment of complex, previously untreatable diseases, including autoimmune, infectious, and genetic diseases, and cancer. The functionality of biopharmaceuticals is directly linked to their complex structure, requiring tailored production processes that, in turn, define product quality. Driven by this tight interconnection of product and process, biopharmaceutical process development consistently aims to enhance process understanding to ensure product quality. Particularly, vector technologies as versatile nanocarrier platforms have opened new avenues beyond recombinant proteins and naked nucleic acids, with promising applications in the field of vaccines and gene therapeutics. Compared to key modalities in the biopharmaceutical industry, such as monoclonal antibodies, vectors exhibit a markedly higher level of structural complexity and diversity as well as a larger size. These characteristics pose new challenges, calling for adaptations in purification processes, analytics, and process analytical technology (PAT) tools.

Non-viral vectors are of particular interest in the field of biopharmaceuticals, as they are associated with lower safety concerns compared to viral vectors. Virus-like particles (VLPs) and lipid nanoparticles (LNPs) represent the current leading non-viral vector classes, with their structural diversity leading to distinct separation objectives in downstream processing (DSP). VLPs are recombinantly produced and need to be purified by multiple DSP steps to separate process- and product-related impurities, and if required, to encapsulate a payload. In contrast, the DSP of synthesized, loaded LNPs primarily targets the removal of residual organic solvent. Nowadays, the maturity of process development exhibits significant variation between both non-viral vector classes, presumably due to the relatively recent emergence of the LNP technology. LNP process development may significantly benefit from standard analytics and dedicated process parameter studies to meet core process requirements covering reproducibility, scalability, and efficiency. VLP process development may advance through progressing towards process integration, intensification, and standardization,

as well as the implementation of PAT tools for real-time monitoring. Focusing on the primary purification of LNPs and VLPs, the objective of this thesis is to advance their process development through (I) standardized processing using size-selective separation techniques combined with (II) sensor-based analytics and PAT tools. Innovations in primary purification will be driven through the integration of cross-flow filtration (CFF), to replace dialysis or CFF combined with precipitation, which all represent scalable, size-selective separation techniques. For these primary purification processes, sensor-based analytics and PAT tools for process monitoring will be tailored, ranging from off-line charged aerosol detection (CAD) and at-line dynamic light scattering (DLS) to on-line Raman spectroscopy.

Lipids, specifically their selection, concentrations, and molar ratio, as well as process parameters during microfluidic mixing, directly modulate LNP attributes such as size and encapsulation efficiency. However, lipid analysis is not routinely performed in process parameter studies where parameters are being screened, nor is the performance of individual process steps regularly determined. For quantitative analysis, high performance liquid chromatography (HPLC)-based methods are valuable due to their accuracy and reproducibility. Since most lipids lack chromophores, CAD provides a sensitive, universal alternative to conventional detection through absorbance in the ultraviolet-visible (UV/Vis) range, independent of the lipids' spectral or physicochemical properties. In the first study (Chapter 3), a reversed-phase (RP)-HPLC-CAD method will be established for lipid quantification and applied for the analysis of LNP process intermediates. The RP-HPLC-CAD method will be designed to analytically separate and quantify lipids in former LNPs. Following the systematic method development, calibration, and validation, it will provide individual lipid concentrations. A process parameter study that covers variations in microfluidic mixing parameters during LNP production, followed by dialysis, will demonstrate its applicability across LNP processing. Derived from lipid concentrations, the lipid molar ratio of LNP process intermediates will complement commonly determined LNP attributes, and process performance will be revealed by the lipid recovery of the individual process steps. This study will aim to intensify LNP and process characterization by implementing an analytical method for lipid quantification, thereby highlighting its potential applicability in other process parameter studies or processes, such as CFF.

For LNP processing, process parameter studies reported in literature primarily cover variations of microfluidic mixing parameters during LNP production, while the following buffer exchange to remove residual solvent and raise the pH received only limited attention. Buffer exchange is often conducted by diffusion-driven dialysis, although pressure-driven, CFF-based diafiltration (DF) offers a scalable, time- and cost-efficient alternative for LNP purification, with optional volume reduction to seamlessly concentrate the LNPs. However, studies on CFF process development for LNP purification are rare, and the impact of specific membrane characteristics and CFF process parameters on LNP attributes remains unexplored. Accordingly, the same applies to CFF monitoring. In the second study (Chapter 4), LNP purification by CFF will be investigated through a dedicated CFF parameter study, monitored using at-line DLS, and compared to LNP purification by dialysis. LNPs will be purified by CFF and dialysis for direct comparison. Across the CFF experiments, distinct membrane characteristics and CFF process parameters will be varied to evaluate their effects on LNP attributes and process performance. The CFF process is monitored using at-line DLS, providing time-resolved insights into particle size. Finally, the LNP attributes during sterile filtration and storage of CFF-purified compared to dialyzed LNPs will be investigated. This study will investigate CFF as an alternative purification method to dialysis, thereby enhancing process understanding and laying a foundation for its future application in LNP purification.

Similar to CFF, selective precipitation represents a cost-effective and scalable separation technique based on size and has emerged for capturing VLPs from clarified lysate. Traditional precipitate recovery suffers from batch-to-batch variability and low productivity due to consecutive centrifugation and resuspension steps. In contrast, CFF-based microfiltration (MF) for precipitate processing and recovery addresses scalability, process integration, and intensification. In one CFF unit, precipitation and two consecutive, constant-volume DF steps can be accomplished, allowing for washing the precipitate to separate soluble impurities and for subsequent product re-dissolution. During the latter, the re-dissolved product passes the MF membrane, thereby separating the product from irreversibly precipitated species. Despite improvements in purity, yield, and productivity, a subsequent ultrafiltration (UF)/DF step is required to remove residual precipitant and concentrate the product, compromising overall productivity. In the third study (Chapter 5), a novel dual-stage CFF set-up will be developed for integrated, seamless recovery of VLP precipitates. The dual-stage CFF set-up will be configured by connecting two CFF units in series with a MF/UF membrane configuration. Following VLP precipitation and precipitate washing in the first membrane stage, VLP recovery will cover VLP re-dissolution, isolation, and concentration. In detail, the re-dissolved VLPs will be retained and isolated in the second membrane stage through DF-based removal of residual precipitant and impurities, as well as further concentrated through a simple switch to UF mode. Dual-stage CFF performance will be assessed relative to single-stage CFF, with a focus on final product concentration and purity. This study will serve as a proof-of-concept for integrated, seamless precipitate processing by CFF, paving the way towards standardized platform processing of diverse biopharmaceuticals exclusively based on precipitation and filtration.

Similar to the developmental maturity of standardized platform processes, the one of sensor-based PAT tools varies across different separation techniques and biopharmaceuticals. Most sensor-based PAT tools established rely on UV/Vis spectroscopy and chemometrics for monitoring chromatographic separation processes, with applications also extending to filtration processes. For precipitation monitoring, however, sensor-based PAT tools are generally rare, as their development entails several challenges, including the presence of impurities and particulate precipitates within the crude, complex lysate, as well as turbidity. The combination of Raman spectroscopy and chemometrics may represent a promising approach for precipitation monitoring; however, systematic data diversification as well as in-depth insights into Raman spectral data and their chemometric preprocessing remain relatively uncommon. In the fourth study (Chapter 6), a systematic approach will be pursued for the development of a Raman-based PAT tool for on-line monitoring of VLP precipitation in crude, complex lysate. Different batch and fed-batch precipitation experiments will be performed using conditioned lysate to generate a diversified data set with variations in precipitation dynamics and backgrounds. Spectral preprocessing operations will be systematically combined and evaluated regarding their ability to eliminate the spectral background and interferences. Partial least squares (PLS) regression will be employed to predict the concentration of precipitated VLPs from preprocessed Raman spectral data, and the effects of individual preprocessing operations on model performance will be evaluated. This study will aim to enhance the development of a Raman-based PAT tool for precipitation monitoring using a systematic approach, with the potential to transfer such approaches to future sensor-based PAT tool development.

While precipitant quantification can be omitted in precipitation screenings or processes where a defined amount of precipitant is added, it becomes essential in dynamic depletion processes, such as during the recovery of precipitated VLPs by dual-stage CFF (cf. Chapter 5). Here, VLPs are accumulated in the second membrane stage, while the precipitant is simultaneously depleted. Next

to providing real-time process insights, the implementation of sensor-based PAT tools for monitoring can minimize the need for sampling, thereby reducing interventions in the process, associated product loss, and, in the case of constant-volume DF, changes in product concentration and hence process dynamics. Compared to the Raman-based PAT tool development for precipitation monitoring (cf. Chapter 6), fewer interferences are expected when monitoring VLP recovery, which may allow for the transfer of models built on pure stock solutions to process-derived spectral data for prediction. In the fifth study (Chapter 7), attribute-specific preprocessing of Raman spectral data will be addressed to systematically develop Raman-based PAT tools and transfer them for monitoring VLP accumulation and precipitant depletion simultaneously during VLP recovery by dual-stage CFF. Based on spectral data from pure VLP and precipitant stock solutions, the sensitivity of Raman spectroscopy towards the protein and precipitant, as well as their spectral features, will be comprehensively investigated. Accordingly, protein- and precipitant-specific preprocessing operations will be selected, and regression models will be developed. To showcase the applicability of the developed PAT tools, the dual-stage CFF set-up (Chapter 5) will be equipped with an on-line monitoring loop in the second membrane stage to enable Raman spectral data acquisition during the VLP recovery step. The developed models will be transferred to CFF-derived spectral data, and their performance will be evaluated based on predicted VLP and precipitant concentrations compared to off-line data. This study will account for differences in sensor selectivity and spectral features of the monitored attributes, thereby highlighting the aspects of attribute-specific selections of sensors, preprocessing operations, and models for sensor-based PAT tool development.

2.2 Comprehensive Overview of Publications

This section presents an overview of the five research articles written within the scope of this thesis. The outlined chapters contain the unchanged content of the respective research articles, with formatting and layout adjustments made to ensure consistency throughout this thesis. As three of the research articles resulted from collaborative work with colleagues to elevate research quality, the first authorship was shared with equal contributions.

All research articles cover the interconnected areas of non-chromatographic, size-selective separation techniques and sensor technologies applied for the primary purification of LNPs (Chapters 3-4) or VLPs (Chapters 5-7), as presented as an illustration in Figure 2.1. Chapter 3 establishes an analytical method for lipid quantification based on CAD and applies it for the analysis of LNPs purified by dialysis. Chapter 4 presents the effects of LNP purification by CFF, evaluated as an alternative technique to traditional dialysis, and introduces at-line size monitoring using DLS. Chapter 5 introduces a dual-stage CFF set-up, enabling integrated purification of VLPs based on precipitation and filtration. Chapters 6 and 7 present systematic approaches for PAT tool development relying on Raman spectroscopy for on-line monitoring of VLP precipitation and the VLP recovery step by dual-stage CFF, respectively.

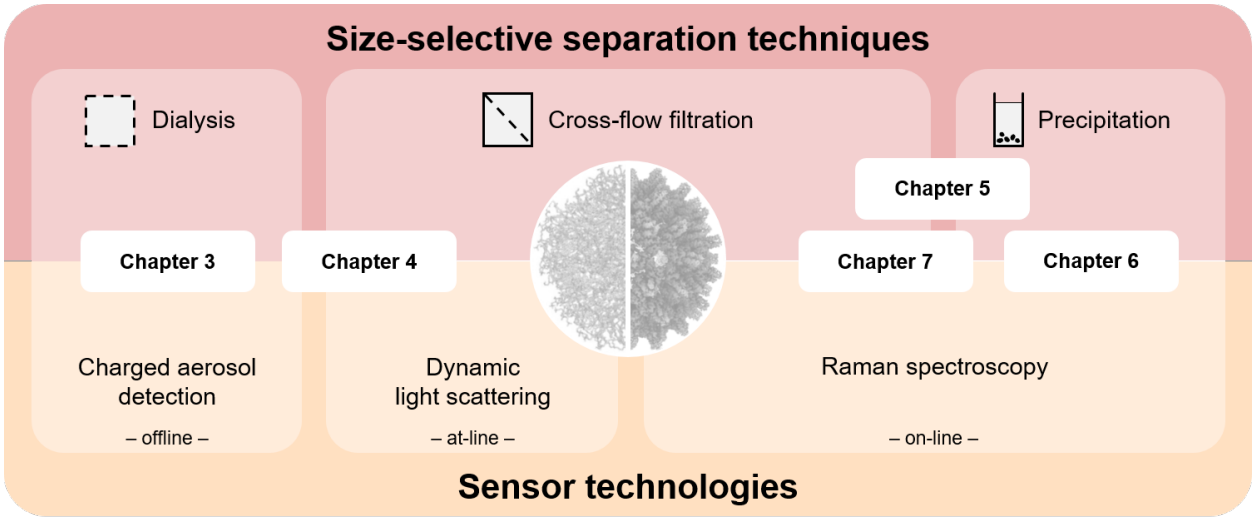

Figure 2.1 Illustration of the thesis overview. The research articles presented cover several non-chromatographic, size-selective separation techniques and sensor technologies for the primary purification of LNPs (Chapters 3-4) and VLPs (Chapters 5-7), with corresponding particle representations adapted from [145] and [146], respectively.

Chapter 3

RP-CAD for Lipid Quantification: Systematic Method Development and Intensified LNP Process Characterization. 29

Nicole Beckert*, Annabelle Dietrich*, and Jürgen Hubbuch *contributed equally

published in *Pharmaceuticals*, Volume 17(9), 2024, Article 1217
https://doi.org/10.3390/ph17091217

Chapter 3 establishes an analytical method for lipid quantification based on RP-HPLC-CAD. An experimental approach is used to optimize the linearity range for six lipids, followed by method calibration and validation. By applying the analytical method on LNP process intermediates, commonly determined LNP attributes are complemented by lipid concentrations and the lipid molar ratio. Further, this method is used to evaluate the process performance of LNP purification by dialysis based on lipid recovery.

Chapter 4

Time-Dependent Particle Size Increase during Lipid Nanoparticle Purification by Cross-Flow Filtration 53

Annabelle Dietrich*, Nicole Beckert*, and Jürgen Hubbuch *contributed equally

published in *Journal of Colloid and Interface Science*, Volume 694, 2025, Article 137663
https://doi.org/10.1016/j.jcis.2025.137663

Chapter 4 presents CFF-processing as an alternative to purification by dialysis. First, a LNP pre-dilution step is introduced to reduce the ethanol concentration prior to the purification. Across the CFF experiments, membrane characteristics and CFF process parameters are varied to evaluate their effects on LNP attributes and process performance. Moreover, at-line monitoring by DLS is implemented, providing time-resolved insights into particle size. Ultimately, the effects of short-term storage and sterile filtration on LNP attributes are evaluated.

Chapter 5

Dual-Stage Cross-Flow Filtration: Integrated Capture and Purification of Virus-Like Particles 77

Annabelle Dietrich, Luca Heim, and Jürgen Hubbuch

published in *Biotechnology and Bioengineering*, Volume 122(4), 2025, pp. 884-894
https://doi.org/10.1002/bit.28914

Chapter 5 introduces a dual-stage CFF set-up for integrated, filtration-based recovery of selectively precipitated VLPs. Two CFF units are connected sequentially and equipped with 0.2 µm and 300 kDa MWCO membranes, respectively. Performing two consecutive DF steps allows for washing the VLP precipitates in the first membrane stage, followed by isolating the re-dissolved VLPs in

the second membrane stage by continuously removing precipitant and contaminants. Further, VLP concentration is accomplished by a seamlessly integrated UF step. A comparison of the dual-stage and single-stage CFF-based processing is presented in terms of final product concentration and purity.

Chapter 6

Annabelle Dietrich*, Robin Schiemer*, Jasper Kurmann, Shiqi Zhang, and Jürgen Hubbuch

*contributed equally

published in *Frontiers in Bioengineering and Biotechnology*, Volume 12, 2024, Article 1399938
https://doi.org/10.3389/fbioe.2024.1399938

Chapter 6 presents a systematic approach to develop an on-line monitoring tool based on Raman spectroscopy for selective VLP precipitation. The study addresses the challenge of developing PAT tools for analyzing crude, complex mixtures. Diversified data sets for model development are generated by batch and fed-batch precipitation experiments performed with conditioned starting material. Various spectral preprocessing operations are combined and compared to evaluate their ability to eliminate spectral background and interferences caused by the precipitate and precipitant. Ultimately, PLS regression is used for predicting the concentration of precipitated VLPs.

Chapter 7

Annabelle Dietrich, Luca Heim, and Jürgen Hubbuch

published in *Frontiers in Bioengineering and Biotechnology*, Volume 13, 2025, Article 1631807
https://doi.org/10.3389/fbioe.2025.1631807

Chapter 7 presents an alternative approach for the development of Raman-based PAT tools, focusing on model transfer. The dual-stage CFF set-up introduced in Chapter 5 is equipped with an on-line monitoring loop including a Raman spectrometer in the second membrane stage for continuous data acquisition during the recovery of VLP precipitate. Conversely, spectral data from pure VLP and precipitant stock solutions are used for model development. The study addresses attribute-specific preprocessing operations to account for differences in Raman spectral features and sensor sensitivity. Eventually, the regression models are transferred to process-derived spectral data acquired from three CFF experiments, and their performance is evaluated based on predicted VLP and precipitant concentrations.

Chapter References

[145] A. Hardianto, Z. S. Muscifa, W. Widayat, M. Yusuf, and T. Subroto. „The Effect of Ethanol on Lipid Nanoparticle Stabilization from a Molecular Dynamics Simulation Perspective“. In: *Molecules* 28.12 (2023). DOI: 10.3390/molecules28124836.

[146] S. Pfister et al. „Structural conservation of HBV-like capsid proteins over hundreds of millions of years despite the shift from non-enveloped to enveloped life-style“. In: *Nature Communications* 14.1 (2023), pp. 1–15. DOI: 10.1038/s41467-023-37068-w.

3

RP-CAD for Lipid Quantification: Systematic Method Development and Intensified LNP Process Characterization

Nicole Beckert[1,*], Annabelle Dietrich[1,*], and Jürgen Hubbuch[1]

[1] Institute of Process Engineering in Life Sciences, Section IV: Biomolecular Separation Engineering, Karlsruhe Institute of Technology (KIT), Karlsruhe, Germany

[*] Contributed equally.

Abstract

Lipid nanoparticles (LNPs) and their versatile nucleic acid payloads bear great potential as delivery systems. Despite their complex lipid composition, their quality is primarily judged by particle characteristics and nucleic acid encapsulation. In this study, we present a holistic reversed-phase (RP)-charged aerosol detection (CAD)-based method developed for commonly used LNP formulations, allowing for intensified LNP and process characterization. We used an experimental approach for power function value (PFV) optimization termed exploratory calibration, providing a single PFV (1.3) in an appropriate linearity range for all six lipids. Followed by the procedure of method calibration and validation, linearity (10–400 ng, $R^2 > 0.996$), precision, accuracy, and robustness were effectively proven. To complement the commonly determined LNP attributes and to evaluate the process performance across LNP processing, the developed RP-CAD method was applied in a process parameter study varying the total flow rate (TFR) during microfluidic mixing. The RP-CAD method revealed a constant lipid molar ratio across processing but identified deviations in the theoretical lipid content and general lipid loss, which were both, however, entirely TFR-independent. The deviations in lipid content could be successfully traced back to the lipid stock solution preparation. In contrast, the observed lipid loss was attributable to the small-scale dialysis following microfluidic mixing. Overall, this study establishes a foundation for employing RP-CAD for lipid quantification throughout LNP processing, and it highlights the potential to extend its applicability to other LNPs, process parameter studies, or processes such as cross-flow filtration.

3.1 Introduction

As the potential of small interfering RNA (siRNA) for gene silencing was revealed a few decades ago [147], lipid-based delivery systems—flexible in their structural complexity and composition—evolved in parallel, unlocking the full potential of lipid-based siRNA delivery, which was recently demonstrated by the approval of Onpattro (patrisan) [6].

For the encapsulation of nucleic acid payloads, as well as for the nucleic acid release, the role of a cationic lipid (CL) is crucial as anionic siRNA has been shown to be complexed with the CL [21]. The CL is part of a delivery system called LNP with three additional lipids, namely cholesterol, a phospholipid, and a polyethylene glycol lipid (PEGL). The structure of LNPs has already been visualized by transmission electron microscopy (TEM) and exhibits non-continuous lipid bilayers with an electron-dense core [12, 21].

As each lipid component in LNPs serves distinct purposes [22], lipid selection, as well as their lipid molar ratio, are crucial for proper functionality. Phospholipid content, cholesterol content, and phospholipid type affect LNP morphology [30], while variations in size have been observed for different CLs [23]. Since the concentration of PEGL constitutes the smallest proportion within an LNP, a precise adjustment of its content is critical due to its influence on LNP size, as well as on the prevention of inter-particle fusion [28, 31, 32], the circulation time, and activity in vivo [148]. The role of lipid components in LNPs was comprehensively summarized by Albertsen et al. [22]. To fulfill these varieties of functions, the incorporated particular lipid content in LNPs, termed the lipid molar ratio, has been widely reported within a similar range. For siRNA-LNPs, with a lipid molar ratio of 50:10:38.5:1.5 mol% (CL:phospholipid:cholesterol:PEGL), potency was early on verified in vivo [25, 26, 149], and, consequently, this ratio has been extensively utilized in fundamental research and development [27, 31, 122, 123, 150–152]. Thus far, this ratio has not only demonstrated efficacy

in Onpattro (patrisan), being the first LNP approved by the FDA, but it was also employed for the messenger RNA (mRNA)-1273 vaccine during the COVID-19 pandemic [6].

Besides the impact of lipids on a molecular basis, the impact of the production and purification parameters on the physicochemical properties of LNPs has been investigated in the literature, hereafter referred to as parameter studies. Microfluidic mixing devices enable the reproducible and scalable mixing of the lipid-containing organic and the nucleic acid-containing aqueous phase, inducing LNP formation [12]. Key microfluidic process parameters, such as TFR and flow rate ratio (FRR) [23, 29, 34], along with aqueous phase characteristics [23, 29] and lipid concentration in the organic phase [29, 34], have been shown to significantly influence particle size and polydispersity. The N/P ratio describing the molar ratio of positively charged nitrogen (N) within the amines of the charged lipid to the negatively charged phosphate (P) groups in the nucleic acid backbone has been found to affect LNP morphology [27] and the encapsulation efficiency of nucleic acids [28, 29]. Since nucleic acids are commonly dissolved in buffers with a pH of 4–5, microfluidic mixing is typically followed by dialysis to neutralize pH and remove the remaining organic solvent. Except for the pH variations of formulation buffers studied by Terada et al. [34], the impact of dialysis as a purification step remains rather unexplored.

To summarize, LNP quality attributes imply characteristics regarding the intact LNP, as well as the nucleic acids and lipids themselves. Although a variety of analytical techniques quantitatively assessing these characteristics exist, as comprehensively reviewed by Fan et al. [153], only a restricted set of analytical methods has been consistently utilized in the context of parameter studies [23, 28, 29, 34]. In particular, LNP physicochemical property assessment comprises surface charge using electrophoretic light scattering (ELS), particle size, and the polydispersity commonly measured by dynamic light scattering (DLS). Additionally, the encapsulation efficiency of nucleic acids in LNPs is determined using fluorescence-based assays. However, lipid content analysis to quantify all lipid components and determine the lipid molar ratio is not routinely conducted, especially not across LNP processing.

High performance liquid chromatography (HPLC) approaches are deployed for lipid separation and quantification across their molecular diversity. RP-HPLC serves for the separation of lipid molecular species according to their relative hydrophobicity that arises from differences in head group polarity, tail unsaturation, and alkyl chain length [154]. As most lipids lack chromophores, typical spectrophotometric detection for lipid quantification is not applicable. Here, CAD can be deployed, where the mobile phase is nebulized and dried, the formed particles are positively charged by a stream of nitrogen, and the charge is measured by a highly sensitive electrometer [117, 118]. CAD outperforms the other widespread aerosol-based evaporative light scattering detection in terms of sensitivity and width of the dynamic range [119]. Both performance parameters can be further improved by optimizing the built-in PFV, which linearizes the detector's response. Here, several strategies to determine the optimal PFV were explored, including experimental, empirical, and mathematical approaches [155–158]. These studies exclusively optimized the PFV for one particular substance, while the literature lacks PFV optimization studies considering multi-component systems such as LNPs.

Thus far, the developed RP-CAD methods for various components of LNPs comprise the lipid quantification of phospholipids [156], PEGLs [159, 160], liposomes [161], LNPs [120–124], and further stability studies to monitor the degradation products of the prior listed components [121, 156, 160, 161]. Considering the RP-CAD method application on LNP formulations, different objectives were pursued

besides method validation. Li et al. [120] focused on the variation of key chromatographic parameters critical for separation such as the stationary phase, ion-pair agent, and column temperature, while Kinsey et al. [121] and Bender et al. [123] further studied forced lipid degradation. For method development, Kim et al. [122] pursued an alternative strategy, employing an analytical quality-by-design approach. However, these studies proved their methods with solely final formulated LNPs and, except for Kim et al. [122] and Bender et al. [123], with partly unknown lipids and lipid molar ratio specifications. Thus far, no analytical method has been employed across processing nor has the effect of process parameter variations on lipid-related LNP attributes been considered.

In this study, we present a novel holistic RP-CAD method for lipid quantification across LNP production and processing. Based on an experimental approach, we systematically varied the PFV using a simplified lipid stock solution set, focusing on identifying a single PFV for multiple lipids. By expanding the stock solution set for method calibration and validation studies, we demonstrated adequate linearity, precision, accuracy, and robustness according to the International Council for Harmonisation (ICH) Q2(R2) guideline [162], enabling lipid quantification in pure and mixed lipid solutions. To demonstrate the RP-CAD method's applicability for quantifying lipids at various stages of the LNP process regardless of specific process parameters, the impact of the TFR as a production parameter on the LNP attributes was studied using LNPs encapsulating a DNA-based model-siRNA. In addition to the commonly determined attributes, particle size, surface charge, and nucleic acid encapsulation, we simultaneously assessed lipid quantities and lipid molar ratio with the newly developed RP-CAD method. These lipid quantities allow for the calculation of lipid recoveries, providing an indicator of the process performance in LNP purification and thus enabling intensified process characterization.

3.2 Materials and Methods

3.2.1 Materials and Buffers

Chemicals were purchased from Merck (Darmstadt, Germany), if not otherwise stated. All the lipids used were delivered in powder form and stored at −20 °C until usage. 1,2-Dioleoyl-3-trimethylammonium-propane (chloride salt) (DOTAP) and 1,2-Dioctadecanoyl-sn-glycero-3-phosphocholin (DSPC) were kindly provided by Lipoid (Ludwigshafen, Germany). N-(4-carboxybenzyl)-N,N-dimethyl-2,3-bis(oleoyloxy)propan-1-aminium (DOBAQ),1,2-Dimyristoyl-rac-glycero-3-methoxypolyethylene glycol-2000 (DMG-PEG), 1,2-Dimyristoyl-sn-glycero-3-phosphoethanolamine-N-[methoxy-(polyethylene glycol)-2000] (ammonium salt) (DMPE-PEG) from Avanti Polar Lipids (Alabaster, AL, USA), and cholesterol were used. Ultrapure water (Purelab ultra, ELGA LabWater, High Wycombe, UK) and HPLC grade ethanol were used for buffer and stock solution preparation. Furthermore, 25 mM acetate buffer at pH 4.0 consisted of sodium acetate trihydrate and acetic acid. Tris(hydroxymethyl)aminomethane (Tris) was used for 10 mM Tris buffer at a pH of 7.4. Buffers were pH-adjusted with 32% hydrochloric acid solution using a SenTix62 pH electrode (WTW, Weilheim, Germany) coupled to a HI 3220 pH meter (Hanna Instruments, Woonsocket, RI, USA), filtered through a 0.2 µm cellulose acetate filter (VWR International, Radnor, PA, USA). Both, LC-MS grade 0.1% trifluoroacetic acid (TFA) (*v*/*v*) in water and in acetonitrile (ACN) from Thermo Fisher Scientific Inc. (Waltham, MA, USA) and pure ACN in LC-MS grade from VWR Chemicals (VWR International) were used. NoLimits™ 20 bp DNA fragments, 5'-ATGGTGAGCAAGGGCGAGTT-3' as forward primer, 5'-CTCGCCCTTGCTCACCATTT-3' as

reverse primer, as well as Triton™ X-100, Quant-iT™ PicoGreen™, and RiboGreen™ Assay Kits were obtained from Thermo Fisher Scientific Inc.

3.2.2 Development of the RP-HPLC-CAD Method

3.2.2.1 Preparation of Lipid Stock Solutions

Based on preliminary experiments, 0.3 mg mL^{-1} lipid stock solutions were prepared by individually dissolving each lipid in ethanol using a Branson Ultrasonics sonifier SFX550 (Thermo Fisher Scientific Inc.). The solutions were subsequently 0.2 µm-filtered (Sartorius Stedim Biotech GmbH, Göttingen, Germany) and stored at −20 °C. Standards were prepared by dilution with ethanol, and 200 µL samples were loaded into 96-well half-area microplates (Greiner BioOne, Kremsmünster, Germany) for HPLC analysis.

3.2.2.2 Instrumentation

An Ultimate 3000 RS HPLC system (Dionex Corporation, Sunnyvale, CA, USA) controlled by Chromeleon 6.8 (Thermo Fisher Scientific Inc.) and consisting of an HPG-3400RS pump, a WPS-3000TFC autosampler, a TCC-3000RS column compartment, a 3000RS diode array detector and a Corona Veo CAD RS. The CAD was supplied with nitrogen gas from the Corona Nitrogen 1010 (Peak Scientific Instruments GmbH, Düren, Germany) connected to the in-house compressed air system. A 2.1 × 150 mm ACQUITY® BEH Phenyl column (particle size 1.7 µm, pore size 130 Å, Waters, Milford, CT, USA) was used in combination with the corresponding VanGuard™ pre-column 2.1 × 5 mm. The column temperature, autosampler temperature, flow rate, and injection volume were set to 50 °C, 8 °C, 0.3 mL min^{-1}, and 8 µL, respectively. The settings for the CAD were 35 °C for the evaporation temperature and 3.6 s for the filter constant. The developed method, with 0.1% TFA (*v*/*v*) in water as mobile phase A and 0.1% TFA (*v*/*v*) in ACN as mobile phase B, started at 40 % B with a 4 min hold time, followed by two linear gradients to 70 % B and 100 % B for 1 min and 11.25 min, respectively. After a hold time of 2 min at 100 % B, a linear gradient of 1 min was used to reset to initial conditions.

3.2.2.3 Variation of PFV and the Linearity Range

For the PFV variation study, standards were prepared in duplicates ($n = 2$) by serial dilutions of the lipid stock solutions and measured twice ($m = 2$). Measurements were recorded for each lipid with total lipid quantities of 37.5, 75, 150, 300, 600, 1200, and 2400 ng on column for PFV = 1.0, 1.1, 1.2, and 1.3, respectively. Regarding linearity, mass ranges I, II, and III were evaluated, which differed in their maximum lipid quantities (2400, 1200, and 600 ng) and thus in the amount of data points ($5 \leq p \leq 7$). For each range, PFV, and lipid, the linear regression was performed by the method of least squares and evaluated by the coefficient of determination R^2. The authors referred to this procedure as exploratory calibration.

3.2.2.4 RP-CAD Method Calibration and Validation

For the RP-CAD method calibration and validation at PFV = 1.3, all standards were prepared in triplicates ($n = 3$) and measured twice ($m = 2$). For nine-point calibration ($p = 9$), measurements were recorded for each lipid with lipid quantities of 10, 20, 40, 80, 120, 160, 200, 240, and 400 ng on

column. According to the Q2(R2) guideline [162] by the ICH, the RP-CAD method was validated considering linearity, precision, accuracy, and robustness. Regression by the method of least squares was used to evaluate the linearity with the coefficient of determination R^2. Precision was considered as repeatability, intermediate precision, and reproducibility. Residual standard deviations of all lipid standards with 40, 120, and 240 ng were used for repeatability. Intermediate precision and reproducibility were investigated exemplarily for DSPC. Intermediate precision was performed on two separate days for lipid standards of 40, 120, and 240 ng, while reproducibility was investigated by repeated calibration and linearity validation. Accuracy was investigated for 40, 120, and 240 ng DSPC and determined as the ratio of the measured to the expected value, expressed as the percentage recovery. Robustness was assessed by repeated injections of a lipid mixture standard with variations in the column oven temperature (50 ± 2 °C), flow rate (0.3 ± 0.01 mL min^{-1}), and CAD evaporation temperature (35 ± 2 °C), and it was determined by the procentual deviation from the standard value. The lipid mixture standard contained DOTAP, DSPC, cholesterol, and DMG-PEG with a total lipid quantity of 800 ng (200 ng per lipid) on column.

3.2.3 Lipid Nanoparticle Process Characterization

3.2.3.1 Preparation of Aqueous Nucleic Acid Stock Solution

Both reverse and forward primers were rehydrated with Tris-EDTA (TE) buffer to 0.1 mmol L^{-1}, equimolar mixed, and hybridized in a C1000 Touch™ Thermal Cycler (Bio-Rad Laboratories Inc., Hercules, FL, USA). The annealing process comprised a 7 min incubation at 95 °C, step-wise cooldowns (9 °C every 5 min) to 68 °C, and a final cooldown at room temperature. Annealing and stability against 1% Triton™ X-100 were evaluated by the Quant-iT™ PicoGreen™ assay according to the manufacturer's protocol with further adaptions. The assay was standardized with NoLimits™ 20 bp DNA fragments with three replicates of six concentrations (0, 20, 100, 300, 500, and 1000 ng mL^{-1}). For both standards and samples, the assay was performed with and without 1% Triton™ X-100 treatment in 384-well black polystyrene microplates (Biozym Scientific GmbH, Hessisch Oldendorf, Germany) in a 20 µL scale. Excitation (λ_{ex} = 480 nm) and emission (λ_{em} = 520 nm) were recorded by a Spark® microplate reader (Tecan Group Ltd., Männedorf, Switzerland). The annealed primer solution was adjusted to 119 µg mL^{-1} with acetate buffer, serving as the aqueous nucleic acid stock solution with model-siRNA for all experiments.

3.2.3.2 Microfluidics and Purification

To reach a N/P ratio of 5 after LNP synthesis, the DOTAP, DSPC, cholesterol, and DMG-PEG were dissolved (50:10:38.5:1.5 mol%) as described in Section 3.2.2.1 to a 12 mg mL^{-1} total lipid concentration. The setup for LNP synthesis comprised a Nemesys pump (Cetoni GmbH, Korbußen, Germany) equipped with 1 mL (Innovative Labor Systeme GmbH, Stützerbach, Germany) and 10 mL glass syringes (SETsonic GmbH, Ilmenau, Germany), as well as a herringbone-structured microfluidic chip (Microfluidic ChipShop, Jena, Germany). The LNPs were synthesized in duplicates at a constant FRR of 5:1 (aqueous:organic), while the TFR was varied with 10, 15, and 20 mL min^{-1}. The LNPs were dialyzed using 10 kDa Slide-A-Lyzer® dialysis cassettes (Thermo Fisher Scientific Inc.) in 10 mM Tris buffer (pH 7.4) at 2–8 °C for 4 h and overnight. The final formulated LNPs were stored at 2–8 °C for 14 days.

3.2.3.3 Lipid Concentration, Molar Ratio, and Recovery

Single lipid concentrations, a lipid molar ratio, and a total lipid recovery rate were determined by applying the developed RP-CAD method with the corresponding calibration curves. Samples were prepared in duplicates and diluted with ethanol to the final concentrations within the calibration curves. The lipid recovery rate was calculated based on the measured lipid quantities, the weights of the LNP solutions prior to and after dialysis, and the densities of the respective solution compositions regarding the ethanol-to-water content.

3.2.3.4 Particle Size and Surface Charge

The particle size as the Z-average and the polydispersity index (PDI) of the LNPs were determined by applying DLS using a Zetasizer Nano ZSP equipped with the Zetasizer software 7.12 (both Malvern Instruments Ltd., Malvern, UK). Measurements were performed using a 633 nm laser, a 173° scatter detection angle, and a low-volume quartz batch cuvette ZEN2112 (Malvern Panalytical Ltd., Malvern, UK). The LNPs refractive index (RI) was 1.333 and the absorption was 0.01. For the dispersant, a RI of 1.341 and a viscosity of 1.919 cP were determined. Samples were diluted to a lipid concentration of 1 mg mL^{-1}. Measurements were performed in duplicates with three sub-measurements, an automatic measurement duration, and a laser attenuation of 5.

To examine the surface charge as the zeta potential of the dialyzed LNP, the ELS was applied using the identical device and software but with a folded capillary cell DTS1070 (Malvern Panalytical Ltd.). For the measurements, a dielectric constant ϵ_r of 78.5 was set and the Helmholtz–Smoluchowski equation was applied. Each sample was measured in duplicates and five measurements per sample were performed with a minimum of 10 runs at 60 V.

3.2.3.5 Nucleic Acid Encapsulation

The proportion of encapsulated nucleic acids in LNPs, referred to as encapsulation efficiency, was determined by the Quant-iT™ RiboGreen™ assay according to the manufacturer's protocol with further adaptations. The fluorescent dye was diluted and added to the LNP sample with or without 1% Triton™ X-100. A calibration curve was obtained for each condition in the range of 20 to 1000 ng mL^{-1} using NoLimits™ 20 bp DNA fragments. The samples and the calibration curves were prepared in 384-well black polystyrene microplates in duplicates and fluorescence-scanned (λ_{em} = 520 nm, λ_{ex} = 480 nm) using a Spark® microplate reader. The encapsulation efficiency EE was calculated according to Equation (3.1):

$$EE = \frac{m_{total} - m_{free}}{m_{total}} * 100\,\%, \tag{3.1}$$

where m_{total} and m_{free} describe the total nucleic acid mass of the sample after treatment with Triton™ X-100 and the mass of free nucleic acids outside the LNP, respectively.

3.2.4 Statistical Evaluation

Data evaluation and data visualization were performed with MATLAB® R2021a (TheMathWorks Inc., Natick, MA, USA). Replicate measurements are presented as the mean ± standard deviation, and uncertainty propagation was used for the error determination. To underline the observed trends, significance was determined using Welch's t-test of normally distributed data (Shapiro–Wilk test).

3.3 Results

3.3.1 Lipid Quantification—Method Development, Calibration, and Validation

The RP-CAD method was developed for cholesterol; the phospholipid DSPC; two CLs: DOTAP and DOBAQ; two PEGLs: DMG-PEG and DMPE-PEG.

3.3.1.1 Method Development

For lipid separation, RP-CAD solvents and method settings, including column temperature, CAD evaporation temperature, injection volume, flow rate, and gradient design, were determined in preliminary experiments. Figure 3.1 shows the RP-CAD chromatograms of all the used lipids with a lipid quantity of 400 ng on the column at a PFV of 1.3.

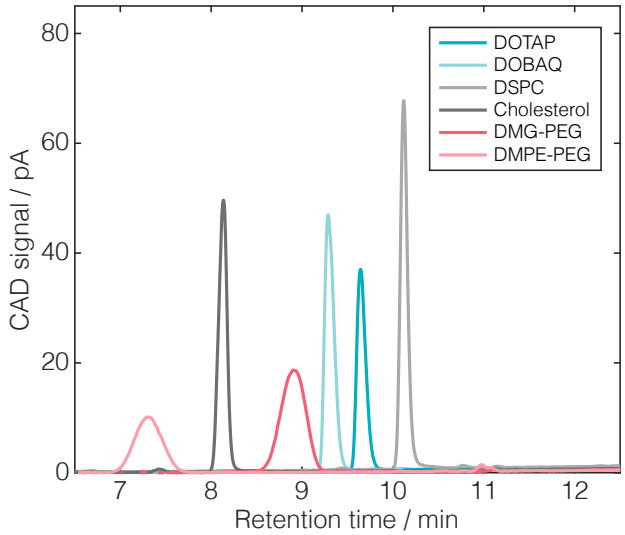

Figure 3.1 Overlaid HPLC chromatograms of the common lipids used in the LNP formulations: DOTAP, DOBAQ, DSPC, cholesterol, DMG-PEG, and DMPE-PEG.

Overall, baseline separation was achieved for all lipids. Considering peak shapes, wider and less sharp peaks were observed for PEGLs compared to other lipid types, which can be attributed to the distribution of the molecular weights within the polyethylene glycol (PEG) chains. Moreover, the differences in the peak areas for equivalent lipid quantities on the column emphasize the importance of employing lipid-specific calibration.

To maintain the linearity between the injected lipid quantity and peak area, preliminary experiments were performed to find an appropriate linearity range in combination with the built-in PFV. To cover wide lipid mass ranges for all lipids while maintaining a manageable level of effort, a simplified lipid stock solution set with a limited number of replicates ($n = 2$, $m = 2$) and data points ($p \leq 7$) was deployed for exploratory calibration. Despite the three investigated linearity ranges, increased PFVs resulted in decreased peak areas for the same lipid quantity on column (Figure A3.1a). For the exploratory calibration curves in the three linearity ranges, the R^2 values are illustrated in Figure 3.2 for all lipids.

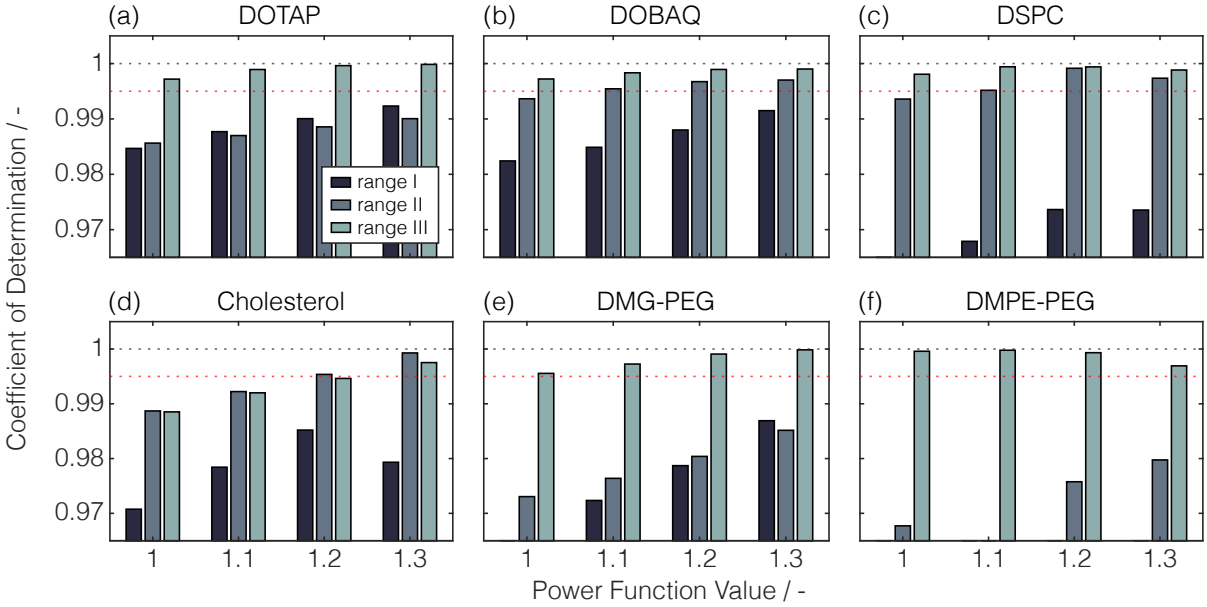

Figure 3.2 Illustration of the variations in linearity range and PFV. Coefficients of determination (R^2) are shown for all exploratory calibration curves for the lipids DOTAP (**a**), DOBAQ (**b**), DSPC (**c**), cholesterol (**d**), DMG-PEG (**e**), and DMPE-PEG (**f**). The PFVs were varied between 1.0–1.3 in 0.1 increments. The linearity ranges I, II, and III differed in their maximum lipid quantity on column: 2400, 1200, and 600 ng. R^2 values above 0.995 represent adequate linearity, marked here with red dashed horizontal lines. For visual purposes, the R^2 values below 0.965 are not depicted.

Comparing the linearity ranges, the range with the lowest maximum lipid quantities on column, termed range III, showed the highest R^2 for almost all tested lipids and PFVs. Except for DOBAQ, DOTAP, and cholesterol, ranges I and II with higher maximum lipid quantities than 600 ng showed insufficient linearity as R^2 values larger than 0.995 were defined for adequate linearity. In both of these ranges, the residuals were not evenly distributed, as exemplarily shown for PFV = 1.3 (Figure A3.1b).

By comparing the selected PFVs, higher PFVs resulted in comparable or even higher R^2 values for DOTAP, DOBAQ, cholesterol, and DMG-PEG, while for DMPE-PEG, a decreased linearity with increasing PFV was observed. Interestingly, when comparing the R^2 decrease with the peak shape, sharper peaks demonstrated better correlations across broader lipid mass ranges. It has to be noted that a single PFV has to be selected for the RP-CAD method. As R^2 values larger than 0.995 were obtained at a PFV of 1.3 for all tested lipids, this setting was selected in combination with the linearity range III.

As part of the method development, this strategy of exploratory calibration using a simplified lipid stock solution set with a limited number of replicates ($n = 2$, $m = 2$) and data points ($p \leq 7$) proved to find a single PFV for all lipids in combination with an appropriate linearity range.

3.3.1.2 Method Calibration and Validation

To provide a broader basis for method calibration and validation, new measurements were performed within the selected linearity range by expanding the number and type of replicates ($n = 3$ & $m = 2$) and the number of data points ($p = 9$) for the calibration curves.

The RP-CAD method was evaluated regarding the linearity in the range of 10-400 ng lipids on column, precision, accuracy, and robustness. Besides the retention times, the regression parameters slope, y-intercept, R^2, and $Sy.x$ are listed in Table 3.1 for all lipids.

Table 3.1 Linearity. The analyzed lipids are listed with their respective slope and y-intercept of the linear regression, the corresponding coefficient of determination (R^2), and the standard error of the regression ($Sy.x$). The linearity range was tested between 10 and 400 ng lipids on column.

Lipid	**Retention Time**	**Linear Regression**			
		Slope	**y-Intercept**	$\boldsymbol{R^2}$	$\boldsymbol{Sy.x}$
	min	**ng (pA min)$^{-1}$**	**ng**	**-**	**-**
DOTAP	9.69	0.0107	0.0774	0.9995	0.0010
DOBAQ	9.33	0.0153	0.1735	0.9966	0.0146
DSPC	10.13	0.0162	0.0671	0.9990	0.0050
CHOL	8.14	0.0125	0.0742	0.9988	0.0035
DMG-PEG	8.91	0.0157	−0.0973	0.9998	0.0009
DMPE-PEG	7.31	0.0094	−0.0291	0.9981	0.0031

The mean peak areas with corresponding standard deviations, the linear regression, and the 95% confidence intervals are additionally depicted in Figure A3.2a–f. The linearity criterion was met with obtained R^2 values equal to or higher than 0.995, $Sy.x$ below 0.015, and with evenly distributed residuals (Figure A3.2g) for all lipids. Precision was demonstrated by repeatability, intermediate precision, and reproducibility. Residual standard deviations less than 4% were observed for repeatability (Figure A3.3a) and intermediate precision (Figure A3.3b). No statistically significant deviations were obtained for repeated calibrations of DSPC, proving the reproducibility of the method (Figure A3.3c). Accuracy was displayed by recoveries of 96%, 98%, and 101% for 40, 120, and 240 ng DSPC, respectively.

Robustness was assessed by minor variations in either the column oven temperature, flow rate, or CAD evaporation temperature using lipid mixtures. Lipid-specific deviations in the peak area and retention time compared to those of standard method parameters are illustrated in Figure 3.3.

Inverse trends were observed for the peak areas and retention times by column oven temperature variations as smaller peak areas were accompanied by higher retention times for lower temperatures and vice versa (Figure 3.3a,b). Conversely, and despite parameter in- or decrease, all parameter variations in the flow rate and CAD evaporation temperature resulted in increased peak area deviations from the standard method up to 9% (Figure 3.3c,e). Regarding retention times, similar trends were observed for both column oven temperature and flow rate variations as the retention time increased by higher parameters and vice versa (Figure 3.3b,d). Here, deviations up to ±2% were found, while deviations of <0.3% were observed for CAD evaporation temperature variations

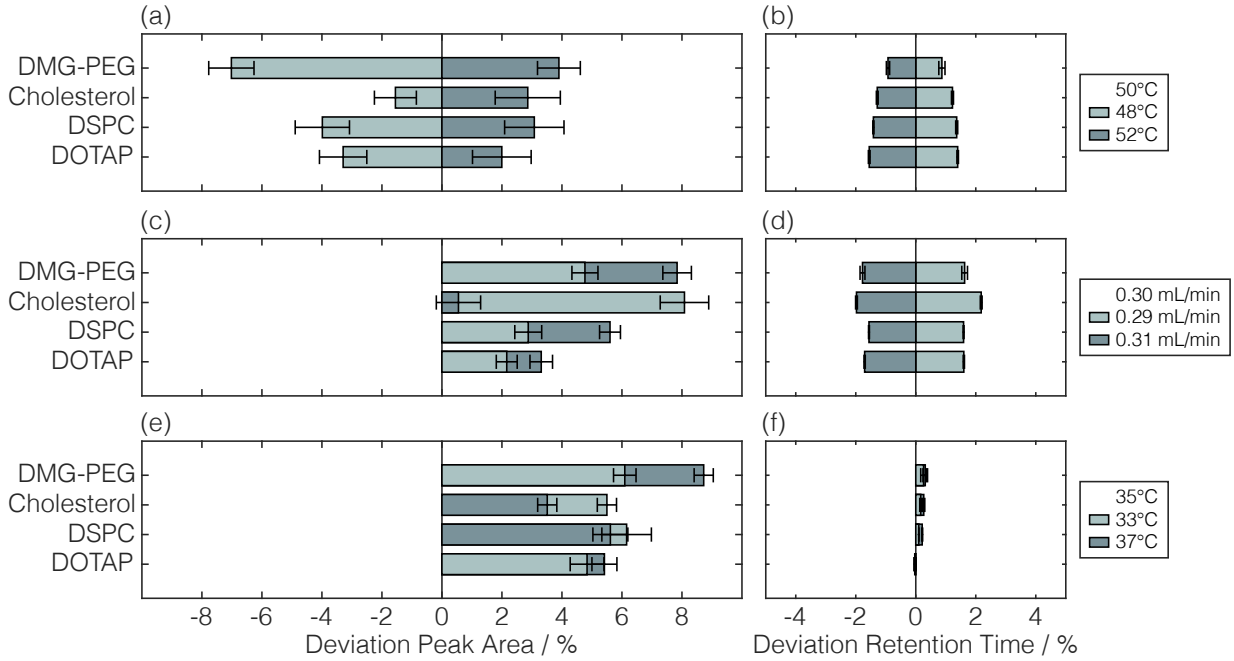

Figure 3.3 Robustness assessment. The impact of variations in the column oven temperature (**a**,**b**), flow rate (**c**,**d**), and CAD evaporation temperature (**e**,**f**) are shown as a percentage deviation from the standard peak area and retention time per lipid. Standard errors were determined by uncertainty propagation. For visual purposes, the standard method parameters are listed on the top of the legend entries.

(Figure 3.3f). Overall, the observed changes by method parameter variations revealed the sensitivity of the detector's response, underlining the need for reliable HPLC systems.

In addition, this robustness assessment further confirmed the lipid quantification in lipid mixtures—various lipids were present in 100% organic solvent—compared to pure lipid solutions. Moreover, the analysis of the LNP process solutions still containing aqueous buffer components and nucleic acids could be demonstrated by appropriate sample dilution with ethanol.

In summary, this novel holistic RP-CAD method was thoroughly calibrated and validated for the quantification of specific lipids in lipid mixtures. Further, this method will find its application for lipid quantification across LNP processing.

3.3.2 Applicability for Lipid Nanoparticle Process Characterization

A process parameter study was performed to demonstrate the applicability of the newly developed RP-CAD method for molar ratio and lipid concentration measurements, as well as for lipid recovery. The TFR was varied to evaluate its impact as an isolated production parameter on the LNP attributes across production, processing, and short-term storage. Besides the RP-CAD analytic, measurements for particle size, surface charge, and nucleic acid encapsulation were employed and collectively termed the standard analytical panel.

3.3.2.1 Standard Analytical Panel

Figure 3.4 illustrates changes in the Z-average, PDI, and zeta potential across processing and storage. Together, these three attributes provided a comprehensive impression of the colloidal stability of the particles.

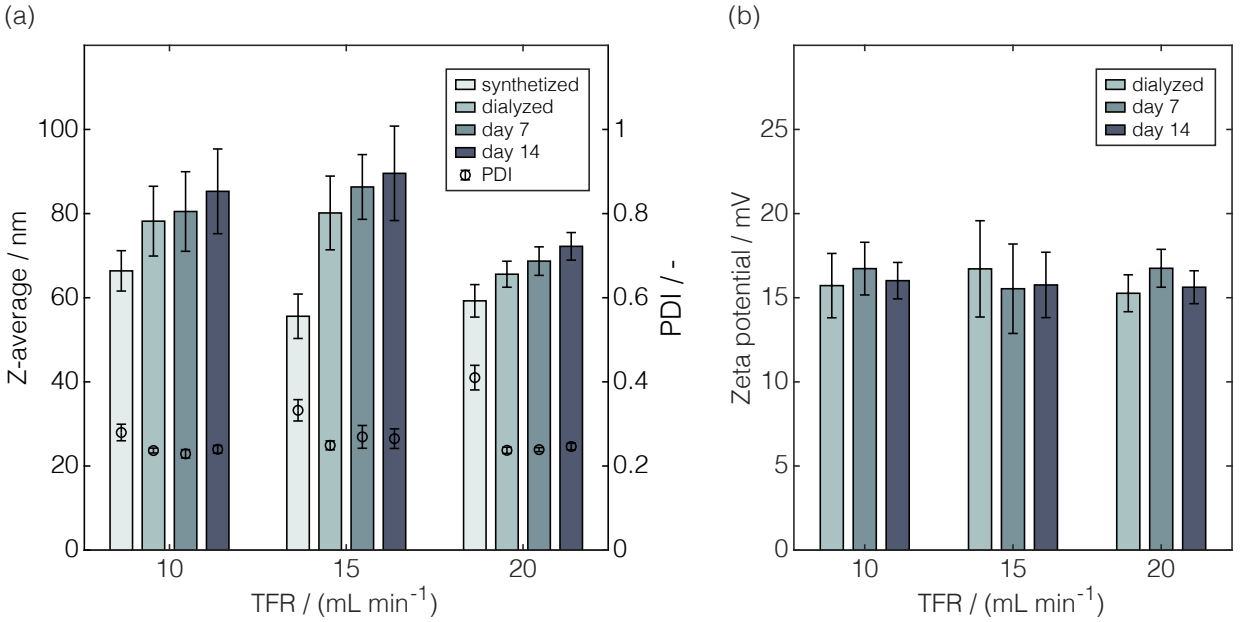

Figure 3.4 Comparison of the Z-average, PDI, and zeta potential of LNPs, which were produced at different TFRs. The produced LNPs were dialyzed and stored for up to 14 days at 2–8 °C. The Z-average and corresponding PDI (**a**) and zeta potential (**b**) were measured twice from independently diluted samples.

Regardless of the TFR, the Z-average of the particles increased during processing and storage, with a more pronounced increase observed during processing (Figure 3.4a). The lowest Z-average increase was identified for 20 mL min^{-1} TFR, which was accompanied by the smallest standard deviations, as well as the overall lowest Z-average with 72.2 nm after storage for 14 days. It has to be noted that the highest Z-average values were observed for 15 mL min^{-1} TFR, contradicting the trend expectation from the literature where higher TFRs were anticipated to result in smaller particle sizes [23, 29]. However, the trend of smaller particles for higher TFRs could clearly be demonstrated by assessing the significance for 10 and 20 mL min^{-1} TFRs.

An opposite trend was observed for the PDI, showing decreasing values across processing, whereas they remained constant during storage (Figure 3.4a). Comparing the PDI across the TFRs after synthesis, higher PDIs were identified for higher TFRs. For both 15 and 20 mL min^{-1} TFRs, PDIs above 0.3 were observed with 0.33 and 0.41, respectively. However, after dialysis, lower but comparable PDIs were recorded with values between 0.24–0.25 regardless of the TFR. During storage, all of these PDI measurements exhibited smaller standard deviations compared to those during synthesis, except for the 15 mL min^{-1} TFR where, concurrently, the highest Z-averages were observed. The intensity-weighted size distribution exemplarily shown for the 15 mL min^{-1} TFR (Figure A3.4) provided a representative illustration of the particle size distribution leading to the Z-average and PDI.

Table 3.2 Encapsulation efficiency of the LNPs produced at different TFRs. The percentage encapsulation efficiencies (EE) of the LNPs produced at 10, 15, and 20 mL min^{-1} TFR.

Total Flow Rate mL min^{-1}	$EE_{\text{Synthesized}}$ %	EE_{Dialyzed} %
10	97.07 ± 1.19	98.04 ± 1.42
15	98.45 ± 0.47	99.88 ± 0.56
20	99.99 ± 0.44	100.06 ± 0.49

Overall, the observed zeta potentials of approximately 16 mV showed no statistic significance regarding both the TFR and time point of analysis (Figure 3.4b), indicating stable surface charges during processing and storage. Note that conducting zeta potential measurements was not feasible for synthesized LNPs due to the presence of ethanol.

Besides the colloidal stability in terms of surface charge and particle size, the percentage of encapsulated nucleic acids was determined during processing for each TFR. Encapsulation efficiencies for the synthesized and dialyzed LNPs are listed in Table 3.2. Across the varied TFRs, encapsulation efficiencies between 97–100% were achieved. No clear differences were observed comparing the encapsulation efficiencies over varied TFRs and across processing. The stability of the free annealed primers, used as model-siRNAs for encapsulation, against Triton™ X-100 was confirmed beforehand through a fluorescence assay that was sensitive for double-stranded DNA (data not shown). This observation points out the absence of model-siRNAs degradation by Triton™ X-100 for encapsulation efficiency determination, ensuring the validity of the encapsulation efficiencies obtained.

In summary, the application of the standard analytical panel (i) proved a stable surface charge of the LNPs and near-complete nucleic acid encapsulation; (ii) revealed the dependencies between the TFRs during LNP synthesis and size, as well as PDI; and (iii) entirely verified the TFR-independent changes of these LNP attributes during production, processing, and short-term storage.

3.3.2.2 Charged Aerosol Detection for Lipid Quantification and Process Performance

To complement the LNP attributes by lipid characteristics, the developed RP-CAD method was applied. Figure 3.5 illustrates the LNP composition in terms of the lipid molar ratio and the total lipid concentration prior to the process parameter study and during production and processing.

When comparing the theoretical lipid molar ratio with that of the lipid stock solution (Figure 3.5a), the DOTAP content exceeded the theoretical content of 50 mol%, while lower contents of cholesterol, DSPC, and DMG-PEG than 38.5, 10, and 1.5 mol% were observed, respectively. Considering the relative deviations, DMG-PEG showed the highest deviations from the nominal molar content of approximately 50%.

When comparing the lipid molar ratios during production and processing (Figure 3.5b), comparable lipid molar ratios were observed regardless of the processing states synthesized or dialyzed and those across the varied TFR. Here, the lipid molar ratio with the 20 mL min^{-1} TFR closely resembled that of the lipid stock solution. Interestingly, despite their different processing states—whether synthesized or dialyzed—the lipid molar ratios at the selected TFRs were even more similar. However, all these lipid molar ratios differed from the theoretical lipid molar ratio in the same manner.

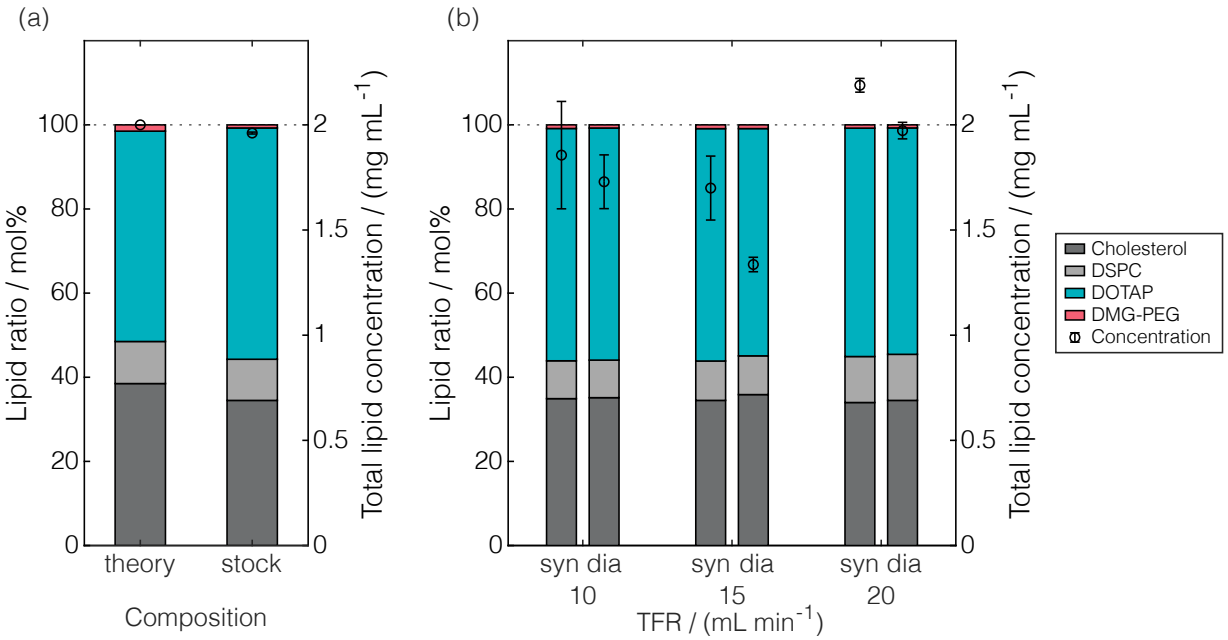

Figure 3.5 Comparison of the theoretical and measured lipid molar ratio and total lipid concentration. The lipid molar ratio and total lipid concentrations are illustrated as stacked bars and circles, respectively, in the theory and of the stock solution (**a**), and of the LNPs synthesized (syn) at 10, 15, and 20 mL min^{-1} TFR, as well as those dialyzed (dia) (**b**). The theoretical total lipid concentration of 2 mg mL^{-1} is marked as a dashed horizontal line.

In summary, the RP-CAD method revealed deviations from the theoretical lipid molar ratio already existing in the stock solution, which indicates a loss in the totality of lipids and not a loss of certain lipid types over processing.

Considering the total lipid concentration, all of the experiments were designed to reach a target concentration of 2 mg mL^{-1} lipids, which is illustrated by a dashed horizontal line in Figure 3.5. Diluting the lipid stock solution to an equal extent, a total lipid concentration of 1.96 mg mL^{-1} was obtained (Figure 3.5a). Note that all lipid concentrations during production and processing (Figure 3.5b) were calculated based on a constant volume due to appropriate sample dilutions with ethanol during RP-CAD sample preparation. When comparing the total lipid concentrations of synthesized LNPs, they were found to considerably differ by scattering around the theoretical lipid concentration. Here, deviations of approximately 10% accompanied by high standard errors were observed. Correlations between the standard error observations and the TFRs were not apparent. Throughout all the TFRs, a reduction in the total lipid concentrations was visible across the processing states—synthesized to dialyzed—indicating a dilution effect during dialysis or lipid loss. Here, the largest concentration deviation of approximately 22% occurred for the 15 mL min^{-1} TFR, which already represented the condition with the lowest total lipid concentration after synthesis. Conclusively, the RP-CAD method revealed deviations from the theoretical lipid concentration, which are attributable to either the production (synthesis) or processing (dialysis) step regardless of the examined TFR.

To evaluate the process performance of purification by dialysis, lipid recoveries were determined based on the lipid quantities prior to and after dialysis. The densities of the respective ethanol-

to-water content were considered for the lipid recovery rates. The lipid recoveries ranged between 88.6 ± 1.2%–100.4 ± 7.6%, with the highest recovery observed for 10 mL min^{-1} TFR. In general, lower lipid recoveries represent lipid loss during dialysis, which implies a loss in LNPs. In summary, the RP-CAD method builds a foundation to determine the process performance of LNP purification, which is exemplarily shown here for purification by dialysis.

3.4 Discussion

The objectives of this work were to develop a RP-CAD method to quantify all lipids in LNPs simultaneously and to apply this method across LNP processing—hence, providing novel, lipid-related LNP attributes and process insights.

3.4.1 RP-CAD for Lipid Quantification

Highly sensitive and precise analytical methods are crucial for process development and manufacturing. In the context of LNP processing, the standard practice rarely involves the quantification of their lipid components. In this study, HPLC in combination with RP for lipid separation and CAD for lipid detection served as the basis for analytical method development. Similar methodologies for lipid quantification were already reported for individual LNP components such as PEGLs [159, 160] or DSPC [156]. Further studies have presented RP-CAD methods to quantify several lipids in liposomes [161] and LNPs [120–124]. In general, developing such methodologies requires extensive laboratory work for improvements in chromatographic separation and precise detection.

In essence, the fundamental concept of lipid separation through RP is their relative hydrophobicity, leading to observed differences in retention times. The level of hydrophobicity is determined by a complex interplay involving lipids' head group polarity, tail unsaturation, and the length of its alkyl chain [154]. The PEGLs DMG-PEG and DMPE-PEG have similar short-chain lengths (saturated C14) but vary in their polar head group, with DMG-PEG being more hydrophobic. Overall, higher retention times were observed for DOBAQ, DOTAP, and DSPC, with all having longer alkyl chain lengths (C18). When comparing CLs (C18 with two double bonds), DOTAP exhibited greater hydrophobicity compared to DOBAQ due to a larger hydrophobic segment and the absence of the benzoic acid group. In contrast, the tails of the amphiphilic phospholipid DSPC are fully saturated and, despite the hydrophilic phosphatidylcholine headgroup, DSPC is even more hydrophobic than both CLs. Cholesterol needs to be considered separately as it is classed as a steroid and is predominantly hydrophobic except for its polar hydroxyl head group. The observation that the retention time of cholesterol is shorter than that of DSPC is consistent with previous observations [123, 161]. However, several studies have reported higher retention times for cholesterol [121–124] than for DMG-PEG, which is contrary to our findings.

This phenomenon is likely attributed to the addition of an ion-pair reagent in the mobile phase. Originally, ion-pair reagents were meant to form ion pairs with ionic compounds to improve separation and are typically used for oligonucleotides [163, 164]. The ion-pair reagent enhances the analyte's accessibility to the mobile phase as well as shields its polar groups, thereby modulating its hydrophobic interactions with the stationary phase. Li et al. [120] systematically investigated the impact of type and concentration of ion-pair reagents on the retention behavior of hydrophilic siRNAs and hydrophobic phospholipids to reduce their retention time gap. Besides retention time shifts for phospholipids, their study found peak broadening for DOTAP under certain ion-pair reagents

attributable to secondary interactions with the stationary phase, which was, however, not observed in our study when using TFA. Our method, utilizing a specific stationary phase and gradient design in combination with an ion-pair quantity of 0.1% TFA (v/v) and a binary gradient of ACN/water, offers an alternative approach to the methods proposed by Bender et al. [123], who employed 0.15/0.1% TFA (v/v) in methanol/water, or those by Weber et al. [161], who utilized 0.2% TFA (v/v) and a ternary gradient ACN/methanol/water. ACN offers advantages over methanol due to its lower viscosity changes in gradients and its higher elution strength [165]. Apart from the ion-pair reagent, organic solvent, and gradient design, several other key chromatographic parameters critical for separation have been thoroughly explored, such as variations in the stationary phase chemistry [120, 156, 160] or the organic mobile phase complexity [121, 159], which are, however, beyond the scope of this study.

As expected, differences in CAD-derived peak areas for identical lipid quantities were observed, which can be attributed to retention time-dependent gradient compositions. These differences, along with the non-linear behavior of the detector's response across broad ranges [117], underscore the need for a lipid-specific calibration of the detector.

Our strategy, termed exploratory calibration, is an experimental approach and comparable to the strategies presented by Soliven et al. [155] and Tam et al. [156], broadening the apparent linear range by systematic PFV variation. While both studies [155, 156] exclusively optimized the PFV for one particular substance, our approach introduces a novel aspect by targeting a single PFV applicable to all lipids, facilitating the use of the RP-CAD method for multi-component systems such as LNPs. Alternative strategies for PFV optimization may be based on empirical models [157] or mathematical transformations [158] with data acquired at PFV = 1. Our exploratory approach involving lipid standards spanning a wide range of lipid masses enables us to identify a single linearity range for all lipids. At the optimal PFV of 1.3, the signal-to-noise ratio remains acceptably low, even though increased PFVs reduce the detector's sensitivity [155–157]. It should be noted that the authors decided to use a uniform lipid mass range for method calibration and validation, although a lipid quantity of up to 1200 ng for DOBAQ, DSPC, and cholesterol would have resulted in adequate linearity ($R^2 > 0.995$). In this context, the lipid mass range was limited by DMPE-PEG, aligning with a reported narrower linearity range for the PEGL than for all other phospholipids [161]. A completely different approach dealing with the non-linear behavior of the detector's response used quadratic fits for non-PEGLs across the entire calibration range instead of PFV optimization [123].

The RP-CAD method calibration and validation at PFV = 1.3 using higher amounts of data points ($p = 9$) and replicates ($n = 3$, $m = 2$) than for the exploratory calibration proved to produce linearity ($R^2 > 0.996$), precision, and accuracy in the range of 10 to 400 ng for all lipids. Comparable nanogram ranges were reported [156, 161], while others have developed methods in the upper nano- to lower microgram range [123, 159, 160]. In contrast, recent studies focusing on RP-CAD method development for LNPs have aligned the lipid mass ranges approximately with the actual lipid content in LNPs to determine the lipid-specific linearity ranges of the detector [121, 122, 124]. In these studies, the maximum lipid mass was two to four times the minimum lipid mass, representing a calibration range of a zero order of magnitude, whereas our calibration range of 40 times covered one order of magnitude.

Our approach with uniform linearity ranges offers the advantage of being applicable to lipid stock solutions prepared in a similar manner. However, evaluating linearity in such large calibration ranges solely based on R^2 might be misleading as percentage deviations in the lower range could

be disregarded. To thoroughly validate the selected linearity range, three lipid masses, equally distributed in the selected range, were used to determine repeatability and intermediate precision—a procedure similar to that of Kim et al. [122]. As all stated deviations lie below 4%, being even lower than that reported for the other RP-CAD methods for LNPs [121, 122, 124], the method was considered precise. The same applies to the accuracy being comparable or even higher when compared to these methods.

In the context of robustness, a lipid mixture (DOTAP, DSPC, cholesterol, and DMG-PEG), possibly present in an LNP formulation, was used to evaluate the effect of minor method parameter variations on the detector's response. In general, experimental procedures to determine the robustness of the RP-CAD methods have been reported to various extents [155, 158, 160, 161]. Alternatively, Kim et al. [122] verified their method robustness by a simulation-defined method operable design region, but they underlined this theoretical robustness by additional experiments in the edge regions. As opposed to robustness studies for only one particular substance [155, 160], our method has to be robust against peak overlapping. Retention time deviations observed for specific variations in separation-determining parameters, i.e., column oven temperature and flow rate, can be traced back to accompanying changes in mobile phase accessibility and hydrophobic interactions. With retention time deviations of $\leq$2% and unaffected baseline separation, the developed RP-CAD method is considered robust. As changes in retention times are accompanied by changed mobile phase compositions, CAD-derived peak area deviations are expected. Even though no considerable alterations in the peak areas were reported in a comparable designed robustness study with lipid mixtures [161], we observed deviations of up to 9%. To apply the here presented RP-CAD method to other HPLC systems, slightly varying method parameters, or other lipids, the generation of new experimental data for lipid-specific detector calibration and validation is strictly necessary.

3.4.2 RP-CAD Complements LNP Attributes and Reveals Process Performance

The key microfluidic process parameters, TFR and FRR [23, 29, 34], along with the buffer type and pH of the aqueous phase [23, 29] and the lipid concentration in the organic phase [29, 34], have been shown to influence the particle size and polydispersity considerably. Thus far, no holistic approach has been applied considering the effect of the process parameter variations on the lipid molar ratio, total lipid concentrations, and process performance. The presented methodology addresses lipid quantification by applying the developed RP-CAD method to the LNPs produced at different TFRs. This quantification approach complements the DLS for particle size and PDI, the ELS for surface charge, as well as a fluorescence assay for nucleic acid encapsulation.

Considering the relationship between particle size and TFR, the lowest Z-average was noted for the highest applied TFRs. The driving force of LNP formation in the presence of nucleic acids is the increase in solvent polarity, leading to a coating of the prior associated hydrophobic inverted micelles by more polar lipids [21]. In consequence, higher TFRs lead to faster polarization and hence might result in smaller particles. Other studies have also observed the inverse relationship regarding TFR and the Z-average [23, 29]. While Roces et al. [23] varied the TFR within a comparable range to ours, i.e., 5 to 20 $\mathrm{mL\,min^{-1}}$, Okuda et al. [29] explored a range lower in magnitude, i.e., 0.1 to 0.5 $\mathrm{mL\,min^{-1}}$, due to the limitations imposed by their system's pressure threshold. Conversely, Terada et al. [34] could not find a significant correlation between the Z-average and TFR for its variation in the range of 1 to 3 $\mathrm{mL\,min^{-1}}$. At a given TFR, various microfluidic systems might have slightly varying channel geometries and hence different flow characteristics compared to our system

with a herringbone design for chaotic flows [166]. Therefore, the authors prioritized general trends over direct comparisons with absolute values. Moreover, other microfluidic mixing designs such as t-junction mixing or microfluidic hydrodynamic focusing are based on other mixing principles for which the TFR has to be aligned specifically, as comprehensively reviewed by Evers et al. [12].

Across LNP processing, DLS-derived data have revealed changes to higher Z-averages, with the strongest increase occurring between synthesized and dialyzed samples concomitantly with a drop in PDI. This interdependency is visualized through intensity-weighted size distributions, which are in agreement with previous studies [23]. In Terada et al. [34], similar changes in size and PDI by dialyzing in various buffers for incrementally evaluating these pH-dependent changes were also observed. During dialysis, both the removal of organic solvents and the pH change proportionally contributed to the size increase of the LNPs [32]. In first suggesting that the size increase was due to particle fusion [27], it was further proven using fluorescence-based lipid tracers [32]. Moreover, this pH-dependent fusion was thought to be restricted by the arrangement of PEGLs on the outer LNP surface, as well as the cholesterol and DSPC content [27, 32]. Roces et al. [23], which further demonstrated that the size and PDI changes during dialysis are highly dependent on the lipid molar ratios and lipids selected. In our study, the short-term storage of 14 days at 2–8 °C was performed after dialysis and revealed slight, TFR-independent Z-average increases, pointing to LNP instabilities. Others conducted similar short-term stability studies in the range of hours [23] to weeks [28, 29].

Although the Onpattro (patisiran) formulation has a shelf-life of three years when stored at temperatures between 2 °C and 8 °C [167], other long-term LNP stability studies for siRNA-loaded LNPs showed stable storage behavior by lyophilization or storage at −70 °C [150, 168, 169]. Contrary to the above-indicated instabilities of our LNPs, low-scattering, constant zeta potentials of approximately 16 mV propose colloidal stability in solution. These strong cationic zeta potentials might be attributed to the protonation of the Tris amine. Roces et al. [23] observed even higher zeta potentials for LNPs in a pH 7.4 Tris buffer, while LNPs in citrate buffer were found to be neutrally charged at pH 7.4.

To draw a more comprehensive picture of the LNP attributes across processing, the herein developed RP-CAD method was applied for lipid quantification. Our method revealed a higher DOTAP content than was theoretically aimed for, which leads to a slightly reduced N/P ratio from 5 to 4.89. However, this N/P ratio is still within the commonly used range of 3–5 for the encapsulation of comparably short nucleic acids, where typical electron-dense core structures [27] combined with high encapsulation efficiencies [28] are achieved. Further, the highest relative deviation from the expected lipid molar ratio was observed with approximately 0.6 mol% PEGL. As already mentioned, the PEGL has proven to be of great importance for the fusion behavior of LNPs [27, 32]. By being located at the LNP surface, a fixed area per PEGL is given, forming the equilibrium size in dependence on the PEGL content [21, 32, 170]. To maintain colloidal stability during storage, it is essential to have an adequate amount of PEGL. Although Fan et al. [28] suggested a minimum of 1 mol% of a PEG_{2000} lipid to assure closely packed adjacent PEG chains to circumvent particle aggregation, stable LNPs have been observed comprising 0.5 mol% of PEGLs [32]. It has to be noted that these studies did not involve lipid quantification, and the findings are solely based on theoretical values. For our study, we have to state that, due to the low PEGL content within the LNPs, the measured peak areas are located in the lower range of our respective RP-CAD calibration curve. To definitively exclude that the PEGL content is underestimated, the approach presented by

Bender et al. [123] could have been applied, calibrating a second calibration curve for the lower calibration range for PEGLs, which might have led to an even more accurate quantification.

However, across the processing, regardless of the applied TFR, all lipid contents remained stable within the LNPs, indicating lipid type- and content-independent Z-average increases. The deviations from the theoretical lipid molar ratio can hence be attributed to the lipid stock solution preparation. To the best of our knowledge, this study provides the first comprehensive assessment of the LNP's lipid composition across processing. Considering also liposomal formulations, Weber et al. [161] investigated the lipid composition of a liposome formulation across film hydration and extrusion, and they uncovered a net lipid loss during their liposome production process. However, their PEGL quantification was affected by the peak overlapping of another phospholipid.

The RP-CAD method allows one to estimate whether robust and consistent synthesis was achieved when comparing the lipid concentrations from all synthesized LNPs. The observed scattering of lipid concentrations around target concentration indicates TFR-independent process variability during microfluidic mixing. These variations might be attributed to the procedure of syringe filling and the syringe pump setup.

In our LNP process, the RP-CAD-derived lipid loss was attributed to the purification by dialysis. Overall, we observed batch-dependent lipid recoveries that were entirely independent of the varying TFR prior to dialysis. Material absorption, possibly due to contact with plastic surfaces or membranes of the dialysis cassettes over an extended period, may constitute lipid loss. Avoiding such surfaces entirely during dialysis might be challenging, and, to the best of the authors' knowledge, no studies have been published exploring purification performance. Moreover, the poor process performance in terms of lipid recovery could also be attributed to the lab-scale dialysis (0.3–0.5 mL) performed, as these cassettes exhibit relatively high surface-to-volume ratios and the dialyzed volumes could not be completely retrieved. Additionally, dialysis is prone to product dilution due to osmotic pressure, which was also observed to various extents in this study. To further improve process performance, larger volumes could be processed. Overall, as the deviations from the lipid molar ratio could be traced back to the lipid stock solution, and as the loss of total lipids is likely to be related to the lipid loss during dialysis, the authors considered the use of the RP-CAD method a feasible lipid quantification method.

In summary, the RP-CAD method contributes to a comprehensive analysis of LNP attributes, assists in assessing the process performance, and leads to an intensified process understanding. Furthermore, the presented method has the potential to evaluate the influence of other process- or LNP-specific parameters and to be applied to alternative processes, such as cross-flow filtration.

3.5 Conclusions

In conclusion, we present a novel holistic RP-CAD method for lipid quantification across LNP production and processing. The strategy of exploratory calibration allows for a broadening of the apparent linear range of the detector's response by systematic optimization of the built-in PFV. With the novel aspect aiming for a single PFV applicable to all six lipids, a PFV of 1.3 was identified. Further, linearity, precision, accuracy, and robustness were proved by method calibration and validation according to the ICH Q2(R2) guideline [162]. As the RP-CAD method enables lipid quantification in pure and mixed lipid solutions, the method reveals the lipid quantities and the

lipid molar ratio in a process parameter study, yielding intensified process insights. The lipid molar ratio complements other common LNP attributes—particle size, surface charge, and nucleic acid encapsulation. Furthermore, lipid recovery serves as a general indicator for process performance. The RP-CAD method uncovers a constant lipid molar ratio across production and processing, and it is entirely independent of the varied TFR during production. Overall, the developed RP-CAD method provides a foundation for integrating lipid quantification as a common analysis in LNP processes, and it bears the potential to be applied to other LNP formulations and processes such as cross-flow filtration.

Author Contributions

Conceptualization, N.B., A.D., and J.H.; methodology, N.B. and A.D.; software, N.B and A.D; validation, N.B. and A.D.; formal analysis, N.B. and A.D.; investigation, N.B. and A.D.; resources, N.B. and A.D.; data curation, N.B. and A.D.; writing—original draft preparation, N.B. and A.D.; writing—review and editing, J.H.; visualization, N.B. and A.D.; supervision, J.H.; project administration, J.H; funding acquisition, J.H. All authors have read and agreed to the published version of the manuscript.

Appendix

Appendix **A3** contains the Supporting Figures associated with this chapter.

Chapter References

[6] L. Schoenmaker et al. „mRNA-lipid nanoparticle COVID-19 vaccines: Structure and stability“. In: *International Journal of Pharmaceutics* 601 (2021), p. 120586. DOI: 10.1016/j.ijpharm.2021.120586.

[12] M. J. W. Evers, J. A. Kulkarni, R. van der Meel, P. R. Cullis, P. Vader, and R. M. Schiffelers. „State-of-the-Art Design and Rapid-Mixing Production Techniques of Lipid Nanoparticles for Nucleic Acid Delivery“. In: *Small Methods* 2.9 (2018), p. 1700375. DOI: 10.1002/smtd.201700375.

[21] A. K. Leung et al. „Lipid nanoparticles containing siRNA synthesized by microfluidic mixing exhibit an electron-dense nanostructured core“. In: *Journal of Physical Chemistry C* 116.34 (2012), pp. 18440–18450. DOI: 10.1021/jp303267y.

[22] C. H. Albertsen, J. A. Kulkarni, D. Witzigmann, M. Lind, K. Petersson, and J. B. Simonsen. „The role of lipid components in lipid nanoparticles for vaccines and gene therapy“. In: *Advanced Drug Delivery Reviews* 188 (2022), p. 114416. DOI: 10.1016/j.addr.2022.114416.

[23] C. B. Roces et al. „Manufacturing considerations for the development of lipid nanoparticles using microfluidics“. In: *Pharmaceutics* 12.11 (2020), pp. 1–19. DOI: 10.3390/pharmaceutics12111095.

[25] K. T. Love et al. „Lipid-like materials for low-dose, in vivo gene silencing“. In: *Proceedings of the National Academy of Sciences of the United States of America* 107.5 (2010), pp. 1864–1869. DOI: 10.1073/pnas.0910603106.

[26] M. Jayaraman et al. „Maximizing the potency of siRNA lipid nanoparticles for hepatic gene silencing in vivo“. In: *Angewandte Chemie - International Edition* 51.34 (2012), pp. 8529–8533. DOI: 10.1002/anie.201203263.

[27] J. A. Kulkarni et al. „On the Formation and Morphology of Lipid Nanoparticles Containing Ionizable Cationic Lipids and siRNA“. In: *ACS Nano* 12.5 (2018), pp. 4787–4795. DOI: 10.1021/acsnano.8b01516.

[28] Y. Fan et al. „Automated high-throughput preparation and characterization of oligonucleotide-loaded lipid nanoparticles“. In: *International Journal of Pharmaceutics* 599 (2021). DOI: 10.1016/j.ijpharm.2021.120392.

[29] K. Okuda et al. „On the size-regulation of RNA-loaded lipid nanoparticles synthesized by microfluidic device“. In: *Journal of Controlled Release* 348 (2022), pp. 648–659. DOI: 10.1016/j.jconrel.2022.06.017.

[30] A. K. Leung, Y. Y. C. Tam, S. Chen, I. M. Hafez, and P. R. Cullis. „Microfluidic Mixing: A General Method for Encapsulating Macromolecules in Lipid Nanoparticle Systems“. In: *Journal of Physical Chemistry B* 119.28 (2015), pp. 8698–8706. DOI: 10.1021/acs.jpcb.5b02891.

[31] J. A. Kulkarni, D. Witzigmann, J. Leung, Y. Y. C. Tam, and P. R. Cullis. „On the role of helper lipids in lipid nanoparticle formulations of siRNA“. In: *Nanoscale* 11.45 (2019), pp. 21733–21739. DOI: 10.1039/c9nr09347h.

[32] J. A. Kulkarni et al. „Fusion-dependent formation of lipid nanoparticles containing macromolecular payloads“. In: *Nanoscale* 11.18 (2019), pp. 9023–9031. DOI: 10.1039/C9NR02004G.

[34] T. Terada et al. „Characterization of Lipid Nanoparticles Containing Ionizable Cationic Lipids Using Design-of-Experiments Approach“. In: *Langmuir* 37.3 (2021), pp. 1120–1128. DOI: 10.1021/acs.langmuir.0c03039.

[117] P. H. Gamache et al. „HPLC analysis of nonvolatile analytes using charged aerosol detection“. In: *LC-GC Europe* 18.6 (2005), pp. 345–354.

[118] P. H. Gamache and S. L. Kaufman. *Principles of Charged Aerosol Detection*. John Wiley & Sons, Ltd, 2017, pp. 1–65. DOI: 10.1002/9781119390725.ch1.

[119] R. A. Moreau. „The analysis of lipids via HPLC with a charged aerosol detector“. In: *Lipids* 41.7 (2006), pp. 727–734. DOI: 10.1007/s11745-006-5024-7.

[120] L. Li, J. P. Foley, and R. Helmy. „Simultaneous separation of small interfering RNA and lipids using ion-pair reversed-phase liquid chromatography“. In: *Journal of Chromatography A* 1601 (2019), pp. 145–154. DOI: 10.1016/j.chroma.2019.04.061.

[121] C. Kinsey et al. „Determination of lipid content and stability in lipid nanoparticles using ultra high-performance liquid chromatography in combination with a Corona Charged Aerosol Detector“. In: *Electrophoresis* 43.9-10 (2022), pp. 1091–1100. DOI: 10.1002/elps.202100244.

[122] K. H. Kim et al. „Optimization of HPLC–CAD method for simultaneous analysis of different lipids in lipid nanoparticles with analytical QbD“. In: *Journal of Chromatography A* 1709 (2023), p. 464375. DOI: 10.1016/j.chroma.2023.464375.

[123] V. Bender, L. Fuchs, and R. Süss. „RP-HPLC-CAD method for the rapid analysis of lipids used in lipid nanoparticles derived from dual centrifugation“. In: *International Journal of Pharmaceutics: X* 7 (2024), p. 100255. DOI: 10.1016/j.ijpx.2024.100255.

[124] X. Yu et al. „Validation of an HPLC-CAD Method for Determination of Lipid Content in LNP-Encapsulated COVID-19 mRNA Vaccines“. In: *Vaccines* 11.5 (2023). DOI: 10.3390/vaccines11050937.

[147] A. Fire, S. Xu, M. K. Montgomery, S. A. Kostas, S. E. Driver, and C. C. Mello. „Potent and specific genetic interference by double-stranded RNA in Caenorhabditis elegans“. In: *Nature* 391.6669 (1998), pp. 806–811. DOI: 10.1038/35888.

[148] B. L. Mui et al. „Influence of Polyethylene Glycol Lipid Desorption Rates on Pharmacokinetics and Pharmacodynamics of siRNA Lipid Nanoparticles“. In: *Molecular Therapy - Nucleic Acids* 2 (2013), e139. DOI: https://doi.org/10.1038/mtna.2013.66.

[149] Y. Dong et al. „Lipopeptide nanoparticles for potent and selective siRNA delivery in rodents and nonhuman primates“. In: *Proceedings of the National Academy of Sciences of the United States of America* 111.11 (2014), pp. 3955–3960. DOI: 10.1073/pnas.1322937111.

[150] R. Ball, P. Bajaj, and K. Whitehead. „Achieving long-term stability of lipid nanoparticles: examining the effect of pH, temperature, and lyophilization“. In: *International Journal of Nanomedicine* Volume 12 (2016), pp. 305–315. DOI: 10.2147/IJN.S123062.

[151] R. L. Ball, K. A. Hajj, J. Vizelman, P. Bajaj, and K. A. Whitehead. „Lipid Nanoparticle Formulations for Enhanced Co-delivery of siRNA and mRNA“. In: *Nano Letters* 18.6 (2018), pp. 3814–3822. DOI: 10.1021/acs.nanolett.8b01101.

[152] R. Mildner et al. „Improved multidetector asymmetrical-flow field-flow fractionation method for particle sizing and concentration measurements of lipid-based nanocarriers for RNA delivery“. In: *European Journal of Pharmaceutics and Biopharmaceutics* 163 (2021), pp. 252–265. DOI: 10.1016/j.ejpb.2021.03.004.

[153] Y. Fan, M. Marioli, and K. Zhang. „Analytical characterization of liposomes and other lipid nanoparticles for drug delivery“. In: *Journal of Pharmaceutical and Biomedical Analysis* 192 (2021), p. 113642. DOI: 10.1016/j.jpba.2020.113642.

[154] T. Cajka and O. Fiehn. „Comprehensive analysis of lipids in biological systems by liquid chromatography-mass spectrometry“. In: *TrAC - Trends in Analytical Chemistry* 61 (2014), pp. 192–206. DOI: 10.1016/j.trac.2014.04.017.

[155] A. Soliven et al. „A simplified guide for charged aerosol detection of non-chromophoric compounds—Analytical method development and validation for the HPLC assay of aerosol particle size distribution for amikacin“. In: *Journal of Pharmaceutical and Biomedical Analysis* 143 (2017), pp. 68–76. DOI: 10.1016/j.jpba.2017.05.013.

[156] J. Tam, I. A. Ahmad, and A. Blasko. „A four parameter optimization and troubleshooting of a RPLC – charged aerosol detection stability indicating method for determination of S-lysophosphatidylcholines in a phospholipid formulation“. In: *Journal of Pharmaceutical and Biomedical Analysis* 155 (2018), pp. 288–297. DOI: 10.1016/j.jpba.2018.03.067.

[157] I. A. H. Ahmad et al. „Revealing the inner workings of the power function algorithm in Charged Aerosol Detection: A simple and effective approach to optimizing power function value for quantitative analysis“. In: *Journal of Chromatography A* 1603 (2019), pp. 1–7. DOI: 10.1016/j.chroma.2019.04.017.

[158] R. Pawellek, T. Muellner, P. Gamache, and U. Holzgrabe. „Power function setting in charged aerosol detection for the linearization of detector response – optimization strategies and their application“. In: *Journal of Chromatography A* 1637 (2021). DOI: 10.1016/j.chroma.2020.461844.

[159] R. Díaz-López, D. Libong, N. Tsapis, E. Fattal, and P. Chaminade. „Quantification of pegylated phospholipids decorating polymeric microcapsules of perfluorooctyl bromide by reverse phase HPLC with a charged aerosol detector“. In: *Journal of Pharmaceutical and Biomedical Analysis* 48.3 (2008), pp. 702–707. DOI: 10.1016/j.jpba.2008.06.027.

[160] M. Kurmi et al. „Development of HPLC-CAD stability indicating assay method for polyethylene glycol-conjugated phospholipid (DMPE-PEG 2000) and identification of its degradation products“. In: *Journal of Pharmaceutical and Biomedical Analysis* 198 (2021). DOI: 10.1016/j.jpba.2021.113967.

[161] F. Weber, L. Rahnfeld, and P. Luciani. „Analytical profiling and stability evaluation of liposomal drug delivery systems: A rapid UHPLC-CAD-based approach for phospholipids in research and quality control“. In: *Talanta* 220 (2020), p. 121320. DOI: 10.1016/j.talanta.2020.121320.

[162] ICH. *Q2(R2) Guideline on validation of analytical procedures*. 2022. URL: https://www.ema.europa.eu/en/documents/scientific-guideline/ich-q2r2-guideline-validation-analytical-procedures-step-5-revision-1%7B%5C_%7Den.pdf (visited on 07/08/2024).

[163] V. Murugaiah, W. Zedalis, G. Lavine, K. Charisse, and M. Manoharan. „Reversed-phase high-performance liquid chromatography method for simultaneous analysis of two liposome-formulated short interfering RNA duplexes“. In: *Analytical Biochemistry* 401.1 (2010), pp. 61–67. DOI: 10.1016/j.ab.2010.02.012.

[164] S. Studzińska, L. Pietrzak, and B. Buszewski. „The Effects of Stationary Phases on Retention and Selectivity of Oligonucleotides in IP-RP-HPLC“. In: *Chromatographia* 77.23-24 (2014), pp. 1589–1596. DOI: 10.1007/s10337-014-2766-x.

[165] L. R. Snyder, M. A. Quarry, and J. L. Glajch. „Solvent-strength selectivity in reversed-phase HPLC“. In: *Chromatographia* 24.1 (1987), pp. 33–44. DOI: 10.1007/BF02688465.

[166] A. D. Stroock, S. K. W. Dertinger, A. Ajdari, I. Mezić, H. A. Stone, and G. M. Whitesides. „Chaotic Mixer for Microchannels“. In: *Science* 295.5555 (2002), pp. 647–651. DOI: 10.1126/science.1066238.

[167] EMA. *Onpattro: Summary of Product Characteristics*. 2018. URL: https://www.ema.europa.eu/en/documents/product-information/onpattro-epar-product-information%7B%5C_%7Den.pdf (visited on 07/08/2024).

[168] Y. Suzuki, K. Hyodo, Y. Tanaka, and H. Ishihara. „SiRNA-lipid nanoparticles with long-term storage stability facilitate potent gene-silencing in vivo“. In: *Journal of Controlled Release* 220 (2015), pp. 44–50. DOI: 10.1016/j.jconrel.2015.10.024.

[169] Z. J. Jakubek, S. Chen, J. Zaifman, Y. Y. C. Tam, and S. Zou. „Lipid Nanoparticle and Liposome Reference Materials: Assessment of Size Homogeneity and Long-Term -70 °C and 4 °C Storage Stability“. In: *Langmuir* 39.7 (2022). DOI: 10.1021/acs.langmuir.2c02657.

[170] N. M. Belliveau et al. „Microfluidic synthesis of highly potent limit-size lipid nanoparticles for in vivo delivery of siRNA“. In: *Molecular Therapy - Nucleic Acids* 1.8 (2012), e37. DOI: 10.1038/mtna.2012.28.

4

Time-Dependent Particle Size Increase during Lipid Nanoparticle Purification by Cross-Flow Filtration

Annabelle Dietrich[1,*], Nicole Beckert[1,*] and Jürgen Hubbuch[1]

[1] Institute of Process Engineering in Life Sciences, Section IV: Biomolecular Separation Engineering, Karlsruhe Institute of Technology (KIT), Karlsruhe, Germany

[*] Contributed equally.

Graphical Abstract

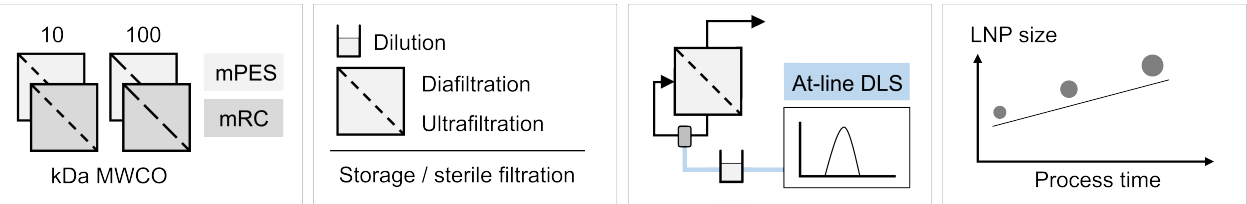

Abstract

Although cross-flow filtration (CFF) is a time- and resource-efficient purification method, CFF has rarely been explored for lipid nanoparticle (LNP) purification as a scalable alternative to dialysis. CFF-based processing allows for buffer exchange by diafiltration (DF) and setting a target product concentration by ultrafiltration (UF). Herein, we investigate the effect of CFF-based processing on LNP characteristics and process performance by performing a parameter study through the variation of selected membrane-related and operational parameters. We used a pre-dilution approach prior to LNP purification to reduce the ethanol content while maintaining LNP characteristics. Taking advantage of the integration potential of CFF for process analytical technology (PAT), we successfully established size monitoring for LNPs by integrating at-line dynamic light scattering (DLS), providing near real-time process insights. During processing, we observed an increase in LNP size and a change in their size distribution, dependent on processing time but not on the varied process parameters. Following comprehensive off-line analyses, all other LNP characteristics remained constant and final lipid recoveries were achieved in the range of 86–89% for all CFF processes. Long-term, the CFF-purified LNPs showed a lower increase in size compared to the dialyzed LNPs during storage of 14 days. Lastly, examination of purified LNP behavior during sterile filtration revealed changes in particle size in the upper size range. In general, we provide comprehensive insights into CFF-based LNP processing and its impact on LNP characteristics and process performance. Such studies are expected to contribute to the understanding of CFF-based LNP processing and their future application for size-controlled LNP production.

4.1 Introduction

LNPs as clinically advanced non-viral, lipid-based vector systems have demonstrated significant potential in nucleic acid delivery over the past decade [10, 171]. In addition to cationic lipids, which play a key role in nucleic acid encapsulation and release by forming complexes with anionic nucleic acids, LNPs are composed of three other essential components: cholesterol, a phospholipid, and a polyethylene glycol (PEG) lipid, each contributing to the overall functionality of the particle, as reviewed in detail by Albertsen et al. [22]. Next to a desired lipid molar ratio of the aforementioned LNP components, the N/P ratio—representing the balance between cationic lipid amines and nucleic acid phosphate groups—is essential in ensuring efficient nucleic acid encapsulation while maintaining functional stability [28, 29]. Overall, achieving a precise LNP composition relies on a controlled LNP synthesis process, while maintaining particle characteristics across further processing requires LNP processing stability.

Using microfluidic mixing devices allows for reproducible and scalable LNP synthesis by mixing the nucleic acid-containing aqueous phase with the lipid-containing organic phase [12]. Here, the mixing parameters total flow rate (TFR) and flow rate ratio (FRR) have been found to have a significant impact on particle size [23, 29, 34, 35]. Nevertheless, the subsequent purification step should not be neglected, as further changes in the physicochemical characteristics of the LNPs have been observed.

Despite its well-known scalability limitations, dialysis is commonly employed to remove the residual organic solvent and adjust the pH to neutrality. Kulkarni et al. [31] and Terada et al. [34] have demonstrated that both solvent removal and pH adjustment contribute concurrently to the particle size increase of LNPs during dialysis. Pre-treatment approaches prior to dialysis have also been investigated to enhance particle stability. One pre-treatment method involves direct dilution with a buffer solution to reduce the ethanol content. This pre-dilution approach was originally introduced by Jeffs et al. [172], who employed it directly after the mixing step to improve the in-process stability of cationic lipid-containing vesicles. Pre-dilution with low-pH buffer has been later applied to LNPs [173] and further advanced through the development of an integrated microfluidic device designed to rapidly dilute the LNPs under controlled conditions [174]. However, merely diluting the ethanol is insufficient, as a subsequent buffer exchange to physiological pH remains necessary.

Compared to dialysis, CFF represents a time- and resource-efficient alternative, offering superior scalability and integration potential. CFF operated in constant-volume DF mode allows for gradual buffer exchange with a DF buffer while maintaining the product volume or in UF mode to concentrate the product to the desired concentration [36]. While only one study has applied CFF for LNP purification [37], other studies have dealt with CFF applications for other related particle types within the broader category of lipid-based particles. The work of Hirsjärvi et al. [175] is among the few that have explicitly compared CFF with dialysis for hybrid lipid-polymer particles.

Unlike diffusion-driven dialysis, pressure-driven CFF requires consideration of operational CFF parameters beyond the membrane-related parameters. However, comprehensive studies on the impact of those parameters on particle characteristics have rarely been reported. Some studies have exclusively explored two types of membrane material [176], molecular weight cut-off (MWCO) [175], or membrane area [177], but no studies have yet investigated those in combination or different membrane formats like hollow fiber or flat sheet. Sakurai et al. [176] has suggested that the hydrophobicity of the membrane is one key factor leading to particle adsorption to the membrane. Typical operational parameters for CFF include feed and filtrate flow rates and the transmembrane pressure (TMP), which is determined by the operating pressures. To date, the reported studies on the variation of those operational parameters cover DF modes other than constant-volume DF, such as single-pass DF [177] and discontinuous DF [178].

Others focused on innovative CFF set-ups, such as in-line DF for continuous processing high in efficiency [179] or a two-step CFF process for improved particle characteristics [37]. Interestingly, Worsham et al. [179] found a permeability limitation of the membrane caused by the initial exposure to ethanol, suggesting a pre-dilution strategy to significantly reduce the amount of DF stages. Efforts to improve scalability have driven the development of a miniaturized, on-chip CFF purification system that enables synthesis and purification on a micro-volume scale [178]. Alongside scalability, another area of innovation lies in integrating real-time measurement of particle characteristics, building on the PAT framework introduced by the FDA [14]. While measuring particle characteristics between process steps is common practice, at-line measurements [180] remain relatively rare. Significant progress has been made in using sensors for real-time process monitoring, allowing for time-resolved

insights within a single process step [15]. However, particle size measurements of LNPs during the constant-volume DF process have so far only been conducted off-line [37], with at-line monitoring still not achieved.

Thus far, comprehensive insights into CFF-based LNP processing have not been reported, nor have CFF parameter variations and their impact on LNP characteristics been considered.

In this study, we investigate the impact of membrane-related and operational CFF parameters on process performance and LNP characteristics during LNP purification by CFF. To estimate the effect of dilution with low-pH buffer as a pretreatment procedure on LNP characteristics, we initially performed dialysis experiments with pre- and undiluted LNPs. The pre-diluted LNPs also served as the starting material for the CFF experiments, making the dialysis experiments a direct reference for the corresponding CFF processes. To address time- and resource-efficient buffer exchange and product concentration, we applied CFF with constant-volume DF mode over six diafiltration volumes (DVs) followed by concentration of LNPs using the UF mode. Across the CFF experiments, we varied either the membrane characteristics material, format, and area, or the membrane MWCO and the system pressure setting, as schematically illustrated in Figure 4.1. Further, we established at-line DLS measurements to gain time-resolved insights into changes in particle size and size distribution in near real-time, also emphasizing the potential to integrate PAT tools into CFF set-ups for process monitoring. Subsequently, LNP samples taken between process steps and at various points throughout the CFF process were subjected to thorough stability assessment over a 14-day storage period and evaluated regarding particle size, surface charge, encapsulation efficiency, as well as lipid concentration, molar ratio, and recovery. Lastly, the effect of sterile filtration on particle size, size distribution, and lipid recovery was investigated.

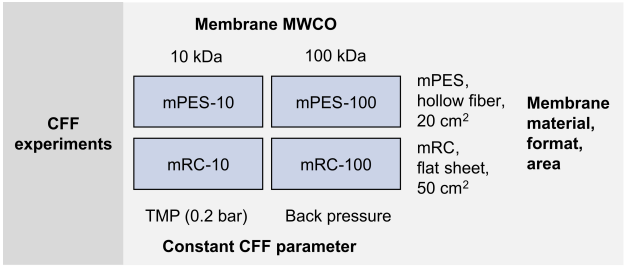

Figure 4.1 Illustration of membrane characteristics and operational filtration parameters for the four CFF experiments performed. Abbreviations: CFF: cross-flow filtration, mPES: modified polyethersulfone, mRC: modified regenerated cellulose, MWCO: molecular weight cut-off, TMP: transmembrane pressure.

4.2 Materials and Methods

4.2.1 Materials, Buffers, and Solvents

Unless otherwise specified, chemicals were obtained from Merck (Darmstadt, Germany). The lipids 1,2-Dioleoyl-3-trimethylammonium-propane (chloride salt) (DOTAP) and 1,2-Dioctadecanoyl-sn-glycero-3-phosphocholin (DSPC), kindly provided by Lipoid (Ludwigshafen, Germany), were used alongside 1,2-Dimyristoyl-rac-glycero-3-methoxypolyethylene glycol-2000 (DMG-PEG) purchased from Avanti Polar Lipids (Alabaster, AL, USA) and cholesterol. Ultrapure water (Purelab ultra,

ELGA LabWater, High Wycombe, UK), sodium acetate trihydrate, acetic acid, and Tris(hydroxymethyl)aminomethane (Tris) were used for the preparation of acetate (25mM, pH 4.0) and Tris (10mM, pH 7.4) buffers. A SenTix62 pH electrode (WTW, Weilheim, Germany) combined with a HI 3220 pH meter (Hanna Instruments, Woonsocket, RI, USA) was employed for pH adjustments of the buffers using hydrochloric acid solution (32%), followed by sterile filtration through 0.2 µm cellulose acetate filters (VWR International, Radnor, PA, USA). For high performance liquid chromatography (HPLC), water and acetonitrile (ACN) containing 0.1% trifluoroacetic acid (TFA) (v/v) were obtained in LC-MS grade from Thermo Fisher Scientific Inc. (Waltham, MA, USA), LC-MS grade ACN was purchased from VWR Chemicals (VWR International) and HPLC grade ethanol was used. Primers (forward: 5'-ATGGTGAGCAAGGGCGAGTT-3', reverse: 5'-CTCGCCCTTGCTCACCATTT-3'), Quant-iT^{TM} RiboGreen^{TM} Assay Kit, NoLimits^{TM} 20 bp DNA fragments, Triton^{TM} X-100, and 384-well Nunclon^{TM} Delta Surface microplates were purchased from Thermo Fisher Scientific Inc.

4.2.2 Lipid Nanoparticle Synthesis and Purification

The sequential process steps for lipid nanoparticle synthesis and purification are illustrated in Figure 4.2.

The aqueous nucleic acid stock solution with a concentration of 119 µg mL^{-1} in acetate buffer was prepared according to Beckert et al. [181]. For the lipid stock solution with a total lipid concentration of 12 mg mL^{-1}, DOTAP, DSPC, DMG-PEG, and cholesterol (50:10:38.5:1.5 mol%) were dissolved in ethanol using a Branson Ultrasonics sonifier SFX550 (Thermo Fisher Scientific Inc.). Glass syringes in 10mL (SETsonic GmbH, Ilmenau, Germany) and 1mL (Innovative Labor Systeme GmbH, Stützerbach, Germany) scales were filled with nucleic acid and lipid stock solutions, respectively, and clamped into a Nemesys pump (Cetoni GmbH, Korbußen, Germany). LNPs with an N/P ratio of 5 were synthesized in a connected herringbone-structured microfluidic chip (Microfluidic ChipShop, Jena, Germany) at a FRR of 5:1 (aqueous:organic) and a TFR of 20 mL min^{-1}. Synthesized LNPs by microfluidics (M) were either used directly or further pre-diluted 1:4 (M-D) with pH 4 acetate buffer to reduce the ethanol content. Subsequent purification was performed by dialysis or CFF using pH 7.4 Tris buffer.

For reference, both synthesized and pre-diluted LNPs were further dialyzed (M-Dia and M-D-Dia) using 10 kDa Slide-A-Lyzer® dialysis cassettes (1–3mL, regenerated cellulose, Thermo Fisher Scientific Inc.). The dialysis process involved at least 500 volumes of buffer relative to the sample and was carried out at 2–8°C for 4h and overnight.

For purification by CFF, a KrosFlo Research KRIIi CFF system equipped with an automatic back pressure valve (Spectrum Labs, Rancho Dominguez, CA, USA), a stirred 50 mL reservoir (Sartorius Stedim Biotech GmbH, Göttingen, Germany), and an Ohaus® Scout® Pro balance (Ohaus, Parsippany, NJ, USA) was used. The filter modules used differ in MWCO (10 kDa and 100 kDa) as well as in the membrane's characteristics material, format, and area: modified polyethersulfone (mPES) hollow fiber filter modules with 20 cm^2 (Spectrum® MicroKros, Repligen, Waltham, MA, USA) and modified regenerated cellulose (mRC) flat sheet filter modules with 50 cm^2 (Hydrosart®, Sartocon® Slice 50, Sartorius). It has to be noted that the shear rates induced by the membrane vary between the two membrane formats but are independent of the MWCO. With each filter module, one DF/UF process was performed at room temperature with a constant feed flow rate of 15 mL min^{-1}, which represents a consistent shear rate induced by the pump.

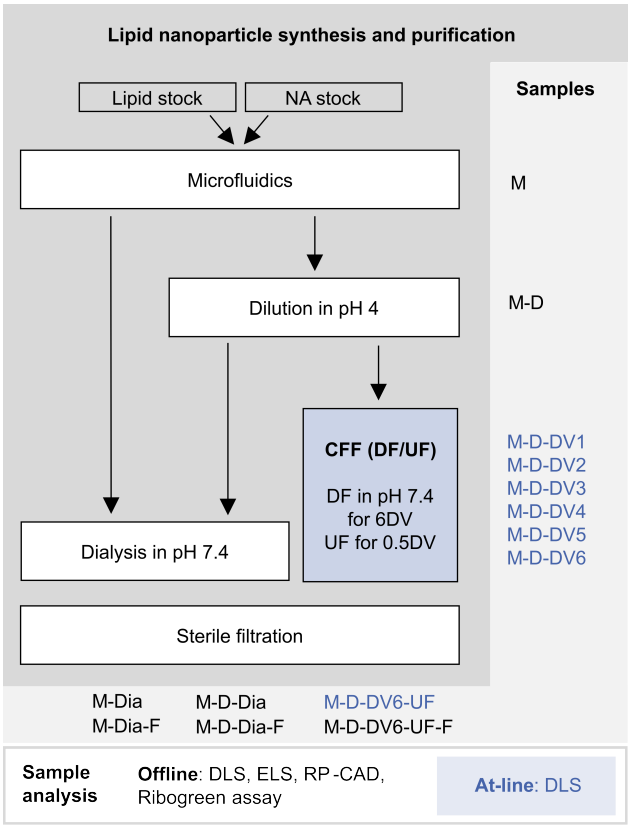

Figure 4.2 Workflow illustration of sequential process steps for LNP synthesis and purification, sampling, and sample analysis. At-line DLS was performed for CFF intermediates and final CFF-purified LNPs. Abbreviations: CAD: charged aerosol detection, CFF: cross-flow filtration, D: dilution, DF: diafiltration, Dia: dialysis, DLS: dynamic light scattering, DV: DF volume, ELS: electrophoretic light scattering, F: sterile filtration, M: microfluidics, NA: nucleic acid, RP: reversed-phase, UF: ultrafiltration.

For simplicity, the CFF experiments are named based on the combination of membrane material and MWCO in kDa: mPES-10, mPES-100, mRC-10, mRC-100. Aiming for a processing time within fifty to seventy minutes, the CFF set-ups were adjusted by setting required pressures to account for MWCO-related differences in membrane permeability. The TMP was set to 0.2 bar for both processes with the 10 kDa membranes (mPES-10, mRC-10) to increase the permeate flux, whereas for the ones with the 100 kDa membranes (mPES-100, mRC-100) a permeate capillary smaller in diameter adjusted the back pressure to restrict the permeate flux. Constant-volume DF (12 mL DV) was conducted with pre-diluted LNPs exchanging six DV. The retentate was sampled through an injection plug (Fresenius Kabi, Bad Homburg, Germany) every DV (M-D-DV[1-6]). By decoupling the DF buffer, LNPs were subsequently concentrated twofold by UF (M-D-DV6-UF).

All CFF-derived samples were immediately analyzed by at-line DLS. All samples were stored at 2–8 °C and analyzed off-line by DLS, electrophoretic light scattering (ELS), reversed-phase (RP)-charged aerosol detection (CAD), and a fluorescence-based assay after 1, 7, and 14 days. After 7 days, 400 µL of the final samples derived from dialysis and CFF processes were manually

sterile-filtered through 0.22 µm, 0.1 cm^2 Millex® polyvinylidene fluoride syringe filters (M-Dia-F, M-D-Dia-F, M-D-DV6-UF-F), which corresponds to 40 L m^{-2}, and analyzed.

Supplementary dialysis experiments with pre-diluted and undiluted LNP solution were executed as described in Section A4.

4.2.3 Analytics

4.2.3.1 Light Scattering

Light scattering techniques were employed to monitor particle size and surface charge. DLS was used to measure at-line and off-line particle sizes. Measurements were performed using a Zetasizer Nano ZSP with the Zetasizer software version 7.12 (Malvern Instruments Ltd., Malvern, UK). Measurements were performed in a low-volume quartz cuvette (ZEN2112, Malvern Panalytical Ltd., Malvern, UK) and with a laser beam focused at a wavelength of 633 nm with an attenuation of 5. Scattering was detected at an angle of 173°. The refractive index (RI) of the LNPs was set to 1.333 with an absorption value of 0.01, while the dispersant had a RI of 1.341 and a viscosity of 1.919 cP. Samples derived from processes without the dilution step (M, M-Dia, M-Dia-F) were diluted to a lipid concentration of 0.5 mg mL^{-1}, while all other samples were measured directly. Duplicate measurements were performed using automatic measurement durations, with two sub-measurements for at-line samples and three sub-measurements for off-line samples.

Using the same device and software, ELS was performed to assess the surface charge of the LNPs. Measurements were carried out using a folded capillary cell (DTS1070, Malvern Panalytical Ltd.). A dielectric constant (ε_r) of 78.5 was applied, and the Helmholtz–Smoluchowski equation was used for calculations. Samples were measured directly except for those from processes without the dilution step (M, M-Dia, M-Dia-F), which were set to a total lipid concentration of 1 mg mL^{-1}. Each sample was measured in duplicate at 60 V, with two sub-measurements interrupted by a 120 s delay.

4.2.3.2 Reversed Phase - Charged Aerosol Detection

Lipid concentration and molar ratio were analyzed using the previously developed and calibrated RP-CAD method by Beckert et al. [181]. In brief, a 2.1 × 150 mm ACQUITY® BEH Phenyl column (1.7 µm particle size, 130 Å pore size, Waters, Milford, CT, USA) was employed alongside a VanGuard™ pre-column (2.1 × 5 mm). The column was connected to a 3000 RS HPLC system (Dionex Corporation, Sunnyvale, CA, USA) equipped with a 3000 RS diode array detector and a Corona Veo CAD RS, all operated via Chromeleon 6.8 software (Thermo Fisher Scientific Inc.). The column and autosampler temperatures were set to 50 °C and 8 °C, respectively. CAD settings comprised a 35 °C evaporation temperature, a 3.6 s filter constant, and a power function value of 1.3. Under a flow rate of 0.3 mL min^{-1}, with 0.1% TFA (v/v) in water as mobile phase A and 0.1% TFA (v/v) in ACN as mobile phase B, the method started at 40% B for 4 min, followed by two linear gradients to 70% B (1 min) and 100% B (11.25 min). After 2 min at 100% B, a one-minute gradient was applied to return to initial conditions. Samples were diluted with ethanol to achieve final concentrations corresponding to those within the calibration curves and measured in duplicate using an 8 µL injection volume. The total lipid concentrations prior to and after the process steps dialysis and CFF and the volume were used for lipid recovery calculations.

4.2.3.3 Fluorescence-Based Assay

Nucleic acid encapsulation was determined using the fluorescence-based assay kit Quant-iT^{TM} RiboGreen^{TM}. Samples were analyzed according to the manufacturer's protocol, with the following modifications: NoLimits^{TM} 20 bp DNA fragments were used for reference measurement with and without 1% Triton^{TM} X-100. Samples were diluted and treated with dye in both conditions. Samples were prepared in duplicate, 384-well black polystyrene microplates were used, and fluorescence was measured ($\lambda_{ex} = 480\,nm$, $\lambda_{em} = 520\,nm$) with a Spark® microplate reader (Tecan Group Ltd., Männedorf, CH). The encapsulation efficiency (EE), defined as the proportion of nucleic acids encapsulated within LNPs, was determined using equation (4.1):

$$EE = \frac{f_{total} - f_{free}}{f_{total}} * 100\,\%. \tag{4.1}$$

Here, f_{total} denotes the blank-corrected fluorescence of nucleic acids in the sample after treatment with Triton^{TM} X-100 and f_{free} represents the blank-corrected fluorescence of the unencapsulated nucleic acids located outside the LNPs.

4.2.3.4 Statistical Evaluation

MATLAB® R2021a (The MathWorks Inc., Natick, MA, USA) was used for data analysis and visualization. Replicate measurements are reported as the mean ± standard deviation.

4.3 Results

4.3.1 Reduction of Ethanol Content by Dilution

To evaluate a potential stabilizing effect of dilution with pH 4 buffer as a pre-treatment procedure prior to dialysis into pH 7.4 buffer, LNPs were synthesized, dialyzed either undiluted or pre-diluted (cf. Figure 4.2), and stored at 2–8 °C. Figure 4.3 illustrates changes in the Z-average and zeta potential values of LNPs across those different process stages.

Post-synthesis by microfluidics, particle sizes of undiluted (M) and pre-diluted (M-D) LNPs were within the same range. While dialysis led to an overall size increase, no substantial differences were observed between directly dialyzed (M-Dia) and pre-diluted (M-D-Dia) LNPs. Similarly, consistent size increases over time were observed for synthesized or dialyzed LNPs, regardless of whether they were un- or pre-diluted. Zeta potential measurements exhibit significant variability for synthesized LNPs, while a consistent surface charge of 20 to 25 mV was observed for dialyzed LNPs.

The effect of the surrounding solution composition on zeta potential measurements was assessed by an additional dialysis experiment into pH 4 buffer (cf. Supplementary Figure A4.1). Stable zeta potential measurements were observed for LNPs present in pH 4 buffer after the removal of ethanol (cf. Supplementary Figure A4.2).

The effect of the dialysis buffer pH on the size increase during dialysis was further evaluated by step-wise dialysis in an additional dialysis experiment (cf. Supplementary Figure A4.1). The two-step dialysis allows for the initial removal of ethanol, followed by a subsequent adjustment to physiological pH. Regardless of the pre-dilution, dialysis into pH 4 buffer led to a size increase, further enhanced upon subsequent dialysis into pH 7.4 buffer, eventually reaching a comparable

size as observed with direct dialysis into pH 7.4 buffer (cf. Supplementary Figure A4.2). Further, a similar increase in particle size was observed over the storage period for direct or two-step dialyzed LNPs.

In summary, dilution with pH 4 buffer after LNP synthesis reduces the ethanol content of the surrounding solution, but neither stabilizing nor destabilizing effects on the particle size were observed.

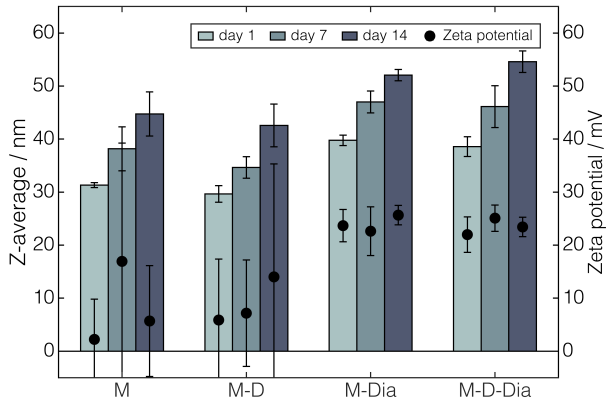

Figure 4.3 Effects of dilution as a pre-treatment step prior to dialysis on LNP Z-average and zeta potential. The procedure of LNP synthesis, pre-dilution, dialysis, and storage at 2–8°C for up to 14 days was carried out four times (n=4) and samples were measured in duplicates (m=2). Abbreviations: D: dilution, Dia: dialysis, LNP: lipid nanoparticle, M: microfluidics.

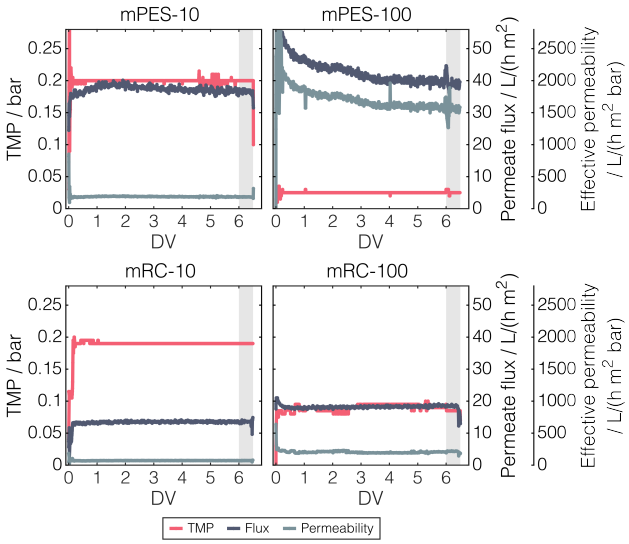

Figure 4.4 Profiles of TMP, permeate flux, and effective permeability during CFF-based processing. CFF experiments were performed with mPES-10 (a), mPES-100 (b), mRC-10 (c), and mRC-100 (d) membranes in DF/UF mode with UF highlighted with shaded bars. Abbreviations: CFF: cross-flow filtration, DF: diafiltration, DV: diafiltration volume, mPES: modified polyethersulfone, mRC: modified regenerated cellulose, TMP: transmembrane pressure, UF: ultrafiltration.

4.3.2 Cross-Flow Filtration—Flow and Pressure Characteristics

Membrane-related and operational CFF parameters were varied in a process parameter study to investigate their impact on LNP characteristics during LNP purification by CFF. The four CFF experiments systematically differed in membrane MWCO and pressure setting as well as membrane material, format, and area (cf. Figure 4.1). Figure 4.4 illustrates changes in the monitored TMP, permeate flux, and effective permeability throughout CFF-based DF for buffer exchange and UF for product concentration.

Comparing the runs using 10 kDa MWCO membranes under constant TMP, a higher permeate flux was observed for the mPES than mRC membrane (cf. Figure 4.4 (a), (c)), which might be attributed to the membrane material and format. A similar observation occurred during the runs with 100 kDa MWCO membranes under constant permeate back pressure (cf. Figure 4.4 (b), (d)). Comparing those runs under constant permeate back pressure, a three-times lower TMP was observed for the mPES than mRC membrane, which may be linked to the membrane format and area. Interestingly, changes in the permeate fluxes were observed for 100 kDa MWCO membranes under constant permeate back pressure, with a pronounced decrease for mPES-100 throughout the entire process compared to a rather moderate drop for mRC-100 during the first 0.5 DV (cf. Figure 4.4 (b), (d)). However, the TMP remained constant in both cases.

Through the effective permeability, which relates the permeate flux to the TMP, it can be derived that the membrane material and format—mPES hollow fiber filter modules are generally more permeable than mRC flat sheet filter modules—as well as the MWCO—larger MWCO are more permeable—affect the CFF process. Lower TMPs and higher permeate fluxes were observed for the 100 kDa than the 10 kDa MWCO membranes, which is further attributed to the MWCO-related pressure control applied in the respective CFF set-ups.

Overall, no difference in terms of pressure or permeate flux was observed in either of the processes regarding the two CFF-based processing modes—DF for buffer exchange and UF for concentration. In summary, the observed profiles of the TMP, permeate flux, and effective permeability throughout processing can be linked to the membrane-related and operational CFF parameters.

4.3.3 Cross-Flow Filtration—Lipid Nanoparticle Characteristics

Throughout LNP purification by CFF, the Z-average was directly measured at-line for every DV and supplemented with off-line data from day 1, as shown in Figure 4.5.

The increase in LNP particle size represents the key finding throughout processing by CFF. Final Z-average values ranging between 90 to 116 nm were observed by at-line DLS after DF for six DV and UF, representing a substantially higher increase in particle size compared to those purified by dialysis (cf. Figure 4.5 (a)–(d)). With an increase of approximately 10 nm, the final Z-average values of dialyzed LNPs were less than 50% of those measured for the DF/UF-purified LNPs.

The comparison of at-line and off-line DLS measurements reveals a consistent pattern in particle size. For CFF-purified LNPs from the third or fourth DV onward, Z-average values from at-line DLS analyses consistently exceed those obtained from off-line analyses on day 1 (cf. Figure 4.5 (a)–(d)). It has to be noted that the at-line DLS measurements confirm the Z-average increase observed in the off-line data, which highlights DLS as a suitable at-line monitoring tool.

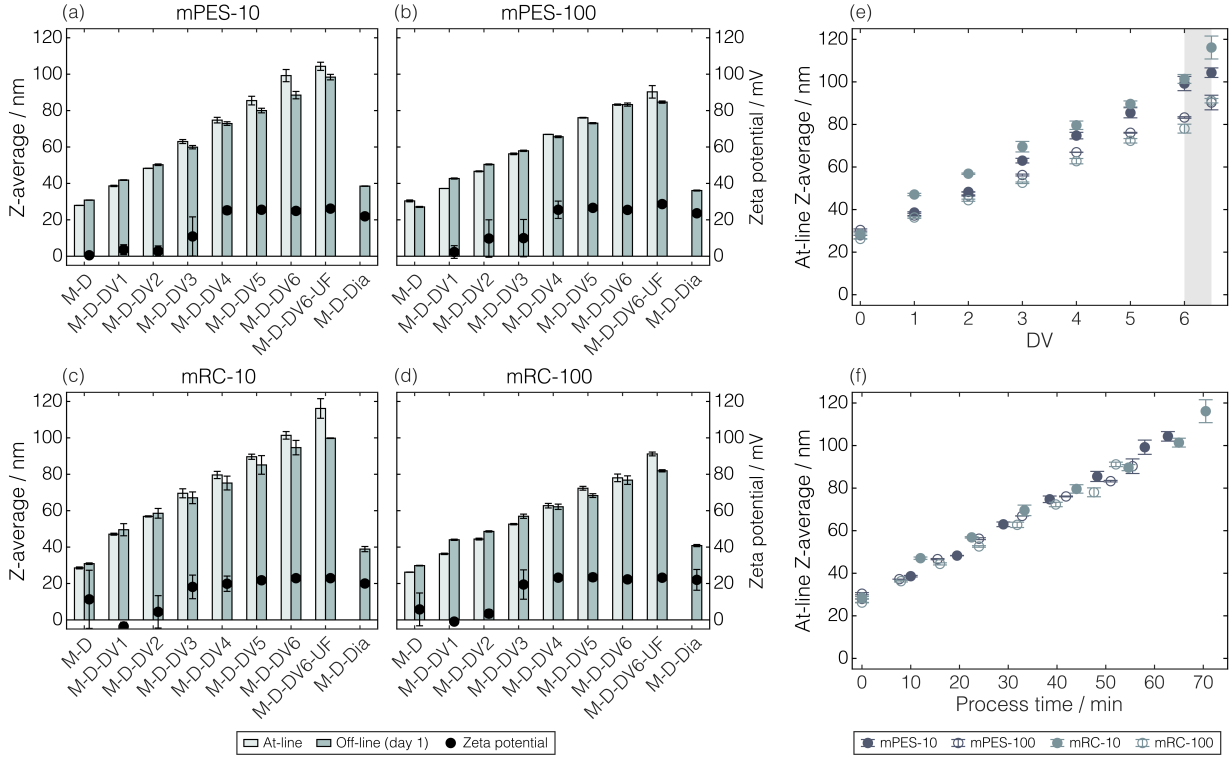

Figure 4.5 Changes in Z-average of LNPs across processing. Z-average values for at-line and off-line measurements are illustrated for mPES-10 (a), mPES-100 (b), mRC-10 (c), and mRC-100 (d) membranes with the corresponding zeta potential values. For each membrane, the at-line derived Z-average is shown over DV with UF highlighted by a shaded bar (e) and over processing time (f). Abbreviations: D: dilution, Dia: dialysis, DV: diafiltration volume, M: microfluidics, mPES: modified polyethersulfone, mRC: modified regenerated cellulose, LNP: lipid nanoparticle, UF: ultrafiltration.

The increase in Z-average occurred proportionally with the number of DVs, with noticeable differences between each of the four CFF runs, as shown in Figure 4.5 (e). Starting from the measurement at the first DV, the CFF run with the mRC-10 membrane consistently produced the largest LNPs, with progressively smaller LNPs observed in the order of mPES-10, mPES-100, and mRC-100. Overall, the increase in particle size seems independent of the varied membrane-related and operational CFF parameters as well as the DV.

However, the illustration of the Z-average over the processing time exhibits a clear trend (cf. Figure 4.5 (f)) of the time-dependent increase in particle size. Differences in membrane characteristics or applied operational CFF parameters appear to influence LNP size primarily through their effect on processing time. Consequently, the lower the permeate flow rate, the longer the processing time, resulting in larger final particle sizes.

Generally, the Z-average is derived from the intensity-weighted size distribution. The progression of the change in the intensity-weighted size distribution throughout the CFF is exemplarily shown for mPES-10 in Figure 4.6, with the Z-average values for the starting material (M-D) and the final CFF-purified LNPs (M-D-DV6-UF) indicated by vertical lines.

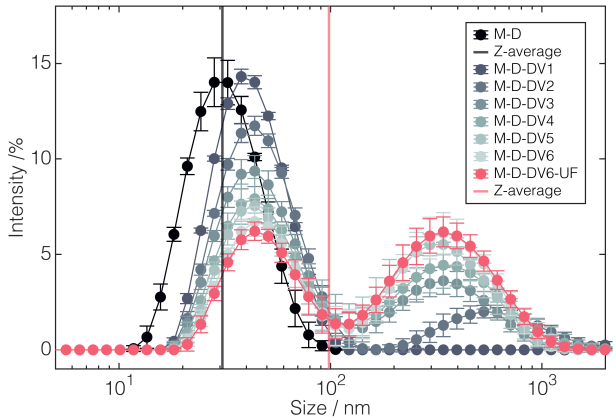

Figure 4.6 Changes in the intensity-weighted size distribution for mPES-10. Next to the shown intensity-weighted size distributions for the CFF intermediates of the mPES-10 CFF run, the Z-average values for the synthesized, diluted LNPs (M-D), which served as the starting material for the CFF, and the final CFF-purified LNPs (M-D-DV6-UF) are marked by vertical lines. Abbreviations: CFF: cross-flow filtration, D: dilution, Dia: dialysis, DV: diafiltration volume, LNP: lipid nanoparticle, mPES: modified polyethersulfone, UF: ultrafiltration.

Initially starting from a mono-disperse distribution, a second population is observed that increases in intensity throughout the CFF. Similar trends were observed for the other CFF runs (cf. Supplementary Figure A4.3), with a more or less pronounced second population or overlap between the two populations. It has to be noted that the formation of a second population could not be observed for purification by dialysis (data not shown). Instead, only a shift of the mono-disperse distribution along the X-axis compared to the starting material was observed, which explains the increase in the Z-average.

Along with the Z-average and size distribution, a trend throughout CFF-based processing can also be observed for the zeta potential (cf. Figure 4.5 (a)–(d)). For synthesized, diluted LNPs containing 4.17% ethanol (M-D), which served as the starting material for the CFF, the zeta potential values are around zero but exhibit large standard deviations. As the CFF processing progresses, the zeta potential increases, eventually reaching a plateau after four DVs (M-D-DV4). Prior to reaching this plateau, larger standard deviations of the zeta potential measurements were observed, which can be attributed to the presence of ethanol (cf. Section 4.3.1). Overall, the surface charge profile of LNPs indicates the progression of buffer exchange throughout CFF-based processing.

Throughout LNP purification by CFF, lipid concentration, molar ratio, and recovery were determined every DV by RP-CAD to complement LNP characteristics and evaluate the process performance. Figure 4.7 illustrates changes in total lipid concentration and recovery for all four CFF processes across processing. Similar trends were observed for all four processes. The total lipid concentration decreased with each DV, which can be attributed to the sampling procedure. Here, one-twelfth of the process volume is sampled every DV and automatically replaced by the DF buffer due to constant-volume DF mode. By UF-based product concentration, the initial concentration (M-D) was again reached or exceeded. No changes in the lipid molar ratio could be observed (cf. Supplementary Figure A4.4). Further, final recoveries ranging from 86% to 89% were achieved, reflecting the overall performance of CFF processes in such small scales. Although dialysis experiments yielded higher recoveries ranging from 89% to 99%, notable dilution effects were observed with dilution

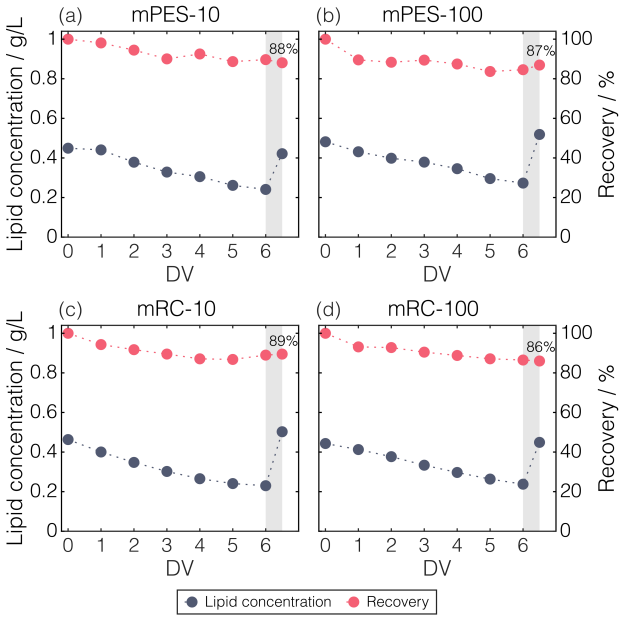

Figure 4.7 Changes in total lipid concentration and recovery across processing. RP-CAD-derived total lipid concentration and percentage recovery are illustrated for the CFF runs with mPES-10 (a), mPES-100 (b), mRC-10 (c), and mRC-100 (d) membranes. UF is highlighted by shaded bars. Abbreviations: CAD: charged aerosol detection, CFF: cross-flow filtration, DV: diafiltration volume, mPES: modified polyethersulfone, mRC: modified regenerated cellulose, RP: reversed-phase, UF: ultrafiltration.

factors between 1.3 and 1.5. The encapsulation efficiencies are comparable across all experiments and remained constant throughout the process, regardless of whether the LNPs were pre-diluted, dialyzed, or purified by CFF.

In summary, both at-line and off-line measurements showed a similar trend of increasing z-average values across CFF-based processing. Here, intensity-based size distributions revealed the appearance of a second population, with a continuous increase in its proportion. Overall, LNP particle size is primarily influenced by the effect of applied CFF settings on total processing time.

4.3.4 Storage Stability

LNPs were subjected to a short-time storage stability examination at 2–8°C for up to 14 days. Changes in Z-average and zeta potential at all processing states are depicted for mPES-10 in Figure 4.8. Over storage, the Z-average of LNPs increased slightly. Interestingly, the Z-average increase during storage was more pronounced for dialyzed LNPs compared to LNPs purified by CFF. Similar trends were observed for the other CFF runs (cf. Supplementary Figure A4.5). Dialyzed LNPs showed mono-disperse size distributions during storage (data not shown). Along with the zeta potential remaining constant (cf. Supplementary Figure A4.5), no changes were observed in the other LNP characteristics of lipid concentration, lipid molar ratio, and encapsulation efficiencies throughout the storage period (data not shown). In summary, a more pronounced particle size increase over the storage period was found for the dialyzed LNPs compared to the CFF-purified LNPs.

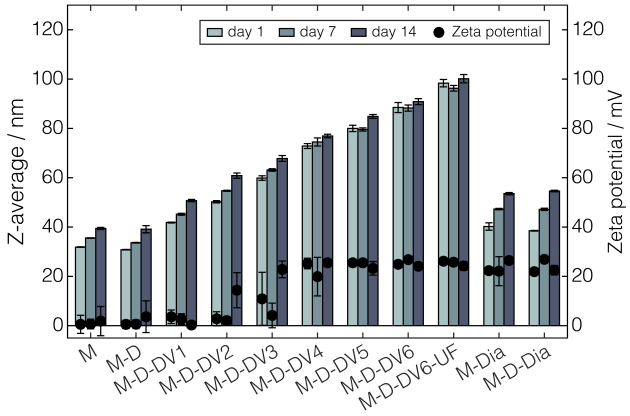

Figure 4.8 Changes in Z-average and zeta potential during storage. Z-average and zeta potential values during the storage of 14 days at 2–8 °C are shown for LNPs processed by dialysis or CFF using a mPES-10 membrane. Abbreviations: CFF: cross-flow filtration, D: dilution, Dia: dialysis, DV: diafiltration volume, LNP: lipid nanoparticle, M: microfluidics, mPES: modified polyethersulfone, UF: ultrafiltration.

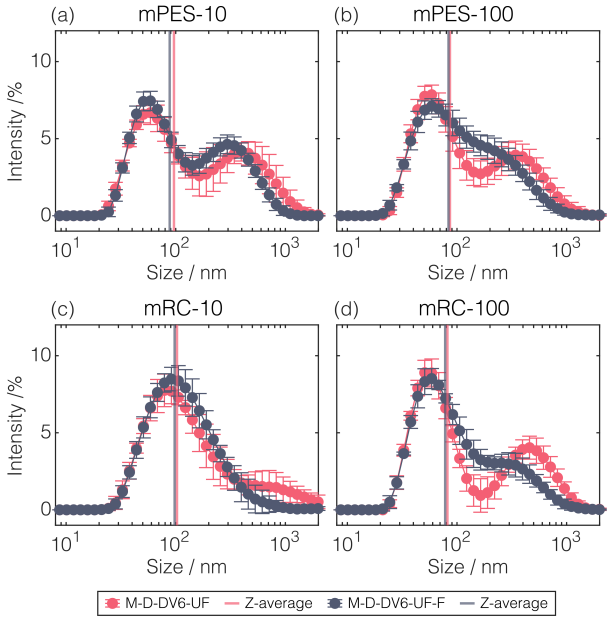

Figure 4.9 Intensity-weighted size distribution for CFF-purified and sterile-filtered LNPs. Next to the size distributions, the Z-average values for the CFF-purified (M-D-DV6-UF) and further sterile filtered LNPs (M-D-DV6-UF-F) are marked by vertical lines. Abbreviations: CFF: cross-flow filtration, D: dilution, DV: diafiltration volume, F: sterile filtration, LNP: lipid nanoparticle, M: microfluidics, mPES: modified polyethersulfone, mRC: modified regenerated cellulose, UF: ultrafiltration.

Table 4.1 Lipid recoveries after sterile filtration. The percentage lipid recoveries of sterile-filtered LNPs after purification by CFF or dialysis are listed. Abbreviations: CFF: cross-flow filtration, D: dilution, Dia: dialysis, DV: diafiltration volume, F: sterile filtration, LNP: lipid nanoparticle, M: microfluidics, mPES: modified polyethersulfone, mRC: modified regenerated cellulose, UF: ultrafiltration.

	Recovery / %			
	mPES-100	mPES-10	mRC-100	mRC-10
M-D-DV6-UF-F	91	72	83	91
M-Dia-F	n.d.	87	96	96
M-D-Dia-F	76	74	89	79

4.3.5 Sterile Filtration

Filter experiments were conducted after dialysis and CFF to assess the impact of sterile filtration on the removal of larger particles. CFF in DF-UF mode led to the formation of a second, larger-sized LNP population (cf. Figure 4.6), resulting in larger Z-average values for CFF-purified LNPs compared to dialyzed LNPs (cf. Figure 4.5). Figure 4.9 illustrates the intensity-weighted size distribution for CFF-purified LNPs (M-D-DV6-UF) and further sterile filtered LNPs (M-D-DV6-UF-F) for all performed CFF experiments.

Through sterile filtration of CFF-purified LNPs, the presence of intermediate-sized species increased, the Z-average decreased, and recoveries ranged between 73% and 91% (cf. Table 4.1). Sterile filtration of the CFF-purified LNPs by mRC-10, which showed the largest Z-average and rather broad size distribution, resulted in an overall Z-average reduction of 5 nm and clearance of the larger LNP population at 1000 nm. It has to be noted that no particles larger than 1000 nm were observed in any of the other systems either. These intensity-weighted size distributions still exhibit a more or less pronounced second population, which can be attributed to the size distribution before sterile filtration.

On the contrary, no substantial changes in size distribution, and therefore in Z-average, were observed after sterile filtration of dialyzed LNPs. Generally, lower lipid recoveries were found after sterile filtration of pre-diluted (M-D-Dia-F) than undiluted, dialyzed LNPs (M-Dia-F) (cf. Table 4.1), indicating a concentration dependency.

In summary, sterile filtration of LNPs introduced changes in the particle size distribution in the larger size range, resulting in a higher proportion of intermediate-sized particles.

4.4 Discussion

4.4.1 Effects of Pre-Dilution prior to Purification by Dialysis

Initially, a series of dialysis experiments was conducted with pre-diluted and undiluted LNPs to assess the impact of pre-dilution with a low-pH buffer as a pre-treatment step on LNP characteristics.

In general, pre-dilution was reported to improve particle characteristics of lipid-based particles. Jeffs et al. [172] observed enhanced process stability and higher encapsulation efficiencies for cationic, lipid-containing vesicles, while Kimura et al. [174] specifically identified a slight decrease in particle

size for LNPs. Although we did not observe any of those changes in LNP characteristics due to pre-dilution, it is worth noting that the LNPs showed stable behavior.

As LNP dilution with a buffer reduces the ethanol content, related changes in particle characteristics may be linked to the altered behavior of lipids. Ethanol interacts with the polar head groups of lipids at the lipid-water interface due to its dual lipophilic and hydrophilic nature. In the case of lipid bilayers, this ethanol-lipid interaction expands the membrane surface, creating cavities within the hydrophobic core, which are subsequently occupied by lipid tails from the opposing membrane leaflet, leading to a reduction in membrane thickness [182, 183]. Next to this so-called interdigitation process, ethanol-lipid interactions might also enhance the likelihood of fusion due to reduced lipid hybridization and enhanced exposure of lipid tails [184]. Their study also demonstrated increased fusion activity for liposomes with non-protein-containing lipid bilayers next to elevated membrane fluidity. So far, fusion processes in the presence of ethanol have only been studied in the context of liposomes fusing to model bilayer membranes, but to the best of the authors' knowledge, neither studied for LNPs fusing to model bilayer membranes nor LNP-LNP fusion.

The dilution process design for LNPs is rarely reported in the literature. Next to dilution by simple pipetting, Kimura et al. [174] designed a microfluidic on-device dilution system integrating dilution next to LNP synthesis. Compared to pipette-induced dilution or direct dialysis, their rapid dilution approach yielded smaller LNPs, with the smallest particles observed at the highest dilution flow rates. They also hypothesized that ethanol dilution within milliseconds prevents the formation of interdigitated structures and particle fusion. Reducing the ethanol content immediately after LNP synthesis is further supported by molecular dynamics simulations [145] and the observations that longer hold times before dilution [174] or dialysis [185] led to an increase in particle size. So far, no studies on buffer selection for pre-dilution of LNPs have been reported. The authors ultimately chose the synthesis buffer as the dilution buffer, which has also been used for liposomes [186]. However, others selected a dilution buffer pH of 6 for LNPs, which fell between the pH of the synthesis and dialysis buffers [174]. In contrast to the effect of buffer selection for pre-dilution of LNPs, the impact of buffer pH during dialysis on the size increase of LNPs has already been studied [31, 34].

In summary, pre-dilution with pH 4 buffer specifically reduced the ethanol content without altering the LNP characteristics, making it suitable for use as a pre-treatment for LNPs prior to CFF-based purification.

4.4.2 Design of Cross-Flow Filtration-Based Processing

A CFF-based process in DF/UF mode allows for setting a target product concentration directly after buffer exchange, which is not possible with dialysis. In such filtration-based processes, it is crucial to consider membrane-related and operational parameters, their relationship, and their interaction with or influence on the target product to be filtered. As ethanol is known to influence the permeability of membranes, LNPs were pre-diluted to lower the ethanol content by a factor of four. Although some studies on liposomes incorporated ethanol dilution prior to constant-volume DF [187, 188] or continuous in-line DF [179, 189] resulting in increased efficiency [179], this approach has not yet been applied to LNPs. An ethanol-dependent limited permeability of the membrane at the beginning of the process would be reflected by either a lower permeate flux under constant TMP (mPES-/mRC-10) or a higher TMP under constant permeate back-pressure (mPES-/mRC-100) compared to the following process profiles, which, however, could not be observed in our CFF runs.

In the design of filtration processes, membrane-related parameters influence the configuration of operational parameters, which, unlike in diffusion-driven dialysis, must be considered in pressure-driven, CFF-based DF. Since most of all referred CFF studies employed membrane MWCOs of 100 kDa or higher to keep the processing time within limits, we additionally included a 10 kDa MWCO, which is commonly used for dialysis, alongside the 100 kDa MWCO membrane to provide a comparative perspective. The authors decided on a constant TMP enabled through an automatic valve on the retentate side for the CFF runs with the 10 kDa MWCO membrane. In comparison, a capillary on the permeate side led to a constant permeate back pressure for the runs using the 100 kDa MWCO membrane. Comprehensive parameter studies considering membrane-related next to operational parameter variations in constant-volume DF have not been reported within the broader category of lipid-based particles.

Specifically, those lipid-based particles may be sensitive to applied pressures and specific types of pumps, valves, membrane material, or membrane format, as each of these factors can generate its shear rate, leading to various shear forces that could further affect the particle characteristics. The selected membrane materials mPES and mRC exhibit a hydrophilic nature, facilitating water permeability and preventing fouling [36]. Regardless of the membrane material, comparable lipid recoveries of approximately 86% to 89% were achieved, significantly surpassing the reported 73% recovery for LNP purification by CFF [176] and closely aligning with studies on liposome purification by CFF [178, 180, 188]. Comparable lipid recoveries stand in contrast to the differently pronounced permeability drops observed throughout the different CFF runs, which typically indicate fouling behavior. Overall, optimizing surface areas or processing larger volumes can help reduce product accumulation on the membrane, thereby enhancing overall recovery.

Besides potential interactions, membrane-related and operational parameters may influence the target product. Our strategy to include monitoring tools aligns with the PAT initiative [14], as at-line measurements provide near real-time process insights. To the best of the authors' knowledge, we are the first to have implemented at-line DLS enabling tracking of the LNP particle size and size distribution throughout CFF-based processing, resolving characteristic changes from DV to DV. Among lipid-based particles, Forbes et al. [180] claimed at-line monitoring of liposome particle size but focused on in-process monitoring between process steps rather than on time- or DV-resolved insights into CFF using CFF intermediates. DLS would also be suitable for on-line implementation using a suitable flow cell, but this has not yet been reported for LNPs. An advancement has led to spatially resolved DLS, which has already been applied to turbid nanoemulsions [190] and liposomes purified by single-pass CFF [177]. Sheybanifard et al. [177] not only monitored the product but also employed in-line near-infrared spectroscopy to quantify residual ethanol, which could similarly be applied to monitor ethanol depletion over constant-volume DF and UF.

4.4.3 Effects of Cross-Flow Filtration-Based Purification on Lipid Nanoparticles

Despite being a time- and resource-efficient purification procedure, CFF is rarely reported for LNPs, and even less frequently are the UF/DF process dynamics examined through a holistic analysis of CFF intermediates. Given the limited research on CFF intermediates in CFF-based LNP purification, the following summarizes the key findings and their implications.

We found a time-dependent size increase of LNPs, which seems independent of selected processing parameters. So far, the LNP size increase over CFF-based DF has been merely described by Geng et al. [37]. They examined a DF process for three different LNP formulations and observed

a stabilized LNP size after two DV for all three formulations. After two DV, approximately 87% of the initial buffer and ethanol are expected to be removed, assuming unrestricted membrane permeability for smaller molecules [36].

Moreover, Geng et al. [37] observed differences in the way of particle fusion depending on the purification procedure, as the initial absence of ethanol led to more homogeneous particles than its initial presence during DF to physiological pH, but clearly stated that the fusion is pH-driven. Fusion behavior is also observed to be pH-dependent during dialysis [31] and is hypothesized to depend on the ionizable lipid and its pKa [34]. Although DOTAP is a pH-insensitive, permanent cationic lipid, changes in the amount of positive charge seem to affect LNP fusion behavior. In particular, the PEG lipid plays a key role in the colloidal stability and fusion behavior of LNPs. The molar content of the PEG lipid affects particle size and defines its equilibrium size, which also depends on the pH of the solution [27, 32]. Overall, the size increase of LNPs may be linked to the PEG-dependent equilibrium size and the presence of a cationic lipid, combined with a pH increase throughout the process. Studies on CFF-based DF processes of liposomes have shown no particle size increase [180, 188], which might be attributed to the structural differences between LNP and liposomes. Another factor that might have influenced this outcome is the process condition applied in those studies, where ethanol was solely removed without increasing the pH or altering the buffer [180, 188]. Others observed similar behavior of cationic liposomes performing discontinuous DF with DF cycles consisting of concentration and manual dilution [178].

Since the observed size increase during our DF/UF processes is closely linked to the processing time of LNPs, the potential influence of shear forces must be considered. The time-dependent LNP size increase indicates that the pump-induced shear rate has more impact on particle size than the membrane-induced shear rates. This conclusion is drawn from the fact that the membrane-induced shear rates are format-dependent, while the pump-induced shear rates were constant across all experiments. Thus, the time-dependent increase in LNP size can be attributed to the pump cycles, which correspond to the processing time. To reduce processing time, single-pass CFF may offer an effective strategy for LNP purification. Here, too, liposome studies have shown no size increase of their PEGylated liposomes during continuous processing by single-pass CFF [177] or during continuous, in-line single-pass DF using such serially connected filter membranes [189].

Besides the observed size increase across CFF-based LNP purification, an increase in size was also observed in the individual CFF intermediates over the storage time, which contrasts with the observed size deviations seen from at-line to off-line (day 1) of later CFF intermediates. The observed deviations between at-line and off-line DLS measurements could be assigned to two overlapping phenomena. A systematic, method-derived offset upwards in size for at-line DLS for all CFF intermediates may co-occur with the tendency of enhanced size increase of early CFF intermediates compared to later CFF intermediates. The latter tendency can be observed across 14 days of storage.

LNP size was the only measured particle characteristic that changed during storage. All LNPs exhibited a size increase, with the most pronounced growth in early CFF intermediates and dialyzed LNPs, which initially measured half the size of the final CFF-purified LNPs. Storage-related size increase for dialyzed LNPs with an identical lipid mola ratio and cargo has already been shown in our previous work [181]. Although PEG-lipid content plays a crucial role in preventing fusion, final DF/UF-purified LNPs exhibit less fusion than dialyzed LNPs, even though the PEG content is identical, suggesting that storage-induced fusion behavior may be independent of PEG-lipid concentration. Storage-related size increase of LNP purification intermediates and after CFF-based

purification was so far only observed by Geng et al. [37]. Their final DF-purified LNPs after eight DV showed a size increase of 6.1 nm over a 2-month storage. Due to the different LNP sizes of the starting material, overall processing time, and DV, absolute size comparisons were omitted. Our DF processes for six DV had comparable or higher process times and hence resulted in different sizes after DF due to the found time dependency. Exemplarily, DF time in the mRC-100 CFF process was comparable to the DF process presented by Geng et al. [37], leading to a size increase of 2.1 nm over two weeks of storage. Overall, storage-induced size increases of CFF intermediates appear comparable across the CFF runs. For further concentrated LNPs by UF following DF, storage stability data has not been reported in the literature.

Many studies have highlighted the importance of production parameters during microfluidic mixing [23, 29, 34] when controlling LNP characteristics such as size. However, Vargas et al. [35] has also found that those identified correlations change through subsequent dialysis, emphasizing the consideration of dialysis or any other treatment or purification step. On-chip dilution has been introduced as a size-controlled treatment strategy [174], which still had to undergo a purification step. In this context, LNP purification by CFF is far too little explored and reported in the literature. With the observed time-dependent increase in particle size, the authors state that CFF might be the purification process for targeted, size-controlled LNPs. However, this is why several questions in this study still require further investigation. The question arises about how far the LNPs are from their equilibrium size. Our observations that dialyzed LNPs increased in size over storage to a greater extent than CFF-purified LNPs may indicate CFF as a representable purification method to achieve the equilibrium size faster. Additionally, modifications in CFF design, such as extending the processing time, might enable the LNPs to reach equilibrium size. The influence of pump-induced shear rates on the size increase of LNPs remains a key consideration, and since shear-sensitive pumps are now available on the market, a comparative study would be interesting. Furthermore, the emergence of a second larger LNP population raises the question of what triggers this behavior and whether it could indicate particle instability, making an investigation into the formation and morphology of such particles urgently required. Progress toward optimizing filtration performance can only be made after reassessing and clarifying these questions related to controlling the target LNP characteristics. In the future, an investigation into various operating conditions, membranes, and advanced membrane technologies, along with their associated shear forces and fouling behavior, may be undertaken.

4.4.4 Effects of Sterile Filtration on Lipid Nanoparticles Purified by Cross-Flow Filtration

Although sterile filtration is a crucial step in biopharmaceutical manufacturing, it is often seen as problematic regarding nanoparticle therapeutics due to the similarity between nanoparticle size and filter pore size. Besides filtration capacity, nanoparticle characteristics and their recovery are essential parameters for evaluation.

Sterile filtration of the CFF-purified LNPs led to significant changes in the intensity-weighted size distributions but resulted only in a minor reduction in Z-average. According to the size distribution and contrary to our expectations, LNPs larger than the 0.22 µm pore size were still found in the filtrate. Due to a lack of literature describing this phenomenon, the authors propose several hypotheses. One possibility may be that LNPs undergo deformation into a more elliptical or oval shape due to filtration forces, allowing them to pass through the filter pores. Literature

on nanoparticle deformability is relatively rare, but Hirsjärvi et al. [175] found same-sized hybrid polymer-lipid particles in the CFF filtrate, even though their particle size exceeded the evaluated MWCO. Conversely, the increased intensity of particles between the two most pronounced populations suggests simultaneous fragmentation and hence formation of intermediate-sized particles, which may be due to experienced shear forces during filtration. However, those hypotheses could not be evaluated in this study. It has to be noted that the hydrodynamic diameter assessed encompasses the hydration shell of the particle, which is the underlying principle of the DLS measurement.

In contrast to our findings, no substantial change in the particle size and size distribution was observed in the sterile filtration study of Messerian et al. [191] with similar-sized LNPs. Further, our lipid recoveries ranged between 72% and 96%, with 96% being close to those reported lipid recoveries. Messerian et al. [191] examined the effects of different pressures on filtration and found deposits on the membrane, which were further analyzed in-depth by Messerian et al. [192]. They observed an amorphous 100 nm-thick deposit on the surface of a 0.2 µm polyethersulfone filter, suggesting that it may form due to a combination of size-based retention, adsorption, filtration forces, and LNP coalescence. Adsorption is based on material-product interactions, and given that LNP surfaces exhibit a broad range of functional groups, physical or chemical interactions may occur. The adhesion forces of hydrophobic functional groups on the filter could be evaluated using the method described by Wang et al. [193], who utilized atomic force microscopy to study the interactions between hydrophilic functional groups and LNPs.

Compared to filtration studies under desired pressures [191, 192], we performed sterile filtration by hand, which could be linked to variations in recovery. Further, a concentration dependence is evident, as higher recoveries were observed for the dialyzed LNPs compared to pre-diluted, dialyzed LNP. In general, adjusting the process volume, LNP concentration, or filter area could further contribute to optimizing recovery. For high lipid concentrations, sterile filtration of purified PEGylated liposomes has been reported to achieve recoveries of up to 100% [189].

In summary, sterile filtration affected LNP size distribution but did not erase populations larger than or around 200 nm completely, possibly due to shear-induced deformation or fragmentation of LNPs.

4.5 Conclusion

In conclusion, we present a CFF parameter study for LNP purification by DF/UF, investigating the impact of CFF-based processing on process performance and particle characteristics. A series of dialysis experiments revealed that pre-dilution of LNPs with synthesis buffer as a pretreatment procedure allows for reducing the ethanol content prior CFF-based purification without affecting the LNP characteristics. Time- and resource-efficient buffer exchange and product concentration were addressed by constant-volume DF mode over six DV followed by LNP concentration by UF. Although the systematic strategy varying either the membrane characteristics material, format, and area, or the membrane MWCO and the system pressure setting has been introduced to investigate their parameter impact on particle characteristics, a contrary dependency was found—a processing time-dependent particle size increase. With the novel aspect aiming for near real-time monitoring by implementing at-line DLS measurements, time-resolved insights into changes in particle size and size distribution were provided. A noticeable trend was observed in particle size increases during storage, with an enhanced size increase of dialyzed LNPs and early CFF intermediates compared to later

CFF intermediates and final CFF-purified LNPs, leading to several hypotheses for the underlying reason, including the equilibrium size of LNPs. Sterile filtration of purified LNPs again introduced changes in the particle size and size distribution, suggesting shear-induced particle deformation and fragmentation. Overall, this parameter study, combined with at-line and off-line analytics yielding intensified process insights, provides a solid foundation for future investigations into the formation behavior and morphology changes by CFF-based LNP processing, hence paving the way for future CFF applications for size-controlled LNP purification.

CRediT authorship contribution statement

Annabelle Dietrich: Writing – review & editing, Writing – original draft, Visualization, Validation, Software, Methodology, Investigation, Formal analysis, Data curation, Conceptualization. **Nicole Beckert**: Writing – review & editing, Writing – original draft, Visualization, Validation, Software, Methodology, Investigation, Formal analysis, Data curation, Conceptualization. **Jürgen Hubbuch**: Writing – review & editing, Supervision, Funding acquisition, Conceptualization.

Supplementary Material

Appendix **A4** contains the Supplementary Material associated with this chapter.

Chapter References

[10] P. R. Cullis and P. L. Felgner. „The 60-year evolution of lipid nanoparticles for nucleic acid delivery“. In: *Nature Reviews Drug Discovery* 23.9 (2024), pp. 709–722. DOI: 10.1038/s41573-024-00977-6.

[12] M. J. W. Evers, J. A. Kulkarni, R. van der Meel, P. R. Cullis, P. Vader, and R. M. Schiffelers. „State-of-the-Art Design and Rapid-Mixing Production Techniques of Lipid Nanoparticles for Nucleic Acid Delivery“. In: *Small Methods* 2.9 (2018), p. 1700375. DOI: 10.1002/smtd.201700375.

[14] FDA. *Guidance for Industry: PAT—a framework for innovative pharmaceutical development, manufacturing, and quality assurance*. 2004.

[15] M. Rüdt, T. Briskot, and J. Hubbuch. „Advances in downstream processing of biologics – Spectroscopy: An emerging process analytical technology“. In: *Journal of Chromatography A* 1490 (2017), pp. 2–9. DOI: 10.1016/j.chroma.2016.11.010.

[22] C. H. Albertsen, J. A. Kulkarni, D. Witzigmann, M. Lind, K. Petersson, and J. B. Simonsen. „The role of lipid components in lipid nanoparticles for vaccines and gene therapy“. In: *Advanced Drug Delivery Reviews* 188 (2022), p. 114416. DOI: 10.1016/j.addr.2022.114416.

[23] C. B. Roces et al. „Manufacturing considerations for the development of lipid nanoparticles using microfluidics“. In: *Pharmaceutics* 12.11 (2020), pp. 1–19. DOI: 10.3390/pharmaceutics12111095.

[27] J. A. Kulkarni et al. „On the Formation and Morphology of Lipid Nanoparticles Containing Ionizable Cationic Lipids and siRNA“. In: *ACS Nano* 12.5 (2018), pp. 4787–4795. DOI: 10.1021/acsnano.8b01516.

[28] Y. Fan et al. „Automated high-throughput preparation and characterization of oligonucleotide-loaded lipid nanoparticles“. In: *International Journal of Pharmaceutics* 599 (2021). DOI: 10.1016/j.ijpharm.2021.120392.

[29] K. Okuda et al. „On the size-regulation of RNA-loaded lipid nanoparticles synthesized by microfluidic device“. In: *Journal of Controlled Release* 348 (2022), pp. 648–659. DOI: 10.1016/j.jconrel.2022.06.017.

[31] J. A. Kulkarni, D. Witzigmann, J. Leung, Y. Y. C. Tam, and P. R. Cullis. „On the role of helper lipids in lipid nanoparticle formulations of siRNA“. In: *Nanoscale* 11.45 (2019), pp. 21733–21739. DOI: 10.1039/c9nr09347h.

[32] J. A. Kulkarni et al. „Fusion-dependent formation of lipid nanoparticles containing macromolecular payloads“. In: *Nanoscale* 11.18 (2019), pp. 9023–9031. DOI: 10.1039/C9NR02004G.

[34] T. Terada et al. „Characterization of Lipid Nanoparticles Containing Ionizable Cationic Lipids Using Design-of-Experiments Approach“. In: *Langmuir* 37.3 (2021), pp. 1120–1128. DOI: 10.1021/acs.langmuir.0c03039.

[35] R. Vargas et al. „Dialysis is a key factor modulating interactions between critical process parameters during the microfluidic preparation of lipid nanoparticles“. In: *Colloids and Interface Science Communications* 54 (2023). DOI: 10.1016/j.colcom.2023.100709.

[36] R. van Reis and A. Zydney. „Bioprocess membrane technology“. In: *Journal of Membrane Science* 297.1-2 (2007), pp. 16–50. DOI: 10.1016/j.memsci.2007.02.045.

[37] C. Geng et al. „A preparation method for mRNA-LNPs with improved properties“. In: *Journal of Controlled Release* 364 (2023), pp. 632–643. DOI: 10.1016/j.jconrel.2023.11.017.

[145] A. Hardianto, Z. S. Muscifa, W. Widayat, M. Yusuf, and T. Subroto. „The Effect of Ethanol on Lipid Nanoparticle Stabilization from a Molecular Dynamics Simulation Perspective“. In: *Molecules* 28.12 (2023). DOI: 10.3390/molecules28124836.

[171] I. Urits et al. „A Review of Patisiran (ONPATTRO®) for the Treatment of Polyneuropathy in People with Hereditary Transthyretin Amyloidosis“. In: *Neurology and Therapy* 9.2 (2020), pp. 301–315. DOI: 10.1007/s40120-020-00208-1.

[172] L. B. Jeffs, L. R. Palmer, E. G. Ambegia, C. Giesbrecht, S. Ewanick, and I. MacLachlan. „A scalable, extrusion-free method for efficient liposomal encapsulation of plasmid DNA“. In: *Pharmaceutical Research* 22.3 (2005), pp. 362–372. DOI: 10.1007/s11095-004-1873-z.

[173] R. Mihaila et al. „Lipid nanoparticle purification by Spin Centrifugation-Dialysis (SCD): A facile and high-throughput approach for small scale preparation of siRNA-lipid complexes“. In: *International Journal of Pharmaceutics* 420.1 (2011), pp. 118–121. DOI: 10.1016/j.ijpharm.2011.08.017.

[174] N. Kimura et al. „Development of a Microfluidic-Based Post-Treatment Process for Size-Controlled Lipid Nanoparticles and Application to siRNA Delivery“. In: *ACS Applied Materials and Interfaces* 12.30 (2020), pp. 34011–34020. DOI: 10.1021/acsami.0c05489.

[175] S. Hirsjärvi, G. Bastiat, P. Saulnier, and J. P. Benoît. „Evaluation of surface deformability of lipid nanocapsules by drop tensiometer technique, and its experimental assessment by dialysis and tangential flow filtration“. In: *International Journal of Pharmaceutics* 434.1-2 (2012), pp. 460–467. DOI: 10.1016/j.ijpharm.2012.06.019.

[176] Y. Sakurai, T. Hada, and H. Harashima. „Scalable preparation of poly(ethylene glycol)-grafted siRNA-loaded lipid nanoparticles using a commercially available fluidic device and tangential flow filtration“. In: *Journal of Biomaterials Science, Polymer Edition* 28.10-12 (2017), pp. 1086–1096. DOI: 10.1080/09205063.2017.1291297.

[177] M. Sheybanifard et al. „Liposome manufacturing under continuous flow conditions: towards a fully integrated set-up with in-line control of critical quality attributes“. In: *Lab on a Chip* 23.1 (2022), pp. 182–194. DOI: 10.1039/d2lc00463a.

[178] N. Dimov, E. Kastner, M. Hussain, Y. Perrie, and N. Szita. „Formation and purification of tailored liposomes for drug delivery using a module-based micro continuous-flow system“. In: *Scientific Reports* 7.1 (2017). DOI: 10.1038/s41598-017-11533-1.

[179] R. D. Worsham, V. Thomas, and S. S. Farid. „Impact of ethanol on continuous inline diafiltration of liposomal drug products“. In: *Biotechnology Journal* 18.11 (2023), pp. 1–9. DOI: 10.1002/biot.202300194.

[180] N. Forbes et al. „Rapid and scale-independent microfluidic manufacture of liposomes entrapping protein incorporating in-line purification and at-line size monitoring“. In: *International Journal of Pharmaceutics* 556 (2019), pp. 68–81. DOI: 10.1016/j.ijpharm.2018.11.060.

[181] N. Beckert, A. Dietrich, and J. Hubbuch. „RP-CAD for Lipid Quantification: Systematic Method Development and Intensified LNP Process Characterization“. In: *Pharmaceuticals* 17.9 (2024). DOI: 10.3390/ph17091217.

[182] T. McIntosh, R. McDaniel, and S. Simon. „Induction of an interdigitated gel phase in fully hydrated phosphatidylcholine bilayers“. In: *Biochimica et Biophysica Acta (BBA) - Biomembranes* 731.1 (1983), pp. 109–114. DOI: 10.1016/0005-2736(83)90403-0.

[183] F. W. Stetter and T. Hugel. „The nanomechanical properties of lipid membranes are significantly influenced by the presence of ethanol“. In: *Biophysical Journal* 104.5 (2013), pp. 1049–1055. DOI: 10.1016/j.bpj.2013.01.021.

[184] J. Paxman, B. Hunt, D. Hallan, S. R. Zarbock, and D. J. Woodbury. „Drunken Membranes: Short-Chain Alcohols Alter Fusion of Liposomes to Planar Lipid Bilayers“. In: *Biophysical Journal* 112.1 (2017), pp. 121–132. DOI: 10.1016/j.bpj.2016.11.3205.

[185] K. J. Hassett et al. „Impact of lipid nanoparticle size on mRNA vaccine immunogenicity“. In: *Journal of Controlled Release* 335 (2021), pp. 237–246. DOI: 10.1016/j.jconrel.2021.05.021.

[186] A. Pittiu et al. „Production of liposomes by microfluidics: The impact of post-manufacturing dilution on drug encapsulation and lipid loss“. In: *International Journal of Pharmaceutics* 664 (2024), p. 124641. DOI: 10.1016/j.ijpharm.2024.124641.

[187] Y. Perrie et al. „The impact of solvent selection: Strategies to guide the manufacturing of liposomes using microfluidics“. In: *Pharmaceutics* 11.12 (2019). DOI: 10.3390/pharmaceutics11120653.

[188] C. Webb et al. „Using microfluidics for scalable manufacturing of nanomedicines from bench to GMP: A case study using protein-loaded liposomes“. In: *International Journal of Pharmaceutics* 582 (2020), p. 119266. DOI: 10.1016/j.ijpharm.2020.119266.

[189] C. B. Roces et al. „Rapid scale-up and production of active-loaded PEGylated liposomes“. In: *International Journal of Pharmaceutics* 586 (2020), p. 119566. DOI: 10.1016/j.ijpharm.2020.119566.

[190] R. Besseling, M. Damen, J. Wijgergangs, M. Hermes, G. Wynia, and A. Gerich. „New unique PAT method and instrument for real-time inline size characterization of concentrated, flowing nanosuspensions“. In: *European Journal of Pharmaceutical Sciences* 133 (2019), pp. 205–213. DOI: 10.1016/j.ejps.2019.03.024.

[191] K. O. Messerian, A. Zverev, J. F. Kramarczyk, and A. L. Zydney. „Pressure-dependent fouling behavior during sterile filtration of mRNA-containing lipid nanoparticles“. In: *Biotechnology and Bioengineering* 119.11 (2022), pp. 3221–3229. DOI: 10.1002/bit.28200.

[192] K. O. Messerian, A. Zverev, J. F. Kramarczyk, and A. L. Zydney. „Characterization and associated pressure-dependent behavior of deposits formed during sterile filtration of mRNA-Lipid nanoparticles“. In: *Journal of Membrane Science* 684 (2023), p. 121896. DOI: 10.1016/j.memsci.2023.121896.

[193] J. Wang et al. „Probing the interaction mechanisms of lipid nanoparticle-encapsulated mRNA with surfaces of diverse functional groups: Implication for mRNA transport“. In: *Chemical Engineering Science* 301 (2025), p. 120693. DOI: 10.1016/j.ces.2024.120693.

5

Dual-Stage Cross-Flow Filtration: Integrated Capture and Purification of Virus-Like Particles

Annabelle Dietrich[1], Luca Heim[1], and Jürgen Hubbuch[1]

[1] Institute of Process Engineering in Life Sciences, Section IV: Biomolecular Separation Engineering, Karlsruhe Institute of Technology (KIT), Karlsruhe, Germany

Abstract

Virus-like particles (VLPs) are a versatile technology for the targeted delivery of genetic material through packaging and potential surface modifications for directed delivery or immunological issues. Although VLP production is relatively simple as they can be recombinantly produced using microorganisms such as *Escherichia coli*, their current downstream processing often relies on individually developed purification strategies. Integrating size-selective separation techniques may allow standardized platform processing across VLP purification. This study presents an innovative dual-stage cross-flow filtration (CFF) set-up for integrated capture and purification of VLPs, enabling processing solely based on the size-selective separation techniques precipitation and filtration. The 2 µm/300 kDa MWCO membrane configuration allows the seamless integration of selective VLP precipitation, two consecutive diafiltration steps—first, for washing the VLP precipitates in the first membrane stage, and second, for isolating the re-dissolved VLPs by continuously removing precipitant and contaminants in the second membrane stage—and ultrafiltration for setting a target VLP concentration. Compared to a single-stage CFF set-up, this dual-stage CFF set-up with its integrative, automated design demonstrated the capabilities of product accumulation and contaminant handling while maintaining high productivity. Overall, this study represents a significant advancement toward standardized platform processing of protein nanoparticles through precipitation and filtration, and underscores the potential to expand its applicability to diverse biological molecules, unique process conditions, other phase behavior-dependent processes, and continuous processing.

5.1 Introduction

Protein nanoparticles serve as a versatile technology for targeted delivery of various cargos and can also be used as vaccines [4, 194]. Similar to the downstream processing of conventional biopharmaceuticals, the downstream processing of protein nanoparticles shares the primary objectives of achieving the required product purity and yield, while effectively managing time and costs in both development and production [57]. Recent advancements have introduced size-selective separation techniques such as precipitation and filtration, capitalizing on the notably large size of protein nanoparticles [13]. However, as high as the diversity of protein nanoparticles, so is the challenge of their processing, contributing to the present rarity of standardized platform process development [57].

Among protein nanoparticles, VLPs exhibit distinct properties compared to other viral vectors while maintaining their versatility [195]. VLPs are multimeric structures mimicking the viruses from which they originate [39, 56] with much lower safety concerns as they lack the viral genome [43]. In addition to their considerable loading capacities, VLPs can undergo surface modifications by genetic engineering or chemical conjugation [4].

The diversity of VLPs and their expression systems is reflected in the impurity profile of the clarified cell lysate. As a result, the subsequent downstream processing involves a wide array of deployable unit operations for capture, intermediate purification, and polishing steps [11]. The main challenge faced by the development of the initial capture step is the targeted removal of process-related impurities to ensure the subsequent separation of their residuals and product-related impurities with only a small number of purification steps [11]. Although steric- and size-exclusion chromatography is employed as a size-selective separation technique for various VLPs [13], selective protein precipitation has already established itself as another alternative, particularly for capture.

A considerable amount of literature has been published on selective VLP precipitation induced by the addition of ammonium sulfate (AMS) [81, 82] or polyethylene glycol [83–85] as precipitant. Precipitation itself is highly scalable but typically involves subsequent centrifugation-based wash and product recovery steps, which suffer from scale-up challenges and hence are highly insufficient in time and effort. Moreover, precipitate compaction may lead to potential difficulties in re-dissolution and residual contaminants in the interstitial pellet liquid [104].

Recent developments in the field of precipitation-based capture processes have led to innovative membrane-aided approaches using CFF-based diafiltration (DF). Venkiteshwaran et al. [102] firstly introduced the washing of precipitated immunoglobulins using a cross-flow microfiltration (MF) membrane to separate them from bovine serum albumin in solution. Similar integrated set-ups have been reported for concentration and washing of antibody precipitate for batch precipitation [103] and sequential precipitation with discontinuous precipitate separation [104]. Further developments have been made toward continuous processing, using two-stage set-ups with two identical MF membranes connected in series, enabling intensified washing of the antibody precipitate in the second stage [105, 106]. In all these studies, however, subsequent product recovery was performed separately by either precipitate dilution or centrifugation and pellet re-dissolution.

A CFF-based re-dissolution strategy for integrated product recovery was proposed by Hillebrandt et al. [88], allowing VLP precipitate to re-dissolve into VLPs to pass through an MF membrane. At the same time, irreversibly precipitated species are retained. With this set-up, the original centrifugation-based procedure is entirely replaced by filtration-based steps, which is beneficial as filtration offers superior scalability and the capability for disposable manufacturing [36, 101]. Although purity, yield, and productivity improvements have been reported compared to the centrifugation-based procedure [88], it still faces limitations. In particular, the product-containing permeate fractions may still have precipitant present, and the ability to integrate additional process steps downstream such as concentration of the re-dissolved, diluted product is not given. Hence, a subsequent DF for precipitant removal and ultrafiltration (UF) for product concentration might be required. Integrating precipitant removal and product concentration may be achieved by adding a second membrane stage with a smaller MWCO than the first-stage MF membrane.

Among multistage membrane set-ups, two-stage configurations with different membrane MWCOs were specifically employed to isolate the product solely based on size in the second stage while retaining larger species and depleting smaller ones. Cheang et al. [196] presented a set-up with 100 and 30 kDa MWCO membranes for alpha-lactalbumin isolation from bovine serum albumin and beta-lactoglobulin. Similarly, bromelain was isolated from crude pineapple waste mixture using 75 and 10 kDa MWCO membranes [197–199]. Further, MF was combined with UF to isolate polymerized human hemoglobin from its product-related high or low-molecular weight species (LMWS) using an integrated 2 µm/500 kDa MWCO membrane configuration [200]. So far, an integrated two-stage set-up for precipitation-based capture and purification has not been reported.

In this study, we introduce a dual-stage CFF (*dsCFF*) set-up with a 2 µm/300 kDa MWCO membrane configuration for a VLP capture process, enabling the seamless, automated integration of VLP precipitation, precipitate washing, VLP re-dissolution, as well as their isolation and concentration. A visual illustration of the integrated, consecutive steps is presented in Figure 5.1.

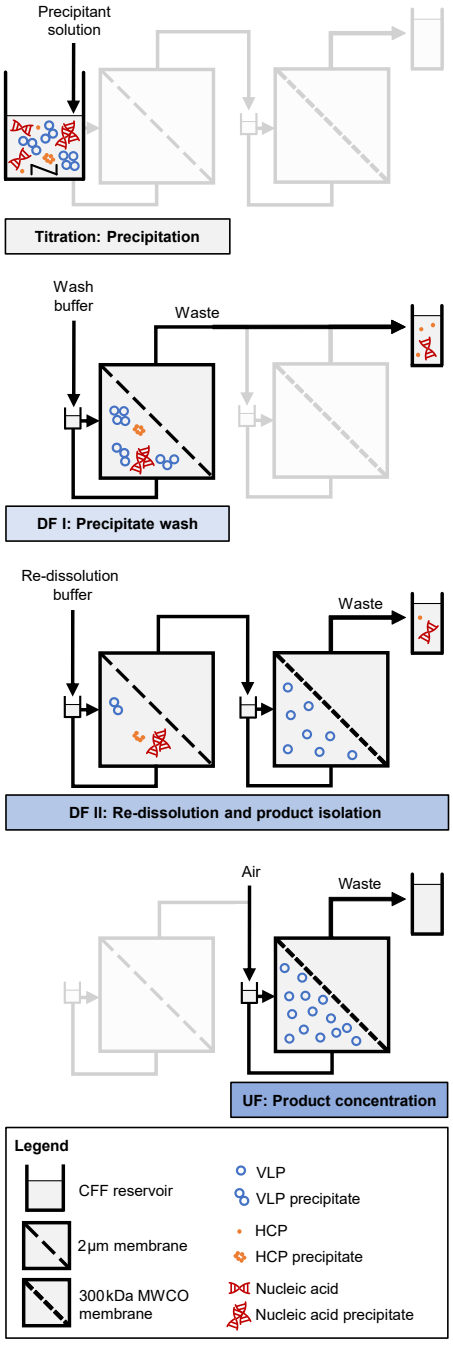

Figure 5.1 Schematic illustration of the integrated *dsCFF* process. Precipitation by titration in the CFF reservoir is followed by washing of the precipitate by constant-volume DF using a 2 µm membrane (DFI). Product re-dissolution by a consecutive DF using the dual-stage 2 µm/300 kDa MWCO membrane configuration (DFII) allows for integrated product isolation in the second membrane stage. Finally, the setup enables product concentration by subsequent UF. Adapted from Hillebrandt et al. [88].

To estimate the impurity profile and the precipitant concentration in CFF-based processes, we initially provide insights into the VLP re-dissolution dynamics and the behavior of host-cell contaminants by a small-scale, centrifugation-based screening approach. As a reference process for the VLP construct used in this study, we evaluate a single-stage CFF (*ssCFF*) process, covering integrated VLP precipitation, washing the precipitate from host-cell contaminants, and separating re-dissolved VLPs through a 2 µm membrane from irreversibly precipitated species. To address product concentration and purity limitations during VLP re-dissolution while maintaining high productivity, we establish the proposed *dsCFF* process by integrating a 300 kDa MWCO membrane as the second membrane stage. Simultaneously with the VLP re-dissolution and their passage through the first into the second membrane stage, we demonstrate (i) integrated VLP isolation through continuous depletion of precipitant and contaminants, and (ii) integrated VLP concentration by subsequent UF.

5.2 Materials and Methods

5.2.1 Buffers, Solutions, and Virus-Like Particles

If not otherwise stated, all chemicals were sourced from Merck KGaA (Darmstadt, DE). Buffers and stock solutions were prepared with ultrapure water (PURELAB Ultra, ELGA LabWater, Lane End, High Wycombe, UK), filtered through 0.2 µm pore-size cellulose acetate filters (VWR International, Radnor, US) and degassed. The target buffer pH was adjusted with hydrochloric acid. Lysis buffer consisting of 50 mM Tris, 100 mM, 1 mM EDTA (AppliChem GmbH, Darmstadt, DE) at pH 8.0, wash buffer (lysis buffer containing 1.1 M AMS), and re-dissolution buffer (50 mM Tris, 100 mM NaCl) at pH 7.2 were used for all experiments. High performance liquid chromatography (HPLC) running buffer was 50 mM potassium phosphate buffer at pH 7.4. For polysorbate adjustment and VLP precipitation experiments, 10% (v/v) polysorbate 20 and 4 M AMS stock solutions were used, respectively. For Raman spectroscopy, a set of 12 reference solutions with varying concentrations of AMS (0.1 M increments) was prepared by mixing wash and re-dissolution buffer at desired levels.

The VLP of interest is composed of C-terminally truncated wild-type Hepatitis B core Antigen (HBcAg) proteins, Cp149 [49]. The plasmid encoding Cp149 was kindly provided by Prof. Adam Zlotnick (Indiana University, US). A similar procedure of the Cp149 production, capsid harvest, cell lysis, and lysate clarification was conducted as described by Hillebrandt et al. [88]. Clarified lysate solutions containing HBcAg VLPs were thawed, 0.2 µm-filtered, conditioned, and adjusted to 0.25% (v/v) polysorbate 20. Conditioning comprised absorbance measurement at 280 nm using a NanoDrop 2000c UV/Vis spectrometer (Thermo Fisher Scientific Inc., Waltham, US) and dilution to a target absorbance with lysis buffer to ensure consistent HBcAg VLP content across centrifugation-based and CFF-based experiments.

5.2.2 Centrifugation-Based Re-Dissolution Screening

A centrifugation-based procedure was employed for the re-dissolution screening, comprising precipitation, washing, re-dissolution, and recovery steps. In previous capture studies, selective precipitation of the HBcAg VLP studied herein is achieved by the addition of 1.1 M AMS [52, 90, 201]. To resolve the VLP re-dissolution dynamics within the range of 1.1 M to 0 M AMS based on identical experimental conditions, both preceding process steps precipitation and wash were performed individually and parallelized in small-scale reaction tubes.

Precipitation was conducted by adjusting 500 µL conditioned clarified lysate to 1.1 M AMS. After incubation in an overhead shaker LD-79 (Labinco, Breda, NL) for 30 min at 10 rpm, precipitates were spun down in a HeraeusPico 17 tabletop centrifuge (Thermo Electron LED GmbH, Osterode am Harz, DE) at 17000 rcf for 3 min and precipitate supernatants ($Prec_S$) were removed. Precipitates were manually re-suspended in 500 µL wash buffer, incubated at 300 rpm in a thermo-shaker ThermoMixer Comfort (Eppendorf, Hamburg, DE) for 150 min, and centrifuged using identical settings. The wash supernatants ($Wash_S$) were replaced by in total 500 µL, containing a proportional mixture of wash and re-dissolution buffer, to span the precipitant concentration range from 1.1 M to 0 M AMS in 0.1 M increments intending to mimic buffer exchange during CFF-based re-dissolution. Re-dissolution supernatants ($Red_{S,i}$) were recovered after incubation and centrifugation with identical settings. To ascertain full VLP recovery, all pellets of the re-dissolution conditions were manually re-suspended in 500 µL re-dissolution buffer, incubated, and centrifuged for supernatant recovery ($Rec_{S,0}$). Conditioned clarified lysate and all supernatants were analyzed by SDS-PAGE and HPLC control runs. Analysis by size-exclusion chromatography (SEC)-HPLC was exclusively performed for the supernatants of the re-dissolution and recovery steps.

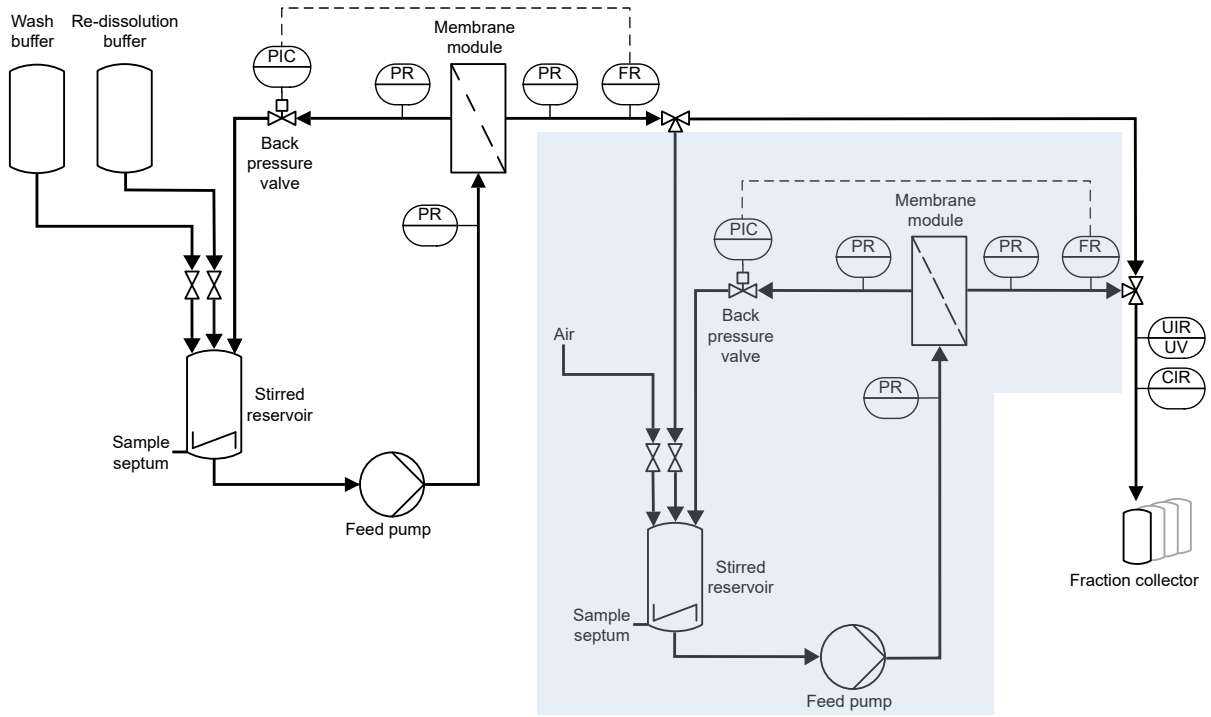

Figure 5.2 Piping and instrumentation diagram of the CFF set-up for precipitation-based capture by constant-volume DF. In addition to the piping used for consecutive wash and re-dissolution of the precipitated product (*ssCFF*), a second membrane stage was included before permeate fractionation for the *dsCFF* set-up, as highlighted in blue. Membrane modules with 2 µm and 300 kDa MWCO were used in the first and second membrane stages, respectively. After re-dissolution in the *dsCFF* process, the permeate of the first stage was closed to further concentrate the product by UF in the second stage. C, conductivity or control; F, flow rate; I, indicate; P, pressure; R, record; U, multivariate; UV, ultraviolet. Adapted from Hillebrandt et al. [88].

5.2.3 CFF-Based Set-Ups and Processing

For the *ssCFF* process, the CFF set-up relies on the set-up proposed by Hillebrandt et al. [88] with minor modifications. The set-up consisted of a KrosFlo Research KRIIi CFF system with an automatic backpressure valve (Spectrum Labs, Rancho-Dominguez, US), a 0.2 µm Hydrosart membrane with a filtration area of 200 cm^2 clamped in the corresponding membrane holder, and a stirred reservoir (all Sartorius Stedim Biotech GmbH, Göttingen, DE). The permeate outlet equipped with a Sensirion Liquid Flow Meter SLS-1500 (Sensirion AG, Stäfa, CH) and connected to an ÄKTA Start (Cytiva, Uppsala, SE) served as the set-up for permeate flow control, in-line ultraviolet (UV) and conductivity measurements, and permeate fractionation. For the *dsCFF* process, a similar, second CFF set-up was inserted between the one described above and the ÄKTA Start. Here, a 300 kDa MWCO Hydrosart membrane (200 cm^2, Sartorius Stedim Biotech GmbH) was implemented. Figure 5.2 displays a detailed piping and instrumentation diagram with the second CFF set-up highlighted in blue. The permeate flow rate of the first membrane stage was automatically controlled by the backpressure valve controller, using the permeate flow rate data of the flow meter as input along with a custom-written communication MATLAB 2018b script (The Mathworks, Natick, MA, United States), while the one of the second membrane stage was maintained by manual valve control.

The integrated processes include the steps precipitation, washing of the precipitate by a first DF step (DFI), product re-dissolution by a second, consecutive DF step (DFII), and – only in the *dsCFF* process – product concentration by UF (cf. Fig. 5.1). Precipitation of the conditioned clarified lysate was conducted by slow, step-wise pipetting of 4 M AMS stock solution under stirred conditions in the reservoir. At a final concentration of 1.1 M AMS, the solution was incubated for 30 min. All constant-volume DF steps were conducted with 25 mL diafiltration volume (DV) for six DV, a feed flow rate of 30 mL min^{-1}, and a permeate flow rate of 2 mL min^{-1}. The first DF step (DFI) for washing the VLP precipitate was performed with wash buffer and the wash permeate was collected as 15 mL fractions at the ÄKTA Start. The second DF (DFII) for VLP re-dissolution was performed with the re-dissolution buffer and the permeate fraction size was set to 5 mL or 12.5 mL fractions for the *ssCFF* or *dsCFF* process, respectively. During the *dsCFF* process, retentate samples were taken through an injection plug (Fresenius Kabi, Bad Homburg, DE) every DV. After DF for re-dissolution in the *dsCFF* process, the first CFF set-up was disconnected and the remaining retentate in the second membrane stage was concentrated by UF by a factor of 2.5 to a final retentate volume of approximately 10 mL. Samples were taken from the retentates of the 0.2 µm-membrane after the precipitation, wash, and re-dissolution, and from the final retentate of the 300 kDa MWCO membrane after UF. After the processes and the removal of the retentates from both CFF systems, both were each flushed with 10 mL re-dissolution buffer at 50 mL min^{-1} to recover the residual product.

5.2.4 Analytics

Raman spectroscopy provided spectral data to quantify AMS. All Raman measurements were conducted offline using a BioReactor BallProbe (MarqMetrix, Seattle, US) inserted into the FlowCell Adapter (MarqMetrix) coupled to a HyperFlux™ PRO Plus 785 with SpectralSoft 3.2.6 (Tornado Spectral Systems, Toronto, CA). The laser power and the exposure time were set to 495 mW and 175 ms, respectively. Spectra were recorded over the spectral range of 200 - 3300 cm^{-1} with a spectral resolution of 1 cm^{-1} and 50 acquisitions per spectrum. Raman spectra were averaged,

normalized at 3299 cm^{-1}, baseline-corrected, and filtered. Baseline correction was performed using a Whittaker filter employing the adaptive smoothness penalized least squares [202] with a λ of 6×10^7, a second-order difference matrix, and 1×10^{-3} tolerance. The spectra were smoothed using a Savitzky-Golay filter [203] with a second-degree polynomial and a window size of 11. A calibration curve created from a set of 12 reference solutions with varying AMS concentrations using the wavenumber 980 cm^{-1} was used to quantify AMS for samples derived from CFF-based processing.

SEC-HPLC was used to quantify differently sized species during VLP re-dissolution/recovery. A Dionex Ultimate 3000 RS UHPLC system (Thermo Fisher Scientific Inc.) was equipped with a BioSEC-5 column (4.6 × 300 mm, 5 μm, 1000 Å; Agilent, Santa Clara, US). SEC-HPLC was performed as previously described by Hillebrandt et al. [88] with 20 μL injection volume, 0.4 mL min^{-1} flow rate, and 14 min isocratic elution. Samples were either undiluted or diluted 10-fold and UV spectra were recorded in the wavelength range from 220 to 400 nm. A260/A280 derived from dividing peak areas at 260 nm (A260) by peak areas at 280 nm (A280). Protein concentrations were calculated from A280 using a theoretical Cp149 extinction coefficient of 1.764 g L^{-1} as provided by the ProtParam tool [204] and Beer's law.

HPLC control runs without a prefilter and column were performed with 10-, 20- or 40-fold diluted samples to assess total UV absorbance at 280 nm for all supernatants across all process steps.

Reduced SDS-PAGE served for quantitative protein analysis and samples were prepared with 50 mM DTT. NuPAGE™ LDS sample buffer, MES running buffer, and 4-12% BisTris Mini Protein Gels were sourced from Invitrogen (Carlsbad, US) and separation was performed on an XCell SureLock Mini-Cell from the same vendor. Protein bands on the gels were selectively stained using InstantBlue™ protein stain (US Biological, Salem, US).

5.3 Results

5.3.1 Re-Dissolution Screening Reveals Fast Re-Dissolution of VLPs and LMWS

Following VLP precipitation and precipitate wash at 1.1 M AMS, VLP re-dissolution was studied over the precipitant concentration range of 1.1–0 M AMS in a small-scale, centrifugation-based screening to mimic the buffer exchange during CFF-based processing.

Total UV absorbance values at 280 nm ($A280_C$) derived from HPLC control runs are shown upon normalization in Figure 5.3 (A), starting from clarified lysate through the supernatants from the precipitation, wash, re-dissolution, and recovery step. Slightly varying $A280_C$ but within constant ranges were observed for both precipitation (∼85%) and wash (∼6%) supernatants, as expected given the identical procedures and indicating soluble contaminants. The corresponding SDS-PAGE scans confirm that both supernatants mostly contain host-cell proteins since diverse protein bands are visible but without the protein band attributed to Cp149 (cf. Supporting Information: Figure A5.3). Additionally, mean A260/A280 ratios of 1.83 for the precipitation and 1.86 for the wash supernatant indicate the presence of host-cell nucleic acids in both supernatants.

For visual purposes, the observed re-dissolution dynamics during the re-dissolution and recovery steps are further resolved and illustrated as absolute $A280_C$ in Figure 5.3 (B). A dynamic re-dissolution

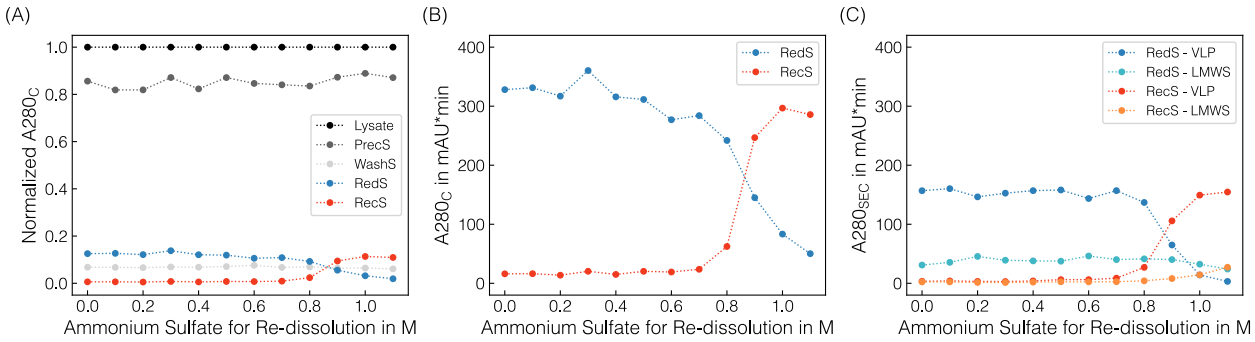

Figure 5.3 Centrifugation-based re-dissolution screening with AMS concentrations ranging from 1.1 to 0 M. Absorbance at 280 nm assessed by HPLC control runs $A280_C$ **(A), (B)** and derived from SEC-HPLC $A280_{SEC}$ **(C)** are shown as symbols with their respective assignment to the process step supernatants after centrifugation: precipitation at 1.1 M AMS (PrecS), wash at 1.1 M AMS (WashS), re-dissolution under varied AMS concentrations ranging from 1.1 to 0 M (RedS), and recovery at 0 M AMS (RecS). Dashed lines are illustrated only for visual purposes. Normalized $A280_C$ values **(A)** enable estimations of the distribution of all species originally present in the lysate across the individual process steps. For the re-dissolution and recovery step, absolute $A280_C$ values are presented in **(B)** and $A280_{SEC}$ values shown in **(C)** represent the individual proportions of VLP and LMWS.

behavior was observed within the range of 1.1–0.7 M AMS. Absorbance values from the recovery step, performed with solely AMS-free re-dissolution buffer, reflect the exact reverse trend, indicating effective VLP re-dissolution. Averaging $A280_C$ from both re-dissolution and recovery steps across the conditions, ∼13% species were re-dissolved (cf. Fig. 5.3 (A)). It has to be noted that residual pellets were visible in the reaction tubes upon final recovery accompanied by a discrepancy in $A260_C$ content, suggesting irreversibly precipitated host-cell nucleic acids (data not shown).

The re-dissolved species upon re-dissolution and recovery were separated and assessed by SEC-HPLC and the $A280_{SEC}$ courses are illustrated in Figure 5.3 (C). For $A280_{SEC,VLP}$, a similar trend as for the $A280_C$ (cf. Fig. 5.3 (B)) is observed reflecting the actual VLP re-dissolution behavior with 0.7–1.1 M AMS as dynamic range. However, VLP re-dissolution is accompanied by re-dissolution of other LMWS. These findings correspond with those from SDS-PAGE (cf. Supporting Information: Figure A5.3). Interestingly, approximately 50% of these LMWS already re-dissolve at 1.1 M AMS, which is representative of a second wash step and in turn resulted in the highest VLP purity upon recovery for the 1.1 M AMS condition. Furthermore, A260/A280 values below 0.65 indicate that the presence of proteins predominates over that of nucleic acids upon re-dissolution and recovery. Overall, a mean VLP recovery of 1.25 ± 0.05 mg per 500 µL conditioned clarified lysate was observed considering the $A280_{SEC,VLP}$ apart from the dynamic range.

Lastly, discrepancies were observed between $A280_C$ and the sum of $A280_{SEC,i}$ (cf. Fig. 5.3 (B),(C)) in terms of absolute absorbance values, suggesting the presence of species being even larger than VLPs and thus being retained in the SEC pre-column filter. The presumption that host-cell nucleic acids were present in the re-dissolution and recovery supernatants is underlined by the observed A260/A280 ratios ranging from 0.8 - 1.0 in the HPLC control runs and by their interferences at 280 nm which might contribute to the observed $A280_C$.

In summary, the re-dissolution screening provides insights into the VLP re-dissolution dynamics and the content of simultaneously present LMWS, while also indicating irreversibly precipitated host-cell nucleic acids. The re-dissolution of VLPs in the upper precipitant range suggests fast re-dissolution during CFF-based processing, accompanied by significant residual precipitant content.

5.3.2 Dual-Stage CFF Isolates and Concentrates VLP

The VLP precipitation and the CFF-based wash by DF were reproducibly performed and allowed for efficient contaminant removal as further presented in Supporting Information Section A5, providing a consistent basis for the subsequent, second DF for VLP re-dissolution. The courses of VLP re-dissolution for both processes—the reference *ssCFF* and the novel introduced *dsCFF* process—are illustrated in Figure 5.4, with the resulting performance indicators summarized in Table 5.1.

For the *ssCFF* process, the buffer exchange into re-dissolution buffer enables the species to re-dissolve and pass through the 2 µm MF membrane for permeate fractionation while simultaneously, aggregated or irreversibly precipitated species are retained. In general, the VLP concentration in the permeate fractions increases sharply at the beginning and then decreases steadily from approximately 0.75 DV onwards throughout the entire process, whereas the proportion of LMWS continuously decreases (cf. Fig. 5.4 (A)). For LMWS, a mean A260/A280 of 1.15 indicates a considerable amount of both host-cell proteins and nucleic acids. Raman spectral analysis revealed the decrease in AMS through buffer exchange following the typical constant-volume DF principle (cf. Fig. 5.4 (C)). The in-line recorded UV and conductivity data from the permeate depicted in Supporting Information: Figure A5.4 (B) qualitatively exhibit the same trends as the off-line SEC and Raman data derived from the permeate fractions, respectively. As expected from the re-dissolution screening, the VLPs re-dissolve fastly (cf. Sec. 5.3.1), and the highest VLP concentrations were found in the permeate fractions 3 to 5 corresponding to 0.5–1 DV. However, these permeate fractions are accompanied by LMWS being present as well as relatively high AMS concentrations of 0.6–0.8 M AMS. Alternative pooling strategies consistently trade off one characteristic for another. The final data, achieved by pooling all VLP-containing permeate fractions, are highlighted by gray bars (cf. Fig. 5.4 (A), (C)) and listed in Table 5.1 (*ssCFF*). The accumulated permeate volume of 145 mL with a VLP concentration of 0.39 g L^{-1} still exhibits 0.22 M AMS and LMWS contaminants, leading to a purity of 73 %. It has to be noted that the purity might have been increased by extending the wash step beforehand. However, the delayed decline in 280 nm absorbance of LMWS between 0.5–0.7 DV (cf. Fig. 5.4 (A)) still indicates prior precipitated and re-dissolved LMWS shortly before or simultaneously to VLPs. This finding aligns once again with the outcome of the re-dissolution screening, where a similar LMWS re-dissolution behavior was found (cf. Sec. 5.3.1). Overall and despite the limitations in product dilution, product purity, AMS depletion, and alternative pooling strategies, the *ssCFF* process is applicable for VLP constructs requiring a considerably high amount of AMS for precipitation.

The *ssCFF* set-up serves as the foundation for the *dsCFF* set-up (cf. Fig. 5.1), where an additional 300 kDa MWCO membrane stage is introduced between permeate outlet and fractionation (cf. Fig. 5.2). Next to the ability to separate re-dissolved species from aggregated or irreversibly precipitated species in the first stage, the set-up enables the integrated isolation of VLPs in the second stage retentate by depleting precipitant and contaminants.

The VLP concentration increases continuously through DF with the greatest increase within the first two DV, while the LMWS concentration starts to decrease again after the first DV (cf. Fig. 5.4 (B)). The depletion of the precipitant AMS follows the same pattern as the depletion of LMWS (cf.

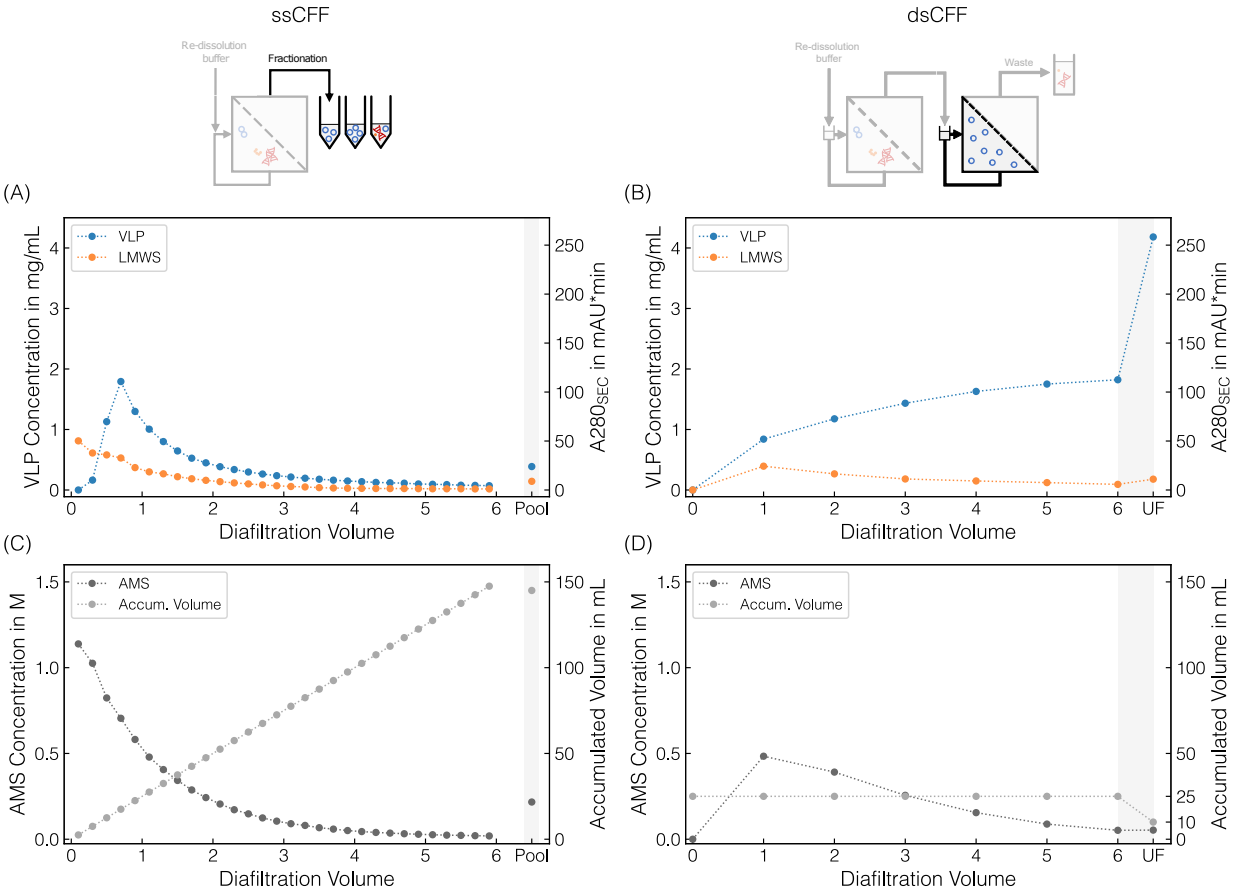

Figure 5.4 Comparison of *ssCFF* and *dsCFF* processes. SEC-derived VLP concentration and 280 nm absorbance of LMWS are displayed against DV for the *ssCFF* process in **(A)** and *dsCFF* process in **(B)**. In **(C)**, **(D)**, the corresponding Raman-derived AMS concentration and the accumulated product volume are shown. For visual purposes, the data points are connected with dashed lines. Data points from the *ssCFF* process **((A), (C))** derived from product-containing permeate fractionations in 5 mL scale. The final data by pooling all VLP-containing fractions are shaded with gray bars (Pool). Data points from the *dsCFF* process **((B), (D))** were obtained by sampling at each DV of the product-containing retentate in the second membrane stage. The *dsCFF* set-up allowed for integrated UF of this second-stage retentate, highlighted with gray bars (UF).

Fig. 5.4 (B), (D)). LMWS and AMS passed through the second stage membrane, which was further supported by SEC/SDS-PAGE and Raman analysis of the permeate fractions (data not shown). To enable this integrated process step, the second membrane stage was rinsed with 1 DV (25 mL) of re-dissolution buffer beforehand, and through constant-volume DF, the total volume remained at 25 mL (cf. Fig. 5.4 (D)). After six DV (cf. Table 5.1, $dsCFF_{\mathrm{DF}}$), a purity of 94.5% was achieved and AMS could be reduced to 0.05 M. It has to be noted that both purity and AMS depletion could have been further improved by further extending this DF step. The progression of integrated UF of the second stage retentate (cf. Table 5.1, $dsCFF_{\mathrm{DF/UF}}$) is highlighted with gray-shaded bars for visual clarity in Figure 5.4 (B), (D). A VLP concentration by a factor of 2.3 was observed through

Table 5.1 Overview of final *ssCFF* and *dsCFF* process data. For the *dsCFF* process, data were evaluated at different stages of the process: after DF for six DV (DF), after UF (DF/UF), and after a flushing procedure of the second membrane stage (DF/UF*). VLP concentration, purity, and relative VLP recovery derived from SEC. The relative VLP recovery is relative to the *ssCFF* process. The A260/A280 was determined by HPLC control runs. Raman-derived spectral data were used for AMS quantification. For each column, values representing the best conditions are highlighted in bold.

	VLP concentration	**Purity**	**A260/A280**	**AMS concentration**	**Relative VLP recovery**
	$g\,L^{-1}$	%	-	M	%
$ssCFF_{Pool}$	0.39	73.0	0.81	0.22	100
$dsCFF_{DF}$	1.82	94.5	0.73	0.05	81
$dsCFF_{DF/UF}$	4.18	**95.3**	**0.72**	0.05	74
$dsCFF_{DF/UF*}$	**5.04**	94.8	0.73	**0.04**	**90**

the 2.5-fold reduction of the retentate volume, while AMS was further depleted. Interestingly, and contrary to the assumption that the depletion of LMWS might also continue almost unhindered, the LMWS concentration significantly increased during UF. As a result, only a marginal improvement of less than 1% in purity was observed. Given the relatively small process volume compared to the CFF system and membrane area, a flush with 10 mL of re-dissolution buffer was performed to maximize the recovery of remaining deposits on the retentate side of the second membrane stage. Theoretical values are summarized in Table 5.1, $dsCFF_{DF/UF*}$. A VLP concentration of $4.5\,g\,L^{-1}$ is accompanied by slightly lower purity and residual AMS, whereas the recovered VLP significantly increased to 90%. Despite the VLP recovery being increased by the flushing procedure, it is still lower than in the *ssCFF* process.

The reproducibility of the re-dissolution processes (cf. Supporting Information: Section A5) allows for a comparison of both. Compared to the *ssCFF* process, the *dsCFF* process achieved a reduction of residual AMS by a factor of 4, a depletion of LMWS by a factor of 8, and a 13-fold VLP concentration. In summary, the *dsCFF* set-up using a 2 µm/300 kDa MWCO membrane configuration successfully integrated VLP isolation and concentration simultaneously to the CFF-based re-dissolution, which was not given by the *ssCFF* set-up.

5.4 Discussion

5.4.1 Screening of Solubility-Driven Processes

In solubility-driven processes, it is crucial to study the product behavior and the behavior of its contaminants under all process conditions. Although precipitation or crystallization are frequently screened processes for various biological molecules [89, 205–209], their re-dissolution behavior has been rarely studied. In the scope of transferring the centrifugation-based VLP precipitation/wash/re-dissolution process to a CFF-based process for buffer exchange, the VLP re-dissolution screening was designed to unveil the re-dissolution dynamics across a range of precipitant concentrations. Studies with a similar screening objective, mimicking a process by resolving the additive concentrations, have been reported for fed-batch VLP precipitation [88, 201] or evaporative protein crystallization [207],

among others. Such screenings allow for estimations of the applicability and limitations of the actual process.

For VLP precipitation, quasi-instantaneous changes upon setting the precipitant condition were observed, which is consistent with observations from a chimeric HBcAg VLP [88] or other truncated wild-type HBcAg VLPs with variations of the nucleic acid binding regions [52]. Comparing the VLP precipitation behavior [201] with the here screened re-dissolution behavior, the dynamic range is within the same precipitant concentrations, hence the respective sigmoidal curves exhibit inverse behavior. This VLP re-dissolution in the higher precipitant range indicates early re-dissolution during CFF-based buffer exchange, along with a substantial amount of residual precipitant. Further, slight co-precipitation and co-re-dissolution of LMWS reduce the selectivity of VLP precipitation, thereby diminishing the purity of the recovered product.

Especially in solubility-driven processes of biological molecules, aggregated or irreversibly precipitated species may form which cannot be recovered. As in our case, indications for irretrievable host-cell nucleic acids emphasize the need for employing separation techniques such as centrifugation, which is considered the standard procedure, or filtration [88]. Overall and in the scope to resolve phase behavior, it is necessary to set the screening conditions individually for fast reactions such as VLP precipitation, or for slower, rather uncontrollable reactions over time such as VLP re-dissolution after precipitate compaction.

5.4.2 Integrated Dual-Stage CFF for VLP Re-dissolution, Isolation, and Concentration

Applying CFF-based processing, selective VLP precipitation is followed by a first DF step for washing the VLP precipitates. The methodology of washing the precipitate using an MF membrane originates from Venkiteshwaran et al. [102], with further innovative contributions enabling product concentration [103], sequential processing [104], or intensified washing using serial MF membranes [105, 106]. Using constant-volume DF, the wash buffer requires the same precipitant concentration as used for precipitation to ensure that the precipitate remains in its precipitated form. In the scope of selective precipitation, the species that remain soluble are considered contaminants to be removed by depletion through the membrane. Generally, a sufficiently long wash step is expected to result in higher purities than centrifugation-based processing, as interstitial pellet liquid is circumvented [104]. To further investigate residual contaminant handling during the second DF step comparing the *ssCFF* and *dsCFF* set-ups, the wash was conducted for a fixed number of DV instead of continuing until the in-line UV signal in the permeate fell below a desired, small enough arbitrary unit as done by Hillebrandt et al. [88]. As a result, a tiny portion of contaminants remained in the retentate. Although Hillebrandt et al. [88] performed an adequate wash step, they also observed insufficient removal of host-cell nucleic acids.

The benefits of employing an MF membrane for integrated, CFF-based precipitate wash with a subsequent, second DF step for VLP re-dissolution have been thoroughly examined by Hillebrandt et al. [88]. Buffer exchange facilitates the re-dissolution of VLP precipitates, allowing the VLPs to pass through the MF membrane. In short, preventing pellet compaction and interstitial pellet liquid leads to faster re-dissolution [88, 104], thereby increasing relative productivity. However, the re-dissolution process by DF results in re-dissolved VLPs present in a highly diluted form accompanied by residual precipitant in the permeate fractions owing to the previous wash step.

Further, co-re-dissolved LMWS can not be handled using the *ssCFF* set-up. Overall, the application of the *ssCFF* set-up requires highly selective precipitation of the target product, while the dilution through DF and the presence of residual precipitant and LMWS remain insufficiently addressed. Consequently, we confirmed the predictions provided by the re-dissolution screening on a small scale about the applicability of the process for our VLP construct. For other biological molecules, such screenings may help verify the conditions for applicability.

Applying the *ssCFF* set-up would require a pooling strategy and sequential processing steps, only achievable through manual intervention. These steps would involve an intermediate UF for volume reduction, DF for residual precipitant and LMWS depletion, and final UF for setting a target product concentration, resulting in a significant drop in productivity. Further and especially in larger scales, this additional intermediate UF step subjects the product to a prolonged processing time. The integrated *dsCFF* set-up using a 2 µm/300 kDa MWCO membrane configuration allows constant-volume buffer exchange by DF followed by product concentration through subsequent UF, hence skipping the intermediate UF step and maintaining high productivity. Similar strategies isolating the target product have been reported using two UF membrane stages [196–199], while Cuddington et al. [200] also used an integrated MF/UF membrane configuration. However, these processes describe simple isolation based on size and do not involve changes in phase behavior.

During the *dsCFF* process, the VLPs are isolated and concentrated in the second stage retentate, while the precipitant and other LMWS are depleted. Moreover, the product volume stays constant, and further concentration of the product by subsequent UF enables the setting of a target product concentration. The depletion of contaminants significantly broadens the applicability of the process, making it applicable for biological molecules where precipitation is not highly selective and contaminants co-re-dissolve. Further, effectively addressing precipitant depletion may allow for potential recycling, marking a major advancement toward sustainability.

Throughout UF, a constant concentration of the depleting species in the retentate would have been expected for unhindered depletion. In contrast to the nearly unhindered depletion of the small solute AMS, the LMWS content increased through UF, resulting from a slower depletion than concentration process, which may be attributed to the electrostatic exclusion of proteins [36]. However, the solute-specific selectivity of pressure-driven membrane processes might also be diminished by high concentrations of solutes. Next to concentration polarization describing restricted solvent flux mainly through protein concentration near the membrane surface, proteins also tend to deposit on membrane surfaces, as these are susceptible to fouling [36]. The membrane surface in the *dsCFF* process is doubled compared to the *ssCFF* process, and hence the surface for deposition as well. The authors suggest that lower VLP recoveries for all evaluated *dsCFF* steps than for the *ssCFF* process are attributable to fouling and system deposits. After DF/UF, the best results in the purity, A260/A280, and residual AMS content were achieved, while a drop in relative VLP recovery was observed. This drop in relative VLP recovery may partly be attributed to VLP deposition on the second-stage membrane surface through concentration, as higher concentrated products tend even more to fouling [36]. Flushing the membrane and system with fresh buffer recovers soluble species from the membrane surface, tubing, and reservoir. A relative VLP recovery of 90% could be achieved with higher VLP concentrations and only minor compromises in purity. Product recovery can generally be optimized through reductions of relative membrane accumulations by processing larger volumes or using optimized surface areas.

In the scope of providing a proof of concept for integrated, automated processing applying the innovative *dsCFF* set-up and to illustrate its versatility, the process was not optimized in terms of transmembrane flux to enhance productivity, membrane surface to product volume/concentration to improve relative VLP recovery, or DV to increase purity. The here performed CFF processes were designed to allow for permeate fractionation by controlling the permeate flow rate to $2\,\mathrm{ml\,min^{-1}}$, enabling full characterization of the process. The transmembrane pressures ranged between 0.01–0.03 bar in all processes with feed pressures up to 0.3 bar. Such relatively high back-pressure on the permeate side is unusual in CFF processes but attributable to the used permeate capillaries small in diameter, necessary to combine a traditional CFF unit with an ÄKTA system for recording in-line signals and enabling permeate fractionation. When transferring the here presented *dsCFF* process to larger scales, an abandonment of the set-up for permeate fractionation allows for further optimizations in the process operating parameters transmembrane flux and membrane surface area.

5.4.3 Versatility of Dual-Stage CFF

The innovative, integrated *dsCFF* set-up using an MF/UF membrane configuration may serve as a valuable platform for diverse advancements.

First, it may be applied for precipitation-based capture and purification processes of other biological molecules such as monoclonal antibodies or viral vectors under the premise that the second membrane MWCO is adjusted to retain the target product selectively. The simultaneous depletion of precipitant and contaminants allows the set-up application even for (i) biological molecules requiring high precipitant concentrations for precipitation and (ii) processes with contaminant co-precipitation/-re-dissolution. Further, these processes could be even more optimized for productivity by shortening the wash step beforehand. Second, the integrative design of a *dsCFF* set-up may be transferable to other phase behavior-dependent processes than precipitation such as dis- and reassembly of VLPs. Lining up several membrane configurations, VLPs could be captured, purified, disassembled, reassembled, and formulated solely CFF-based and fully integrated. Third, developing integrated, robust platform processes is one of three key requirements for transitioning toward continuous bioprocessing of VLPs, alongside developing customized unit operations and real-time monitoring tools [210]. The importance of process integration for continuous processing of biopharmaceuticals is further emphasized by Gerstweiler et al. [211], providing a detailed overview of chromatographic and several non-chromatographic approaches, including precipitation and filtration. Building upon the studies by Burgstaller et al. [105] and Recanati et al. [106], which have already demonstrated continuous precipitation and washing of precipitates for monoclonal antibodies, the integrated *dsCFF* set-up proposed here may serve as a valuable process extension for further continuous precipitate processing in terms of the product re-dissolution, isolation, and concentration. Based on precipitation and filtration technologies, implementing such a continuous VLP capture and purification process could offer a beneficial alternative to fully chromatography-based purification processes of VLPs, such as the fully integrated, continuous capsid protein purification by flow-through anion-exchange and periodic counter-current b&e multimodal chromatography of the modular murine polyomavirus major capsid [212].

In summary, this study significantly contributes toward standardized platform processing through solely size-selective separation techniques precipitation and filtration, thereby broadening the

concept's applicability to diverse biological molecules, extraordinary process conditions, other phase behavior-dependent processes, and continuous processing.

5.5 Conclusion and Outlook

In conclusion, we present an innovative *dsCFF* set-up for integrated VLP capture and purification using a 2 µm/300 kDa MWCO membrane configuration. Through CFF-based processing, selective VLP precipitation is followed by a first DF step for washing the VLP precipitates and a second DF step for VLP re-dissolution. Here, a fast re-dissolution of the VLPs accompanied by a high residual precipitant load and co-re-dissolved contaminants was suggested by a small-scale, centrifugation-based screening. Due to the nature of DF, the reference *ssCFF* process further led to re-dissolved VLPs present in a highly diluted form in the permeate. Both observed limitations—product purity and concentration—are addressed by the *dsCFF* set-up with an MF/UF membrane configuration. Along with VLP re-dissolution and their passage through the MF membrane, the integrated second membrane stage successfully enabled VLP isolation by simultaneous removal of contaminants and precipitant, as well as VLP concentration by subsequent UF. Hence, the *dsCFF* set-up integrates further polishing of the product pool into one unit operation while maintaining higher productivity compared to sequential unit operations. In comparison to the *ssCFF*-derived product pool, the proposed *dsCFF* set-up facilitates 13-fold product concentration, the reduction of residual precipitant by a factor of 4, and the depletion of contaminants by a factor of 8. The *dsCFF* setup's ability to deplete the precipitant could enable precipitant recycling, marking an additional advancement toward enhanced sustainability. Overall, the developed integrated *dsCFF* set-up provides a foundation for standardized platform processing exclusively based on size-selective separation techniques and bears the potential to be applied to diverse biological molecules, extraordinary process conditions, other phase behavior-dependent processes, and even continuous processing.

Author Contributions

Annabelle Dietrich: conceptualization, methodology, investigation, software, formal analysis, visualization, writing–original draft, writing–review and editing. **Luca Heim**: investigation, software, formal analysis, writing-–review and editing. **Jürgen Hubbuch**: conceptualization, supervision, funding acquisition, writing–-review and editing.

Erratum

Appendix **A5** contains the Erratum to "Dual-Stage Cross-Flow Filtration: Integrated Capture and Purification of Virus-Like Particles" associated with this chapter.

Supporting Information

Appendix **A5** contains the Supporting Information associated with this chapter.

Chapter References

[4] Y. H. Chung, H. Cai, and N. F. Steinmetz. „Viral nanoparticles for drug delivery, imaging, immunotherapy, and theranostic applications“. In: *Advanced Drug Delivery Reviews* 156 (2020), pp. 214–235. DOI: 10.1016/j.addr.2020.06.024.

[11] C. L. Effio and J. Hubbuch. „Next generation vaccines and vectors: Designing downstream processes for recombinant protein-based virus-like particles“. In: *Biotechnology Journal* 10.5 (2015), pp. 715–727. DOI: 10.1002/biot.201400392.

[13] N. Hillebrandt and J. Hubbuch. „Size-selective downstream processing of virus particles and non-enveloped virus-like particles“. In: *Frontiers in Bioengineering and Biotechnology* 11 (2023). DOI: 10.3389/fbioe.2023.1192050.

[36] R. van Reis and A. Zydney. „Bioprocess membrane technology“. In: *Journal of Membrane Science* 297.1-2 (2007), pp. 16–50. DOI: 10.1016/j.memsci.2007.02.045.

[39] B. Chackerian. „Virus-like particles: Flexible platforms for vaccine development“. In: *Expert Review of Vaccines* 6.3 (2007), pp. 381–390. DOI: 10.1586/14760584.6.3.381.

[43] S. Nooraei et al. „Virus-like particles: preparation, immunogenicity and their roles as nanovaccines and drug nanocarriers“. In: *Journal of Nanobiotechnology* 19.1 (2021), p. 59. DOI: 10.1186/s12951-021-00806-7.

[49] A. Zlotnick et al. „Dimorphism of Hepatitis B Virus Capsids Is Strongly Influenced by the C-Terminus of the Capsid Protein“. In: *Biochemistry* 35.23 (1996), pp. 7412–7421. DOI: 10.1021/bi9604800.

[52] A. Valentic, J. Müller, and J. Hubbuch. „Effects of Different Lengths of a Nucleic Acid Binding Region and Bound Nucleic Acids on the Phase Behavior and Purification Process of HBcAg Virus-Like Particles“. In: *Frontiers in Bioengineering and Biotechnology* 10 (2022). DOI: 10.3389/fbioe.2022.929243.

[56] A. Zeltins. „Construction and Characterization of Virus-Like Particles: A Review“. In: *Molecular Biotechnology* 53.1 (2013), pp. 92–107. DOI: 10.1007/s12033-012-9598-4.

[57] M. G. Moleirinho, R. J. Silva, P. M. Alves, M. J. T. Carrondo, and C. Peixoto. „Current challenges in biotherapeutic particles manufacturing“. In: *Expert Opinion on Biological Therapy* 20.5 (2020), pp. 451–465. DOI: 10.1080/14712598.2020.1693541.

[81] S. Tsoka, O. C. Ciniawskyj, O. R. T. Thomas, N. J. Titchener-Hooker, and M. Hoare. „Selective Flocculation and Precipitation for the Improvement of Virus-Like Particle Recovery from Yeast Homogenate“. In: *Biotechnology Progress* 16.4 (2000), pp. 661–667. DOI: 10.1021/bp0000407.

[82] T. Koho et al. „Purification of norovirus-like particles (VLPs) by ion exchange chromatography“. In: *Journal of Virological Methods* 181.1 (2012), pp. 6–11. DOI: 10.1016/j.jviromet.2012.01.003.

[83] H. J. Kim, S. Y. Kim, S. J. Lim, J. Y. Kim, S. J. Lee, and H. J. Kim. „One-step chromatographic purification of human papillomavirus type 16 L1 protein from Saccharomyces cerevisiae“. In: *Protein Expression and Purification* 70.1 (2010), pp. 68–74. DOI: 10.1016/j.pep.2009.08.005.

[84] M. Zahin et al. „Scalable production of HPV16 L1 protein and VLPs from tobacco leaves“. In: *PLoS ONE* 11.8 (2016), pp. 1–16. DOI: 10.1371/journal.pone.0160995.

[85] A. Kazaks et al. „Production and purification of chimeric HBc virus-like particles carrying influenza virus LAH domain as vaccine candidates“. In: *BMC Biotechnology* 17.1 (2017), pp. 1–11. DOI: 10.1186/s12896-017-0396-8.

[88] N. Hillebrandt, P. Vormittag, N. Bluthardt, A. Dietrich, and J. Hubbuch. „Integrated Process for Capture and Purification of Virus-Like Particles: Enhancing Process Performance by Cross-Flow Filtration“. In: *Frontiers in Bioengineering and Biotechnology* 8 (2020). DOI: 10.3389/fbioe.2020.00489.

[89] S. Großhans, S. Suhm, and J. Hubbuch. „Precipitation of complex antibody solutions: influence of contaminant composition and cell culture medium on the precipitation behavior“. In: *Bioprocess and Biosystems Engineering* (2019). DOI: 10.1007/s00449-019-02103-y.

[90] C. H. Wegner and J. Hubbuch. „Calibration-free PAT: Locating selective crystallization or precipitation sweet spot in screenings with multi-way PARAFAC models“. In: *Frontiers in Bioengineering and Biotechnology* 10 (2022), pp. 1–18. DOI: 10.3389/fbioe.2022.1051129.

[101] T. Vicente, S. Burri, S. Wellnitz, K. Walsh, S. Rothe, and J. Liderfelt. „Fully aseptic single-use cross flow filtration system for clarification and concentration of cytomegalovirus-like particles“. In: *Engineering in Life Sciences* 14.3 (2014), pp. 318–326. DOI: 10.1002/elsc.201300093.

[102] A. Venkiteshwaran, P. Heider, L. Teysseyre, and G. Belfort. „Selective precipitation-assisted recovery of immunoglobulins from bovine serum using controlled-fouling crossflow membrane microfiltration“. In: *Biotechnology and Bioengineering* 101.5 (2008), pp. 957–966. DOI: 10.1002/bit.21964.

[103] M. Kuczewski, E. Schirmer, B. Lain, and G. Zarbis-Papastoitsis. „A single-use purification process for the production of a monoclonal antibody produced in a PER.C6 human cell line“. In: *Biotechnology Journal* 6.1 (2011), pp. 56–65. DOI: 10.1002/biot.201000292.

[104] N. Hammerschmidt, S. Hobiger, and A. Jungbauer. „Continuous polyethylene glycol precipitation of recombinant antibodies: Sequential precipitation and resolubilization“. In: *Process Biochemistry* 51.2 (2016), pp. 325–332. DOI: 10.1016/j.procbio.2015.11.032.

[105] D. Burgstaller, A. Jungbauer, and P. Satzer. „Continuous integrated antibody precipitation with two-stage tangential flow microfiltration enables constant mass flow“. In: *Biotechnology and Bioengineering* 116.5 (2019), pp. 1053–1065. DOI: 10.1002/bit.26922.

[106] G. Recanati et al. „Integration of a perfusion reactor and continuous precipitation in an entirely membrane-based process for antibody capture“. In: *Engineering in Life Sciences* 23.10 (2023), pp. 1–14. DOI: 10.1002/elsc.202300219.

[194] S. A. Kim et al. „Protein-based nanocages for vaccine development“. In: *Journal of Controlled Release* 353 (2023), pp. 767–791. DOI: 10.1016/j.jconrel.2022.12.022.

[195] C. Qian et al. „Recent Progress on the Versatility of Virus-Like Particles“. In: *Vaccines* 8.1 (2020), p. 139. DOI: 10.3390/vaccines8010139.

[196] B. Cheang and A. L. Zydney. „A two-stage ultrafiltration process for fractionation of whey protein isolate“. In: *Journal of Membrane Science* 231.1-2 (2004), pp. 159–167. DOI: 10.1016/j.memsci.2003.11.014.

[197] M. Nor, L. Ramchandran, M. Duke, and T. Vasiljevic. „Separation of bromelain from crude pineapple waste mixture by a two-stage ceramic ultrafiltration process“. In: *Food and Bioproducts Processing* 98 (2016), pp. 142–150. DOI: 10.1016/j.fbp.2016.01.001.

[198] M. Z. Nor, L. Ramchandran, M. Duke, and T. Vasiljevic. „Integrated ultrafiltration process for the recovery of bromelain from pineapple waste mixture“. In: *Journal of Food Process Engineering* 40.3 (2017), pp. 1–9. DOI: 10.1111/jfpe.12492.

[199] M. Z. M. Nor, L. Ramchandran, M. Duke, and T. Vasiljevic. „Performance of a Two-Stage Membrane System for Bromelain Separation from Pineapple Waste Mixture as Impacted by Enzymatic Pre-Treatment and Diafiltration“. In: *Food Technology and Biotechnology* 56.2 (2018), pp. 218–227. DOI: 10.17113/ftb.56.02.18.5478.

[200] C. T. Cuddington et al. „Pilot scale production and characterization of next generation high molecular weight and tense quaternary state polymerized human hemoglobin“. In: *Biotechnology and Bioengineering* 119.12 (2022), pp. 3447–3461. DOI: 10.1002/bit.28233.

[201] A. Dietrich, R. Schiemer, J. Kurmann, S. Zhang, and J. Hubbuch. „Raman-based PAT for VLP precipitation: systematic data diversification and preprocessing pipeline identification“. In: *Frontiers in Bioengineering and Biotechnology* 12 (2024), pp. 1–20. DOI: 10.3389/fbioe.2024.1399938.

[202] F. Zhang et al. „Baseline correction for infrared spectra using adaptive smoothness parameter penalized least squares method“. In: *Spectroscopy Letters* 53.3 (2020), pp. 222–233. DOI: 10.1080/00387010.2020.1730908.

[203] A. Savitzky and M. J. E. Golay. „Smoothing and Differentiation of Data by Simplified Least Squares Procedures.“ In: *Analytical Chemistry* 36.8 (1964), pp. 1627–1639. DOI: 10.1021/ac60214a047.

[204] E. Gasteiger et al. „Protein Identification and Analysis Tools on the ExPASy Server“. In: *The Proteomics Protocols Handbook* (2005), pp. 571–607. DOI: 10.1385/1-59259-890-0:571.

[205] K. Baumgartner et al. „Determination of protein phase diagrams by microbatch experiments: Exploring the influence of precipitants and pH“. In: *International Journal of Pharmaceutics* 479.1 (2015), pp. 28–40. DOI: 10.1016/j.ijpharm.2014.12.027.

[206] H. Huettmann, S. Zich, M. Berkemeyer, W. Buchinger, and A. Jungbauer. „Design of industrial crystallization of interferon gamma: Phase diagrams and solubility curves“. In: *Chemical Engineering Science* 126 (2015), pp. 341–348. DOI: 10.1016/j.ces.2014.12.018.

[207] M. Barros Groß and M. Kind. „From microscale phase screening to bulk evaporative crystallization of proteins“. In: *Journal of Crystal Growth* 498 (2018), pp. 160–169. DOI: 10.1016/j.jcrysgro.2018.06.010.

[208] Q. Gu, Z. Li, J. L. Coffman, T. M. Przybycien, and A. L. Zydney. „High throughput solubility and redissolution screening for antibody purification via combined PEG and zinc chloride precipitation“. In: *Biotechnology Progress* 36.6 (2020), pp. 1–14. DOI: 10.1002/btpr.3041.

[209] C. H. Wegner, I. Zimmermann, and J. Hubbuch. „Rapid Analysis for Multicomponent High-Throughput Crystallization Screening: Combination of UV-Vis Spectroscopy and Chemometrics“. In: *Crystal Growth and Design* 22.2 (2022), pp. 1054–1065. DOI: 10.1021/acs.cgd.1c00907.

[210] M. Mittal, M. Banerjee, L. H. Lua, and A. S. Rathore. „Current status and future challenges in transitioning to continuous bioprocessing of virus-like particles“. In: *Journal of Chemical Technology and Biotechnology* 97.9 (2022), pp. 2376–2385. DOI: 10.1002/jctb.6821.

[211] L. Gerstweiler, J. Bi, and A. P. Middelberg. „Continuous downstream bioprocessing for intensified manufacture of biopharmaceuticals and antibodies“. In: *Chemical Engineering Science* 231 (2021), p. 116272. DOI: 10.1016/j.ces.2020.116272.

[212] L. Gerstweiler, J. Billakanti, J. Bi, and A. P. J. Middelberg. „An integrated and continuous downstream process for microbial virus-like particle vaccine biomanufacture“. In: *Biotechnology and Bioengineering* 119.8 (2022), pp. 2122–2133. DOI: 10.1002/bit.28118.

6

Raman-Based PAT for VLP Precipitation: Systematic Data Diversification and Preprocessing Pipeline Identification

Annabelle Dietrich[1,*], Robin Schiemer[1,*], Jasper Kurmann, Shiqi Zhang, and Jürgen Hubbuch[1]

[1] Institute of Process Engineering in Life Sciences, Section IV: Biomolecular Separation Engineering, Karlsruhe Institute of Technology (KIT), Karlsruhe, Germany

[*] Contributed equally.

Abstract

Virus-like particles (VLPs) are a promising class of biopharmaceuticals for vaccines and targeted delivery. Starting from clarified lysate, VLPs are typically captured by selective precipitation. While VLP precipitation is induced by step-wise or continuous precipitant addition, current monitoring approaches do not support the direct product quantification, and analytical methods usually require various, time-consuming processing and sample preparation steps. Here, the application of Raman spectroscopy combined with chemometric methods may allow the simultaneous quantification of the precipitated VLPs and precipitant owing to its demonstrated advantages in analyzing crude, complex mixtures. In this study, we present a Raman spectroscopy-based process analytical technology (PAT) tool developed on batch and fed-batch precipitation experiments of Hepatitis B core Antigen VLPs. We conducted small-scale precipitation experiments providing a diversified data set with varying precipitation dynamics and backgrounds induced by initial dilution or spiking of clarified *Escherichia coli* (*E. coli*)-derived lysates. For the Raman spectroscopy data, various preprocessing operations were systematically combined allowing the identification of a preprocessing pipeline, which proved to effectively eliminate initial lysate composition variations as well as most interferences attributed to precipitates and the precipitant present in solution. The calibrated partial least squares (PLS) models seamlessly predicted the precipitant concentration with R^2 of 0.98 and 0.97 in batch and fed-batch experiments, respectively, and captured the observed precipitation trends with R^2 of 0.74 and 0.64. Although the resolution of fine differences between experiments was limited due to the observed non-linear relationship between spectral data and the VLP concentration, this study provides a foundation for employing Raman spectroscopy as a PAT sensor for monitoring VLP precipitation processes with the potential to extend its applicability to other phase-behavior dependent processes or molecules.

6.1 Introduction

VLPs as non-viral vectors have emerged as class of protein nanoparticles for vaccines, surface antigen presentation and targeted delivery [195]. VLPs are composed of viral protein subunits mimicking the structure of the virus they descend from [39, 56]. Since VLPs lack the active viral genome, they are considered safer than other viral nanoparticles such as adeno-associated virus or lentivirus [39, 43]. The recombinant production of VLPs in eukaryotic or prokaryotic cells [40] lead to process material of high variability and complexity, which is even more pronounced for intracellular production as a lysis step is required [11]. Hence, in early downstream processing (DSP), the removal of the majority of process-related host cell impurities is particularly advised [11]. Native precipitation was found highly selective for VLPs and is induced by addition of a precipitation agent, using either polyethylene glycol [81, 82] or ammonium sulfate (AMS) [83–85]. Whereas steric exclusion is typically associated with polyethylene glycol [213, 214], the effect of protein surface charge predominates for precipitation induced by AMS as sulphate is strongly kosmotropic [77]. The protein surface charge is in turn affected by its structural properties, which may impact the precipitation behaviour [215] and hence, the precipitation agent concentration required for precipitation.

The Hepatitis B core Antigen (HBcAg) VLP, a recombinantly produced internal protein capsid of the Hepatitis B virus, is subject to intensive research for diverse medical purposes [53–55, 65, 67, 68, 216]. In previous capture studies, the AMS-induced precipitation of HBcAg VLPs was found highly selective [52], while co-precipitation of impurities was only observed for higher

AMS concentrations [90]. Moreover, the required AMS concentration for precipitation was found to be dependent on the surface properties comparing HBcAg VLPs with and without foreign epitopes rather than on internal structural differences comparing various lengths of nucleic acid binding sites [52, 88]. In the context of process development, the conventional centrifugation-based HBcAg VLP capture has been replaced by an innovative setup involving fed-batch precipitation and diafiltration-based wash and redissolution steps [88]. This development aimed to establish a size-based platform process applicable to various protein nanoparticles. However, the development of a standardized platform process for protein nanoparticle DSP remains uncommon, primarily due to their extensive variety, which presents significant challenges in processing [57].

To be able to operate such a capture platform process for different protein nanoparticles, the implementation of PAT for process monitoring is crucial. Since 2004, the FDA has underscored the importance of real-time process monitoring for its role in enhancing process understanding, ensuring process robustness, and guaranteeing product safety within the biopharmaceutical industry [14, 112, 113]. Besides the optical spectroscopic techniques ultraviolet-visible (UV/Vis) and infrared (IR) spectroscopy, Raman spectroscopy coupled with chemometrics has found extensive applications in monitoring various processes for biopharmaceutical products, including raw material testing [217], cell culture [218–220], chromatography [221–223], filtration [137], freezing [138, 224], or formulation [225]. For VLPs in particular, recent studies demonstrated the real-time monitoring of a baculovirus cultivation for the production of rabies VLPs [133–135] as well as the cross-flow filtration-based polishing operations such as dis- and reassembly of the HBcAg-VLPs [16, 17]. Despite the broad applicability of spectroscopic methods in biopharmaceutical processing, their application to precipitation processes is rather unexplored. While multiple studies have used near-infrared (NIR) spectroscopy for monitoring of acid [226] or alcohol precipitation [227–229], Raman spectroscopy has only been used to track a precipitation polymerization reaction [230] and monoclonal antibody precipitation [18]. A major challenge when working with precipitate-containing solutions is the turbidity of the media, which was reported to affect the overall signal intensity of Raman spectra [230–232]. The loss in signal intensity may either be corrected by isolated Raman bands [230, 232] or be directly used for correlation to a target quality attribute [230]. Similarly, Zelger et al. [233] have used a turbidity sensor for monitoring protein precipitation, foregoing the molecular information that could have been attained through the utilization of spectroscopic techniques.

Among the available spectroscopic techniques, Raman spectroscopy stands out for its selectivity to monitor multiple quality attributes [223, 225, 234] as well as its capability to analyze complex solutions such as fermentation broths [218, 219, 235] or clarified cell lysates [236, 237]. However, Raman spectroscopy comes with a set of challenges, such as low signal intensity and strong background interferences requiring extensive data preprocessing and model optimization [139–141]. Due to this sensitivity, undesired data variability can arise by changes in process material or sample processing, compromising comparability and accuracy in the recorded data. Popular approaches for the removal of undesirable systematic variation include signal corrections, filtering, or variable selection [139, 141, 142]. Most commonly, baseline [202, 238], background [239–241], and scatter [242–244] correction methods are employed to eliminate interferences caused by contaminating species or scattering effects such as fluorescence or Mie scattering. Among those the most commonly applied algorithm is the orthogonal projection to latent structures (OPLS) as proposed by Trygg et al. [240], effectively removing systematic background variation not correlated with the target quality attribute [245, 246]. To further optimize model performance, additional steps like spectral

cropping, derivative filtering, or filter-based variable selection may be used [140, 234]. In principle, the sequence of preprocessing operations, or preprocessing pipeline, should be designed to remove irrelevant variations from the recorded data and provide the multivariate model with consistent information to enable robust and accurate real-time monitoring. Finally, a careful evaluation of the extracted information by the preprocessing pipeline and the selected multivariate model is demanded by the regulatory agencies [247]. For linear models, such as PLS, multiple approaches such as variable importance in projection (VIP)-based feature importance [142] have been proposed to perform this quality check.

In this study, we present a PAT approach based on Raman spectroscopy for a precipitation-based capture process of VLPs. Based on multiple small-scale precipitation experiments with material from various lysate batches and spiking materials, we evaluate the suitability of Raman spectroscopy for analyzing precipitate-containing lysates. By introducing a pretreatment strategy for the UV/Vis reference measurements and identifying a suitable preprocessing pipeline for Raman spectroscopy data, we demonstrate the reduction of variance in both the Raman and the reference data and enable the prediction of the precipitated VLPs from precipitate-containing lysates. We systematically combine numerous preprocessing operations and isolate the effects of the included operations on model performance. Eventually, we transfer this approach to a fed-batch precipitation process, ensuring its adaptability and effectiveness across different operational paradigms.

6.2 Materials and Methods

6.2.1 Experiments

6.2.1.1 Virus-Like Particles

In this study, Cp149, a C-terminally truncated wild-type HBcAg protein [49] was used, for which the plasmid was kindly provided by Prof. Adam Zlotnick (Indiana University, US). The intracellular expression of Cp149 in *E. coli*, cell harvest, cell lysis, and lysate clarification were conducted as previously described by Hillebrandt et al. [88]. Clarified lysate solutions (hereinafter termed lysate) were thawed, 0.2 µm-filtered, directly used raw or conditioned by dilution or spiking depending on the precipitation experiment, and adjusted to 0.25% (v/v) polysorbate 20.

To systematically diversify the lysate for the precipitation experiments, different lysate batches were used and initial lysate conditioning was performed by dilution and spiking for eight batch experiments B1-B8 and three fed-batch experiments F1-F3. Raw lysates of two lysate batches were used for batch experiments B1 and B4, while a third lysate batch served as lysate for all fed-batch experiments. Dilution of the lysates introduced further changes in initial lysate concentration (B2-B3, F1, F3), which is expressed as volume percent lysate content and was simply measured as 280 nm absorbance ($A280_L$) due to the lysates complexity.

To establish a foundation for systematic spiking, the initial composition of raw lysate was first estimated in pre-experiments (data not shown) to estimate a VLP content despite the lysates complexity. For this pre-experiment, selective VLP precipitation was conducted by adjusting raw lysate to 1.1 M AMS and the supernatant was analyzed by reference analytics. The difference between the ultraviolet (UV) absorbance at 280 nm of the initial lysate ($A280_L$) and the volume-corrected supernatant after precipitation ($A280_S$) account for the absorbance of selectively precipitated VLP ($A280_{VLP}$). The calculated ratio $A280_{VLP}/A280_L$ expressing the estimated VLP content resulted in

approximately 10% VLP present in the raw lysate. This ratio served as foundation for experimental spiking design under the assumption of purified VLP- or host-cell protein (HCP)-enriched spiking material. While the estimated VLP content with 10% remained constant using raw lysate (B1, B4) or during lysate conditioning by dilution (B2-B3, F1, F3) or spiking with salt (B8), the estimated VLP content was systematically varied by VLP- or HCP-spiking (B5-B7, F2). Note that spiking the lysates also resulted in a form of dilution; however, the primary focus was here on systematically adjusting the lysate composition. The final lysate conditioning settings of lysate batch, lysate content, and estimated VLP content are summarized for all batch experiments B1-B8 and fed-batch experiments F1-F3 in Table 1 and Table 2, respectively.

More details on preparation and composition of buffers, solutions, and VLP- and HCP-enriched spiking material are stated in Supplementary Sec. A6.

6.2.1.2 Batch Precipitation Experiments

Conditioned lysate varied in lysate batch, concentration or composition across the eight batch VLP precipitation experiments as summarized in Tab. 6.1. For each experiment, eleven solutions were prepared in 1040 µL-scale with precipitant concentrations in the range of 0 to 1.2 M AMS. In general, the solution compositions were designed to maximize the lysate content under the limitation of 4 M AMS stock solution to set the highest target AMS concentration of 1.2 M, resulting in 728 µL lysate and 312 µL 4 M AMS stock solution. Maintaining 728 µL lysate to prevent a dilution effect within the experiments in batch mode, the remaining 312µL was composed of proportionally 4 M AMS stock solution and ultrapure water to cover the other precipitant concentrations below 1.2 M AMS. Solutions were incubated at 22 °C on a thermo-shaker ThermoMixer Comfort (Eppendorf, Hamburg, DE) at 500 rpm for 30 min. For Raman measurements, 200 µL samples of the turbid precipitate solutions were taken and immediately analyzed. To enable measuring the particulate-free supernatants, the remaining turbid precipitate solutions were centrifuged at 12000 rcf for 8 min in a Pico 17 tabletop centrifuge (Thermo Fisher Scientific Inc., Waltham, US). The supernatants were analyzed via Raman spectroscopy and UV reference analytics.

Table 6.1 Overview of the eight batch precipitation experiments B1-B8 comprising parameters for initial lysate conditioning and the final, curve fit-derived, apparent concentration of precipitated VLPs.

Batch	**Condition**	**Lysate conditioning**			**Precipitated VLP**
		Batch	Lysate content	Estimated VLP content	
		-	% (v/v)	% ($A280_{VLP}/A280_{L}$)	$g\,L^{-1}$
B1	raw		100		4.35
B2	dilution	lysate 1	52.5	10	2.96
B3	dilution		35		2.06
B4	raw		100	10	3.92
B5	VLP spike		50	15	4.15
B6	VLP spike	lysate 2	50	13	4.16
B7	HCP spike		31	6	1.49
B8	NaCl spike		80	10	4.69

6.2.1.3 Fed-Batch Precipitation Experiments

The setup for fed-batch VLP precipitation consisted of a stirred reservoir equipped with a Minipuls 3 peristaltic pump (Gilson, Villiers le Bel, FR) for a 4 M AMS feed. For online monitoring, a second peristaltic pump (Gilson), a SLS-1500 flow meter (Sensirion), and a flow cell for Raman measurements were connected with PEEK capillaries with an inner diameter of 0.25 mm in an on-line loop. The on-line loop flow rate was adjusted to 1.4 mL/min. Fed-batch precipitation experiments were performed with 12 mL conditioned lysate. The lysate and processing conditions are listed in Table 6.2. During fed-batch precipitation, 200 µL samples were taken at each time step of in total 30 time steps, from which 22 selected samples were centrifuged at 12000 rcf for 3 min facilitating UV reference analytics of the supernatants. For each time step, lysate and AMS content were calculated considering drawn sample volume and a mean feed volume, which was based on a mean feed flow rate considering total AMS amount and feed density.

Table 6.2 Overview of the three fed-batch precipitation experiments F1-F3 comprising parameters for initial lysate conditioning and fed-batch processing. Lysate batch 3 was used for all experiments.

Fed-batch	**Condition**	**Lysate conditioning**		**Processing**	
		Lysate content % (v/v)	Estimated VLP content % ($A280_{VLP}/A280_{L}$)	Time min	Feed rate mL min^{-1}
F1	dilution	43	10	30	0.16
F2	VLP spike	32	23	30	0.16
F3	dilution	45	10	20	0.30

6.2.1.4 Raman Spectroscopy

The Raman BioReactor BallProbe inserted in the FlowCell Adapter (both MarqMetrix, Seattle, US) was connected to a HyperFlux™ PRO Plus 785 with the software SpectralSoft 3.2.6 (Tornado Spectral Systems, Toronto, CA). All measurements were performed in the flow cell with a laser power of 495 mW and with 50 acquisitions per spectrum. For precipitate and supernatant samples, the exposure time was set to 275 ms and 185 ms, respectively, as with precipitate being present, a higher exposure was necessary to achieve a similar intensity level due to the dampening effect of the precipitates in solution. The entire spectral range from 200 to 3300 cm^{-1} was recorded with a spectral resolution of 1 cm^{-1}. For each of the eleven AMS conditions per experiment, the 50 recorded Raman spectra were averaged. For the fed-batch experiments, the 50 recorded spectra closest to the sampling time point were averaged.

6.2.1.5 Reference Analytics

All supernatant samples were analyzed via UV spectroscopy with a high performance liquid chromatography (HPLC) system equipped with a RS diode array detector and controlled by Chromeleon 6.8 (Dionex Ultimate 3000 RS, Sunnyvale, US). A 0.5 µm pre-column filter catridge (OPTI-SOLV EXP, Supelco, Bellefonte, US) but no column was installed. A buffer containing 50 mM Tris, 100 mM NaCl at pH 8.0 was used as mobile phase with a flow rate of 50 µL min^{-1} and an injection volume of 20 µL. Samples were diluted 100-fold in triplicates in lysis buffer and UV spectra in the wavelength range from 220 to 400 nm were recorded.

6.2.2 Data Analysis and Computation

Data analysis and computation was performed in Python 3.8.

6.2.2.1 Reference Data Pretreatment

Several pretreatments steps for the UV reference data were conducted in order to transform the scattered data into reliable reference data for the chemometric modeling. The pretreatment comprised scatter correction, scaling, precipitation curve estimation, outlier removal, and a final conversion to the apparent precipitated VLP concentration. Scatter correction for the 280 nm peak areas (A280) was performed to remove nucleic acid contributions according to Porterfield et al. [248], whereas AMS content-dependent scatter correction was not required due to the 100-fold sample dilution.

Each batch experiment consisted of A280-triplicates for 11 AMS conditions, resulting in 33 data points. To reduce the effect of outliers in the data within one experiment, a robust least squares fit of the precipitation curve using the Boltzmann function was performed. This model-based approximation assumes that the precipitation can be divided into three distinct phases, namely an initial plateau until the onset of the precipitation, a sigmoidal decrease, and a final plateau once all target molecules have been precipitated. In particular, the optimization problem was set up as

$$\min_{\mathbf{x}} = 0.5 \sum_{i=1}^{N} \delta(f(c_{\mathrm{AMS},i}, \mathbf{x}) - y_i)^2 \tag{6.1}$$

where y_i denote the discrete UV measurements at a certain concentration of AMS i and $f(c_{\mathrm{AMS},i}, \mathbf{x})$ being the Boltzmann function given as

$$f(c_{\mathrm{AMS},i}, \mathbf{x}) = \frac{x_2 - x_4}{1 + \exp\Big(-(x_1 c_{\mathrm{AMS},i} + x_2)\Big)} + x_3. \tag{6.2}$$

The parameter vector $\mathbf{x}$ is defined as $(x_1, x_2, x_3, x_4)^T$. By employing the non-linear transformation of the squared residuals z, a smooth approximation of the absolute value loss by $\delta(z) = 2(\sqrt{(1+z)} - 1)$ was generated to effectively reduce the impact of outliers. To generalize the problem where the threshold between inliers and outliers is different from 1, the formula $\hat{\delta}(r^2) = C^2\delta((r/C)^2)$ was used with C being a scaling factor that determines the threshold between outliers and inliers in the data set. In our case, C was set to 5 for robust parameter estimation across all batch and fed-batch experiments.

The generated Boltzmann fits were used to remove outliers in each experiment. The distribution of the residuals between the Boltzmann curves and the original measurements were analyzed. Data points with residuals outside of the interval $[p_{0.25} - 1.5IQR; p_{0.75} + 1.5IQR]$ were excluded from the data set with the interquartile range IQR being defined as $p_{0.75} - p_{0.25}$ [249] and $p_{0.25}$ and $p_{0.75}$ the 25 and 75% percentiles.

Within one experiment, the conversion to apparent precipitated VLP concentration was done by subtracting the minimum observed A280 mean from all data points, taking the absolute values, and scaling by HPLC device parameters and the theoretical extinction coefficient of the VLP at 280 nm of $1.764\,\mathrm{L\,g^{-1}\,cm^{-1}}$ as provided by the ProtParam tool [204]. This procedure assumes that solely

VLP is precipitating under given precipitation conditions as discussed in Wegner et al. [90] and the absorption is only caused by VLP in solution. Under consideration of other HCPs and nucleic acids in the solution, this procedure is biased and hence the derived VLP content is termed apparent precipitated VLP concentration.

6.2.2.2 Spectral Data Processing

Spectral data processing of averaged spectra was done in order to reduce unwanted differences in the collected Raman data and covered spectral outlier removal, turbidity correction, baseline correction, background correction, difference spectra, derivative and smoothing, and cropping. Multiple combinations of the listed operations were screened to find the optimal configuration. Hence, the individual operations will be explained in detail.

Spectral outlier removal Spectral outlier were removed manually based on visual inspection regarding defective spectra. Defective spectra were found for experiment B2 corresponding to the conditions 1.0, 1.1 and 1.2 M AMS and occurred mainly due to sample handling and hence the inclusion of air bubbles in the flow cell.

Turbidity correction To remove interfering Raman effects caused by turbidity, the spectra were turbidity-corrected by normalization at 3299 cm^{-1}.

Baseline correction All spectra were baseline-corrected using a Whittaker filter employing the adaptive smoothness penalized least squares (asPLS) according to Zhang et al. [202] and implemented in *pybaselines* (v. 1.0.0). The λ parameter was determined manually by visual inspection of the estimated baseline. The optimal λ value of 6×10^{-7} was chosen based on the most consistent baseline estimation over the entire spectral range across all samples. Furthermore, a second-order difference matrix, a maximum number of iterations of 100, and a tolerance of 1×10^{-3} were used.

Background correction To remove the interfering Raman effects of the buffer system and the precipitating agents, two different background correction methods were evaluated. The first one which we will refer to as scaled subtraction (SS) uses reference measurements of the buffer system at the respective concentration levels of AMS. The reference spectra were scaled to the Raman spectra collected in the precipitation experiments by normalization at 750 cm^{-1}. As the SS method can only be applied when reference measurements are available, a second background correction method was evaluated, namely the OPLS as described in Trygg et al. [240]. The OPLS method extracts the orthogonal systematic variation in the spectral data which is not correlated to the target quality attribute and was used as implemented in *pyopls* (v 20.02) using 3 latent variables.

Difference spectra Since only the precipitated material contributes to the changes in Raman intensity, difference spectra were computed per experiment by subtracting the first spectrum of each experiment. This is analogous to using the autozero function of other spectroscopic detectors at the beginning of the experiments. In essence, this is supposed to remove the varying background effects of the lysate matrix of which the exact composition is unknown.

Derivative and smoothing Derivative and smoothing was applied using the Savitzky-Golay filter (SGF) [203]. Unless stated otherwise, the SGF was used with a second-degree polynomial and a window size of 11 as implemented in *scipy* (v. 1.11.4).

Cropping Spectra were cropped to reduce the influence of fluorescent background, scattering, buffers, and precipitant. Multiple intervals were evaluated to study the effect of individual contributions. The selected intervals for cropping of the Raman spectra were 800-1800, 1020-1800 and 1200-1500 cm^{-1}, which were motivated by the exclusion of residual baseline variance, the largest sulfate contribution and the majority of buffer interference.

Preprocessing pipeline The individual preprocessing operations are used in sequence as presented above. In some cases, a differing order may be viable, however the authors decided to keep the order fixed for this study in order to maintain comparability of the different approaches. The preprocessing pipeline configuration identified as optimal for the batch data was utilized for the fed-batch experiments.

Quantitative evaluation To compare preprocessing operations quantitatively without the need to calibrate a multivariate regression model, the metric signal-to-noise ratio (SNR) was used to evaluate the correlation between individual variables with the target quantity. Here, we define the SNR as

$$SNR = \frac{\mathrm{Var}(\mathbf{x}_\lambda \hat{\boldsymbol{\beta}})}{\hat{\sigma}^2} \tag{6.3}$$

with $\hat{\boldsymbol{\beta}}$ being the regression coefficients of a univariate linear model of type $\mathbf{y} = \mathbf{x}_\lambda \boldsymbol{\beta} + \boldsymbol{\varepsilon}$ with normally distributed errors ε and $\hat{\sigma}^2$ being the residual variance of linear model for wavenumber λ according to Soch et al. [250]. To calculate SNR for the Raman spectroscopy data using Eq. 6.3, a linear model was built for each wavenumber individually. The SNR was used to compare multiple combinations of preprocessing operations. All combinations were applied to the precipitate and supernatant data sets. A preprocessing operation is considered beneficial if the metric at a certain variable increases compared to the un-preprocessed state. Further, the variable is considered predictive if it shows high SNR in precipitate and supernatant samples among all experiments.

6.2.2.3 Regression modelling

Data splitting To make maximum use of the recorded data, the batch data (B1-B8) were split using a nested cross-validation scheme. The eight experiments are divided into six training and two test experiments according to a *Leave-Two-Experiments-Out* cross-validation scheme which serves as the outer cross-validation. In total, this results in $8!/(2! * 6!) = 28$ independent test sets on which the calibrated models are evaluated. For the inner cross-validation, the six training experiments are further rotated using a *Leave-One-Experiment-Out* cross-validation scheme to perform hyperparameter optimization in each of the iterations of the outer cross-validation. The fed-batch data were split in two training experiments (F1, F3) and one independent test experiment (F2). Here, the hyperparameters were optimized using a randomized split of the training set with eleven validation data points.

Regression models For the comparison of different combinations of preprocessing operations, two model types were evaluated as multivariate regressors for the quantification of the apparent precipitated VLP concentration, namely multiple linear regression (MLR) and PLS models as implemented in *scikit-learn* (v. 1.3.2). The different model types were selected to resolve potential differences between the working principles of these models with regard to preprocessing pipelines. For the MLR models, 6 wavenumbers of all observed wavenumbers were selected which were known to be protein-related but were not affected by AMS, namely 830, 850, 1241, 1314, 1341 and 1617 cm^{-1} [131, 132, 251]. PLS models were trained using the NIPALS algorithm [144] and the number of latent variables was optimized using a grid-search in the range of 2 to 10 based on the inner cross-validation. Before being passed to the regression models, all spectral data were mean-centered and column-wise scaled to unit variance. PLS models for quantification of AMS were built based on a pipeline including turbidity correction, baseline correction, difference spectra and no further optimization was performed.

Error metrics Accuracy of the calibrated models was assessed using the root mean squared error (RMSE) and the coefficient of determination R^2. For the inner cross-validation, the RMSE was calculated using the left-out experiments. When PLS models were used, the RMSE was scaled by the number of latent variables according to Wold et al. [144]. The importance of individual wavenumbers in PLS models was assessed quantitatively by VIP scores. The VIP score v_j [142] is defined as

$$v_j = \sqrt{N \sum_{a=1}^{A} \left[\left(q_a^2 t_a^T t_a\right) \left(w_{aj} / \left\|w_a\right\|\right)^2 \right] / \sum_{a=1}^{A} \left(q_a^2 t_a^T t_a\right)}, \tag{6.4}$$

for the individual wavenumber $j \in [1, N]$, where N denotes the total number of wavenumbers. The loading weights, the y-loadings, and the score vector corresponding to the PLS component $a \in [1, A]$ are given by w_a, q_a, and t_a, respectively.

6.3 Results

6.3.1 Spiking Diversifies Experimental Data

Experiments in batch and fed-batch mode were conducted in 1 mL and 12 mL scale, respectively. To generate variance in precipitation data, multiple lysate batches and defined spiking solutions were used. In total, 8 batch experiments and 3 fed-batch experiments were conducted (see Tab. 6.1 and 6.2) and samples, taken at different concentrations of AMS, were analyzed by Raman spectroscopy and reference analytics. To extract the apparent precipitated VLP concentration from the reference UV absorbance measurements, the UV data were treated as described in Section 6.2.2.1. The UV pretreatment procedure is schematically depicted in Fig. 6.1 (A)-(D). Fig. 6.1 (A) shows the scatter-corrected UV data for experiment B1 over the precipitation range from 0 to 1.2 M AMS. To approximate the precipitation trend, a Boltzmann function which is shown in Fig. 6.1 (B) was fitted to the displayed data points.

Based on the residuals between the Boltzmann fit and the observed data, outliers were excluded which reduced the spread of observed data as visible in Fig. 6.1 (C). Finally, the UV data were

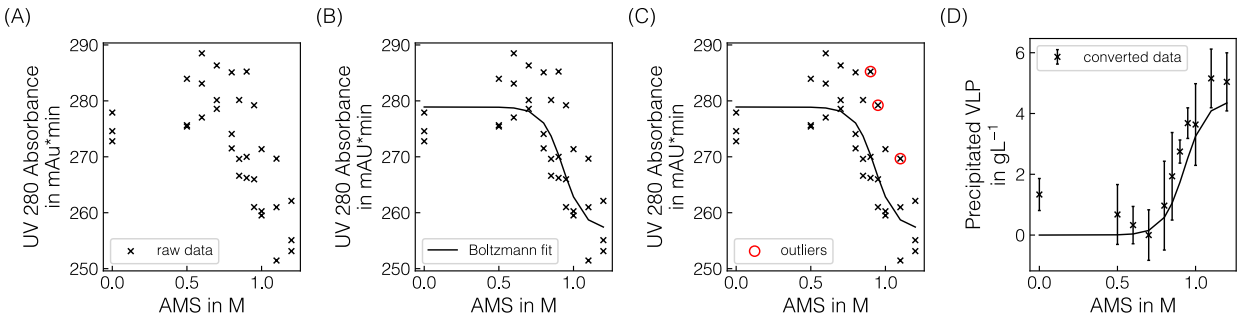

Figure 6.1 Illustration of pretreatment of the UV absorbance measurements. The UV absorbance at 280 nm is exemplarily shown over precipitant concentration for selected pretreatment steps for experiment B1. Raw triplicate UV measurements are shown as black crosses **(A)** and the fitted Boltzmann function is shown as a solid black line **(B)**. The detected outliers are represented by red circles **(C)**. The converted precipitated VLP concentrations are shown as black crosses with one standard deviation from averaging the three replicates per condition **(D)**.

converted to the apparent precipitated VLP concentration as presented in Fig 6.1 (D). The resulting outlier-corrected UV absorbance progression and the corresponding apparent VLP concentration are shown for all experiments in Fig. 6.2.

For the batch experiments, three distinct groups are illustrated, as the experimental conditions were induced by different methodologies. For each experiment, the outlier-corrected absorbance measurements are displayed with one standard deviation and the fitted Boltzmann functions. While the Boltzmann functions aligned well with the UV absorbance for all experiments, the height of the final plateau for the precipitated VLP concentration was underestimated in the case of B3 and B7. Experiments B1 to B3 are shown in Fig. 6.2 (A) and (E) and were generated by diluting the lysate material using lysis buffer. For these curves over the course of the AMS concentration, the reductions of the total UV absorbance as well as the amount of precipitated VLP indicate the reduced concentration of all components by dilution. Experiments B1 and B4 used lysate material from different batches and showed comparable total UV absorbance and precipitated amounts of VLP. Compared to B4, experiments B5-B7 (cf. Fig. 6.2 (B) and (F)) were generated by specifically enriching the VLP or HCP content in the lysate materials by adding spiking material. This resulted in varying total UV absorbance and precipitated amounts of VLP for these individual curves. While a maximum of $2\,\mathrm{gL^{-1}}$ of precipitated VLP was reached in B7, the remaining experiments showed precipitated amounts of VLP up to $5\,\mathrm{gL^{-1}}$. In contrast to B4, experiments B5-B7 varied in the range of 125 and 150 mAU total UV absorbance. In experiment B8 (cf. Fig. 6.2 (C) and (G)), the NaCl concentration was increased to 270 mM, which caused a lower UV absorbance compared to B4 which was based on the same lysate material and reached a maximum amount of precipitated VLP of over $4\,\mathrm{gL^{-1}}$. The final, apparent concentrations of precipitated VLPs derived from the fitted Boltzmann functions are listed in Table 6.1.

In the fed-batch experiments (cf. Fig. 6.2 (D) and (H)), the differences in the precipitation trends were induced by dilution, adding VLP-enriched spiking material and modulating the feeding rate of the precipitant solution (cf. Table 6.2). Here, similar trends to the batch experiments were observed in terms of varying UV absorbance ranges. Note that the observed data include the dilution caused by the addition of the precipitant and hence a more gradual increase in the precipitated

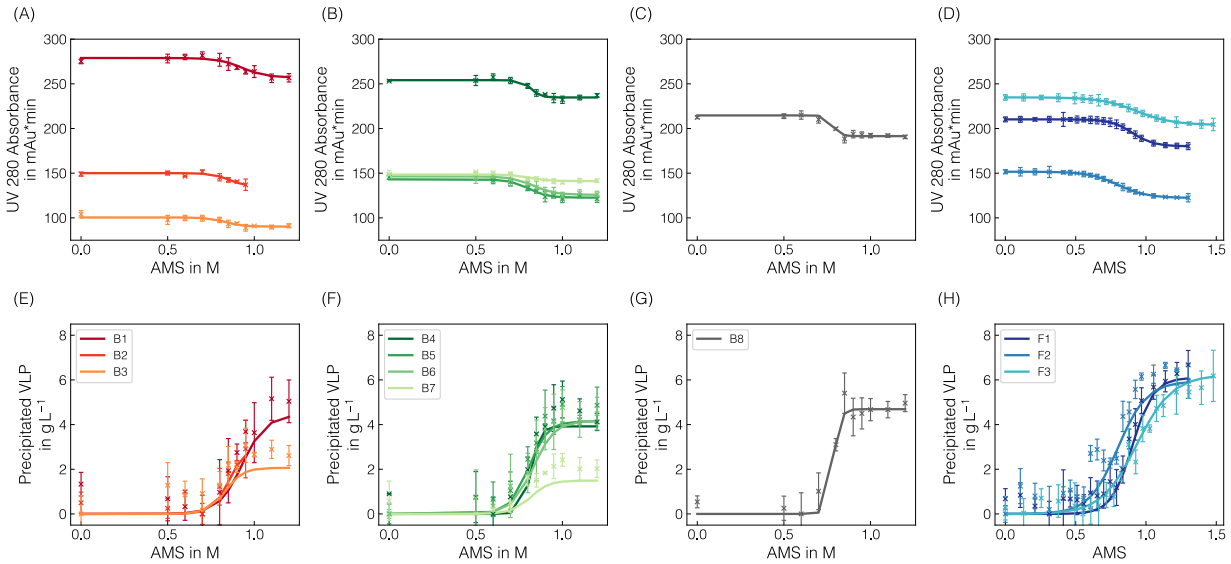

Figure 6.2 Comparison of pretreated UV absorbance data and VLP precipitation curves. Total UV absorbance at 280 nm after scatter- and outlier correction **(A)-(D)** and converted precipitation curves **(E)-(H)** are shown for batch experiments B1-B8 and fed-batch experiments F1-F3. Solid lines represent the fitted Boltzmann functions for outlier detection. The experiments are grouped according to the mode of spiking, where B1-B3, B4-B7 and B8 show the influence of lysate dilution, protein-composition regarding or salt content, respectively. For B2, the data points above 0.95 M were excluded due to defective Raman spectra in the precipitate samples.

VLP concentration is expected compared to the batch experiments. Moreover, the AMS content calculation for F3 revealed a higher mean AMS flow rate than expected, exceeding the initially chosen final concentration of 1.3 M AMS.

In summary, the generated precipitation data provide insights into the precipitation dynamics in the presence of varying backgrounds induced by the addition of spiking material or buffer solution and serve as a diverse data set for chemometric model development.

6.3.2 Raman Spectra Are Affected by Precipitant and Precipitates

Raman spectra are commonly affected by the matrix, buffers and other components present in the sample. Before using the collected Raman data for chemometric modeling, the data require preprocessing to properly evaluate potential interferences from buffers or excipients. A schematic illustration of the effect of the employed preprocessing operations is presented in Fig. 6.3. From left to right, the schematic pipeline shows the averaged raw Raman spectra for each sample in experiments B1, the turbidity- and baseline-corrected spectra using the 3299 cm^{-1}-normalization and asPLS Whittaker filter, the SS-background-corrected spectra and the difference spectra. The combination of turbidity correction with the Whittaker filter removed turbidity effects and baseline drifts reliably over the whole spectral range (cf. Fig. 6.3 (A), (B)). The SS-background correction subtracts the contribution of the AMS, which caused the AMS-related band at 980 cm^{-1} to become negative and the protein-related bands to show larger variations (cf. Fig. 6.3 (C)). Finally, the difference spectra operation sets the Raman intensity in the beginning of the experiments to 0 and

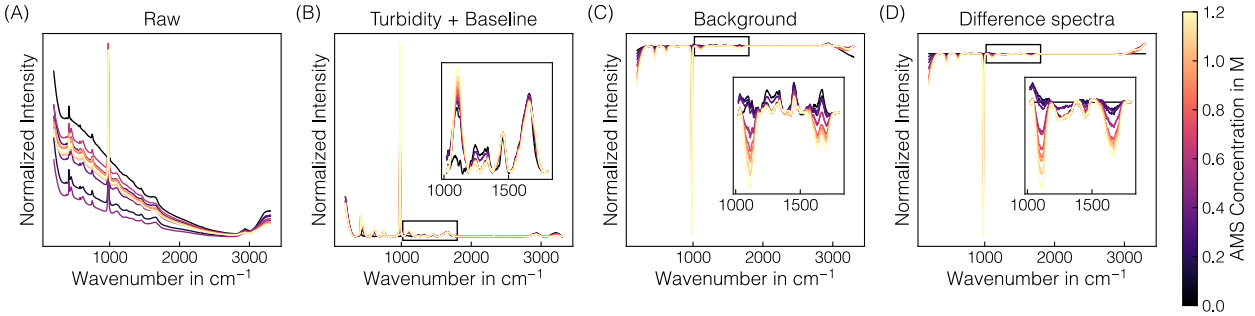

Figure 6.3 Illustration of the preprocessing of the Raman spectra. The preprocessing procedure is exemplarily depicted for experiment B1. The normalized raw Raman spectra **(A)** and selected preprocessing steps **(B-D)** are shown. The spectra are colored according to the AMS concentration with brighter colors denoting higher concentrations.

caused negative bands in the wavenumber region 1200-1700 cm^{-1} (cf. Fig. 6.3 (D)). For a visual interpretation of the difference spectra, the reader is advised to regard positive and negative bands as substances being added and being removed from the solution, respectively. For evaluating the interferences of the precipitant, buffers or excipients, the Raman spectra were firstly treated by turbidity- and baseline correction only.

Fig. 6.4 presents a comparison of the collected Raman spectra in precipitant-containing buffer samples, supernatant samples, precipitate samples from batch experiment B1 without and with turbidity correction (cf. Sec. 6.2.2.2) from top to bottom. Fig. 6.4 (A) shows the raw Raman spectra and Fig. 6.4 (B)-(D) show the baseline-corrected data within selected wavenumber regions. In the raw spectra (cf. Fig. 6.4 (A)), different baseline effects are visible between all sets of spectra with the precipitate data showing the strongest baseline variations. Baseline variations in the precipitate data were less pronounced for the turbidity-corrected spectra. At low concentrations of AMS, the baseline increased while at high AMS concentrations, the baseline decreased again. This effect was accompanied by the increasing contributions of AMS in the Raman spectra with the most prominent Raman band being located at 980 cm^{-1}. Additionally, the increasing AMS contents are visible in the Raman bands at 450, 618 and 1106 cm^{-1} (cf. Fig. 6.4 (B) and (C)) as well as near 1435 and 1693 cm^{-1} (cf. Fig. 6.4 (D)), which can be attributed to sulphate and ammonium ions, respectively [251, 252]. Additional components of the lysis buffer which were contained in all samples can be traced to the bands at 1249 and 1470 cm^{-1} indicative for Tris and EDTA [253]. These bands remained roughly constant over the course of a precipitation experiment as only the AMS concentration was gradually increasing. As expected, the sapphire bands at 379, 418, 430, 450, 577 and 750 cm^{-1} [254], the band of molecular oxygen at 1556 cm^{-1} [255] and the broad water band at 1650 cm^{-1} [251] remained roughly constant as well. Protein-related contributions are located between 600-880 cm^{-1} and 1200-1800 cm^{-1} with amide bands, CH_2-deformation bands and bands of aromatic amino residues [131, 132]. Amide III and I bands are visible near 1241 and 1660 cm^{-1}, respectively. Tyrosine (Tyr) bands appear at 830, 850, 1205 and 1617 cm^{-1} and the bands originating from tryptophan (Trp) and phenylalanine (Phe) appear at 1340 and 1605 cm^{-1}, respectively. CH_2-deformations are visible at 1314, 1340 and 1448 cm^{-1}. While these protein-related contributions were largely unaffected by the AMS or lysis buffer induced Raman activity, the precipitant interfered with the protein-related contributions in several locations (cf. 620, 643, 1004, and 1127 cm^{-1}). Tyr, Phe, and C-C stretching can be associated with these bands at 643 cm^{-1},

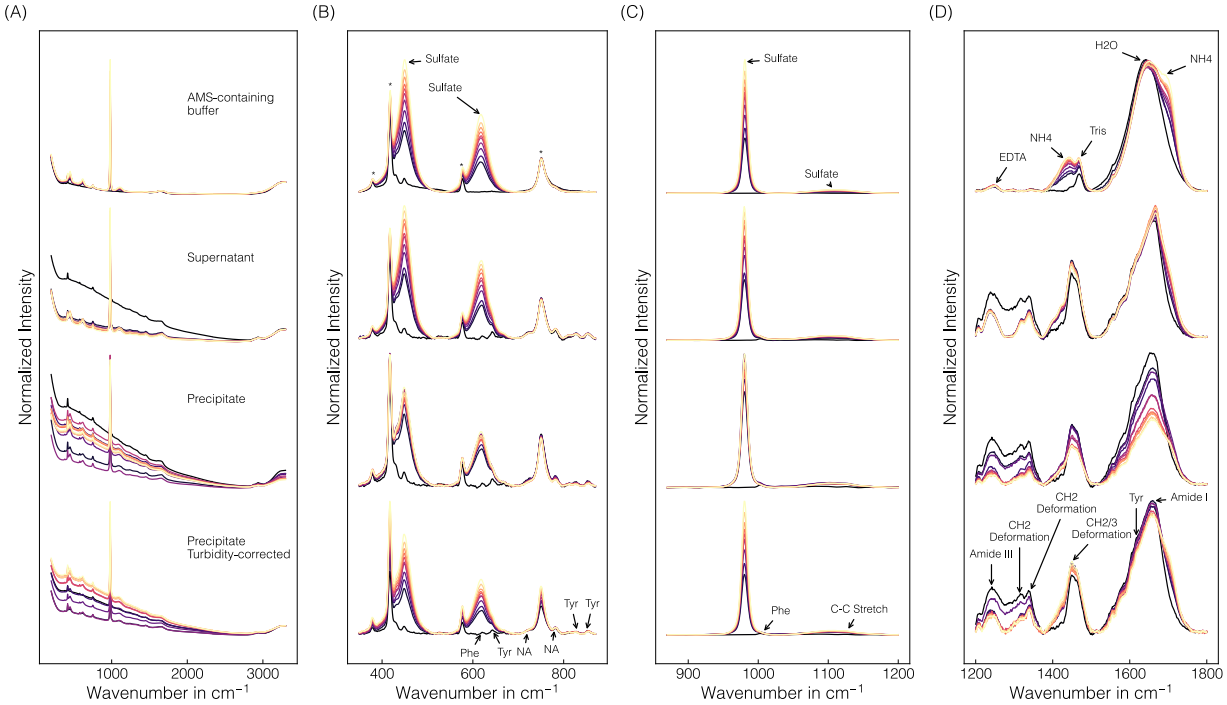

Figure 6.4 Comparison of collected Raman spectra in precipitant-containing buffer, supernatant and precipitate samples. Precipitate and supernatant data are exemplarily shown for batch experiment B1. Full raw spectra **(A)**, and baseline-corrected spectra of selected wavenumber regions **(B)-(D)** are illustrated. Spectra with incorporated turbidity correction are shown in the bottom row for the precipitate samples. The spectra are normalized in each row and subfigure for visual purposes and colored according to the AMS concentration with brighter colors representing higher concentrations. Wavenumber regions indicated by arrows correspond to buffer-, protein- and nucleic acid (NA)-related contributions. Sapphire bands are marked with an asterisk.

620 and 1004 cm^{-1}, and 1127 cm^{-1}, respectively [131, 132, 256]. In addition to the protein-related contributions, the bands at 724 and 781 cm^{-1} are indicative for the presence of nucleic acids [256].

To study the effect of the precipitates in solution formed during the precipitation experiment, the baseline-corrected Raman spectra from precipitate and supernatant samples were compared. In general, similar bands are visible in both the precipitate and the supernatant spectra. The protein bands showed a decreasing trend with increasing AMS concentrations. This effect was more pronounced in the precipitate spectra compared to the supernatant spectra indicating an overall protein band-specific intensity decrease caused by the precipitates in solution. Similarly, the nucleic acid bands at 724 and 781 cm^{-1} were visibly decreasing with increasing concentrations of AMS. By introducing the turbidity correction, the overall intensity decrease was reduced in all mentioned wavenumber regions, effectively making the precipitate spectra more comparable to the supernatant spectra, especially in the bands of the nucleic acids. However, individual Raman bands were adversely effected such as the sapphire band at 750 cm^{-1}, showing minor overcorrection.

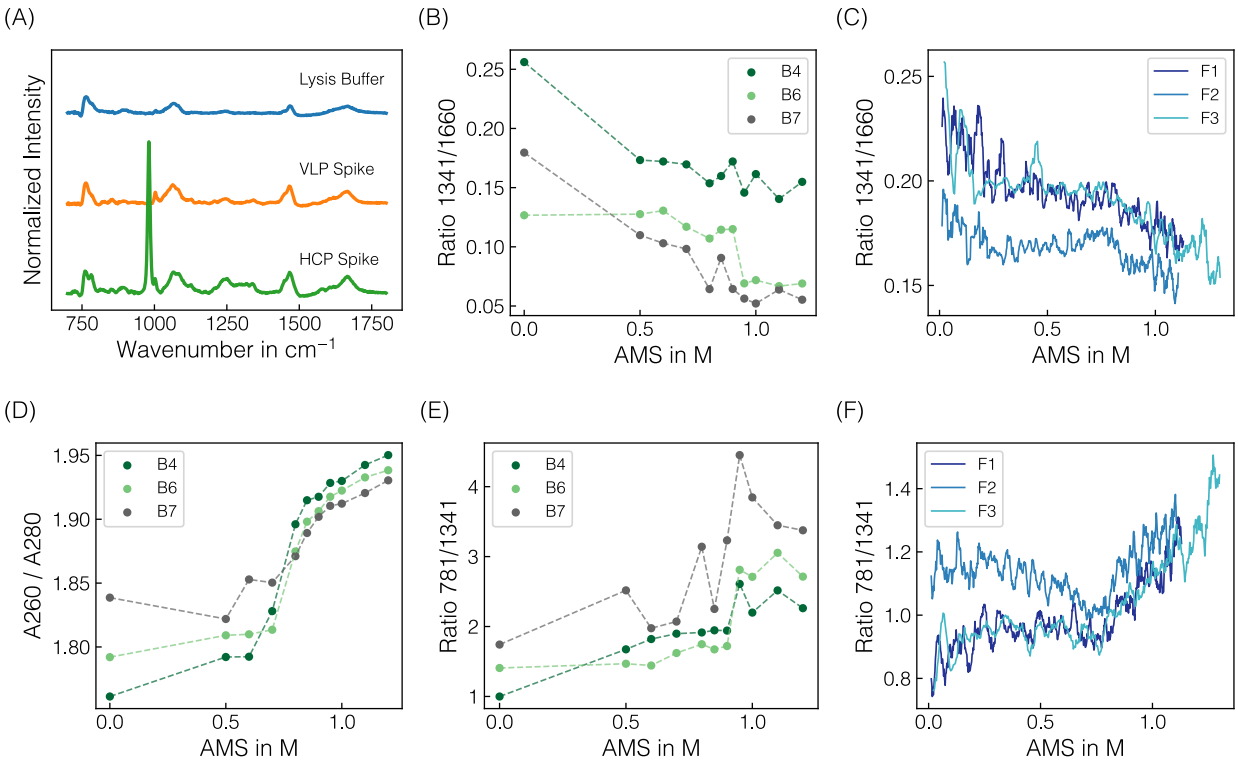

Figure 6.5 Raman spectra of the spiking solutions and comparison of selected wavenumber ratios. Normalized Raman spectra of lysis buffer and VLP- and HCP-enriched spiking materials after baseline-correction and subtraction of water blank are illustrated in **(A)**. The protein-band ratio 1341/1660 is depicted over the course of AMS for batch experiments B4, B6, B7 differing in the protein composition of the lysate batch **(B)** and all fed-batch experiments **(C)**. The UV absorbance-derived A260/A280 ratio **(D)** is shown alongside the band ratio 781/1341 comparing the nucleic acid-associated Raman band with the protein-associated Raman band for batch experiments B4, B6, B7 **(E)** and fed-batch experiments **(F)**. All ratios were calculated with turbidity- and baseline-corrected Raman spectral data. The ratios for fed-batch experiments were calculated using a moving average of 10 spectra to smooth the signal. Dashed lines are only shown for visual purposes.

6.3.3 Raman Data Reveal Structural Differences between Species

To investigate whether structural differences between the target molecules and the other species in the lysates are observable via Raman spectroscopy, the Raman spectra from the VLP- and HCP-enriched spiking materials were compared. Normalized Raman spectra of the lysis buffer and the purified VLP- and the HCP-enriched spiking solutions are presented in Fig. 6.5 (A) after baseline-correction and water blank subtraction. Both solutions exhibited distinct Raman bands in the protein fingerprint region between 800 and 1800 cm^{-1} with slight differences in the shape of the most prominent peaks between 1000-1100 cm^{-1}, 1200-1300 cm^{-1} and 1600-1700 cm^{-1}. Additionally, the nucleic acid-related Raman band at 781 cm^{-1} and the precipitant-related Raman band at 980 cm^{-1} were observed for the HCP spiking solution. As the HCP spiking solution was prepared by recovering the precipitation supernatant and subsequent dialysis, it contained both HCPs and host cell nucleic acids, which was further underlined by a A260/A280 ratio of 1.88. The AMS contribution was

caused by the residual amounts of AMS after buffer exchange. As the peak profiles of the two spiking solutions in the protein fingerprint region differed slightly from one another and the amide bands are commonly used Raman markers for higher-order structures [253], the ratio of selected amide bands are presented in Fig. 6.5 (B)-(C) for selected batch and fed-batch experiments, respectively. The data indicated a shift in the ratio of 1341 and 1660 cm^{-1} over the course of a precipitation experiment depending on the initial conditions of the respective experiment. Exemplarily, the VLP-spike experiments (B6, B7, F2) exhibited slightly lower ratios than the experiments with similar lysate compositions (B4, F1, F3). To compare the intensity decrease observed for the nucleic acid and protein-related bands, the ratio of 781 and 1341 cm^{-1} is shown for batch and fed-batch experiments over increasing AMS content in Fig. 6.5 (E)-(F). The curves show a sigmoidal increase indicating a stronger decrease of protein-related Raman bands than observed for the bands associated with nucleic acids. A comparable trend was observed in the A260/A280 ratio for supernatant samples of the batch experiments as presented in Fig. 6.5 (D).

In summary, the differences in protein-associated Raman bands of the two spiking solutions underline structural differences between VLPs and HCPs. Selected band ratios could be used to track these spectral changes over the course of the precipitation, suggesting the selective precipitation of specific molecular species, namely the VLP.

6.3.4 Background Correction Removes Interferences

The batch experiment data were used to evaluate the suitability of preprocessing pipelines with regard to their universal applicability to all experiments, and their capacity for removing background effects such as buffer and precipitant interferences. Fig. 6.6 (A)-(C) present the difference spectra after turbidity and baseline correction, incorporated SS-background correction or incorporated OPLS-background correction, respectively, for the precipitate samples of all batch experiments B1-B8. In Fig 6.6 (D)-(F), the SNR is presented to quantify the effect of the baseline and background correction methods on the correlation with the precipitated amount of VLP.

The turbidity- and baseline-corrected spectra showed evolving negative bands between 1200 and 1400 cm^{-1} and 1500 and 1700 cm^{-1}. These negative bands exhibited SNR values below 0.5. The Raman bands between 1020 and 1200 cm^{-1} and between 1700 and 1720 cm^{-1} showed a clear trend with increasing levels of AMS. The SNR confirmed this observation with the highest values close to 1 for these intervals. Similar trends was observed between 1400 and 1500 cm^{-1} with SNR values up to 0.9. By subtracting the reference spectra comprising solely buffers and precipitants, an additional negative band between 1020 and 1200 cm^{-1} was unveiled and the peak around 1700 cm^{-1} was removed (cf. Fig. 6.6 (A),(B)), while the wavenumber region between 1200 and 1400 cm^{-1} remained largely unaffected. The SNR confirmed these observations and showed a strong correlation of the bands between 1020 and 1200 cm^{-1} and 1550 and 1750 cm^{-1}, where protein-related Raman bands are located. Bands between 1400 and 1500 cm^{-1} also showed elevated correlation according to SNR compared to sole baseline correction. By incorporating an OPLS-based background correction, the spectra mostly retained positive bands between 1020 and 1200 cm^{-1} and the peaks around 1450 and 1700 cm^{-1} (cf. Fig. 6.6 (C)). However, the SNR revealed that the correlation increase in the range from 1020 to 1200 cm^{-1} and from 1550 to 1750 cm^{-1} is lower than for SS-background correction. Almost no correlation increase was observed near 1600 cm^{-1}. Despite the visual differences between the SS- and OPLS-background correction, the SNR assessment showed a similar profile with correlations between 1020 and 1200 cm^{-1}, near 1450 cm^{-1} and near 1700 cm^{-1}.

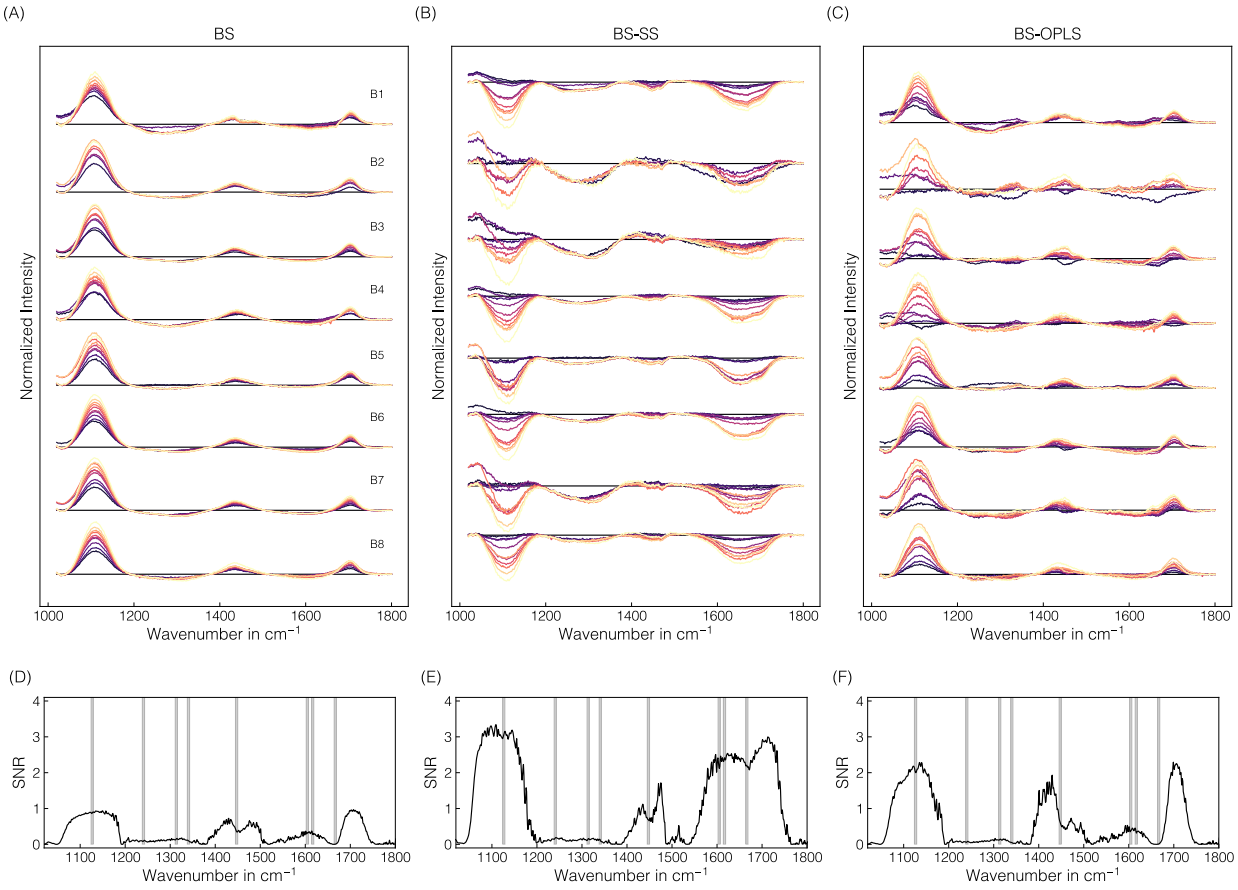

Figure 6.6 Comparison of the effects of preprocessing operations on Raman spectra in precipitate samples for the wavenumber region 1020-1800 cm^{-1}. In **(A)-(C)**, difference spectra for all batch experiments B1-B8 are shown after turbidity and baseline correction, with incorporated SS-background correction, or with incorporated OPLS-background correction, respectively. The spectra are colored according to the AMS concentration with brighter colors denoting higher concentrations. In **(D)-(F)**, the SNR for the respective preprocessing operations are shown. Gray shaded areas indicate protein-related Raman regions according to literature [131, 132].

An analogous illustration of difference spectra and corresponding SNR for the supernatant samples can be found in the Supplementary (Fig. A6.1), where comparable but substantially less pronounced trends were observed.

6.3.5 Systematic Pipeline Optimization Improves Model Accuracy

Upon retrieving information about correlative structures in the collected Raman spectra, the data were used to build multivariate regression models taking the Raman spectra as inputs and predicting the apparent precipitated VLP concentration. Multiple combinations of preprocessing operations and MLR or PLS models were screened with the aim to find the optimal pipeline configuration with respect to model accuracy and robustness. While a strong focus lied on evaluating previously assessed operations such as SS and OPLS-based background correction, their combinations with cropping and derivative filters were also evaluated in this Section.

In Fig. 6.7 (A), the distributions of RMSE of the held-out test sets are shown for all tested model and pipeline configurations, sorted by the mean of the RMSEs. Fig. 6.7 (B)-(G) additionally show the direct comparison of selected model configurations and aim to emphasize the effect of individual changes to the model and preprocessing pipeline on model performance.

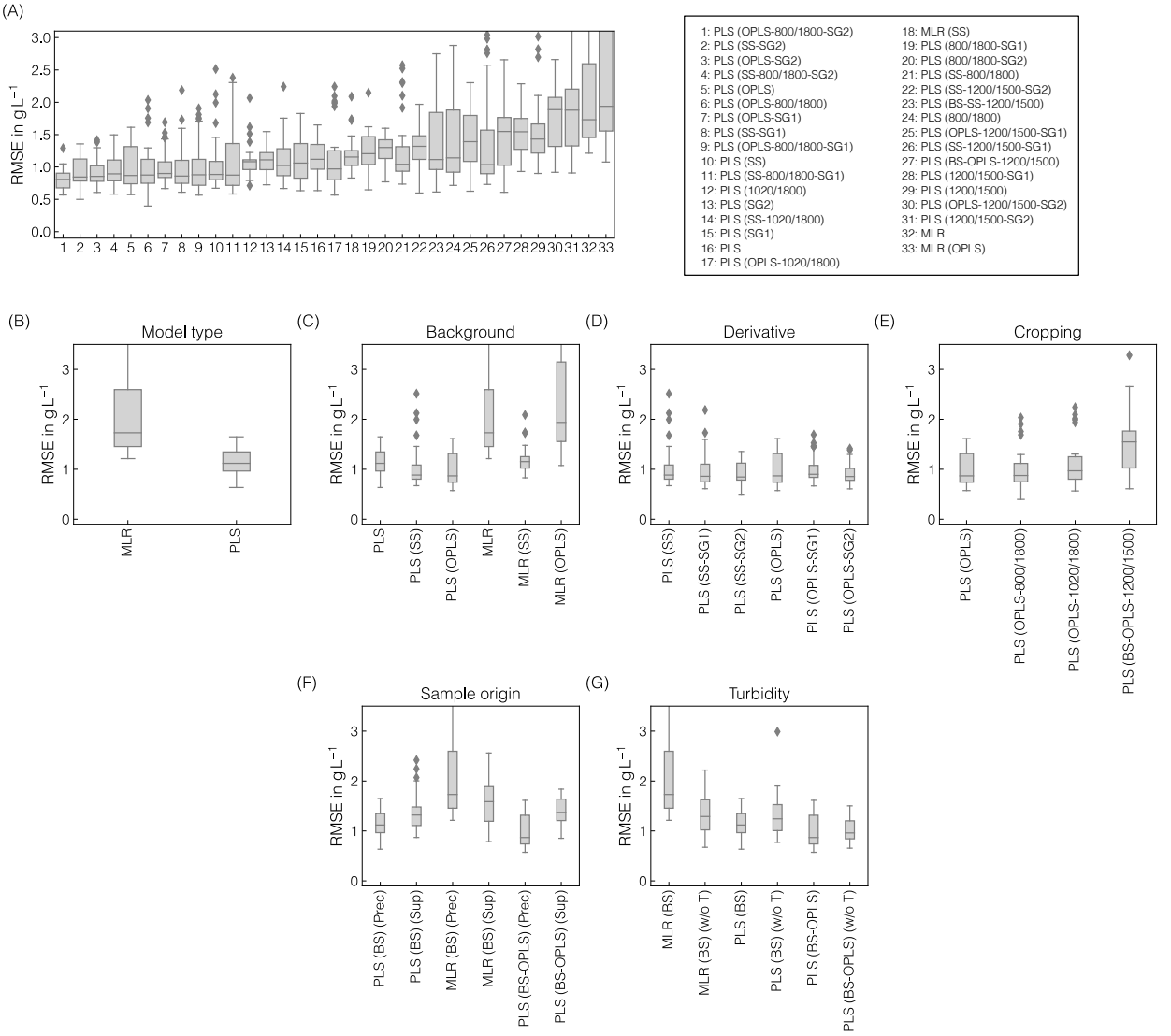

Figure 6.7 Comparison of preprocessing pipelines and model types. The distributions of RMSE of the outer cross-validation are presented and ranked by the mean of the RMSEs for all tested model configurations **(A)**. All tested model configurations comprised turbidity correction, baseline correction, and difference spectra. The solid lines within the boxes represent the median of the obtained performances. Outliers were characterized by errors surpassing 1.5 times the interquartile range and are symbolized by diamonds. RMSEs of selected model configurations are illustrated separately, namely for comparison of model types **(B)**, background correction methods **(C)**, SGF derivative **(D)**, spectral cropping **(E)**, sample origin **(F)**, and models with and without incorporated turbidity correction **(G)**.

While the best models achieved RMSE values of approx. $0.8\,g\,L^{-1}$ on average, the errors increased to up to approx. $2.0\,g\,L^{-1}$ on average. Model configurations with higher average errors also showed larger variance. Among the 4 best performing model configurations (cf. Fig. 6.7 (A)), all pipelines included SS or OPLS-background correction, second order SGFs and PLS regression models. While the best and the model ranking 4th used cropping to 800-1800 cm^{-1}, the remaining used the full wavenumber range. The PLS model applied to turbidity- and baseline-corrected difference spectra achieved better performance than MLR (cf. Fig.6.7 (B)). In general, PLS models benefited from using background correction method with the lowest average RMSE and variance being achieved when applying the OPLS method (cf. Fig. 6.7 (C)). For both SS- and OPLS-corrected data, increasing the order of derivative from 0 to 2 marginally improved the median RMSE and reduced variance (cf. Fig. 6.7 (D)). Cropping the Raman spectra generally showed adverse effects on model accuracy using OPLS-corrected data (cf. Fig. 6.7 (E)). As pointed out above, this was not true for all pipeline configurations but may be pointed out as a general tendency in this case study. To validate that the identified pipelines can not only be applied to Raman spectra recorded from the precipitate-containing samples, but also to the particulate-free supernatant samples, separate models were calibrated on the supernatant Raman spectra as shown in Fig. 6.7 (F). While the PLS and MLR models achieved similar accuracy after turbidity and baseline correction in precipitate and supernatant samples, OPLS-background-corrected models showed considerably increased RMSE on average in the supernatant samples. In Fig. 6.7 (G), separate models were calibrated without turbidity correction to verify that model performance benefit from the incorporated turbidity correction. Although MLR and PLS models achieved comparable performance when applied to solely baseline-corrected difference spectra, MLR performed worse than PLS models when combined with turbidity correction. All tested model and pipeline configurations without turbidity correction can be found in the Supplementary (Fig. A6.2).

6.3.6 Model Pipeline Captures Precipitation Trends

The previously identified best model and preprocessing pipeline PLS(BS-OPLS-800/1800-SG2) was finally evaluated on a representative split of batch data and further transferred to the fed-batch data. Fig. 6.8 presents PLS model predictions for the batch test set (B4, B6) and fed-batch experiments F1-F3 as well as VIP scores for both calibrated models.

Despite having different VLP to impurity ratios in the starting material (cf. Tab. 6.1), the PLS model predictions for batch experiments B4 and B6 aligned well with the experimental data (cf. Fig. 6.8 (A), (B)) with an R^2 of 0.83. Error metrics for calibration, cross-validation and test sets are presented in the Supplementary in Fig. A6.3. Alternatively, PLS model predictions for all calibration runs are shown over AMS content in the Supplementary in Fig. A6.4. While for B4, the sigmoidal shape of the precipitation curve was represented in the model predictions, the model predicted an early onset of the VLP precipitation for B6 and saturate at lower final concentration of approx. $3.5\,g\,L^{-1}$, effectively smoothing out the sigmoidal shape. For the calibration experiments (cf. Fig. A6.4), the sigmoidal shape and onset of the precipitation were predicted accurately while predictions for the initial plateau differed from the observations. Most of the predictions, however, lay within the range of one standard deviation of the observed data points.

In Fig. 6.8 (C)-(E), the predictions of the calibrated PLS model are shown for fed-batch experiments F1, F2 and F3 as symbols with their respective assignment to calibration, validation and test sets. Fig. A6.5 in the Supplementary presents error metrics for all data sets.

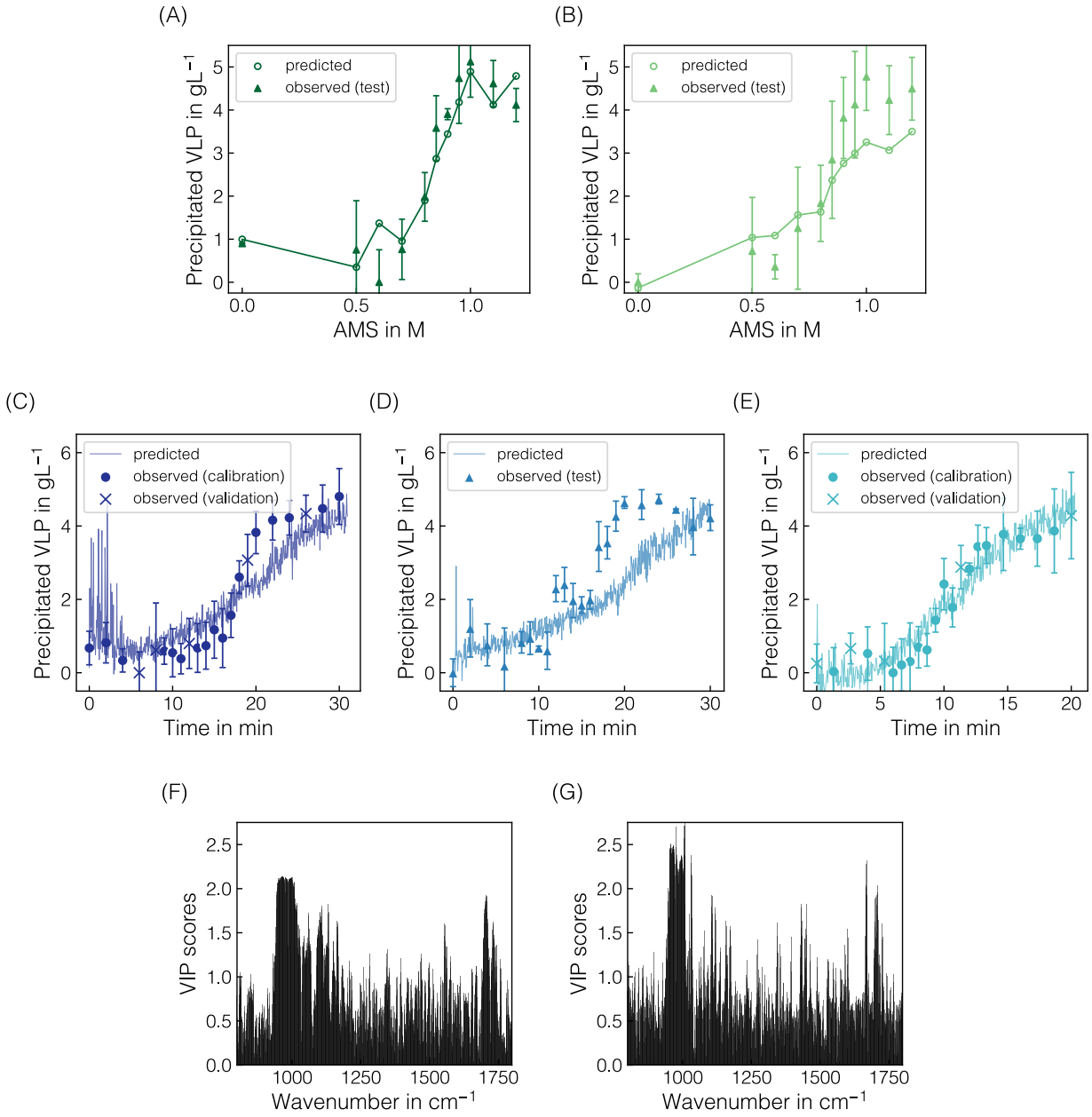

Figure 6.8 PLS model predictions with regard to precipitated VLP for batch and fed-batch experiments and the corresponding VIP scores for both models. For the batch experiments B4 **(A)** and B6 **(B)**, the predicted and observed precipitated VLP concentrations are shown over increasing AMS concentrations. For visual purposes, solid lines are shown to linearly connect the PLS model predictions. For the fed-batch experiments F1-F3 **(C)-(E)**, the observed apparent VLP concentrations are shown as symbols with their respective assignment to calibration, validation and test data. Model predictions from the real-time data after baseline correction and difference spectra are presented as solid lines. The VIP scores are illustrated for both batch **(F)** and fed-batch **(G)** models in the wavenumber region 800-1800 cm^{-1}.

The real-time data used for prediction were not averaged and hence the model predictions were scattered around the observed data points and were available in between reference measurements. While the trajectories of the expected precipitation curves were well represented in the predictions for the training experiments F1 and F3, the trajectory for F2 was underestimated in the range from 15 to 25 min which corresponded to approx. 0.5 to 1 M AMS. Using the averaged Raman spectra, this yielded an R^2 of 0.64 (cf. Fig. A6.5). For F1, the predictions for the spectra during the first 3 minutes strongly scattered and deviated from the expected values. Similar spikes for individual spectra were observed in the start-up phase for F2 and F3. In all cases, the effect reduced over the first 1 to 3 min after which constant scatter can be observed for all experiments until the end of the precipitation process. To evaluate the origin of these scatter, a step-wise visualization of the Raman spectra for all fed-batch experiments is presented in Fig. A6.8 in the Supplementary. The affected Raman spectra show slight distortions to lower intensity in the protein-related and water Raman bands, which are subsequently enhanced through the sequence of preprocessing operations. Towards the end of the process, no plateauing of the predictions based on the Raman data was observed whereas the observed data signals tended to stabilize with individual spikes being present.

Finally, Fig. 6.8 (F), (G) present the VIP-based feature importance for the PLS models based on batch and fed-batch data, respectively, in the wavenumber range between 800 to 1800 cm^{-1}. Both models relied on multiple wavenumber regions as indicated by elevated VIP scores. Most prominently, the interval between 950 and 1000 cm^{-1} originating from the sulfate ions contributed to the model predictions. Additionally, local maxima appeared at wavenumber intervals of 800-900, 1050-1150, 1400-1500 and 1550-1650 cm^{-1} for both the batch and the fed-batch models, mainly encoding protein-related information.

PLS models were further used to quantify the AMS concentration in batch and fed-batch using the same methodology as laid out for the precipitated VLP concentration. In the case of AMS the preprocessing only included turbidity and baseline correction and the formation of difference spectra. The predictions for the batch and fed-batch data are presented in the Supplementary in Fig. A6.6 and Fig. A6.7, respectively. For both data sets, the models showed almost perfect alignment for the test sets with R^2 of 0.98 and 0.97 over the concentration range from 0 to 1.2 M. For the fed-batch runs deviations from the expected values were observed above AMS concentrations of 1.2 M.

6.4 Discussion

6.4.1 Effects of Data Diversification

Data diversification is crucial for generating representative data sets for developing chemometric sensors suitable for PAT in biomanufacturing. The precipitation experiments were designed to mimic multiple sources of experimental variance which may arise in process development studies or manufacturing campaigns. Data were diversified using different lysate batches and conditioning of the lysates by dilution, salt addition, or spiking with purified VLP or HCP solutions. Similar strategies for data diversification were employed in the literature by spiking purified monoclonal antibodies with mock solutions to mimic complex feedstocks [89], spiking with nutrients during cell culture [234], spiking with cells during inoculum maturation [134] or mixing available samples [223]. In general, diversification strategies were reported to improve model robustness and interpretability [234] or enlarge the experimental data set [223]. Alternative strategies may include synthetic enlargement of

the available data sets by data augmentation [257] or the collection of data from multiple products, formulation components and sensors [225] for the diversification of experimental data sets.

In essence, the diversification strategy in this study yielded versatile precipitation experiments covering different precipitation trajectories, varying levels of total concentration of precipitated VLP and impurity content. However, the UV absorbance data exhibited high variance for the triplicate measurements which was enhanced by the conversion to the apparent precipitated VLP concentration, resulting in difficulties in determining the precipitation trajectories. Particularly, samples in the plateau region of the precipitation curves showed unexpected fluctuations. The variance between replicates or individual data points within one experiments, i.e. variable onsets of the precipitation or the initial and final plateau concentration, may be attributed to the precipitation procedure, sampling procedure and sample handling. Since the batch experiments involved the manual addition of the precipitant as well as sampling of the precipitate-containing solution, the heterogeneity of the precipitate solution may introduce analytical variance between data points. Moreover, inadequate mixing during precipitant addition or during the subsequent incubation time could also contribute to variance within a batch experiment. Variance between replicates and individual data points were less pronounced for fed-batch than batch experiments, which can be attributed to the inherent continuity of the fed-batch approach as well as effective mixing in the reservoir, thus, supporting uniform precipitate formation while avoiding co-precipitation of other species [75].

Eventually, the observed variances led to the employment of a pretreatment strategy based on experiment-based curve fitting using the Boltzmann function. This strategy assumed the selective precipitation of VLPs which has been shown for AMS concentrations below approx. 1.3 M [90]. The pretreatment strategy was shown to effectively reduce single-point variation by removing outliers and resolving differences between the precipitation experiments. Treatment of the reference data is uncommon in chemometrics but certainly improved the quality of the data in this study and enabled more robust model calibration (data not shown).

In summary, it is crucial to manage data variance within individual experiments, e.g. by increasing the number of replicates or incorporating a physically-motivated pretreatment, while highly diversifying data across experiments, as the obtained batch and fed-batch data sets served as basis for the development of a chemometric modeling pipeline for the quantification of precipitated VLPs.

6.4.2 Effects of Preprocessing Operations on Raman Data

The Raman spectra are affected by the composition of the lysate, the addition of the precipitant and the formation of precipitates in solution causing multiple independent changes in the Raman spectra to occur simultaneously. While the addition of the precipitant induced the emergence of the sulfate and ammonium-associated Raman bands, the formation of precipitates reduced the overall intensity due to turbidity of the solution. Turbidity is commonly observed in particulate-containing separation processes such as crystallization [42, 258–260] or precipitation [230, 233]. While Zelger et al. [233] directly used the turbidity measurements for monitoring the precipitation progress, Meyer-Kirschner et al. [230] demonstrated that a simple correction using the OH-stretching Raman band is feasible. Since regulatory agencies [247] recommend rigorous qualification of PAT sensors, the authors consider the use of Raman spectroscopy in combination with turbidity correction a viable PAT sensor for monitoring protein precipitation processes. Here, normalization at the OH-stretching Raman band reliably compensated for turbidity in the raw spectra. However, it was also pointed

out that the turbidity correction adversely affects other wavenumber regions in the herein recorded, baseline-corrected spectra such as the sapphire band at 750 cm^{-1}. This may be connected to the non-linear correlation between turbidity and Raman intensity decrease [232].

After turbidity and baseline correction, the variation in the protein-associated Raman bands was comparable to what has been observed for the supernatant spectra while the inexplicable decrease in nucleic acid-associated bands was eliminated. This supports the assumption of selectivity of the precipitation process for VLPs. A direct quantification of the amount of HCPs was not possible due to the unavailability of quantitative reference measurements in this study. The spectral data of the HCP- and VLP-enriched solutions, however, suggest that the VLPs are structurally different from the HCPs contained in the clarified cell lysate which is supported by different amide band ratios at the start and the end of a precipitation experiment. While this study was performed using HBcAg VLPs, the applicability of Raman spectroscopy for HBcAg variants or other types of VLPs is expected. To apply the presented workflow to other VLP systems, the generation of new experimental data is strictly necessary. Furthermore, by incorporating additional reference analytics such as HCP-enzyme-linked immunosorbent assay (ELISA) as done in Großhans et al. [89], the prediction of HCP content via Raman spectroscopic measurements may hence be facilitated. However, the prediction of HCPs using chemometric methods has only rarely been reported [261, 262], most likely due to the diversity of species classified as HCPs [263]. The same applies to nucleic acids and endotoxins, which might affect VLP precipitation, but their analysis exceed the scope of this study.

To prepare spectral data for multivariate modeling, turbidity, baseline and background correction followed by the difference spectra operation were evaluated for their correlation with the amount of precipitated VLP and their capacity to eliminate interferences in the Raman spectra caused by the addition of precipitant. Baseline correction of turbidity-corrected spectra proved to remove baseline drifts reliably across the entire wavenumber range. As the applied asPLS combines baseline estimation with smoothing of the estimated function while preserving the underlying features of interest [202], baseline drifts caused by both sample compounds and instrumental noise can be addressed.

The SNR-based correlation analysis of the baseline-corrected spectra suggested that next to protein-associated Raman bands, wavenumber regions encoding buffer and precipitant-associated information were also correlated with the amount of precipitated VLP. As the increase in precipitated VLP is expected to follow a sigmoidal curve [52, 90], the precipitant concentration in the solution and the amount of precipitated VLP is not linearly correlated. Hence, the contributions of the precipitant should be removed from Raman spectra via background correction. The SS-background correction reliably removed the background signal from the Raman spectra, while overcorrections were visible for samples with AMS concentrations above 0.6 M (cf. Fig. 6.3). This is caused by the discrepancy with regards to the turbidity between the precipitate spectra and the reference spectra where the solution remains clear even at the highest AMS concentrations of 1.2 M. The OPLS method as proposed by Trygg et al. [240] demonstrated improved correlations by removing the non-correlated systematic variation in the Raman spectra without the need for reference measurements. However, also the OPLS-treated spectra showed residual contributions in the dominant 980 cm^{-1} sulfate band and hence could not fully remove the precipitant-associated effects. As the OPLS method extracts the non-correlated variation with respect to the target variable [240], it is likely that the AMS-associated information was partially contained due to its correlation with the amount of precipitated VLP as mentioned before. Alternatively background variations may be modeled using

indirect hard modeling (IHM) [230, 264, 265]. Furthermore, the extended multiplicative signal correction (EMSC) algorithm supports the removal of an interferent spectrum [266]. However, Liland et al. [244] reported its propensity for overfitting and its implementation has been found ineffective in this study (data not shown).

Finally, all Raman data were treated using the difference spectra operation by subtracting the first Raman spectrum in each experiment. Difference spectra are a common method to emphasize temporal changes in spectroscopic data [267] or differences between individual samples [140, 268]. The difference spectra operation was shown to effectively remove all variations in the initial composition of the studied lysate using different conditioning approaches. This improved comparability between experiments and specificity of the Raman signals for the amount of precipitated VLPs which is crucial for generating robust chemometric models [234].

In summary, the preprocessing pipeline comprising turbidity and baseline correction, a background correction technique and difference spectra contributes to the overall quality of the precipitate Raman data, improving model building. The identified preprocessing pipeline may further be transferable to other precipitants such as polyethylene glycol (PEG). In the case of PEG-based systems, it may be more challenging to resolve the differences between the precipitants and protein-related signals due to organic Raman contributions of the PEG polymers [269].

6.4.3 Effects of Preprocessing Pipeline on Model Performance

Chemometric models based on Raman spectroscopy data often employ multiple preprocessing operations in sequence and require optimization of the associated hyperparameters [141, 270, 271]. To study the effect of individual preprocessing operations on model performance, multiple pipeline configurations were screened and evaluated using a nested cross-validation approach. The nested cross-validation enabled the comparison of the pipeline configurations, not only with regard to the overall accuracy, but also their robustness when permuting the training and test sets. By further incorporating interval-based cropping of the Raman spectra and the comparison of MLR with PLS models, the understanding for the relevance of specific features in the Raman data could be increased.

In general, PLS models showed considerably better performance and lower variance in cross-validated test sets than MLR models. This may be explained by the high complexity of Raman data and the experimental variance which was observed for the batch data set. The MLR models solely rely on VLP-associated Raman bands and hence require high-quality data. The PLS models may also use other correlative information available in the Raman spectra [234, 235] which is not necessarily specific for the precipitation of VLPs such as the turbidity or precipitant markers. Nevertheless, the comparison with MLR as a benchmark is a useful strategy as in less complex cases, the relevant information may be reliably contained in a few individual variables [17].

As anticipated from the SNR analysis, both background correction approaches improved the performance of the PLS models due to the removal of precipitant-related Raman bands. As the AMS contribution dominated the Raman spectra and was recovered in the first latent variables of the PLS models, models without prior background correction may rely too strongly on background information and hence not robustly predict the precipitated amount of VLP. Recent studies with biopharmaceuticals often rely on standardization, derivative filtering or baseline correction [137, 223, 225, 234]. Others performed background corrections by subtracting blank spectra but did not further investi-

gate the importance of the respective features on model predictions [89, 138, 222]. Alternatively, Wang et al. [223] performed blank chromatography runs with the elution buffer system and appended the recorded data to the calibration data set.

To assess whether the focus on spectral regions of interest improves model predictions, multiple cropping intervals were explored within this study. Cropping the spectra to 800-1800 cm^{-1} generally improved model performance, whereas further cropping decreased the overall accuracy of the PLS models. While most of spectral information is still contained in the 800-1800 cm^{-1} region, narrowing the wavenumber region to 1200-1500 solely focused on the protein-related information [131, 132]. The narrow bandwidth was not suitable to reliably predict precipitated VLP concentrations and notably broadened the distribution of RMSE while increasing the mean error by over 50%. This may be explained by the strong variances in the sensor data between experiments leading to non-linear correlations between the spectral data and the amount of precipitated VLP. When using B4 and B6 as the hold-out test set, a RMSE of 0.74 gL^{-1} was reached, supporting the VLP-associated information being stored in the respective wavenumber regions. Because the stated RMSE lies in the center of the RMSE distribution of the held-out test sets (cf. Fig. 6.7), the data split is considered representative.

The optimal performance in the permuted batch data was found for the PLS model for the combination of turbidity, baseline, and OPLS-based background corrections with cropping to 800-1800 cm^{-1} and second derivative filtering. When applied to the representative splits of the batch and fed-batch data, the identified model pipeline recovered the observed trends in the experimental data but lacked to resolve the correct sigmoidal shape for experiments B7 and F2. While the pipeline proved robust against background variations induced by lysate conditioning and spiking, the sigmoidal shape of the VLP precipitation trajectories and the height of the final plateau were not exactly met. Due to the overlaying effects occurring in the Raman spectra, the insufficient removal of the background contributions by the OPLS method and the high single-point variance in the reference data, the relationship between the VLP-related Raman bands and the target variable is considered to be non-linear. By inspecting the importance of different wavenumber regions through VIP, the model's reliance on residual precipitant information and the VLP-associated bands became apparent. Moreover, the VIP scores suggested a strong influence of noise in the spectra on the model predictions as no Raman band is clearly recovered.

Despite being robust to background variations, the preprocessing pipeline may also be influenced by unforeseen changes in the Raman spectra due to equipment failure or other experimental factors. In the case of the fed-batch experiments, the scattered predictions for the spectra during the first 3 minutes are likely due to a combination of factors. These include experimentally introduced air bubbles or large flocculates, which can distort the Raman signal, and overcorrections from preprocessing operations that may perform differently when the Raman spectra show unforeseen changes. Local concentration gradients due to possible heterogeneities in precipitant concentration could also cause scattered predictions, but there is no evidence for this in the AMS-related Raman bands. To further study the effect of noise on the model, perturbation studies [223] could be employed or the distribution of PLS weights could be assessed [272]. To effectively reduce the noise in the model, a larger data set preferably from fed-batch experiments would be required. Eventually, due to the non-linear relationship of the Raman spectra and the VLP concentration, non-linear regression models should be evaluated such as kernel-based methods [273–276] or neural networks [223, 257, 272].

6.5 Conclusion and Outlook

In conclusion, we present a Raman spectroscopy-based PAT for real-time monitoring of VLP precipitation from clarified *E. coli*-derived lysate as well as the precipitant concentration. The generated precipitation data provide a challenging data set with varying precipitation dynamics and backgrounds which were induced by spiking and are desirable for robust PAT sensor development. High experimental variance is successfully managed by employing a pretreatment approach for the UV absorbance data. The preprocessing pipeline including turbidity, baseline and OPLS-based background correction, difference spectra, cropping and derivative filtering is identified as optimal for removing all variations in the initial composition of the studied lysates as well as most interferences caused by precipitates and precipitant in solution. The final PLS models recover the observed trends in the batch and fed-batch data but lack to resolve fine differences between experiments owing to the non-linear relationship between spectral data and the precipitated VLP concentration. Additionally, the Raman data reveal structural differences between VLPs and HCPs and qualitatively support the selective precipitation of VLPs while nucleic acids and HCPs remain in solution. Overall, the developed preprocessing pipeline provides a foundation for integrating Raman spectroscopy as a PAT sensor for monitoring particulate-containing bioprocesses and bears the potential to be applied to other phase behavior-dependent processes for protein purification.

Author Contributions

AD: Conceptualization, Formal Analysis, Investigation, Methodology, Visualization, Writing–original draft, Writing–review and editing. RS: Conceptualization, Formal Analysis, Methodology, Software, Visualization, Writing–original draft, Writing–review and editing. JK: Investigation, Software, Writing–review and editing. SZ: Investigation, Writing–review and editing. JH: Conceptualization, Funding acquisition, Supervision, Writing-review and editing.

Supplementary Material

Appendix **A6** contains the Supplementary Material associated with this chapter.

Chapter References

[11] C. L. Effio and J. Hubbuch. „Next generation vaccines and vectors: Designing downstream processes for recombinant protein-based virus-like particles“. In: *Biotechnology Journal* 10.5 (2015), pp. 715–727. DOI: 10.1002/biot.201400392.

[14] FDA. *Guidance for Industry: PAT—a framework for innovative pharmaceutical development, manufacturing, and quality assurance*. 2004.

[16] M. Rüdt, P. Vormittag, N. Hillebrandt, and J. Hubbuch. „Process monitoring of virus-like particle reassembly by diafiltration with UV/Vis spectroscopy and light scattering“. In: *Biotechnology and Bioengineering* 116.6 (2019), pp. 1366–1379. DOI: 10.1002/bit.26935.

[17] N. Hillebrandt, P. Vormittag, A. Dietrich, and J. Hubbuch. „Process monitoring framework for cross-flow diafiltration-based virus-like particle disassembly: Tracing product properties and filtration performance“. In: *Biotechnology and Bioengineering* 119.6 (2022), pp. 1522–1538. DOI: 10.1002/bit.28063.

[18] L. J. Lohmann and J. Strube. „Process analytical technology for precipitation process integration into biologics manufacturing towards autonomous operation—mab case study“. In: *Processes* 9.3 (2021). DOI: 10.3390/pr9030488.

[39] B. Chackerian. „Virus-like particles: Flexible platforms for vaccine development“. In: *Expert Review of Vaccines* 6.3 (2007), pp. 381–390. DOI: 10.1586/14760584.6.3.381.

[40] N. Kushnir, S. J. Streatfield, and V. Yusibov. „Virus-like particles as a highly efficient vaccine platform: Diversity of targets and production systems and advances in clinical development“. In: *Vaccine* 31.1 (2012), pp. 58–83. DOI: 10.1016/j.vaccine.2012.10.083.

[42] Y. Liu, M. Pietzsch, and J. Ulrich. „Determination of the phase diagram for the crystallization of L-asparaginase II by a turbidity technique“. In: *Crystal Research and Technology* 49.4 (2014), pp. 262–268. DOI: 10.1002/crat.201300402.

[43] S. Nooraei et al. „Virus-like particles: preparation, immunogenicity and their roles as nanovaccines and drug nanocarriers“. In: *Journal of Nanobiotechnology* 19.1 (2021), p. 59. DOI: 10.1186/s12951-021-00806-7.

[49] A. Zlotnick et al. „Dimorphism of Hepatitis B Virus Capsids Is Strongly Influenced by the C-Terminus of the Capsid Protein“. In: *Biochemistry* 35.23 (1996), pp. 7412–7421. DOI: 10.1021/bi9604800.

[52] A. Valentic, J. Müller, and J. Hubbuch. „Effects of Different Lengths of a Nucleic Acid Binding Region and Bound Nucleic Acids on the Phase Behavior and Purification Process of HBcAg Virus-Like Particles“. In: *Frontiers in Bioengineering and Biotechnology* 10 (2022). DOI: 10.3389/fbioe.2022.929243.

[53] T. Klamp et al. „Highly Specific Auto-Antibodies against Claudin-18 Isoform 2 Induced by a Chimeric HBcAg Virus-Like Particle Vaccine Kill Tumor Cells and Inhibit the Growth of Lung Metastases“. In: *Cancer Research* 71.2 (2011), pp. 516–527. DOI: 10.1158/0008-5472.CAN-10-2292.

[54] M. Moradi Vahdat et al. „Hepatitis B core-based virus-like particles: A platform for vaccine development in plants“. In: *Biotechnology Reports* 29 (2021), e00605. DOI: 10.1016/j.btre.2021.e00605.

[55] A. M. Hassebroek et al. „A hepatitis B virus core antigen-based virus-like particle vaccine expressing SARS-CoV-2 B and T cell epitopes induces epitope-specific humoral and cell-mediated immune responses but confers limited protection against SARS-CoV-2 infection“. In: *Journal of Medical Virology* 95.2 (2023). DOI: 10.1002/jmv.28503.

[56] A. Zeltins. „Construction and Characterization of Virus-Like Particles: A Review“. In: *Molecular Biotechnology* 53.1 (2013), pp. 92–107. DOI: 10.1007/s12033-012-9598-4.

[57] M. G. Moleirinho, R. J. Silva, P. M. Alves, M. J. T. Carrondo, and C. Peixoto. „Current challenges in biotherapeutic particles manufacturing“. In: *Expert Opinion on Biological Therapy* 20.5 (2020), pp. 451–465. DOI: 10.1080/14712598.2020.1693541.

[65] I. Petrovskis et al. „Production of the HBc Protein from Different HBV Genotypes in E. coli. Use of Reassociated HBc VLPs for Packaging of ss- and dsRNA“. In: *Microorganisms* 9.2 (2021), p. 283. DOI: 10.3390/microorganisms9020283.

[67] A. Cooper and Y. Shaul. „Recombinant viral capsids as an efficient vehicle of oligonucleotide delivery into cells“. In: *Biochemical and Biophysical Research Communications* 327.4 (2005), pp. 1094–1099. DOI: 10.1016/j.bbrc.2004.12.118.

[68] J. Z. Porterfield, M. S. Dhason, D. D. Loeb, M. Nassal, S. J. Stray, and A. Zlotnick. „Full-Length Hepatitis B Virus Core Protein Packages Viral and Heterologous RNA with Similarly High Levels of Cooperativity“. In: *Journal of Virology* 84.14 (2010), pp. 7174–7184. DOI: 10.1128/JVI.00586-10.

[75] M. d. C. Pons Royo, J. L. Beulay, E. Valery, A. Jungbauer, and P. Satzer. „Mode and dosage time in polyethylene glycol precipitation process influences protein precipitate size and filterability“. In: *Process Biochemistry* 114 (2022), pp. 77–85. DOI: 10.1016/j.procbio.2022.01.017.

[77] R. A. Curtis, J. M. Prausnitz, and H. W. Blanch. „Protein-protein and protein-salt interactions in aqueous protein solutions containing concentrated electrolytes“. In: *Biotechnology and Bioengineering* 57.1 (1998), pp. 11–21. DOI: 10.1002/(SICI)1097-0290(19980105)57:1<11::AID-BIT2>3.0.CO;2-Y.

[81] S. Tsoka, O. C. Ciniawskyj, O. R. T. Thomas, N. J. Titchener-Hooker, and M. Hoare. „Selective Flocculation and Precipitation for the Improvement of Virus-Like Particle Recovery from Yeast Homogenate“. In: *Biotechnology Progress* 16.4 (2000), pp. 661–667. DOI: 10.1021/bp0000407.

[82] T. Koho et al. „Purification of norovirus-like particles (VLPs) by ion exchange chromatography“. In: *Journal of Virological Methods* 181.1 (2012), pp. 6–11. DOI: 10.1016/j.jviromet.2012.01.003.

[83] H. J. Kim, S. Y. Kim, S. J. Lim, J. Y. Kim, S. J. Lee, and H. J. Kim. „One-step chromatographic purification of human papillomavirus type 16 L1 protein from Saccharomyces cerevisiae“. In: *Protein Expression and Purification* 70.1 (2010), pp. 68–74. DOI: 10.1016/j.pep.2009.08.005.

[84] M. Zahin et al. „Scalable production of HPV16 L1 protein and VLPs from tobacco leaves“. In: *PLoS ONE* 11.8 (2016), pp. 1–16. DOI: 10.1371/journal.pone.0160995.

[85] A. Kazaks et al. „Production and purification of chimeric HBc virus-like particles carrying influenza virus LAH domain as vaccine candidates“. In: *BMC Biotechnology* 17.1 (2017), pp. 1–11. DOI: 10.1186/s12896-017-0396-8.

[88] N. Hillebrandt, P. Vormittag, N. Bluthardt, A. Dietrich, and J. Hubbuch. „Integrated Process for Capture and Purification of Virus-Like Particles: Enhancing Process Performance by Cross-Flow Filtration“. In: *Frontiers in Bioengineering and Biotechnology* 8 (2020). DOI: 10.3389/fbioe.2020.00489.

[89] S. Großhans, S. Suhm, and J. Hubbuch. „Precipitation of complex antibody solutions: influence of contaminant composition and cell culture medium on the precipitation behavior“. In: *Bioprocess and Biosystems Engineering* (2019). DOI: 10.1007/s00449-019-02103-y.

[90] C. H. Wegner and J. Hubbuch. „Calibration-free PAT: Locating selective crystallization or precipitation sweet spot in screenings with multi-way PARAFAC models“. In: *Frontiers in Bioengineering and Biotechnology* 10 (2022), pp. 1–18. DOI: 10.3389/fbioe.2022.1051129.

[112] A. S. Rathore, R. Bhambure, and V. Ghare. „Process analytical technology (PAT) for biopharmaceutical products“. In: *Analytical and Bioanalytical Chemistry* 398.1 (2010), pp. 137–154. DOI: 10.1007/s00216-010-3781-x.

[113] J. Glassey et al. „Process analytical technology (PAT) for biopharmaceuticals“. In: *Biotechnology Journal* 6.4 (2011), pp. 369–377. DOI: 10.1002/biot.201000356.

[131] N. C. Maiti, M. M. Apetri, M. G. Zagorski, P. R. Carey, and V. E. Anderson. „Raman Spectroscopic Characterization of Secondary Structure in Natively Unfolded Proteins: α-Synuclein“. In: *Journal of the American Chemical Society* 126.8 (2004), pp. 2399–2408. DOI: 10.1021/ja0356176.

[132] A. Rygula, K. Majzner, K. M. Marzec, A. Kaczor, M. Pilarczyk, and M. Baranska. „Raman spectroscopy of proteins: A review“. In: *Journal of Raman Spectroscopy* 44.8 (2013), pp. 1061–1076. DOI: 10.1002/jrs.4335.

[133] L. G. d. O. Guardalini et al. „Comparison of chemometric models using Raman spectroscopy for offline biochemical monitoring throughout the VLP-making upstream process“. In: *Biochemical Engineering Journal* 198 (2023), p. 109013. DOI: 10.1016/j.bej.2023.109013.

[134] L. G. d. O. Guardalini et al. „Biochemical monitoring throughout all stages of rabies virus-like particles production by Raman spectroscopy using global models“. In: *Journal of Biotechnology* 363 (2023), pp. 19–31. DOI: 10.1016/j.jbiotec.2022.12.009.

[135] L. G. d. O. Guardalini et al. „Monitoring by Raman spectroscopy of rabies virus-like particles production since the initial development stages“. In: *Journal of Chemical Technology & Biotechnology* 99 (2023), pp. 658–673. DOI: 10.1002/jctb.7571.

[137] L. Rolinger, J. Hubbuch, and M. Rüdt. „Monitoring of ultra- and diafiltration processes by Kalman-filtered Raman measurements“. In: *Analytical and Bioanalytical Chemistry* 415.5 (2023), pp. 841–854. DOI: 10.1007/s00216-022-04477-7.

[138] D. Weber and J. Hubbuch. „Raman spectroscopy as a process analytical technology to investigate biopharmaceutical freeze concentration processes“. In: *Biotechnology and Bioengineering* 118.12 (2021), pp. 4708–4719. DOI: 10.1002/bit.27936.

[139] Å. Rinnan, L. Nørgaard, F. V. D. Berg, J. Thygesen, R. Bro, and S. B. Engelsen. „Data Pre-processing“. In: *Infrared Spectroscopy for Food Quality Analysis and Control*. Vol. 3. Academic Press, 2009. Chap. 2, pp. 29–50.

[140] R. Gautam, S. Vanga, F. Ariese, and S. Umapathy. „Review of multidimensional data processing approaches for Raman and infrared spectroscopy“. In: *EPJ Techniques and Instrumentation* 2.1 (2015). DOI: 10.1140/epjti/s40485-015-0018-6.

[141] T. Bocklitz, A. Walter, K. Hartmann, P. Rösch, and J. Popp. „How to pre-process Raman spectra for reliable and stable models?“ In: *Analytica Chimica Acta* 704.1-2 (2011), pp. 47–56. DOI: 10.1016/j.aca.2011.06.043.

[142] T. Mehmood, K. H. Liland, L. Snipen, and S. Sæbø. „A review of variable selection methods in Partial Least Squares Regression“. In: *Chemometrics and Intelligent Laboratory Systems* 118 (2012), pp. 62–69. DOI: 10.1016/j.chemolab.2012.07.010.

[144] S. Wold, M. Sjöström, and L. Eriksson. „PLS-regression: a basic tool of chemometrics“. In: *Chemometrics and Intelligent Laboratory Systems* 58.2 (2001), pp. 109–130. DOI: 10.1016/S0169-7439(01)00155-1.

[195] C. Qian et al. „Recent Progress on the Versatility of Virus-Like Particles“. In: *Vaccines* 8.1 (2020), p. 139. DOI: 10.3390/vaccines8010139.

[202] F. Zhang et al. „Baseline correction for infrared spectra using adaptive smoothness parameter penalized least squares method“. In: *Spectroscopy Letters* 53.3 (2020), pp. 222–233. DOI: 10.1080/00387010.2020.1730908.

[203] A. Savitzky and M. J. E. Golay. „Smoothing and Differentiation of Data by Simplified Least Squares Procedures.“ In: *Analytical Chemistry* 36.8 (1964), pp. 1627–1639. DOI: 10.1021/ac60214a047.

[204] E. Gasteiger et al. „Protein Identification and Analysis Tools on the ExPASy Server“. In: *The Proteomics Protocols Handbook* (2005), pp. 571–607. DOI: 10.1385/1-59259-890-0:571.

[213] P. Iverius and T. Laurent. „Precipitation of some plasma proteins by the addition of dextran or polyethylene glycol“. In: *Biochimica et Biophysica Acta (BBA) - Protein Structure* 133.2 (1967), pp. 371–373. DOI: 10.1016/0005-2795(67)90079-7.

[214] A. Poison. „A Theory for the Displacement of Proteins and Viruses with Polyethylene Glycol“. In: *Preparative Biochemistry* 7.2 (1977), pp. 129–154. DOI: 10.1080/00327487708061631.

[215] F. Hämmerling, C. Ladd Effio, S. Andris, J. Kittelmann, and J. Hubbuch. „Investigation and prediction of protein precipitation by polyethylene glycol using quantitative structure–activity relationship models“. In: *Journal of Biotechnology* 241 (2017), pp. 87–97. DOI: 10.1016/j.jbiotec.2016.11.014.

[216] S. Mobini, M. Chizari, L. Mafakher, E. Rismani, and E. Rismani. „Computational Design of a Novel VLP-Based Vaccine for Hepatitis B Virus“. In: *Frontiers in Immunology* 11 (2020). DOI: 10.3389/fimmu.2020.02074.

[217] B. Li, P. W. Ryan, B. H. Ray, K. J. Leister, N. M. Sirimuthu, and A. G. Ryder. „Rapid characterization and quality control of complex cell culture media solutions using Raman spectroscopy and chemometrics“. In: *Biotechnology and Bioengineering* 107.2 (2010), pp. 290–301. DOI: 10.1002/bit.22813.

[218] N. R. Abu-Absi et al. „Real time monitoring of multiple parameters in mammalian cell culture bioreactors using an in-line Raman spectroscopy probe“. In: *Biotechnology and Bioengineering* 108.5 (2011), pp. 1215–1221. DOI: 10.1002/bit.23023.

[219] B. Berry, J. Moretto, T. Matthews, J. Smelko, and K. Wiltberger. „Cross-scale predictive modeling of CHO cell culture growth and metabolites using Raman spectroscopy and multivariate analysis“. In: *Biotechnology Progress* 31.2 (2015), pp. 566–577. DOI: 10.1002/btpr.2035.

[220] A. Golabgir and C. Herwig. „Combining Mechanistic Modeling and Raman Spectroscopy for Real-Time Monitoring of Fed-Batch Penicillin Production“. In: *Chemie-Ingenieur-Technik* 88.6 (2016), pp. 764–776. DOI: 10.1002/cite.201500101.

[221] Feidl et al. „Combining Mechanistic Modeling and Raman Spectroscopy for Monitoring Antibody Chromatographic Purification“. In: *Processes* 7.10 (2019), p. 683. DOI: 10.3390/pr7100683.

[222] L. Rolinger, M. Rüdt, and J. Hubbuch. „Comparison of UV- and Raman-based monitoring of the Protein A load phase and evaluation of data fusion by PLS models and CNNs“. In: *Biotechnology and Bioengineering* 118.11 (2021), pp. 4255–4268. DOI: 10.1002/bit.27894.

[223] J. Wang, J. Chen, J. Studts, and G. Wang. „In-line product quality monitoring during biopharmaceutical manufacturing using computational Raman spectroscopy“. In: *mAbs* 15.1 (2023). DOI: 10.1080/19420862.2023.2220149.

[224] U. Roessl, S. Leitgeb, S. Pieters, T. De Beer, and B. Nidetzky. „In situ protein secondary structure determination in ice: Raman spectroscopy-based process analytical tool for frozen storage of biopharmaceuticals“. In: *Journal of Pharmaceutical Sciences* 103.8 (2014), pp. 2287–2295. DOI: 10.1002/jps.24072.

[225] B. Wei et al. „Multi-attribute Raman spectroscopy (MARS) for monitoring product quality attributes in formulated monoclonal antibody therapeutics“. In: *mAbs* 14.1 (2022). DOI: 10.1080/19420862.2021.2007564.

[226] Z. Sun et al. „Assessment of the human albumin in acid precipitation process using NIRS and multi-variable selection methods combined with SPA“. In: *Journal of Molecular Structure* 1199 (2020), p. 126942. DOI: 10.1016/j.molstruc.2019.126942.

[227] L. Li et al. „The relevance study of effective information between near infrared spectroscopy and chondroitin sulfate in ethanol precipitation process“. In: *Journal of Innovative Optical Health Sciences* 7.6 (2014), pp. 1–7. DOI: 10.1142/S1793545814500229.

[228] Z. Sun et al. „Calibration transfer of near infrared spectrometers for the assessment of plasma ethanol precipitation process“. In: *Chemometrics and Intelligent Laboratory Systems* 181 (2018), pp. 64–71. DOI: 10.1016/j.chemolab.2018.08.012.

[229] H. Huang and H. Qu. „In-situ monitoring of saccharides removal of alcohol precipitation using near-infrared spectroscopy“. In: *Journal of Innovative Optical Health Sciences* 11.5 (2018), pp. 1–12. DOI: 10.1142/S179354581850027X.

[230] J. Meyer-Kirschner et al. „In-line Monitoring of Monomer and Polymer Content during Microgel Synthesis Using Precipitation Polymerization via Raman Spectroscopy and Indirect Hard Modeling“. In: *Applied Spectroscopy* 70.3 (2016), pp. 416–426. DOI: 10.1177/0003702815626663.

[231] M. D. Van Brink, M. Pepers, and A. M. Van Herk. „Raman spectroscopy of polymer latexes“. In: *Journal of Raman Spectroscopy* 33.4 (2002), pp. 264–272. DOI: 10.1002/jrs.834.

[232] J. V. Sinfield and C. K. Monwuba. „Assessment and correction of turbidity effects on Raman observations of chemicals in aqueous solutions“. In: *Applied Spectroscopy* 68.12 (2014), pp. 1381–1392. DOI: 10.1366/13-07292.

[233] M. Zelger, S. Pan, A. Jungbauer, and R. Hahn. „Real-time monitoring of protein precipitation in a tubular reactor for continuous bioprocessing“. In: *Process Biochemistry* 51.10 (2016), pp. 1610–1621. DOI: 10.1016/j.procbio.2016.06.018.

[234] R. M. Santos, J. M. Kessler, P. Salou, J. C. Menezes, and A. Peinado. „Monitoring mAb cultivations with in-situ raman spectroscopy: The influence of spectral selectivity on calibration models and industrial use as reliable PAT tool“. In: *Biotechnology Progress* 34.3 (2018), pp. 659–670. DOI: 10.1002/btpr.2635.

[235] S. Goldrick et al. „High-Throughput Raman Spectroscopy Combined with Innovate Data Analysis Workflow to Enhance Biopharmaceutical Process Development“. In: *Processes* 8.9 (2020), p. 1179. DOI: 10.3390/pr8091179.

[236] M. Hassoun et al. „A droplet-based microfluidic chip as a platform for leukemia cell lysate identification using surface-enhanced Raman scattering“. In: *Analytical and Bioanalytical Chemistry* 410.3 (2018), pp. 999–1006. DOI: 10.1007/s00216-017-0609-y.

[237] E. Genova et al. „SERS of cells: What can we learn from cell lysates?“ In: *Analytica Chimica Acta* 1005 (2018), pp. 93–100. DOI: 10.1016/j.aca.2017.12.002.

[238] S. He et al. „Baseline correction for Raman spectra using an improved asymmetric least squares method“. In: *Anal. Methods* 6.12 (2014), pp. 4402–4407. DOI: 10.1039/C4AY00068D.

[239] S. Wold, H. Antti, F. Lindgren, and J. Öhman. „Orthogonal signal correction of near-infrared spectra“. In: *Chemometrics and Intelligent Laboratory Systems* 44.1-2 (1998), pp. 175–185. DOI: 10.1016/S0169-7439(98)00109-9.

[240] J. Trygg and S. Wold. „Orthogonal projections to latent structures (O-PLS)“. In: *Journal of Chemometrics* 16.3 (2002), pp. 119–128. DOI: 10.1002/cem.695.

[241] H. F. M. Boelens, R. J. Dijkstra, P. H. C. Eilers, F. Fitzpatrick, and J. A. Westerhuis. „New background correction method for liquid chromatography with diode array detection, infrared spectroscopic detection and Raman spectroscopic detection“. In: *Journal of Chromatography A* 1057.1-2 (2004), pp. 21–30. DOI: 10.1016/j.chroma.2004.09.035.

[242] H. Martens, J. P. Nielsen, and S. B. Engelsen. „Light scattering and light absorbance separated by extended multiplicative signal correction. Application to near-infrared transmission analysis of powder mixtures“. In: *Analytical Chemistry* 75.3 (2003), pp. 394–404. DOI: 10.1021/ac020194w.

[243] A. Kohler et al. „Estimating and Correcting Mie Scattering in Synchrotron-Based Microscopic Fourier Transform Infrared Spectra by Extended Multiplicative Signal Correction“. In: *Applied Spectroscopy* 62.3 (2008), pp. 259–266. DOI: 10.1366/000370208783759669.

[244] K. H. Liland, A. Kohler, and N. K. Afseth. „Model-based pre-processing in Raman spectroscopy of biological samples“. In: *Journal of Raman Spectroscopy* 47.6 (2016), pp. 643–650. DOI: 10.1002/jrs.4886.

[245] C. P. Passos, S. M. Cardoso, A. S. Barros, C. M. Silva, and M. A. Coimbra. „Application of Fourier transform infrared spectroscopy and orthogonal projections to latent structures/partial least squares regression for estimation of procyanidins average degree of polymerisation“. In: *Analytica Chimica Acta* 661.2 (2010), pp. 143–149. DOI: 10.1016/j.aca.2009.12.028.

[246] F. F. Abdallah, H. W. Darwish, I. A. Darwish, and I. A. Naguib. „Orthogonal projection to latent structures and first derivative for manipulation of PLSR and SVR chemometric models' prediction: A case study“. In: *PLoS ONE* 14.9 (2019), pp. 1–13. DOI: 10.1371/journal.pone.0222197.

[247] FDA. *Development and Submission of Near Infrared Analytical Procedures Guidance for Industry*. 2015.

[248] J. Z. Porterfield and A. Zlotnick. „A simple and general method for determining the protein and nucleic acid content of viruses by UV absorbance“. In: *Virology* 407.2 (2010), pp. 281–288. DOI: 10.1016/j.virol.2010.08.015.

[249] R. R. Wilcox. *Introduction to Robust Estimation and Hypothesis Testing*. Netherlands: Elsevier Science, 2005, p. 100.

[250] J. Soch and C. Allefeld. „MACS – a new SPM toolbox for model assessment, comparison and selection“. In: *Journal of Neuroscience Methods* 306 (2018), pp. 19–31. DOI: 10.1016/j.jneumeth.2018.05.017.

[251] E. Spinner. „Raman-spectral depolarisation ratios of ions in concentrated aqueous solution. The next-to-negligible effect of highly asymmetric ion surroundings on the symmetry properties of polarisability changes during vibrations of symmetric ions.“ In: *Spectrochimica Acta Part A: Molecular and Biomolecular Spectroscopy* 59.7 (2003), pp. 1441–1456. DOI: 10.1016/S1386-1425(02)00293-7.

[252] M. D. Fontana, K. Ben Mabrouk, and T. H. Kauffmann. „Raman spectroscopic sensors for inorganic salts“. In: *Spectroscopic Properties of Inorganic and Organometallic Compounds*. Ed. by J. Yarwood, R. Douthwaite, and S. Duckett. Vol. 44. RSC Publishing, 2013, pp. 40–67. DOI: 10.1039/9781849737791-00040.

[253] G. Socrates. *Infrared and Raman Characteristic Group Frequencies: Tables and Charts*. Wiley, 2004.

[254] G. H. Watson, W. B. Daniels, and C. S. Wang. „Measurements of Raman intensities and pressure dependence of phonon frequencies in sapphire“. In: *Journal of Applied Physics* 52.2 (1981), pp. 956–958. DOI: 10.1063/1.328785.

[255] A. Weber, S. P. S. Porto, L. E. Cheesman, and J. J. Barrett. „High-Resolution Raman Spectroscopy of Gases with cw-Laser Excitation*“. In: *JOSA* 57.1 (1967), pp. 19–28. DOI: 10.1364/JOSA.57.000019.

[256] W. L. Peticolas. „Raman spectroscopy of DNA and proteins“. In: *Methods in Enzymology*. Vol. 246. Elsevier Inc., 1995, pp. 389–416. DOI: 10.1016/0076-6879(95)46019-5.

[257] R. Schiemer, M. Rüdt, and J. Hubbuch. „Generative data augmentation and automated optimization of convolutional neural networks for process monitoring“. In: *Frontiers in Bioengineering and Biotechnology* 12 (2024), pp. 1–21. DOI: 10.3389/fbioe.2024.1228846.

[258] A. Moreno, J. Mas-Oliva, M. Soriano-García, C. Oliver Salvador, and V. Martín Bolaños-García. „Turbidity as a useful optical parameter to predict protein crystallization by dynamic light scattering“. In: *Journal of Molecular Structure* 519.1-3 (2000), pp. 243–256. DOI: 10.1016/S0022-2860(99)00318-X.

[259] H. Grön et al. „Dynamic in-process examination of particle size and crystallographic form under defined conditions of reactant supersaturation as associated with the batch crystallization of monosodium glutamate from aqueous solution“. In: *Industrial and Engineering Chemistry Research* 42.20 (2003), pp. 4888–4898. DOI: 10.1021/ie021037q.

[260] R. S. Harner, R. J. Ressler, R. L. Briggs, J. E. Hitt, P. A. Larsen, and T. C. Frank. „Use of a fiber-optic turbidity probe to monitor and control commercial-scale unseeded batch crystallizations“. In: *Organic Process Research and Development* 13.1 (2009), pp. 114–124. DOI: 10.1021/op8001504.

[261] F. Capito, R. Skudas, H. Kolmar, and C. Hunzinger. „At-line mid infrared spectroscopy for monitoring downstream processing unit operations“. In: *Process Biochemistry* 50.6 (2015), pp. 997–1005. DOI: 10.1016/j.procbio.2015.03.005.

[262] J. Chen, J. Wang, R. Hess, G. Wang, J. Studts, and M. Franzreb. „Application of Raman spectroscopy during pharmaceutical process development for determination of critical quality attributes in Protein A chromatography“. In: *Journal of Chromatography A* 1718 (2024), p. 464721. DOI: 10.1016/j.chroma.2024.464721.

[263] H. Falkenberg et al. „Mass spectrometric evaluation of upstream and downstream process influences on host cell protein patterns in biopharmaceutical products“. In: *Biotechnology Progress* 35.3 (2019). DOI: 10.1002/btpr.2788.

[264] F. Alsmeyer, H. J. Koß, and W. Marquardt. „Indirect spectral hard modeling for the analysis of reactive and interacting mixtures“. In: *Applied Spectroscopy* 58.8 (2004), pp. 975–985. DOI: 10.1366/0003702041655368.

[265] E. Kriesten, F. Alsmeyer, A. Bardow, and W. Marquardt. „Fully automated indirect hard modeling of mixture spectra“. In: *Chemometrics and Intelligent Laboratory Systems* 91.2 (2008), pp. 181–193. DOI: 10.1016/j.chemolab.2007.11.004.

[266] H. Martens and E. Stark. „Extended multiplicative signal correction and spectral interference subtraction: New preprocessing methods for near infrared spectroscopy“. In: *Journal of Pharmaceutical and Biomedical Analysis* 9.8 (1991), pp. 625–635. DOI: 10.1016/0731-7085(91)80188-F.

[267] S. Andris, M. Rüdt, J. Rogalla, M. Wendeler, and J. Hubbuch. „Monitoring of antibody-drug conjugation reactions with UV/Vis spectroscopy“. In: *Journal of Biotechnology* 288 (2018), pp. 15–22. DOI: 10.1016/j.jbiotec.2018.10.003.

[268] C. Zhou, W. Qi, E. N. Lewis, and J. F. Carpenter. „Concomitant Raman spectroscopy and dynamic light scattering for characterization of therapeutic proteins at high concentrations“. In: *Analytical Biochemistry* 472 (2015), pp. 7–20. DOI: 10.1016/j.ab.2014.11.016.

[269] V. V. Kuzmin, V. S. Novikov, L. Y. Ustynyuk, K. A. Prokhorov, E. A. Sagitova, and G. Y. Nikolaeva. „Raman spectra of polyethylene glycols: Comparative experimental and DFT study“. In: *Journal of Molecular Structure* 1217 (2020), p. 128331. DOI: 10.1016/j.molstruc.2020.128331.

[270] J. Gerretzen et al. „Simple and Effective Way for Data Preprocessing Selection Based on Design of Experiments“. In: *Analytical Chemistry* 87.24 (2015), pp. 12096–12103. DOI: 10.1021/acs.analchem.5b02832.

[271] B. Brunel, F. Alsamad, and O. Piot. „Toward automated machine learning in vibrational spectroscopy - use and settings of genetic algorithms for pre-processing and regression optimization“. In: *Chemometrics and Intelligent Laboratory Systems* 219.104444 (2021), pp. 1–10. DOI: https://doi.org/10.1016/j.chemolab.2021.104444.

[272] C. Cui and T. Fearn. „Modern practical convolutional neural networks for multivariate regression: Applications to NIR calibration“. In: *Chemometrics and Intelligent Laboratory Systems* 182 (2018), pp. 9–20. DOI: 10.1016/j.chemolab.2018.07.008.

[273] U. Thissen, M. Pepers, B. Üstün, W. J. Melssen, and L. M. C. Buydens. „Comparing support vector machines to PLS for spectral regression applications“. In: *Chemometrics and Intelligent Laboratory Systems* 73.2 (2004), pp. 169–179. DOI: 10.1016/j.chemolab.2004.01.002.

[274] I. Barman, C.-R. Kong, N. C. Dingari, R. R. Dasari, and M. S. Feld. „Development of Robust Calibration Models Using Support Vector Machines for Spectroscopic Monitoring of Blood Glucose“. In: *Analytical Chemistry* 82.23 (2010), pp. 9719–9726. DOI: 10.1021/ac101754n.

[275] D. A. Zavala-Ortiz et al. „Support Vector and Locally Weighted regressions to monitor monoclonal antibody glycosylation during CHO cell culture processes, an enhanced alternative to Partial Least Squares regression“. In: *Biochemical Engineering Journal* 154 (2020), p. 107457. DOI: 10.1016/j.bej.2019.107457.

[276] R. Schiemer, J. T. Weggen, K. M. Schmitt, and J. Hubbuch. „An adaptive soft-sensor for advanced real-time monitoring of an antibody-drug conjugation reaction“. In: *Biotechnology and Bioengineering* 120.7 (2023), pp. 1914–1928. DOI: 10.1002/bit.28428.

7

Raman-Based PAT for Multi-Attribute Monitoring during VLP Recovery by Dual-Stage CFF: Attribute-Specific Spectral Preprocessing for Model Transfer

Annabelle Dietrich[1], Luca Heim[1], and Jürgen Hubbuch[1]

[1] Institute of Process Engineering in Life Sciences, Section IV: Biomolecular Separation Engineering, Karlsruhe Institute of Technology (KIT), Karlsruhe, Germany

Abstract

Spectroscopic soft sensors are developed by combining spectral data with chemometric modeling, and offer as process analytical technology (PAT) tools powerful insights into biopharmaceutical processing. In this study, soft sensors based on Raman spectroscopy and linear or partial least squares (PLS) regression were developed and successfully transferred to a filtration-based recovery step of precipitated virus-like particles (VLPs). For near real-time monitoring of product accumulation and precipitant depletion, the dual-stage cross-flow filtration (CFF) set-up was equipped with an on-line loop in the second membrane stage. With this set-up, spectral data from three CFF runs were collected, differing in initial product concentration and process parameters. Under the scope of multi-attribute monitoring, a comprehensive investigation of the sensor sensitivity towards protein and precipitant and their Raman spectral features was carried out. This study reveals much higher sensitivity towards the precipitant ammonium sulfate (AMS) than the VLPs and the need for attribute-specific spectral preprocessing. To enhance the detector's sensitivity towards proteins, a higher exposure time was applied during CFF processing than during model building from pure-component stock solutions. As a result of this increased exposure time, the predominant sulfate band exhibited oversaturation effects, which otherwise could have been used for AMS quantification via linear regression. Nevertheless, AMS prediction using purpose-driven preprocessing operations and PLS models was achieved with normalization and a data-driven variable selection technique, next to baseline correction and signal smoothing. For VLP monitoring, a novel pre-cropping approach improved spectral appearance after further preprocessing in protein-associated wavenumber regions. However, fluctuations in prediction were much higher for VLPs than for AMS, and prediction accuracy was especially limited in low protein concentration ranges. These results highlight the potential of Raman-based PAT sensors for real-time monitoring of biopharmaceutical processes, while underscoring the general importance of attribute-specific selections of sensors, preprocessing operations, and models for PAT tool development.

7.1 Introduction

VLPs have emerged as a promising alternative to viral vectors, with applications ranging from vaccines to drug and gene delivery systems [195]. Structurally mimicking native viruses but lacking viral genetic material, VLPs offer a unique combination of safety and efficacy [39, 43, 56]. In vaccine application, their higher immunogenicity compared to subunit vaccines [41] can be even further directed or enhanced by surface modifications using genetic or chemical approaches [4]. Since Hepatitis B core Antigen (HBcAg) VLPs were expressed [46] and visualized [47] as one of the first VLPs, they continue to be the subject of ongoing research and recent advancements have been achieved in surface displays [54, 55] or payload packaging [65, 67, 68].

Due to the diverse structural complexity of different VLP types, purification strategies are usually developed individually, which may lead to costly manufacturing processes involving numerous unit operations [57]. The need for broadly applicable, scalable, and cost-effective manufacturing processes drives the development of novel purification strategies [11]. Due to the relatively large size of the VLPs, processes based on size-selective separation techniques such as precipitation or filtration exhibit standardized platform characteristics and provide an alternative to chromatographic methods [13]. Using CFF, buffer exchange by constant-volume diafiltration (DF) enables dynamic processes previously achieved only through dialysis or dilution, while also allowing product concentration

by ultrafiltration (UF) [36]. Recent developments have demonstrated the applicability of CFF throughout downstream processing of HBcAg VLPs, from the initial capture step for VLP re-dissolution from VLP precipitates [88, 277], to the final polishing steps including their disassembly into subunits [61] and subsequent reassembly into capsids [16]. These developments position filtration-based purification technologies at the forefront of standardized platform technologies for protein nanoparticle purification.

Filtration set-ups typically include in-line flow and pressure sensors to monitor and control standard process parameters such as transmembrane pressure and permeate flux [36]. However, gaining further insights into such dynamic processes typically relies on manual sampling and off-line analytics, limiting the scope of process understanding and resulting in product loss, especially in small-scale unit operations. In 2004, the FDA formally established the framework for PAT to support enhanced process understanding, monitoring, and control by measuring process parameters and product quality attributes [14]. Through sensor integration and evaluation of the collected data, process data can be continuously gathered in (near) real-time [112, 113]. In filtration set-ups, sensors are implemented directly in-line or within an on-line measurement loop. For the monitoring of quality attributes in biopharmaceutical filtration processes, several soft sensors have been recently developed by coupling spectroscopic sensors and chemometrics, including ultraviolet-visible (UV/Vis) [16, 17, 19], mid-infrared (MIR) [278], near-infrared (NIR) [20, 279, 280], and Raman spectroscopy [20, 137]. These spectroscopic sensors differ in their underlying measurement principles and inherent sensitivity to specific substances. While UV/Vis spectroscopy is highly accurate for protein concentrations and has already been used to monitor product variants [281] and quaternary structure [16, 17], the simultaneous monitoring of protein and excipient concentrations can be realized by MIR [278], NIR [280], or Raman spectroscopy [137, 138]. For Raman spectroscopy, recent advancements have been made towards monitoring of particulates in phase-behavior dependent processes, such as crystallized enzymes [136] or precipitated VLPs [201], as well as monitoring of multiple quality attributes during fermentation [234], chromatography [223], and formulation [225] of monoclonal antibodies.

Given the high sensitivity of Raman spectroscopy, raw Raman spectral data exhibit undesired variability, requiring considerable effort in data preparation before being used for modeling. Such pre-processing operations comprise signal correction techniques to correct baseline, background, or scattering effects, filter techniques to reduce uncorrelated noise or extract spectral features by derivative-filtering, and cropping techniques to reduce dimensions or focus on relevant spectral regions [139, 141]. Beyond manual selection of cropping intervals, ranging from solely discarding the edge regions to selecting spectral regions of interest, variable selection techniques offer data-driven selection, aiming to minimize the loss of important spectral data while improving model robustness [282]. Variable importance in projection (VIP) represents such a data-driven strategy, quantifying the contribution of each wavenumber to PLS models [142].

In many studies, however, a sequence of preprocessing operations with their parameters is given for a model presented, with limited in-depth analysis of Raman spectral features beforehand or explanations for choosing those operations. An approach addressing systematic soft sensor development was reported by Dietrich et al. [201], who first studied the effects of selected preprocessing operations on Raman spectral data before screening multiple combinations of preprocessing operations, so-called preprocessing pipelines, to assess the impact of individual operations on model performance. Although they demonstrated the quantification of selectively precipitated VLPs

in crude, clarified lysate through incorporation of specific preprocessing operations to account for turbidity and eliminate interferences caused by contaminating species, they reported limited transferability of the VLP models from off-line screening to on-line fed-batch data. Model transfer may be more successful in process stages with increased product purity, such as in the recovery step of these precipitated VLPs after reducing the impurity load.

Seamless VLP recovery is enabled by integrated dual-stage CFF, isolating the re-dissolved VLPs through precipitant depletion in the second membrane stage [277]. Here, Raman spectroscopy has already been used for off-line quantification of the precipitant, AMS, but so far, no attempt has been made to develop multi-attribute monitoring to provide simultaneous insights into VLP enrichment and AMS depletion.

In this study, we present a systematic, purpose-driven approach for PAT tool development for multi-attribute monitoring by Raman spectroscopy. The development aims for simultaneous insights into product accumulation and precipitant depletion during a filtration-based recovery step of precipitated VLPs using the integrated, dual-stage CFF set-up proposed by Dietrich et al. [277]. First, we investigate the contributions of product and precipitant to the spectral data using stock solutions of the pure components. Based on these insights and aiming to ultimately transfer the developed models to process data containing contributions of both species simultaneously, the effects of individual preprocessing operations on the Raman spectral data are thoroughly assessed. We develop regression models of varying complexity using either product- or precipitant-containing stock solutions and attribute-specific spectral preprocessing operations, thereby addressing challenges such as differences in detector sensitivity and detector saturation effects. By implementing Raman spectroscopy in an on-line loop in the second membrane stage of the dual-stage CFF setup, we collect process data in near real-time from three CFF experiments with variations in initial product concentration and process parameters. Eventually, we transfer the developed models to on-line process data to visualize the process dynamics of VLP recovery and precipitant depletion and demonstrate the importance of individual preprocessing operations for model transfer.

7.2 Materials and Methods

7.2.1 Virus-Like Particles

The VLP of interest assembles of C-terminally truncated wild-type HBcAg proteins (Cp149), for which the plasmids were initially provided by Prof. Adam Zlotnick from Indiana University [49]. The procedure of their intracellular expression in *Escherichia coli* (*E. coli*), cell harvest, cell lysis, and lysate clarification was performed as described in Hillebrandt et al. [88]. All clarified lysate material was pooled to create a single batch for all experiments. Clarified lysate was stored in aliquots at -20°C and thawed on the day of the experiments, followed by sterile filtration and conditioning for immediate use. Conditioning involved diluting the clarified lysate with pH 8.0 lysis buffer (50 mM Tris, 100 mM NaCl, 1 mM EDTA) to achieve a specific ultraviolet (UV) absorbance (EXP1–2) or spiking with VLP-enriched material (EXP3), and adjusting to 0.25% (v/v) polysorbate 20 for all experiments (EXP1–3). Note that the spiking (EXP3) was meant to match the level of host-cell impurities in the EXP1–2 material, so the spiking material replaced the amount of dilution material initially needed. The conditioning of clarified lysate is summarized for all experiments in Table 7.1. The VLP-enriched material was derived from the final product of EXP2, which was further dialyzed

Table 7.1 Experimental conditions of the three CFF experiments (EXP1–3).

Experiment	**Clarified lysate**	**Process**	**Process monitoring**		
	Condition	DV	On-line loop flow rate	Acquisition mode	Raman exposure time
	-	-	mL min^{-1}	-	ms
EXP1	dilution	6	0.6	semi-continuous	175 / 1250
EXP2	dilution	7	1.2	continuous	1250
EXP3	spike	7	1.2	continuous	1250

into the lysis buffer overnight using a 10 kDa MWCO Slide-A-Lyzer G2 cassette (Thermo Fisher Scientific Inc., Waltham, US).

7.2.2 Capture Process and Process Monitoring

Fully integrated processing was enabled using the dual-stage CFF setup presented by Dietrich et al. [277] with minor modifications. With this dual-stage CFF set-up, the VLP capture process involves selective VLP precipitation, followed by two consecutive, constant-volume DF steps for washing the VLP precipitates (DFI) and final recovery of the re-dissolved VLPs (DFII/UF). Precipitation and washing were similarly performed for all experiments according to Dietrich et al. [277], while several settings during VLP recovery (DFII/UF) differ between the experiments EXP1 and EXP2–3, as summarized in Table 7.1.

All consecutive process steps are illustrated schematically in Figure 7.1, and a piping and instrumentation diagram is additionally provided in Figure A7.1. Two serially connected KrosFlo Research KRIIi CFF units (Spectrum Labs, Rancho-Dominguez, US) were equipped with 0.2 µm and 300 kDa MWCO Hydrosart membranes (200 cm^2; Sartorius Stedim Biotech GmbH, Göttingen, DE), respectively. The permeate flow rates were controlled at 2 mL min^{-1} by an in-house developed, MATLAB-based backpressure valve controller, involving automatic backpressure valves (Spectrum Labs) in the retentate streams and SLS-1500 flow sensors (Sensirion AG, Stäfa, CH) in the permeate streams. An ÄKTA Start (Cytiva, Uppsala, SE) connected in series enabled permeate stream monitoring by in-line UV and conductivity sensors and collecting permeate stream fractions by the fraction collector. Valves were included in the setup to bypass the second CFF unit in the wash step (DFI). An on-line loop was further installed in the second CFF unit, including a Minipuls 3 peristaltic pump (Gilson, Villiers le Bel, FR), and a flow cell for Raman measurements. The on-line loop flow rate was set to 0.6 mL min^{-1} (EXP1) or 1.2 mL min^{-1} (EXP2–3).

Selective VLP precipitation was performed in the reservoir of the first CFF unit, which was induced by gradually adding the precipitant stock solution (4 M AMS) to the conditioned, clarified lysate until reaching the target precipitant concentration of 1.1 M AMS. Following a 30-minute incubation under stirring conditions, the wash step (DFI) was carried out, and the permeate bypassed the second CFF unit to monitor and collect the permeate stream directly. The VLP precipitates were washed with wash buffer (lysis buffer containing 1.1 M AMS) for 6 to 6.5 diafiltration volume (DV), until the UV absorbance of the permeate stream dropped below 60 mAU to ensure that the majority of still soluble impurities passed the 0.2 µm membrane. It has to be noted that the conductivity data have been qualitatively used as an indicator for the presence of AMS during the wash step (data not shown).

The VLPs were recovered in the second DF step (DFII) with pH 7.2 re-dissolution buffer (50 mM Tris, 150 mM NaCl) for six (EXP1) or seven DVs (EXP2–3) using the dual-stage CFF setup. DF induced VLP re-dissolution, the re-dissolved VLPs passed the 0.2 µm membrane and accumulated in the second CFF retentate, as they are not able to pass the 300 kDa MWCO membrane of the second CFF unit. By decoupling the first CFF unit, the accumulated VLPs were further concentrated from 25 mL (DV) to a final volume of 10 mL by integrated UF.

During this VLP recovery (DFII/UF), process monitoring was performed by semi-continuous (EXP1, alternating exposure times: 175 and 1250 ms) or continuous (EXP2–3, 1250 ms exposure time) Raman measurements in the implemented on-line loop to obtain on-line spectral data. Further, process samples for off-line analysis were taken at 0.5 DV, at each DV, and the final UF step. Off-line Raman measurements at 175 ms and 1250 ms were performed on each process sample to obtain off-line spectral data, alongside off-line UV spectroscopy to quantify the VLP content.

7.2.3 Stock Solutions for Model Building

AMS-containing stock solutions were prepared by proportionally mixing wash buffer and re-dissolution buffer to mimic the DF dynamic in the VLP recovery step (DFII) and hence fully cover the buffer composition and AMS content (0 - 1.1 M AMS). Raman spectra were recorded off-line at 110 and 175 nm exposure times and used for model building.

The VLP stock solution was derived from the final product of the dual-stage CFF process presented in the study by Dietrich et al. [277], which was further concentrated by UF using Vivaspin 20 centrifugal filters (Sartorius Stedim Biotech GmbH). A dilution series of the VLP stock solution using the re-dissolution buffer was prepared and off-line measured by Raman spectroscopy at an exposure time of 1250 ms. The spectral data were used for model building.

7.2.4 Analytics

7.2.4.1 Raman Spectroscopy

The Raman spectrometer HyperFlux™ PRO Plus 785 (Tornado Spectral Systems, Toronto, CA) was equipped with a BioReactor BallProbe within a flow cell (both MarqMetrix, Seattle, US) and controlled by SpectralSoft 3.2.6 (Tornado Spectral Systems). The spectra were recorded in the spectral range from 200 to 3300 cm^{-1} with 1 cm^{-1} resolution, a laser power of 495 mW, and exposure times of 175 or 1250 ms. For off-line Raman measurements, the flow cell was equipped with inlet and outlet capillaries and manually filled with the sample using a syringe.

7.2.4.2 UV Spectroscopy

The UV spectrometer consisted of an RS diode array detector integrated into a high performance liquid chromatography (HPLC) system, all controlled by Chromeleon 6.8 (Dionex Ultimate 3000 RS, Sunnyvale, US). Size-exclusion chromatography (SEC) using a BioSEC-5 column (4.6×300 mm, 5 µm, 1000 A; Agilent, Santa Clara, US) was used to separate differently sized species with method settings similar to Hillebrandt et al. [88]: 20 µL injection volume, 0.4 mL min^{-1} flow rate, and 14 min isocratic elution. The UV spectra were recorded in the spectral range from 220 to 400 nm. With peak areas at 280 nm, a universal purity measure regarding host-cell proteins (HCPs) and nucleic acids derived by dividing $A280_{VLP}$ by $A280_{total}$ and is described as SEC-purity. $A280_{VLP}$-derived

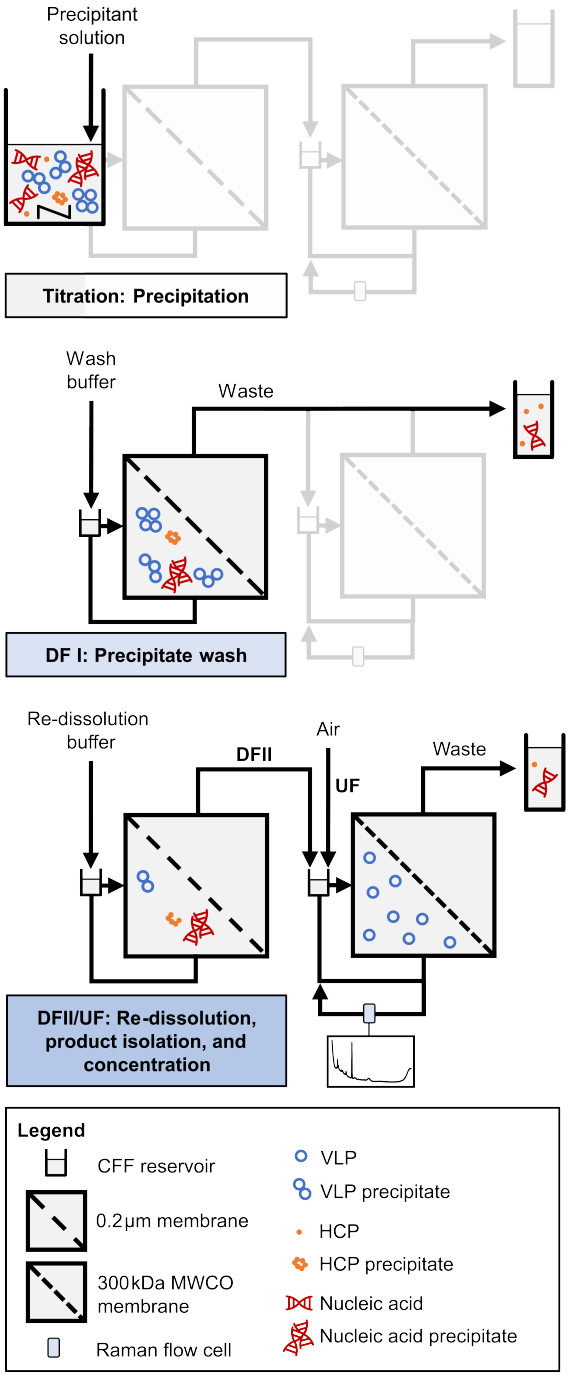

Figure 7.1 Schematic illustration of VLP processing by integrated dual-stage CFF. A dual-stage CFF set-up with a 0.2µm/300kDa MWCO membrane configuration is used for the process steps precipitation, precipitate wash (DFI), and VLP recovery (DFII/UF). VLP recovery involves DF-induced VLP re-dissolution, VLP isolation in the second membrane stage, and VLP concentration by subsequent UF. An on-line loop equipped with a Raman flow cell in the second membrane stage allows for near real-time monitoring by Raman spectroscopy. Adapted from Dietrich et al. [277].

VLP concentrations were calculated using Beer's law and a theoretical Cp149 extinction coefficient of 1.764 $g\,L^{-1}$ (ProtParam tool; Gasteiger et al. [204]).

7.2.5 Data Analysis and Computation

Data analysis and computation were performed in Python 3.8. Different strategies were used for spectral data preprocessing and regression modeling for AMS and VLP quantification. Model building was exclusively performed with off-line spectral data derived from stock solutions. The evaluated error metrics included the root mean squared error (RMSE) and the coefficient of determination (R^2) to assess model accuracy.

7.2.5.1 Spectral Data Processing and Model Building—AMS

Spectral data preprocessing covered averaging, normalization, baseline correction, smoothing, and cropping. Averaged spectra from 50 recordings were normalized using the OH Raman band at 3299 cm^{-1} to account for turbidity effects and variations in applied exposure times. A Whittaker filter employing the adaptive smoothness penalized least squares (asPLS) [283] was applied for baseline correction (λ value of 6×10^7, second-order difference matrix, tolerance of 1×10^{-3}), followed by a Savitzky-Golay filter (SGF) for spectral smoothing (second-degree polynomial, window size of 11). Three cropping strategies were applied to account for selected features attributed to AMS. The wavenumber 980 cm^{-1} reflecting the highest intensity was used for a linear regression model (LR_{AMS}). Unaffected by edge effects from prior baseline correction, the spectral interval 340–2650 cm^{-1} was selected for a PLS model (PLS_{AMS}). To qualitatively assess the importance of specific wavenumbers and identify AMS-associated regions, VIP scores were applied according to Mehmood et al. [142]. The resulting spectral intervals, 427–471, 600–634, 960–999, and 1103–1115 cm^{-1}, were scaled to unit variance and subsequently used for regression modeling for refined PLS models (PLS-VIP4$_{AMS}$, PLS-VIP2$_{AMS}$).

Spectra recorded at 175 ms exposure time were used for model building. For both PLS models, hyperparameter optimization with the number of latent variables in the range of 2–10 was performed by cross-validation using a random split of 80% training data and 20% validation data. The NIPALS algorithm was applied according to Wold et al. [144]. For all regression models, spectra recorded at 110 ms exposure time were used as test data.

7.2.5.2 Spectral Data Processing and Model Building—VLP

Spectral data preprocessing included averaging, pre-cropping, baseline correction, smoothing, and cropping. Two pre-cropping (P1/P2) and cropping (C1/C2) intervals were combined, resulting in four differently preprocessed spectra for model building (PLS-PX-CY$_{VLP}$). Averaged spectra from 50 recordings were first pre-cropped by excluding the wavenumber ranges between 920 and 1030 cm^{-1} (P1) or between 920 and 1200 cm^{-1} (P2), which includes the region with the highest AMS-associated intensity. Baseline correction was performed by employing the Whittaker filter (λ value of 1×10^9, third-order difference matrix, tolerance of 1×10^{-4}), followed by SGF-based spectral smoothing. Further, the spectra were cropped to the interval 1203–1349 cm^{-1} (C1) or 1331–1349 cm^{-1} (C2). Hyperparameter optimization and model building were performed, as described in Sec. 7.2.5.1, but spectra recorded at 1250 ms exposure time were used as test data.

7.3 Results

7.3.1 AMS: Raman Spectroscopy and Linear Regression for Precipitant Quantification

Raman spectra of AMS-containing stock solutions were recorded over the precipitant concentration range of 0–1.1 M AMS covering the range for VLP recovery by CFF. Spectral data recorded at 175 ms exposure time were used for preprocessing pipeline development and model building. Table 7.2 summarizes the parameter settings for spectral preprocessing operations and model building.

The spectral preprocessing pipeline involved normalization, baseline correction, and signal smoothing derived from the pipeline development of Dietrich et al. [277] to remove baseline drifts and enhance spectral differences. Figure 7.2 illustrates raw and preprocessed spectra of the AMS-containing stock solution set over the entire spectral range. In the raw spectra, precipitant-dependent baseline drifts are visible with baseline increases with higher AMS concentrations (cf. Figure 7.2 (A)). Baseline correction using the asPLS Whittaker filter, combined with smoothing using the SGF filter, consistently removed these baseline drifts across the entire recorded wavenumber range (cf. Figure 7.2 (B)). The distinct resolution of the predominant Raman band near 980 cm^{-1} is attributable to gradually increasing sulfate ions of AMS [251, 252]. In general, several components of precipitant and buffer contribute to the spectral appearance, which is described in Supplementary Sec. A7 and presented in a higher resolution in Supplementary Figure A7.2.

The uniformly preprocessed spectra have been cropped to a distinct wavenumber or wavenumber interval prior to regression modeling. Besides linear regression using the predominant sulfate-associated band maximum at 980 cm^{-1}, several PLS models were evaluated, differing in the cropped wavenumber intervals used for model building (cf. Table 7.2, Figure 7.2 (B)). Simple linear regression aligned well for the test set with a R^2 of 0.999 and a RMSE of 0.013 M AMS over the concentration range from 0 to 1.1 M AMS.

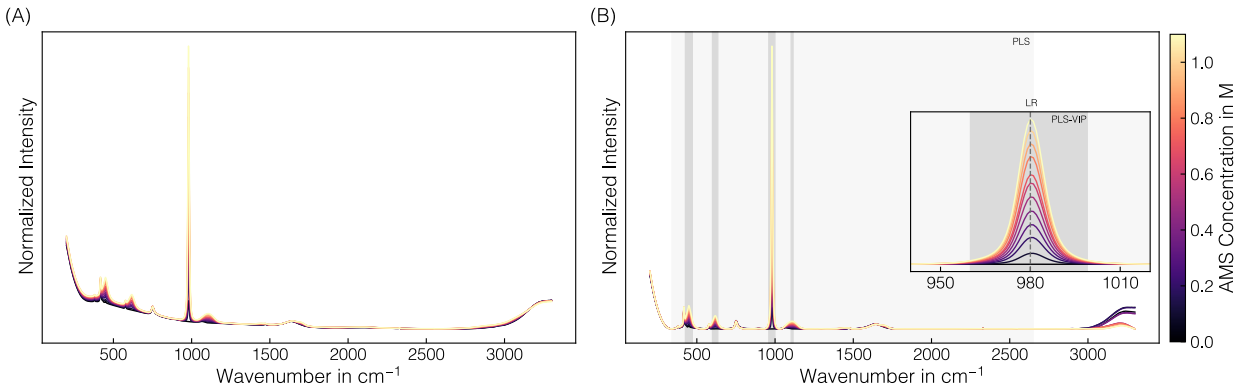

Figure 7.2 Raman spectral data: AMS. Derived from a set of stock solutions with varying AMS concentrations, averaged raw spectral data **(A)** were preprocessed by normalization, baseline correction, and smoothing **(B)**. The predominant Raman band near 980 cm^{-1} corresponding to the sulfate ion is used for linear regression. The PLS model includes the wavenumber interval 340–2650 cm^{-1} highlighted in light-gray, while the VIP-based intervals selected for the PLS-VIP models are shaded gray. The spectra are colored with brighter colors representing higher AMS concentrations.

Table 7.2 Spectral preprocessing and model building.

Model	**Normalization**	**Pre-cropping**	**Baseline**		**Smoothing**		**Cropping**	**Hyperparameter**
	Wavenumber cm^{-1}	Wavenumber cm^{-1}	Lambda	Derivative	Window	Polynom	Wavenumber cm^{-1}	Number of components -
LR_{AMS}	3299	-	6e-7	2	11	2	980	-
PLS_{AMS}	3299	-	6e-7	2	11	2	[340, 2650]	2
PLS-VIP4$_{AMS}$	3299	-	6e-7	2	11	2	[427,471],[600,634],[960,999],[1103,1115]	2
PLS-VIP2$_{AMS}$	3299	-	6e-7	2	11	2	[427,471],[1103,1115]	2
PLS-P1-C1$_{VLP}$	-	[920, 1030]	6e-9	2	11	2	[1203, 1349]	2
PLS-P1-C2$_{VLP}$	-	[920, 1030]	6e-9	2	11	2	[1331, 1349]	2
PLS-P2-C1$_{VLP}$	-	[920, 1200]	6e-9	3	11	2	[1203, 1349]	2
PLS-P2-C2$_{VLP}$	-	[920, 1200]	6e-9	3	11	2	[1331, 1349]	2

It has to be noted that cross-validated PLS models using the entire spectral range or selected wavenumber intervals identified through VIP scores showed comparable error metrics, with similar R^2 values and RMSE ranging between 0.010 and 0.013 M AMS. Interestingly, the VIP scores applied to qualitatively assess the importance of specific wavenumbers identified higher contributions of sulfate-associated than ammonium-associated regions. Further, scaling to unit variance improved error metrics for PLS-VIP$_{\mathrm{AMS}}$ models, but resulted in higher errors for a PLS model build with scaled spectral intensities (R^2: 0.990, RMSE: 0.035 M) than the presented PLS$_{\mathrm{AMS}}$ model without scaling (R^2: 0.999, RMSE: 0.012 M). Due to distinct sulfate Raman bands, noise-dominated regions may be mistakenly weighted as important in the scaled PLS model with noise-induced variations in areas lacking true signal.

In summary, simple spectral preprocessing followed by linear regression using the intensity at 980 cm^{-1} enables Raman spectroscopy for AMS content quantification. Spectral comparison suggests model transferability to CFF-based processes without buffer or protein species interference.

7.3.2 AMS: On-line Precipitant Quantification by PLS-VIP Model Transfer despite Different Exposure Times and Detector Saturation Effects

All the AMS models built on stock solutions were transferred to process-derived spectra to determine the AMS depletion throughout the CFF-based recovery step of the re-dissolved VLPs (DFII/UF). Figure 7.3 presents the predicted AMS concentrations for the applied AMS models on the off-line and on-line spectral data for the three CFF experiments (EXP1–3) performed.

Across all CFF experiments, the observed progression of the AMS concentration follows a distinct pattern, with first increasing and then, from the second DV onward, decreasing AMS concentrations. This progression in the second membrane stage is attributable to the process step (DFII). DF with re-dissolution buffer in the dual-stage CFF set-up leads to an overall AMS depletion present in the first membrane stage, resulting in an overlap of AMS accumulation and simultaneous AMS depletion in the second membrane stage. Comparable AMS progressions observed within the first six DVs of the DFII process indicate consistent and reproducible processing by dual-stage CFF. Extending the DFII process from six (EXP1) to seven DVs (EXP2–3) further reduced the AMS content in the final retentate before the subsequent UF, representing an improvement in the overall VLP recovery process.

All AMS models applied on off-line spectral data recorded at 175 ms Raman exposure time show comparable AMS content predictions at the sampling points (cf. Figure 7.3 (A)–(C)). With only one exception, the predictions of the PLS models fluctuate only marginally and without a distinct pattern around the prediction obtained using linear regression. However, all PLS-based AMS content predictions for the 0.5 DV sample in EXP2 deviate significantly from those of the linear regression (cf. Figure 7.3 (B)). Those observed deviations in prediction can be attributed to spectral appearance as PLS models incorporate additional spectral intervals beyond the 980 cm^{-1} band maximum used for linear regression. Since both under- and overestimations are observed, a generally defective spectrum has been suspected and identified (cf. Supplementary Figure A7.3 (A)). Overall, simple linear regression relying on the 980 cm^{-1} band intensity of preprocessed Raman spectra was successfully transferred to process-derived spectra for off-line AMS quantification.

For on-line AMS quantification, the on-line spectra derived from either semi-continuous (175 ms, EXP1) or continuous (1250 ms, EXP2–3) spectral acquisition were assessed regarding AMS pre-

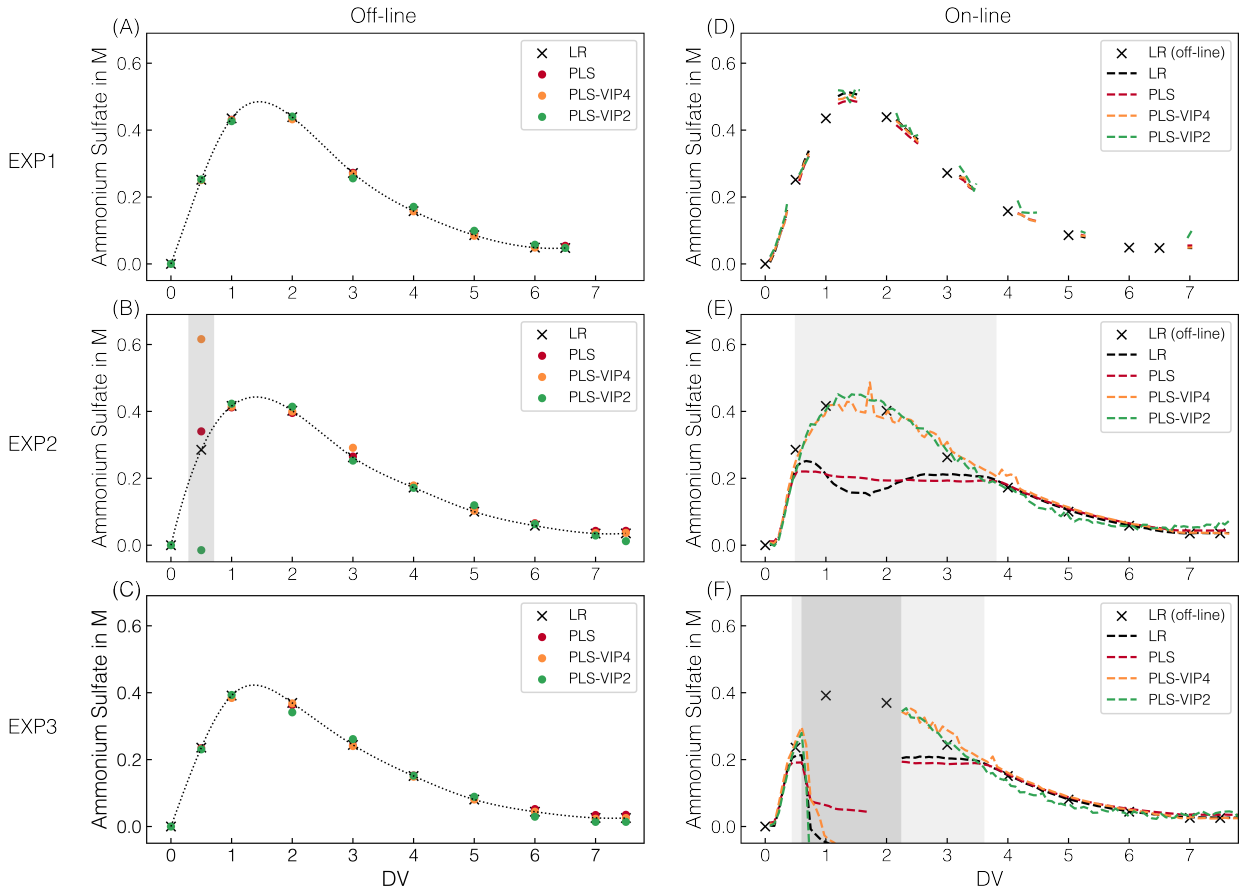

Figure 7.3 AMS model predictions. For all CFF runs, the predicted AMS concentrations are shown, which derived from individual off-line measurements at 175 ms exposure time (**(A)**–**(C)**) and on-line measurements (**(D)**–**(F)**) in semi-continuous (175 ms, EXP1) or continuous (1250 ms, EXP2–3) acquisition mode; along with their corresponding color assignments for the models used. Dotted lines (off-line) using a quadratic fit serve solely as visual guides to facilitate interpretation. The dashed lines (on-line) represent continuous prediction. Predictions by defective spectra are highlighted with dark-gray shaded areas. Predictions by spectra with oversaturation of the 980 cm^{-1} band at 1250 ms exposure time are shaded light-gray.

dictions (cf. Figure 7.3 (D)–(F)). In the semi-continuous spectral acquisition mode during EXP1, spectra were continuously recorded in time frames around the sampling points using the same Raman exposure time of 175 ms as for off-line AMS quantification.

The PLS-VIP2$_{AMS}$ model predictions exhibit marginal fluctuations within those time frames compared to the more consistent predictions of all other models (cf. Figure 7.3 (D)). However, those consistent and to off-line quantification comparably precise predictions provide a solid basis for continuous process monitoring in near real-time.

Given that a higher exposure time of 1250 ms is required for the later model transfer for simultaneous VLP prediction, continuous spectral acquisition at 1250 ms was performed during EXP2–3. The higher applied exposure time led to an oversaturation of the predominant 980 cm^{-1} sulfate band, resulting in a distinctive appearance of the corresponding band region. Exemplarily illustrated for

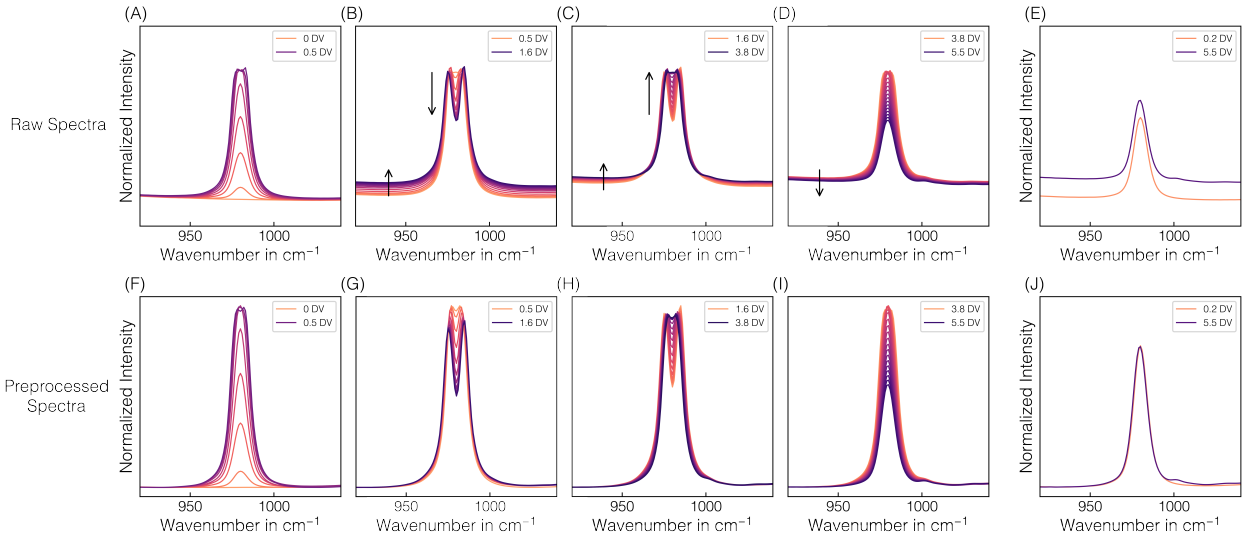

Figure 7.4 Spectral oversaturation effects. The changes in spectral appearance of the predominant 980 cm^{-1} sulfate band in the raw (**(A)**–**(E)**) and preprocessed (**(F)**–**(J)**) Raman spectra from EXP2 on-line Raman measurements are depicted and resolved by DV in panels to visualize the spectral effects of oversaturation: reaching saturation after 0.5 DV (**(A)**, **(F)**), remaining in a oversaturated state due to the still increasing AMS concentration until 1.6 DV (**(B)**, **(G)**) and a further decreasing AMS concentration (**(C)**, **(H)**) until reaching the AMS concentration at 3.8 DV after which the system falls below saturation again (**(D)**, **(I)**). Arrows serve as visual guides to highlight the formation or decay of the split peak depending on the AMS concentration in the saturated state (**(B)**, **(C)**) and baseline shifts (**(B)**–**(D)**). Additionally, two spectra obtained at 0.2 DV and 5.5 DV at identical AMS concentrations are shown (**(E)**, **(J)**).

EXP2, Figure 7.4 shows raw and preprocessed spectral data of the 980 cm^{-1} sulfate band region, resolved by DV in panels to visualize the spectral effects of oversaturation.

The greater the oversaturation with higher AMS concentrations until 1.6 DV, the more pronounced the resulting split peak appears, and the more distinct the baseline shift towards higher intensities is observed (cf. Figure 7.4 (B)). With afterwards decreasing AMS concentrations and the corresponding reformation of the split peak, the baseline shifts slightly further towards higher intensities, contrary to the expectation (cf. Figure 7.4 (C)). Only later in the process is a slight baseline shift towards lower intensities observed (cf. Figure 7.4 (D)), but the baseline no longer reaches its initial level. The difference in the baseline level is exemplified by two spectra with identical AMS concentration but recorded at different DVs (cf. Figure 7.4 (E)). As expected, this difference in the baseline level is no longer apparent after preprocessing (cf. Figure 7.4 (J)), as is the case for all previously described baseline shifts (cf. Figure 7.4 (G)–(I)). The unexpected behavior of the baseline shift suggests the influence of a secondary factor unrelated to AMS concentration.

The split peak appearance is reflected in the incorrect predictions between 0.5 and 3.6–3.8 DVs when applying the linear regression and the PLS_{AMS} model (cf. Figure 7.3 (E),(F)). These two models can only reliably predict the AMS concentration as long as saturation does not occur, which corresponds to approximately 0.2 M AMS as critical AMS concentration at the exposure time of 1250 ms. As expected, the progression of the predicted AMS concentration during oversaturation using linear

regression directly reflects the split peak behavior at 980 cm^{-1}. In contrast, the two other presented PLS-VIP models are indeed capable of predicting AMS concentrations higher than 0.2 M AMS despite the observed spectral appearance (cf. Figure 7.3 (E),(F)). While the PLS-VIP4$_{AMS}$ model predictions exhibit minor fluctuations in the time frame of band oversaturation, the predictions below 0.2 M AMS are fairly consistent and comparable to those of the PLS$_{AMS}$ or linear regression model. It has to be noted that besides the PLS-VIP4$_{AMS}$ model using all VIP-selected wavenumber intervals attributed to sulfate contributions, model building with a combination of either three or two intervals have shown comparable error metrics during model building using 175 ms exposure time where no band oversaturation was present. However, except for the wavenumber combination of the PLS-VIP2$_{AMS}$ model, all failed in prediction accuracy when applied to EXP2–3 data derived from on-line Raman spectral data at 1250 ms exposure time (data not shown), even though the saturated band interval was excluded. The PLS-VIP2$_{AMS}$ model demonstrates more stable predictions in the time frame of band oversaturation. However, compared to all other models, it exhibits slightly shifted predictions below 0.2 M AMS towards lower or higher AMS concentrations within the range of 0.2 to 0.08 M AMS or at the final stages of the process, respectively.

Notably, defective spectra were recorded from 0.7 to 1.8 DV in EXP3, exhibiting immense baseline shifts (cf. Supplementary Figure A7.3 (B)), ultimately leading to false predictions (cf. Figure 7.3 (F)). Only manually decoupling the on-line loop, flushing it with re-dissolution buffer, and reconnecting it provided expected spectral appearances from 2.2 DV onward.

In summary, the process-derived spectra define the required models for AMS quantification. Although differences in spectral appearance existed as the exposure times varied between model building and process-derived, continuously recorded Raman spectral data, the progression of AMS depletion throughout the CFF-based recovery step (DFII/UF) could be continuously monitored through precise adjustment and refinement of the models using VIP scores.

7.3.3 VLP: Spectral Pre-Cropping Improves Further Spectral Preprocessing and PLS Model Building

Raman spectra of VLP-containing stock solutions were recorded over a VLP concentration range of 0–2.2 gL^{-1}. Spectral data recorded at 1250 ms exposure time were used for preprocessing pipeline development and model building. Table 7.2 summarizes the parameter settings for spectral preprocessing operations and model building.

The spectral preprocessing pipeline involved pre-cropping, baseline correction using the asPLS Whittaker filter, and signal smoothing using the SGF filter to remove baseline drifts and enhance spectral differences. Figure 7.5 illustrates raw and preprocessed spectral data of the VLP-containing stock solution set over the entire spectral range or selected wavenumber intervals. In the raw spectra, baseline drifts are visible with baseline increases with higher VLP concentrations (cf. Figure 7.5 (A)). By simple baseline correction and signal smoothing without the pre-cropping step beforehand, these baseline drifts could not be consistently removed in the wavenumber region 1200–1400 $^{-1}$ (cf. Figure 7.5 (B)). Additionally, the spectra show the 980 cm^{-1} band attributable to sulfate ions [251, 252], indicating residual AMS in the VLP stock solutions deriving from its preparation. As the pronounced phenylalanine band at 1004 cm^{-1} and other protein-associated wavenumber regions 600–880 cm^{-1} and 1200–1800 cm^{-1} [131, 132] will be partly obscured when a

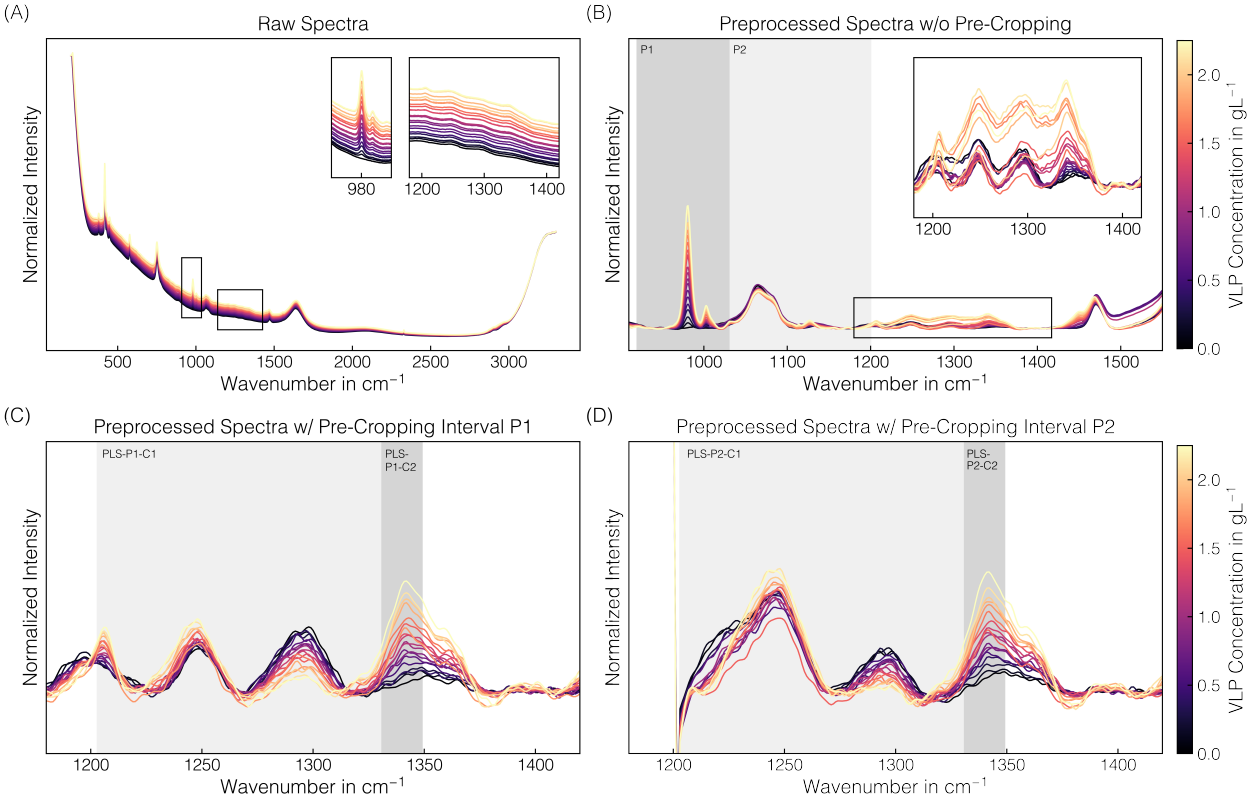

Figure 7.5 Raman spectral data: VLP. Derived from a set of stock solutions with varying VLP concentrations, averaged raw spectral data **(A)** were differently preprocessed (**(B)**–**(D)**). For raw spectra **(A)** and baseline-corrected, signal-smoothed spectra **(B)**, the wavenumber region around the predominant Raman band near 980 cm^{-1} and the wavenumber region associated with proteins are additionally presented on an enlarged scale. The wavenumber intervals 920–1030 cm^{-1} (P1) or 920–1200 cm^{-1} (P2) removed by pre-cropping prior to preprocessing are highlighted in gray **(B)**. Including pre-cropping changed the spectral appearance in the protein-associated region, as presented in **(C)** and **(D)**, respectively. Pre-cropped, baseline-corrected, and signal-smoothed spectra were further cropped to the wavenumber intervals 1203–1349 cm^{-1} (C1) or 1331–1349 cm^{-1} (C2) for PLS modeling, as highlighted in gray (**(C)**, **(D)**). The spectra are colored with brighter colors representing higher VLP concentrations.

considerable amount of the precipitant AMS is present, 1200–1400 cm^{-1} region, being not affected by AMS obscuration, was chosen for further preprocessing and model development.

A pre-cropping strategy was introduced, removing selected wavenumber intervals of the spectrum to account for the baseline shifts in this protein-associated region. The wavenumber interval 920–1030 cm^{-1} (P1) was used to eliminate the contributions of the predominant 980 cm^{-1} sulfate band, resulting in a more consistent spectral appearance of preprocessed spectra, allowing trends in the 1200–1400 cm^{-1} region to be observed (cf. Figure 7.5 (C)). The Raman band at 1206 cm^{-1} is attributed to tyrosine, the band at 1249 cm^{-1} originates from the polypeptide backbone, and the band at 1341 cm^{-1} is a composite of overlapping signals from both the polypeptide backbone and tryptophan [131, 132]. The band at 1249 cm^{-1} originates from the buffer component Tris [253]. A larger pre-cropping interval of 920–1200 cm^{-1} (P2) to further account for the broad sulfate

band around 1106 cm^{-1} resulted in a similar spectral appearance in the 1270–1400 cm^{-1} region but essentially obscured the 1206 cm^{-1} tyrosine band (cf. Figure 7.5 (D)). Both preprocessed spectra differing in the pre-cropping interval (P1/P2) have been further cropped to a distinct wavenumber interval prior to regression modeling (cf. Table 7.2, Figure 7.5 (C-D)). The error metrics R^2 and RMSE of the PLS-P2-$C2_{VLP}$ model are with 0.999 higher and 0.02 gL^{-1} lower than PLS-P2-$C1_{VLP}$ with 0.994 and 0.05 gL^{-1}, respectively. In contrast, both models with the smaller pre-cropping interval (P1) achieved R^2 values of 0.984 and RMSE values of 0.08 gL^{-1}.

In summary, spectral preprocessing was developed through spectral comparison considering (i) the spectral appearance in the protein region and (ii) potential interferences from the precipitant to make the model suitable for data from CFF-based processes. The combination of pre-cropping to remove certain wavenumber intervals, baseline correction, signal smoothing, and further cropping to select intervals in the protein-associated region allows for uniform spectral preprocessing and model building for VLP quantification.

7.3.4 VLP: On-line Raman Spectral Data Reveal VLP Accumulation and Sensor Fouling

All the PLS_{VLP} models built on stock solutions were transferred to process-derived spectra to determine the accumulation of re-dissolved VLPs in the second membrane stage throughout the CFF-based recovery step (DFII/UF). The PLS_{VLP} models differ in the pre-cropping (P1/P2) and cropping (C1/C2) intervals used in the respective preprocessing operations. Figure 7.6 presents the predicted VLP concentrations for the applied VLP models on the off-line and on-line spectral data for the three CFF experiments (EXP1–3) performed.

Across all CFF experiments, the observed progression of the HPLC-derived VLP concentration follows a distinct pattern, attributable to the CFF-based VLP recovery step (DFII/UF). DF with re-dissolution buffer in the dual-stage CFF set-up leads to VLP re-dissolution in the first membrane stage, their passage through the microfiltration membrane, and their accumulation in the second membrane stage. DF is followed by UF, resulting in an approximately twofold concentration of the VLPs in the second membrane stage. The higher VLP concentrations observed in EXP3 compared to EXP1–2 are attributable to the VLP-enriched lysate used as starting material for EXP3, representing a diversification of the process data. Final SEC-purity values of the concentrated VLPs ranged between 94–96%, consistent with the purity values reported by Dietrich et al. [277], demonstrating reproducible processing by dual-stage CFF.

Applying the PLS_{VLP} models to off-line spectral data, the trend observed in the HPLC-derived data is reflected in all of the model predictions. However, the prediction accuracy varies between and within the experiments EXP1–3 (cf. Figure 7.6 (A)–(C)). In general, the predictions for EXP3 are slightly scattered around the observed VLP concentrations. On the contrary, the ones for EXP2 lie slightly above, seeming to be systematic, and the predictions for EXP1 are significantly higher and exhibit a broader spread. Such a process-dependent occurrence of these deviations can be linked to underlying process-specific factors, resulting in deviating and inconsistent spectral features. When comparing the model predictions for EXP2–3, the predicted VLP concentrations of the PLS-P2 models are almost identical, while those of the PLS-P1 models show higher or lower predicted VLP concentrations at specific DVs (cf. Figure 7.6 (B)–(C)). This observation suggests that using the pre-cropping interval P2 results in more consistent spectral features after further

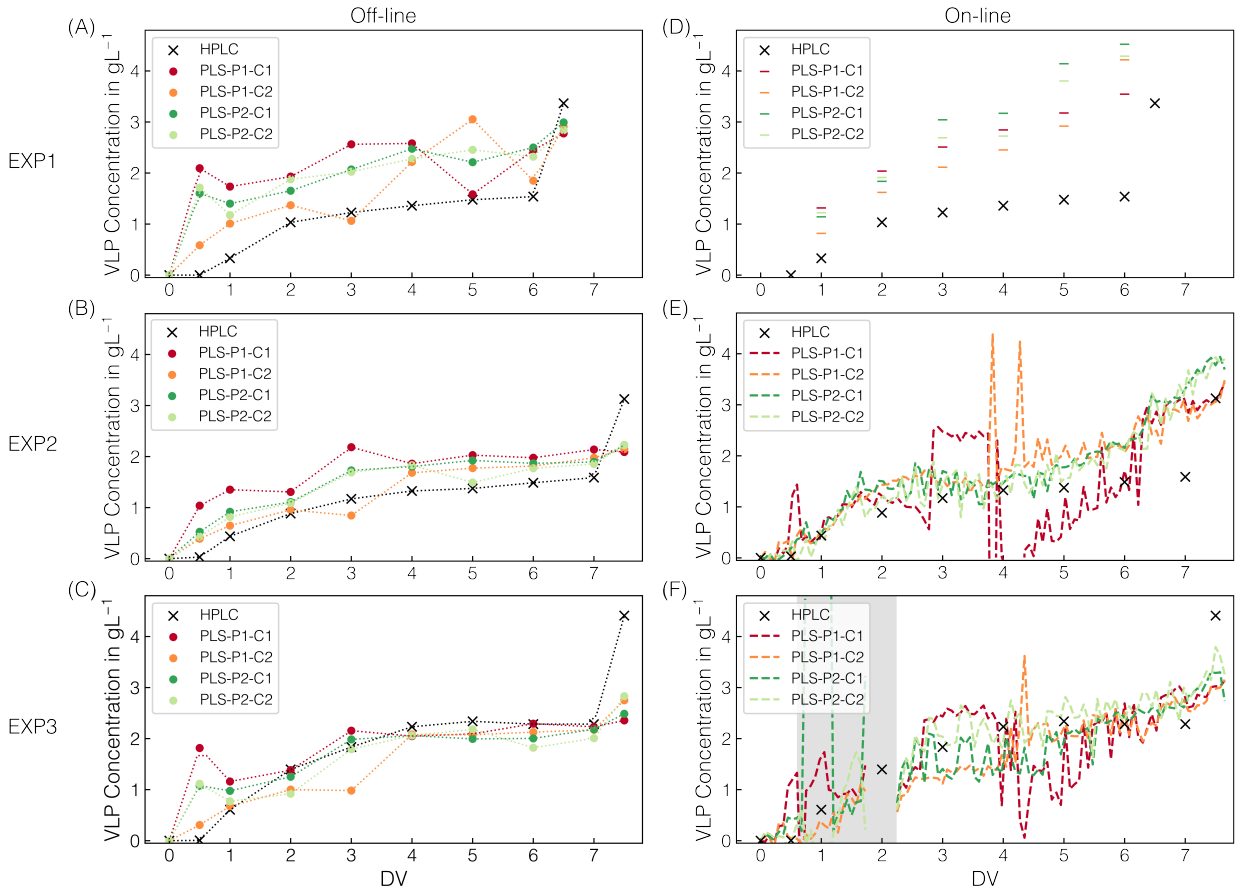

Figure 7.6 VLP model predictions. Next to HPLC-derived VLP concentrations, the predicted VLP concentrations are shown for all CFF runs. The predictions derived from individual Raman measurements at 1250 ms exposure time. Predictions from off-line and on-line measurements in semi-continuous (EXP1) or continuous (EXP2–3) acquisition mode are shown in **(A)**–**(C)** and **(D)**–**(F)**, respectively, along with their corresponding color assignments for the models used. The models differ in pre-cropping and cropping operations, with their respective intervals P1/P2 and C1/C2. Dotted lines (off-line) serve solely as visual guides to facilitate interpretation. The dashed lines (on-line) represent continuous prediction. Predictions by defective spectra are highlighted with dark-gray shaded areas.

spectral preprocessing and less dependence on the cropping interval (C1/C2). Notably, the most noticeable deviations between the HPLC-derived and the predicted VLP concentrations are observed in the range of relatively low and high VLP concentrations at the beginning and the end of the CFF processes, respectively. Overall, the PLS-P2 models show consistent predictions in the range of moderate protein concentrations but lack accuracy at low and high protein concentrations, especially during the concentration step with protein concentrations up to twice as high.

A similar pattern in prediction accuracy emerges when the models are applied to on-line spectral data (cf. Figure 7.6 (D)–(F)). For EXP1, fouling on the Raman probe was observed after on-line spectral data acquisition, which, however, did not impact the prediction of AMS (cf. Section 7.3.2). The deviations in the predictions of the VLP concentration suggest that there was a gradual accumulation of protein on the probe throughout the process, leading to the increasing overestimation of the

VLP concentrations (cf. Figure 7.6 (D)). Concerning fouling, the flow rate of the on-line loop was doubled from EXP1 to EXP2–3, which, along with the switch to continuous spectral data acquisition, represents a process adjustment. For EXP2–3, all predictions seem to scatter around the observed VLP concentrations, with even more pronounced scatter spikes for the PLS-P1 than the PLS-P2 models (cf. Figure 7.6 (E),(F)). Further and consistent with the off-line data predictions, the models also fail to predict the concentration step based on the on-line spectral data. Especially for EXP2, the observed gradual increase in VLP concentration from the fifth DV onward is not reflected by the off-line data (cf. Figure 7.6 (E)), which may also be indicative of fouling.

No difference in accuracy was observed for predictions from both off-line and on-line spectral data, regardless of whether the sulfate peak at 980 cm^{-1} in the raw spectra was saturated, which the pre-cropping operation was intended to address.

In summary, PLS_{VLP} models were transferred to continuously monitor the accumulation of re-dissolved VLPs in the second membrane stage throughout the CFF-based VLP recovery step (DFII/UF). The PLS-P2 models show the most consistent predictions in the range of moderate protein concentrations, both for off-line and on-line spectral data, across all processes where fouling behavior was neither observed nor suspected.

7.4 Discussion

7.4.1 Sensor Selection and Implications for Multi-Attribute Monitoring

Raman spectroscopy was selected for multi-attribute monitoring during recovery of precipitated VLPs by dual-stage CFF—a dynamic DF process isolating the re-dissolved VLPs through precipitant depletion in the second membrane stage [277]. Sensitivity and selectivity significantly differed when comparing precipitant or protein monitoring using Raman spectroscopy and chemometrics.

Precipitant quantification is not routinely performed during small-scale screenings with predefined precipitant conditions where the results can be directly correlated. However, its quantification becomes essential in dynamic processes due to varying precipitant concentrations throughout these processes. While Barros Groß et al. [207] calculated the theoretical precipitant content based on the volume reduction through evaporative crystallization, Dietrich et al. [201] further combined the theoretical content with Raman spectral data derived from fed-batch precipitation and chemometrics to predict AMS contents in unseen fed-batch precipitation processes. Accordingly, Dietrich et al. [201] had already demonstrated the use of Raman spectroscopy for near real-time AMS monitoring through PLS modeling.

With stock solutions covering the AMS concentration range, simple spectral processing, and linear regression using the predominant sulfate band at 980 cm^{-1} [251, 252], Raman spectroscopy is highly selective for AMS quantification. Linear regression has already been applied for off-line AMS quantification to reveal integrated AMS depletion, representing one advantage for VLP recovery by the dual-stage CFF compared to the single-stage CFF set-up [277]. Our study demonstrates the successful transfer of a linear regression model for AMS quantification to process-derived, on-line spectral data, under the condition that no band oversaturation is present, thereby extending its use beyond prior off-line applications. Further, model development for model transfer to accommodate spectral data exhibiting oversaturation effects is successfully demonstrated.

Although conductivity and density measurements, which are both influenced by salts like AMS, also enable real-time monitoring [17, 222], these techniques may lack selectivity, which can compromise accuracy in processes with varying environmental concentrations or compositions. Particularly throughout this dual-stage CFF process for VLP recovery, changes occur not only in precipitant content but also in buffer composition, protein composition, and total protein concentration. Moreover, relying solely on univariate signals from conductivity or density measurements is insufficient for simultaneously predicting both precipitant and product concentrations. Other techniques for AMS quantification pose similar challenges in selectivity and are further limited to off-line measurements as multiple steps are involved. Among others, ammonium is traditionally quantified spectrophotometrically through complex formation [284, 285], while sulfate can be determined fluorescence-based [286].

Considering polyethylene glycol (PEG), the other widely used precipitant, using Raman spectroscopy for quantification may pose challenges due to its suspected contributions overlapping with protein-associated wavenumber regions [269], which is why enhanced spectral processing and models of higher complexity, such as PLS or non-linear models, may be required. It has to be noted that using PEG in such filtration-based processes in general may have disadvantages, particularly concerning its influence on viscosity and, consequently, filtration behavior [105, 287, 288] as well as its larger molecular size compared to salts, which may hinder its depletion in the here presented dual-stage CFF process.

Among protein quality attributes, protein concentration is one of the most monitored during the downstream processing of biopharmaceuticals. Several spectroscopic methods and their applicability to protein monitoring are outlined in detail by Rolinger et al. [114], among which Raman and UV spectroscopy are sensitive for aromatic amino acids, peptide bonds, and disulfide bonds. Although water interference in Raman spectroscopy is relatively low [114], a limited sensor applicability was found at low protein concentrations, attributable to the increasing dominance of the water band. Moreover, the protein predictions exhibit much higher fluctuations than the precipitant predictions, which might result from the substantially lower intensity of protein contributions than sulfate contributions. Raman spectroscopy has recently been compared with UV spectroscopy for predicting monoclonal antibody concentrations in Protein A chromatography, highlighting the significantly superior prediction accuracy of UV spectroscopy [222]. The authors suggest that UV spectroscopy would likely have been more accurate for protein concentration monitoring, which would have resulted in a multimodal spectroscopy setup in this study. Raman spectroscopy has already been implemented together with UV for monitoring enzyme crystallization in complex lysate [136] and as a basis for data fusion to improve prediction accuracy [222]. In such multi-sensor setups, however, the different spectroscopic data require distinct data preprocessing, and, if combined, additional preprocessing may be needed due to signal dispersion between detectors [114].

Sensor fouling is a known but rarely reported challenge in spectroscopic process monitoring, describing unintended material accumulation or burning by the laser light. After the first CFF run, spectral inconsistencies were observed in the protein-associated wavenumber region during off-line analysis of process samples, suggesting sensor fouling on the sensor surface or within the flow cell. Although sapphire surfaces and convex geometries tend to be less favorable for material deposition [289], the observed fouling may indicate the influence of residence time within the flow cell. Doubling the flow rate, thereby reducing the residence time by half, prevented the occurrence of spectral inconsistencies in the data of the following CFF runs. In filtration processes, spectroscopic sensors are frequently

implemented on-line [16, 17, 19] or in-line [20, 137, 278, 279] using a flow cell, providing precise control over measurement conditions. Installing sensors directly *in situ* by immersing them into the well-stirred process solution within the system's reservoir [136, 278, 280] may offer a practical alternative to mitigate fouling. Further, the authors suggest that *in situ* monitoring may be less prone to spectra diverging from the others—termed 'defective spectra' in this study.

In summary, spectroscopic sensors should be selected based on their sensitivity and selectivity towards the target quality attributes to be monitored. Moreover, sensor implementation should be carefully considered to ensure reliable spectroscopic measurements.

7.4.2 Effects of Detector Saturation on Raw Raman Spectral Data

The contributions of precipitant and protein to the spectral data were investigated using stock solutions of pure components. A substantially higher sensor sensitivity towards precipitant than protein was observed concerning the spectral features observed in the raw spectral data. The initial objective involved increasing the exposure time to enhance the sensor's sensitivity to proteins, which, however, led to oversaturation of the predominant sulfate band at 980 cm^{-1} [251, 252] directly related to the precipitant. To the best of the author's knowledge, the analysis and use of spectral data exhibiting saturation effects at specific wavenumber regions has not been reported in the literature yet.

The raw on-line spectral data collected during processing show a characteristic split peak formation, which stands in contrast to reported oversaturation characteristics observed in the low wavenumber regions, where entire bands disappear due to the baseline being elevated to the saturation level [290]. The manufacturer recommends increasing the exposure time only below the saturation limit of the detector, thereby preventing saturation and the associated increase in uncorrelated noise [290]. A comparison of the baseline levels before and after oversaturation at the same AMS concentration revealed a baseline shift, suggesting the influence of a secondary factor beyond detector saturation. The authors hypothesize that the baseline shift may be attributable to intrinsic fluorescence or scattering effects caused by the proteins [140], as the VLPs accumulate throughout the process. As expected, spectral preprocessing removed those differences in baseline level; however, the split peak remained present in the spectral data.

7.4.3 Effects of Preprocessing Operations on Raman Spectral Data and Model Transfer

The differences in sensor selectivity and Raman spectral features towards AMS and VLP underscore the importance of individual spectral preprocessing. Attribute-specific preprocessing operations beyond baseline correction and signal smoothing were selected to enhance computational selectivity. All preprocessing operations were specified and applied in a defined sequence to enable the model transfer to the process data.

Prior normalization of the spectra before baseline correction and signal smoothing allows not only for accounting for turbidity effects in the previous precipitation step [201] but also facilitates model transfer to spectral data obtained at different exposure times, which is the case for the AMS models. A Raman band of the OH-bond of water was used for normalization as neither the analytes nor the background interferes in this spectral region, according to the approach of Sinfield et al. [232]. This strategy was chosen for the AMS models to maintain their applicability across different exposure

times and across the earlier process steps of precipitation and wash, where turbidity was observed. To solely account for intensity differences caused by the varying applied exposure times, normalization by exposure time [137] or standard normal variate (SNV) normalization of already preprocessed spectra [20, 225] have been reported. In this study, however, SNV normalization was omitted since the absolute intensity differences of the major peak—the sulfate band at 980 cm^{-1} [251, 252], which represents a target analyte—would be diminished. For the VLP models, OH-band normalization was not implemented as an additional preprocessing step, as its implementation likely limited model performances, possibly due to introducing a larger error in the relatively smaller intensity ranges of the proteins.

Cropping allows for selecting spectral regions of interest by targeted discarding of the others. A comparison of different, manually selected cropping intervals to systematically improve model performance has been reported by Dietrich et al. [201], driven by the exclusion of residual baseline variance and impurity- or buffer-related interferences. For AMS monitoring, the predominant sulfate band at 980 cm^{-1} [251, 252] was chosen for the linear regression model, and the edge regions potentially exhibiting unintended variability introduced by prior preprocessing steps were discarded for PLS modeling. Both models reliably predict AMS from off-line and on-line spectral data, but lack prediction accuracy at higher exposure times when oversaturation of the predominant sulfate band is present, attributable to the observed split peak behavior. To refine the PLS model for AMS quantification, VIP was used as a data-driven variable selection technique [142] for metric-based cropping. Such variable selection techniques aim to minimize the loss of important spectral data while improving model robustness [282]. In studies dealing with spectral data processing, VIP scores have been used as a spectral region selection criterion [219, 234, 291] or simply as feature importance to quantitatively evaluate which spectral regions contribute to PLS models [201, 225, 257, 292]. Cropping is typically applied as one of the final preprocessing steps before PLS modeling. For VLP modeling, a pre-cropping approach is presented, describing the manual removal of AMS-associated regions next to the protein-associated region. Pre-cropping was introduced as insufficient baseline correction was observed in the protein-associated region, which could not be removed using alternative baseline correction settings. The authors hypothesize that this effect is again attributable to the much higher sensor sensitivity towards AMS than the proteins. Eventually, preprocessed spectra were manually cropped to only use protein-associated regions for modeling, free from potential interferences from the precipitant. In addition to the already relatively small interval of 147 wavenumbers, a further reduced interval comprising only 19 wavenumbers was also tested. Generally, it is worth noting that variable reduction to such narrow intervals may also remove useful information for prediction.

Both presented PLS-VIP models accommodate precipitant predictions from spectral data exhibiting saturation effects. In ranges without saturation, the continuous predictions of the PLS-VIP models exhibit more noise than those from linear regression or the PLS model, which could be attributed to the smaller spectral range resulting from the spectral cropping, and, consequently, a lower information density. To our knowledge, using spectra with such a saturation-induced split peak behavior for prediction has not been previously reported in the literature. In general, the AMS predictions exhibit much lower fluctuations than the VLP predictions, regardless of which developed PLS model is applied for VLP prediction. In addition to the even lower information density used for model building, this phenomenon can also be attributed to Raman spectroscopy's inherent sensitivity and selectivity towards proteins.

Another multivariate modeling approach for multi-attribute monitoring from spectral data obtained from a single sensor may be indirect hard modeling regression, which describes the spectrum as a sum of prior parameterized peak functions assigned to individual components. First introduced by Alsmeyer et al. [264] in combination with Raman spectroscopy, indirect hard modeling has been shown to account for non-linear spectral changes [230, 265]. In biopharmaceutical processing, it has been applied for in-line monitoring [293] and control [294] of fermentation processes; however, its use for multi-attribute monitoring during downstream processing has not yet been reported.

In summary, attribute-specific preprocessing operations were strategically employed beyond baseline correction and signal smoothing to enable model transfer.

7.5 Conclusion and Outlook

In conclusion, soft sensors based on Raman spectroscopy and chemometrics were developed and transferred to a filtration-based recovery step of precipitated VLPs for monitoring product accumulation and precipitant depletion. The Raman spectrometer was implemented in an on-line loop in the second membrane stage of the dual-stage CFF setup, and near real-time process data were collected from three CFF experiments with variations in initial product concentration and process parameters. Through the initial investigation of individual contributions of precipitant and product to the spectral data using stock solutions of the pure components, a substantially higher sensor sensitivity was found for AMS than VLPs. Increasing the exposure time to enhance the sensor's sensitivity towards VLPs led to the oversaturation of the predominant sulfate band directly related to AMS, which impaired the prediction accuracy for AMS by linear regression. With attribute-specific preprocessing operations next to baseline correction and signal smoothing, namely normalization and VIP-based cropping, and PLS modeling, we successfully demonstrated model transfer for AMS monitoring despite these detector saturation effects. For simultaneous VLP monitoring, spectral data were differently preprocessed using a pre-cropping approach before baseline correction and signal smoothing, which effectively improved the spectral appearance, as without, insufficient baseline correction was observed in the protein-associated spectral regions. Even though the larger of the two tested pre-cropping intervals led to more consistent PLS model predictions, the VLP predictions exhibit generally much higher fluctuations than the AMS predictions. This study highlights that soft sensor selectivity towards target quality attributes is highly dependent on, but also, to some extent, limited by the sensor's inherent selectivity, although it can be further improved by enhancing the computational selectivity using attribute-specific operations for spectral preprocessing.

Author Contributions

Annabelle Dietrich: Conceptualization, Formal Analysis, Methodology, Software, Investigation, Visualization, Writing –- original draft, Writing –- review and editing. **Luca Heim**: Investigation, Software, Writing –- review and editing. **Jürgen Hubbuch**: Funding acquisition, Supervision, Writing –- review and editing.

Supplementary Material

Appendix **A7** contains the Supplementary Material associated with this chapter.

Chapter References

[4] Y. H. Chung, H. Cai, and N. F. Steinmetz. „Viral nanoparticles for drug delivery, imaging, immunotherapy, and theranostic applications“. In: *Advanced Drug Delivery Reviews* 156 (2020), pp. 214–235. DOI: 10.1016/j.addr.2020.06.024.

[11] C. L. Effio and J. Hubbuch. „Next generation vaccines and vectors: Designing downstream processes for recombinant protein-based virus-like particles“. In: *Biotechnology Journal* 10.5 (2015), pp. 715–727. DOI: 10.1002/biot.201400392.

[13] N. Hillebrandt and J. Hubbuch. „Size-selective downstream processing of virus particles and non-enveloped virus-like particles“. In: *Frontiers in Bioengineering and Biotechnology* 11 (2023). DOI: 10.3389/fbioe.2023.1192050.

[14] FDA. *Guidance for Industry: PAT—a framework for innovative pharmaceutical development, manufacturing, and quality assurance*. 2004.

[16] M. Rüdt, P. Vormittag, N. Hillebrandt, and J. Hubbuch. „Process monitoring of virus-like particle reassembly by diafiltration with UV/Vis spectroscopy and light scattering“. In: *Biotechnology and Bioengineering* 116.6 (2019), pp. 1366–1379. DOI: 10.1002/bit.26935.

[17] N. Hillebrandt, P. Vormittag, A. Dietrich, and J. Hubbuch. „Process monitoring framework for cross-flow diafiltration-based virus-like particle disassembly: Tracing product properties and filtration performance“. In: *Biotechnology and Bioengineering* 119.6 (2022), pp. 1522–1538. DOI: 10.1002/bit.28063.

[19] L. Rolinger et al. „Multi-attribute PAT for UF/DF of Proteins—Monitoring Concentration, particle sizes, and Buffer Exchange“. In: *Analytical and Bioanalytical Chemistry* 412.9 (2020), pp. 2123–2136. DOI: 10.1007/s00216-019-02318-8.

[20] D. Vaskó et al. „Raman and NIR spectroscopy-based real-time monitoring of the membrane filtration process of a recombinant protein for the diagnosis of SARS-CoV-2“. In: *International Journal of Pharmaceutics* 660 (2024), p. 124251. DOI: 10.1016/j.ijpharm.2024.124251.

[36] R. van Reis and A. Zydney. „Bioprocess membrane technology“. In: *Journal of Membrane Science* 297.1-2 (2007), pp. 16–50. DOI: 10.1016/j.memsci.2007.02.045.

[39] B. Chackerian. „Virus-like particles: Flexible platforms for vaccine development“. In: *Expert Review of Vaccines* 6.3 (2007), pp. 381–390. DOI: 10.1586/14760584.6.3.381.

[41] H. Tariq, S. Batool, S. Asif, M. Ali, and B. H. Abbasi. „Virus-Like Particles: Revolutionary Platforms for Developing Vaccines Against Emerging Infectious Diseases“. In: *Frontiers in Microbiology* 12 (2022). DOI: 10.3389/fmicb.2021.790121.

[43] S. Nooraei et al. „Virus-like particles: preparation, immunogenicity and their roles as nanovaccines and drug nanocarriers“. In: *Journal of Nanobiotechnology* 19.1 (2021), p. 59. DOI: 10.1186/s12951-021-00806-7.

[46] C. J. Burrell, P. Mackay, P. J. Greenaway, P. H. Hofschneider, and K. Murray. „Expression in Escherichia coli of hepatitis B virus DNA sequences cloned in plasmid pBR322“. In: *Nature* 279.5708 (1979), pp. 43–47. DOI: 10.1038/279043a0.

[47] S. Stahl, P. MacKay, M. Magazin, S. A. Bruce, and K. Murray. „Hepatitis B virus core antigen: Synthesis in Escherichia coli and application in diagnosis“. In: *Proceedings of the National Academy of Sciences of the United States of America* 79.5 (1982), pp. 1606–1610. DOI: 10.1073/pnas.79.5.1606.

[49] A. Zlotnick et al. „Dimorphism of Hepatitis B Virus Capsids Is Strongly Influenced by the C-Terminus of the Capsid Protein“. In: *Biochemistry* 35.23 (1996), pp. 7412–7421. DOI: 10.1021/bi9604800.

[54] M. Moradi Vahdat et al. „Hepatitis B core-based virus-like particles: A platform for vaccine development in plants“. In: *Biotechnology Reports* 29 (2021), e00605. DOI: 10.1016/j.btre.2021.e00605.

[55] A. M. Hassebroek et al. „A hepatitis B virus core antigen-based virus-like particle vaccine expressing SARS-CoV-2 B and T cell epitopes induces epitope-specific humoral and cell-mediated immune responses but confers limited protection against SARS-CoV-2 infection“. In: *Journal of Medical Virology* 95.2 (2023). DOI: 10.1002/jmv.28503.

[56] A. Zeltins. „Construction and Characterization of Virus-Like Particles: A Review“. In: *Molecular Biotechnology* 53.1 (2013), pp. 92–107. DOI: 10.1007/s12033-012-9598-4.

[57] M. G. Moleirinho, R. J. Silva, P. M. Alves, M. J. T. Carrondo, and C. Peixoto. „Current challenges in biotherapeutic particles manufacturing“. In: *Expert Opinion on Biological Therapy* 20.5 (2020), pp. 451–465. DOI: 10.1080/14712598.2020.1693541.

[61] N. Hillebrandt, P. Vormittag, A. Dietrich, C. H. Wegner, and J. Hubbuch. „Process development for cross-flow diafiltration-based VLP disassembly: A novel high-throughput screening approach“. In: *Biotechnology and Bioengineering* 118.10 (2021), pp. 3926–3940. DOI: 10.1002/bit.27868.

[65] I. Petrovskis et al. „Production of the HBc Protein from Different HBV Genotypes in E. coli. Use of Reassociated HBc VLPs for Packaging of ss- and dsRNA“. In: *Microorganisms* 9.2 (2021), p. 283. DOI: 10.3390/microorganisms9020283.

[67] A. Cooper and Y. Shaul. „Recombinant viral capsids as an efficient vehicle of oligonucleotide delivery into cells“. In: *Biochemical and Biophysical Research Communications* 327.4 (2005), pp. 1094–1099. DOI: 10.1016/j.bbrc.2004.12.118.

[68] J. Z. Porterfield, M. S. Dhason, D. D. Loeb, M. Nassal, S. J. Stray, and A. Zlotnick. „Full-Length Hepatitis B Virus Core Protein Packages Viral and Heterologous RNA with Similarly High Levels of Cooperativity“. In: *Journal of Virology* 84.14 (2010), pp. 7174–7184. DOI: 10.1128/JVI.00586-10.

[88] N. Hillebrandt, P. Vormittag, N. Bluthardt, A. Dietrich, and J. Hubbuch. „Integrated Process for Capture and Purification of Virus-Like Particles: Enhancing Process Performance by Cross-Flow Filtration“. In: *Frontiers in Bioengineering and Biotechnology* 8 (2020). DOI: 10.3389/fbioe.2020.00489.

[105] D. Burgstaller, A. Jungbauer, and P. Satzer. „Continuous integrated antibody precipitation with two-stage tangential flow microfiltration enables constant mass flow“. In: *Biotechnology and Bioengineering* 116.5 (2019), pp. 1053–1065. DOI: 10.1002/bit.26922.

[112] A. S. Rathore, R. Bhambure, and V. Ghare. „Process analytical technology (PAT) for biopharmaceutical products“. In: *Analytical and Bioanalytical Chemistry* 398.1 (2010), pp. 137–154. DOI: 10.1007/s00216-010-3781-x.

[113] J. Glassey et al. „Process analytical technology (PAT) for biopharmaceuticals“. In: *Biotechnology Journal* 6.4 (2011), pp. 369–377. DOI: 10.1002/biot.201000356.

[114] L. Rolinger, M. Rüdt, and J. Hubbuch. „A critical review of recent trends, and a future perspective of optical spectroscopy as PAT in biopharmaceutical downstream processing“. In: *Analytical and Bioanalytical Chemistry* 412.9 (2020), pp. 2047–2064. DOI: 10.1007/s00216-020-02407-z.

[131] N. C. Maiti, M. M. Apetri, M. G. Zagorski, P. R. Carey, and V. E. Anderson. „Raman Spectroscopic Characterization of Secondary Structure in Natively Unfolded Proteins: α-Synuclein“. In: *Journal of the American Chemical Society* 126.8 (2004), pp. 2399–2408. DOI: 10.1021/ja0356176.

[132] A. Rygula, K. Majzner, K. M. Marzec, A. Kaczor, M. Pilarczyk, and M. Baranska. „Raman spectroscopy of proteins: A review“. In: *Journal of Raman Spectroscopy* 44.8 (2013), pp. 1061–1076. DOI: 10.1002/jrs.4335.

[136] C. H. Wegner, S. M. Eming, B. Walla, D. Bischoff, D. Weuster-Botz, and J. Hubbuch. „Spectroscopic insights into multi-phase protein crystallization in complex lysate using Raman spectroscopy and a particle-free bypass“. In: *Frontiers in Bioengineering and Biotechnology* 12 (2024), pp. 1–16. DOI: 10.3389/fbioe.2024.1397465.

[137] L. Rolinger, J. Hubbuch, and M. Rüdt. „Monitoring of ultra- and diafiltration processes by Kalman-filtered Raman measurements“. In: *Analytical and Bioanalytical Chemistry* 415.5 (2023), pp. 841–854. DOI: 10.1007/s00216-022-04477-7.

[138] D. Weber and J. Hubbuch. „Raman spectroscopy as a process analytical technology to investigate biopharmaceutical freeze concentration processes“. In: *Biotechnology and Bioengineering* 118.12 (2021), pp. 4708–4719. DOI: 10.1002/bit.27936.

[139] Å. Rinnan, L. Nørgaard, F. V. D. Berg, J. Thygesen, R. Bro, and S. B. Engelsen. „Data Pre-processing“. In: *Infrared Spectroscopy for Food Quality Analysis and Control*. Vol. 3. Academic Press, 2009. Chap. 2, pp. 29–50.

[140] R. Gautam, S. Vanga, F. Ariese, and S. Umapathy. „Review of multidimensional data processing approaches for Raman and infrared spectroscopy“. In: *EPJ Techniques and Instrumentation* 2.1 (2015). DOI: 10.1140/epjti/s40485-015-0018-6.

[141] T. Bocklitz, A. Walter, K. Hartmann, P. Rösch, and J. Popp. „How to pre-process Raman spectra for reliable and stable models?“ In: *Analytica Chimica Acta* 704.1-2 (2011), pp. 47–56. DOI: 10.1016/j.aca.2011.06.043.

[142] T. Mehmood, K. H. Liland, L. Snipen, and S. Sæbø. „A review of variable selection methods in Partial Least Squares Regression“. In: *Chemometrics and Intelligent Laboratory Systems* 118 (2012), pp. 62–69. DOI: 10.1016/j.chemolab.2012.07.010.

[144] S. Wold, M. Sjöström, and L. Eriksson. „PLS-regression: a basic tool of chemometrics“. In: *Chemometrics and Intelligent Laboratory Systems* 58.2 (2001), pp. 109–130. DOI: 10.1016/S0169-7439(01)00155-1.

[195] C. Qian et al. „Recent Progress on the Versatility of Virus-Like Particles“. In: *Vaccines* 8.1 (2020), p. 139. DOI: 10.3390/vaccines8010139.

[201] A. Dietrich, R. Schiemer, J. Kurmann, S. Zhang, and J. Hubbuch. „Raman-based PAT for VLP precipitation: systematic data diversification and preprocessing pipeline identification“. In: *Frontiers in Bioengineering and Biotechnology* 12 (2024), pp. 1–20. DOI: 10.3389/fbioe.2024.1399938.

[204] E. Gasteiger et al. „Protein Identification and Analysis Tools on the ExPASy Server“. In: *The Proteomics Protocols Handbook* (2005), pp. 571–607. DOI: 10.1385/1-59259-890-0:571.

[207] M. Barros Groß and M. Kind. „From microscale phase screening to bulk evaporative crystallization of proteins“. In: *Journal of Crystal Growth* 498 (2018), pp. 160–169. DOI: 10.1016/j.jcrysgro.2018.06.010.

[219] B. Berry, J. Moretto, T. Matthews, J. Smelko, and K. Wiltberger. „Cross-scale predictive modeling of CHO cell culture growth and metabolites using Raman spectroscopy and multivariate analysis“. In: *Biotechnology Progress* 31.2 (2015), pp. 566–577. DOI: 10.1002/btpr.2035.

[222] L. Rolinger, M. Rüdt, and J. Hubbuch. „Comparison of UV- and Raman-based monitoring of the Protein A load phase and evaluation of data fusion by PLS models and CNNs“. In: *Biotechnology and Bioengineering* 118.11 (2021), pp. 4255–4268. DOI: 10.1002/bit.27894.

[223] J. Wang, J. Chen, J. Studts, and G. Wang. „In-line product quality monitoring during biopharmaceutical manufacturing using computational Raman spectroscopy“. In: *mAbs* 15.1 (2023). DOI: 10.1080/19420862.2023.2220149.

[225] B. Wei et al. „Multi-attribute Raman spectroscopy (MARS) for monitoring product quality attributes in formulated monoclonal antibody therapeutics“. In: *mAbs* 14.1 (2022). DOI: 10.1080/19420862.2021.2007564.

[230] J. Meyer-Kirschner et al. „In-line Monitoring of Monomer and Polymer Content during Microgel Synthesis Using Precipitation Polymerization via Raman Spectroscopy and Indirect Hard Modeling“. In: *Applied Spectroscopy* 70.3 (2016), pp. 416–426. DOI: 10.1177/0003702815626663.

[232] J. V. Sinfield and C. K. Monwuba. „Assessment and correction of turbidity effects on Raman observations of chemicals in aqueous solutions“. In: *Applied Spectroscopy* 68.12 (2014), pp. 1381–1392. DOI: 10.1366/13-07292.

[234] R. M. Santos, J. M. Kessler, P. Salou, J. C. Menezes, and A. Peinado. „Monitoring mAb cultivations with in-situ raman spectroscopy: The influence of spectral selectivity on calibration models and industrial use as reliable PAT tool“. In: *Biotechnology Progress* 34.3 (2018), pp. 659–670. DOI: 10.1002/btpr.2635.

[251] E. Spinner. „Raman-spectral depolarisation ratios of ions in concentrated aqueous solution. The next-to-negligible effect of highly asymmetric ion surroundings on the symmetry properties of polarisability changes during vibrations of symmetric ions.“ In: *Spectrochimica Acta Part A: Molecular and Biomolecular Spectroscopy* 59.7 (2003), pp. 1441–1456. DOI: 10.1016/S1386-1425(02)00293-7.

[252] M. D. Fontana, K. Ben Mabrouk, and T. H. Kauffmann. „Raman spectroscopic sensors for inorganic salts“. In: *Spectroscopic Properties of Inorganic and Organometallic Compounds*. Ed. by J. Yarwood, R. Douthwaite, and S. Duckett. Vol. 44. RSC Publishing, 2013, pp. 40–67. DOI: 10.1039/9781849737791-00040.

[253] G. Socrates. *Infrared and Raman Characteristic Group Frequencies: Tables and Charts*. Wiley, 2004.

[257] R. Schiemer, M. Rüdt, and J. Hubbuch. „Generative data augmentation and automated optimization of convolutional neural networks for process monitoring“. In: *Frontiers in Bioengineering and Biotechnology* 12 (2024), pp. 1–21. DOI: 10.3389/fbioe.2024.1228846.

[264] F. Alsmeyer, H. J. Koß, and W. Marquardt. „Indirect spectral hard modeling for the analysis of reactive and interacting mixtures“. In: *Applied Spectroscopy* 58.8 (2004), pp. 975–985. DOI: 10.1366/0003702041655368.

[265] E. Kriesten, F. Alsmeyer, A. Bardow, and W. Marquardt. „Fully automated indirect hard modeling of mixture spectra“. In: *Chemometrics and Intelligent Laboratory Systems* 91.2 (2008), pp. 181–193. DOI: 10.1016/j.chemolab.2007.11.004.

[269] V. V. Kuzmin, V. S. Novikov, L. Y. Ustynyuk, K. A. Prokhorov, E. A. Sagitova, and G. Y. Nikolaeva. „Raman spectra of polyethylene glycols: Comparative experimental and DFT study“. In: *Journal of Molecular Structure* 1217 (2020), p. 128331. DOI: 10.1016/j.molstruc.2020.128331.

[277] A. Dietrich, L. Heim, and J. Hubbuch. „Dual-Stage Cross-Flow Filtration: Integrated Capture and Purification of Virus-Like Particles“. In: *Biotechnology and Bioengineering* 122.4 (2025), pp. 884–894. DOI: 10.1002/bit.28914.

[278] D. P. Wasalathanthri et al. „Real-time monitoring of quality attributes by in-line Fourier transform infrared spectroscopic sensors at ultrafiltration and diafiltration of bioprocess“. In: *Biotechnology and Bioengineering* 117.12 (2020), pp. 3766–3774. DOI: 10.1002/bit.27532.

[279] G. Thakur, S. Thori, and A. S. Rathore. „Implementing PAT for single-pass tangential flow ultrafiltration for continuous manufacturing of monoclonal antibodies“. In: *Journal of Membrane Science* 613 (2020), p. 118492. DOI: 10.1016/j.memsci.2020.118492.

[280] G. Thakur, V. Hebbi, and A. S. Rathore. „Near Infrared Spectroscopy as a PAT tool for monitoring and control of protein and excipient concentration in ultrafiltration of highly concentrated antibody formulations“. In: *International Journal of Pharmaceutics* 600 (2021), p. 120456. DOI: 10.1016/j.ijpharm.2021.120456.

[281] N. Brestich, M. Rüdt, D. Büchler, and J. Hubbuch. „Selective protein quantification for preparative chromatography using variable pathlength UV/Vis spectroscopy and partial least squares regression“. In: *Chemical Engineering Science* 176 (2018), pp. 157–164. DOI: 10.1016/j.ces.2017.10.030.

[282] C. M. Andersen and R. Bro. „Variable selection in regression—a tutorial“. In: *Journal of Chemometrics* 24.11-12 (2010), pp. 728–737. DOI: 10.1002/cem.1360.

[283] N. N. Zhang et al. „A Thermostable mRNA Vaccine against COVID-19“. In: *Cell* 182.5 (2020), 1271–1283.e16. DOI: 10.1016/j.cell.2020.07.024.

[284] F. J. Krug, J. Růžička, and E. H. Hansen. „Determination of ammonia in low concentrations with Nessler's reagent by flow injection analysis“. In: *The Analyst* 104.1234 (1979), pp. 47–54. DOI: 10.1039/an9790400047.

[285] C. J. Patton and S. R. Crouch. „Spectrophotometric and Kinetics Investigation of the Berthelot Reaction for the Determination of Ammonia“. In: *Analytical Chemistry* 49.3 (1977), pp. 464–469. DOI: 10.1021/ac50011a034.

[286] R. Saini and S. Kumar. „A fluorescent probe for the selective detection of sulfate ions in water“. In: *RSC Advances* 3.44 (2013), p. 21856. DOI: 10.1039/c3ra44220a.

[287] T. V. Plisko, A. V. Bildyukevich, V. V. Usosky, and V. V. Volkov. „Influence of the concentration and molecular weight of polyethylene glycol on the structure and permeability of polysulfone hollow fiber membranes“. In: *Petroleum Chemistry* 56.4 (2016), pp. 321–329. DOI: 10.1134/S096554411604006X.

[288] Z. Li and A. L. Zydney. „Effect of zinc chloride and PEG concentrations on the critical flux during tangential flow microfiltration of BSA precipitates“. In: *Biotechnology Progress* 33.6 (2017), pp. 1561–1567. DOI: 10.1002/btpr.2545.

[289] R. Prasad, S. H. Crouse, R. W. Rousseau, and M. A. Grover. „Quantifying Dense Multicomponent Slurries with In-Line ATR-FTIR and Raman Spectroscopies: A Hanford Case Study“. In: *Industrial and Engineering Chemistry Research* 62.39 (2023), pp. 15962–15973. DOI: 10.1021/acs.iecr.3c01249.

[290] Tornado. *Achieving Superior Raman Measurements: Understanding And Avoiding Detector Saturation*. 2021. URL: https://tornado-spectral.com/blog/achieving-superior-raman-measurements-understanding-and-avoiding-detector-saturation/ (visited on 05/19/2025).

[291] B. Bayer, M. von Stosch, M. Melcher, M. Duerkop, and G. Striedner. „Soft sensor based on 2D-fluorescence and process data enabling real-time estimation of biomass in Escherichia coli cultivations“. In: *Engineering in Life Sciences* 20.1-2 (2020), pp. 26–35. DOI: 10.1002/elsc.201900076.

[292] J. Kuligowski, G. Quintás, C. Herwig, and B. Lendl. „A rapid method for the differentiation of yeast cells grown under carbon and nitrogen-limited conditions by means of partial least squares discriminant analysis employing infrared micro-spectroscopic data of entire yeast cells“. In: *Talanta* 99 (2012), pp. 566–573. DOI: 10.1016/j.talanta.2012.06.036.

[293] D. H. Müller, C. Flake, T. Brands, and H.-J. Koß. „Bioprocess in-line monitoring using Raman spectroscopy and Indirect Hard Modeling (IHM): A simple calibration yields a robust model“. In: *Biotechnology and Bioengineering* 120.7 (2023), pp. 1857–1868. DOI: 10.1002/bit.28424.

[294] D. H. Müller, M. Börger, J. Thien, and H. J. Koß. „Bioprocess in-line monitoring and control using Raman spectroscopy and Indirect Hard Modeling (IHM)“. In: *Biotechnology and Bioengineering* 121.7 (2024), pp. 2225–2233. DOI: 10.1002/bit.28724.

8

General Discussion and Conclusion

The objective of this thesis was to advance process development for non-viral vectors, in detail, the downstream processing (DSP) of lipid nanoparticles (LNPs) and virus-like particles (VLPs), through (I) non-chromatographic, size-selective separation techniques for their primary purification and (II) sensor-based analytics and process analytical technology (PAT) tools. An analytical method for lipid quantification was established in order to assess lipid-related LNP quality attributes and process performance (Chapter 3). Cross-flow filtration (CFF) was explored for LNP purification, compared to conventional dialysis, and monitored using at-line dynamic light scattering (DLS) (Chapter 4). A tailored dual-stage CFF set-up was developed for integrated, precipitation-based capture and purification of VLPs (Chapter 5). By combining Raman spectroscopy and chemometrics, Raman-based PAT tools were systematically developed to monitor VLP precipitation (Chapter 6) and their recovery by dual-stage CFF (Chapter 7). Overall, the integration of CFF enabled efficient processing, and the developed sensors provided valuable insights into these purification processes.

The primary focus of the LNP process development is microfluidic mixing for LNP synthesis, along with the analysis of physicochemical characteristics, including particle size, surface charge, and encapsulation efficiency. Despite its direct impact on these LNP attributes, analysis of lipid composition is rarely undertaken. To demonstrate the importance of lipid quantification in LNP process development, a reversed-phase (RP)-high performance liquid chromatography (HPLC) method employing charged aerosol detection (CAD) was leveraged in Chapter 3 for the analysis of LNP process intermediates. The development of the method, along with its calibration and validation, was conducted using pure lipids and lipid mixtures. The developed method was thoroughly, lipid-specifically calibrated and validated, whereby its linearity, precision, accuracy, and robustness were effectively demonstrated. For the first time, a process parameter study was conducted in which lipids were quantitatively analyzed. In this study, LNPs were produced by microfluidic mixing at different total flow rates (TFRs) and subsequently dialyzed for buffer exchange. The method provided lipid concentrations, thereby revealing the lipid molar ratio and lipid recoveries, which

could be used to draw multiple conclusions about the LNPs and the process steps. Importantly, all these findings were consistent regardless of variations in TFR, unlike LNP size, whose inverse dependence on TFR is widely reported and was likewise observed here. The lipid molar ratio was found to be batch-independent and remained constant throughout the processing. Consequently, any deviation from the theoretical ratio could be traced back to the preparation of the lipid stock solution. A comparison of lipid concentrations in LNPs synthesized by microfluidic mixing revealed a batch-dependent effect, whereas lipid concentrations generally decreased during the subsequent dialysis step. In terms of lipid recovery, it has been demonstrated that the observed decrease in lipid concentration can be attributed, at least in part, to a dilution effect. The remaining reduction in lipid concentration is attributable to actual lipid loss, which in turn is indicative of the performance of the dialysis step. Overall, lipid quantification by RP-HPLC-CAD supports a thorough characterization of LNPs and an evaluation of the process performance. Moreover, this methodological approach may also be employed to investigate other processes, thereby providing new perspectives on LNP process development and enhancing overall process understanding.

In contrast to microfluidic mixing, the impact of the subsequent buffer exchange step on LNP attributes is rarely investigated, particularly when using CFF, despite representing an efficient and scalable alternative to dialysis. In Chapter 4, a CFF parameter study was conducted to investigate the impacts of parameters on LNP attributes and process performance in terms of lipid recoveries. In four distinct CFF experiments, LNPs were purified by constant-volume diafiltration (DF), followed by their concentration through ultrafiltration (UF). Although membrane characteristics (material, format, and area, or molecular weight cut-off (MWCO)) and system pressure settings (transmembrane pressure (TMP) or back pressure) were systematically varied, it was shown that none of these parameters had a systematic impact on LNP attributes. The RP-HPLC-CAD method (cf. Chapter 3) revealed a consistent lipid molar ratio throughout CFF-based processing, with final lipid recoveries ranging from 86 to 89%. Conversely, the particle size of LNPs was the only attribute that was reproducibly affected, showing a linear dependency on CFF processing time through the emergence of a second, larger population. Time-resolved insights into these changes in LNP size and size distribution were further supported through near real-time monitoring using at-line DLS. A comparison was made between the size increase of dialyzed and CFF-purified LNPs during purification and subsequent short-term storage. This comparison led to the underlying hypothesis of the interplay of pump-induced shear forces, LNP fusion, and the equilibrium size of LNPs. To conclude, Chapter 4 provides novel insights into CFF-induced changes in LNP size and size distribution, which, combined with future studies on the underlying mechanisms to confirm the aforementioned hypothesis, lay the groundwork for the promising concept of CFF-based processing for size-controlled LNP purification.

Standardized DSP for VLPs is rare due to their structural diversity. Independent of their diversity, the size difference between VLPs and impurities can be exploited by precipitation and filtration. Selective precipitation is a widely used VLP capture step, and CFF-based microfiltration (MF) for precipitate processing in DF mode offers higher performance than centrifugation-based processing in terms of productivity, product purity, and yield. In the first DF step, the precipitates are retained and washed, whereas in the subsequent DF step, the VLPs are re-dissolved, allowing them to pass through the MF membrane. However, due to the inherent characteristics of the process, the re-dissolved VLPs exhibit relatively low concentrations and contain residual precipitant. To overcome these limitations through process integration, a dual-stage CFF set-up was developed, in which a MF/UF membrane configuration was implemented (Chapter 5). Here, the integration of

the second membrane stage enabled integrated VLP recovery beyond their re-dissolution, as after passing through the MF membrane into this second stage, the re-dissolved VLPs could first be isolated through simultaneous depletion of residual precipitant and subsequently concentrated by integrated UF. Another outcome of this study was that co-precipitated and hence co-redissolved impurities could also be depleted. The benefit from precipitate recovery with the dual-stage CFF set-up was proven with regard to VLP concentration and purity. In comparison with the single-stage configuration, the dual-stage CFF setup enabled a 13-fold increase in product concentration, a fourfold decrease in residual precipitant, and an eightfold reduction of impurities. Overall, the integrated dual-stage CFF set-up provides a framework for standardized processing of precipitate, with promising future applications covering precipitation or crystallization processes of diverse biological molecules beyond VLPs.

PAT tool development for precipitation is associated with several challenges, particularly particulate precipitates, turbidity, and generally high impurity levels, which is why Raman spectroscopy offers superior suitability compared to the widely used PAT tools based on ultraviolet-visible (UV/Vis) spectroscopy. Nevertheless, the development of robust Raman-based PAT tools would clearly benefit from systematic data diversification, a thorough understanding of Raman spectral data, and its spectral preprocessing. In Chapter 6, a Raman-based PAT tool for monitoring VLP precipitation from clarified lysate was developed using a systematic approach. Diverse precipitation data were generated by conditioning the clarified lysate prior to the batch and fed-batch experiments, which resulted in varying precipitation backgrounds and dynamics. Next to spectral background variations, interferences caused by the particulate precipitates and precipitant could be eliminated through the systematic combination of spectral preprocessing operations, in the order of turbidity, baseline, and background correction, difference spectra, cropping, and derivative filtering. With partial least squares (PLS) models, the concentration of precipitated VLPs in batch and fed-batch precipitation could be predicted; however, limitations were observed in the transferability from batch to fed-batch data, as well as in resolving fine differences. The reason for the latter was assumed to be a non-linear relationship between the spectral data and the concentration of precipitated VLP. Another outcome of this study was that structural differences between VLPs and impurities could be seen in the spectral data, qualitatively confirming selective VLP precipitation. To conclude, the concept of systematic PAT tool development provides a new perspective on the importance of experimental data generation and targeted spectral preprocessing for robust models, laying the groundwork for future Raman-based PAT tool development to monitor processes containing particulates.

While the quantification of precipitant is not required in batch or fed-batch precipitation, it becomes essential in dynamic depletion processes, such as for the VLP recovery step by dual-stage CFF (cf. Chapter 5). However, sampling during the DF process can alter its dynamics, thereby rendering sensor-based PAT tools for real-time monitoring advantageous. Compared to PAT tool development for precipitation monitoring (cf. Chapter 6), fewer spectral interferences are expected for monitoring the VLP recovery step, as already re-dissolved VLPs and fewer impurities are present. In Chapter 7, Raman-based PAT tools for simultaneous monitoring of VLP accumulation and precipitant depletion during the filtration-based VLP recovery step by dual-stage CFF were developed. Under the scope of model transfer, spectral contributions of VLPs and precipitant were initially investigated using stock solutions of the pure components. A higher inherent sensor sensitivity towards the precipitant than VLPs was revealed. For the first time, Raman spectral data exhibiting detector saturation effects were used, with the saturation occurring in the predominant Raman band associated with the precipitant, which rendered a previously linear regression over this exact band for precipitant

quantification no longer feasible. Despite the presence of detector saturation effects, model transfer for precipitant monitoring proved effective through the selection of precipitant-specific preprocessing operations, including variable importance in projection (VIP)-based cropping, and PLS models. In detail, models were built from spectral data derived from stock solutions and transferred to on-line process data, which were derived from three diversified CFF experiments, each exhibiting differences in process parameters and initial VLP concentration. For VLP monitoring, a tailored pre-cropping operation effectively improved the spectral appearance in the protein-associated spectral regions; however, the lower prediction accuracy compared to that for the precipitant could be attributed to the inherent sensor's selectivity, although this limitation was partially mitigated through VLP-specific spectral preprocessing. Consequently, this study demonstrates the importance of tailored spectral preprocessing, while also underlining sensor and model selection itself.

In conclusion, this thesis presents advancements for the DSP of LNPs and VLPs through targeted implementation of (I) precipitation and filtration as size-selective separation techniques and (II) sensor-based analytics and PAT tools. Lipid analytics clearly proved valuable for LNP process development (Chapter 3). The potential of CFF for efficient, standardized processing was demonstrated through its implementation for LNP purification (Chapter 4) as well as its integration for the recovery of VLP precipitates (Chapter 5). For the former, initial steps towards LNP purification monitoring were taken through at-line DLS. The latter laid the groundwork for standardized, streamlined DSP of VLPs. In addition, the benefits of systematic approaches for Raman-based PAT tool development became evident, covering data diversification and spectral preprocessing, which overall provided valuable insights into VLP precipitation (Chapter 6) and CFF-based VLP recovery (Chapter 7). The aforementioned developments emerged from addressing unique purification and analytical challenges of non-viral vectors using size-selective purification and scattering-based sensor technologies. In essence, these developments contribute to enhanced process understanding and pave the way towards standardized and controlled DSP of vector technologies.

References

[1] S. Plotkin. „History of vaccination“. In: *Proceedings of the National Academy of Sciences of the United States of America* 111.34 (2014), pp. 12283–12287. DOI: 10.1073/pnas.1400472111.

[2] W. J. McAleer, E. B. Buynak, R. Z. Maigetter, D. E. Wampler, W. J. Miller, and M. R. Hilleman. „Human hepatitis B vaccine from recombinant yeast“. In: *Nature* 307.5947 (1984), pp. 178–180. DOI: 10.1038/307178a0.

[3] L. H. Lua, N. K. Connors, F. Sainsbury, Y. P. Chuan, N. Wibowo, and A. P. Middelberg. „Bioengineering virus-like particles as vaccines“. In: *Biotechnology and Bioengineering* 111.3 (2014), pp. 425–440. DOI: 10.1002/bit.25159.

[4] Y. H. Chung, H. Cai, and N. F. Steinmetz. „Viral nanoparticles for drug delivery, imaging, immunotherapy, and theranostic applications“. In: *Advanced Drug Delivery Reviews* 156 (2020), pp. 214–235. DOI: 10.1016/j.addr.2020.06.024.

[5] N. McCann, D. O'Connor, T. Lambe, and A. J. Pollard. „Viral vector vaccines“. In: *Current Opinion in Immunology* 77 (2022), p. 102210. DOI: 10.1016/j.coi.2022.102210.

[6] L. Schoenmaker et al. „mRNA-lipid nanoparticle COVID-19 vaccines: Structure and stability“. In: *International Journal of Pharmaceutics* 601 (2021), p. 120586. DOI: 10.1016/j.ijpharm.2021.120586.

[7] C. Wang et al. „Emerging non-viral vectors for gene delivery“. In: *Journal of Nanobiotechnology* 21.1 (2023), p. 272. DOI: 10.1186/s12951-023-02044-5.

[8] J. Gu et al. „Building a Better Silver Bullet: Current Status and Perspectives of Non-Viral Vectors for mRNA Vaccines“. In: *Advanced Healthcare Materials* 13.3 (2024), pp. 444–456. DOI: 10.1002/adhm.202302409.

[9] M. F. Bachmann, P. van Damme, F. Lienert, and T. F. Schwarz. „Virus-like particles: a versatile and effective vaccine platform“. In: *Expert Review of Vaccines* 24.1 (2025), pp. 444–456. DOI: 10.1080/14760584.2025.2508517.

[10] P. R. Cullis and P. L. Felgner. „The 60-year evolution of lipid nanoparticles for nucleic acid delivery“. In: *Nature Reviews Drug Discovery* 23.9 (2024), pp. 709–722. DOI: 10.1038/s41573-024-00977-6.

[11] C. L. Effio and J. Hubbuch. „Next generation vaccines and vectors: Designing downstream processes for recombinant protein-based virus-like particles“. In: *Biotechnology Journal* 10.5 (2015), pp. 715–727. DOI: 10.1002/biot.201400392.

[12] M. J. W. Evers, J. A. Kulkarni, R. van der Meel, P. R. Cullis, P. Vader, and R. M. Schiffelers. „State-of-the-Art Design and Rapid-Mixing Production Techniques of Lipid Nanoparticles for Nucleic Acid Delivery“. In: *Small Methods* 2.9 (2018), p. 1700375. DOI: 10.1002/smtd.201700375.

[13] N. Hillebrandt and J. Hubbuch. „Size-selective downstream processing of virus particles and non-enveloped virus-like particles“. In: *Frontiers in Bioengineering and Biotechnology* 11 (2023). DOI: 10.3389/fbioe.2023.1192050.

[14] FDA. *Guidance for Industry: PAT—a framework for innovative pharmaceutical development, manufacturing, and quality assurance*. 2004.

[15] M. Rüdt, T. Briskot, and J. Hubbuch. „Advances in downstream processing of biologics – Spectroscopy: An emerging process analytical technology“. In: *Journal of Chromatography A* 1490 (2017), pp. 2–9. DOI: 10.1016/j.chroma.2016.11.010.

[16] M. Rüdt, P. Vormittag, N. Hillebrandt, and J. Hubbuch. „Process monitoring of virus-like particle reassembly by diafiltration with UV/Vis spectroscopy and light scattering“. In: *Biotechnology and Bioengineering* 116.6 (2019), pp. 1366–1379. DOI: 10.1002/bit.26935.

[17] N. Hillebrandt, P. Vormittag, A. Dietrich, and J. Hubbuch. „Process monitoring framework for cross-flow diafiltration-based virus-like particle disassembly: Tracing product properties and filtration performance“. In: *Biotechnology and Bioengineering* 119.6 (2022), pp. 1522–1538. DOI: 10.1002/bit.28063.

[18] L. J. Lohmann and J. Strube. „Process analytical technology for precipitation process integration into biologics manufacturing towards autonomous operation—mab case study“. In: *Processes* 9.3 (2021). DOI: 10.3390/pr9030488.

[19] L. Rolinger et al. „Multi-attribute PAT for UF/DF of Proteins—Monitoring Concentration, particle sizes, and Buffer Exchange“. In: *Analytical and Bioanalytical Chemistry* 412.9 (2020), pp. 2123–2136. DOI: 10.1007/s00216-019-02318-8.

[20] D. Vaskó et al. „Raman and NIR spectroscopy-based real-time monitoring of the membrane filtration process of a recombinant protein for the diagnosis of SARS-CoV-2“. In: *International Journal of Pharmaceutics* 660 (2024), p. 124251. DOI: 10.1016/j.ijpharm.2024.124251.

[21] A. K. Leung et al. „Lipid nanoparticles containing siRNA synthesized by microfluidic mixing exhibit an electron-dense nanostructured core“. In: *Journal of Physical Chemistry C* 116.34 (2012), pp. 18440–18450. DOI: 10.1021/jp303267y.

[22] C. H. Albertsen, J. A. Kulkarni, D. Witzigmann, M. Lind, K. Petersson, and J. B. Simonsen. „The role of lipid components in lipid nanoparticles for vaccines and gene therapy“. In: *Advanced Drug Delivery Reviews* 188 (2022), p. 114416. DOI: 10.1016/j.addr.2022.114416.

[23] C. B. Roces et al. „Manufacturing considerations for the development of lipid nanoparticles using microfluidics“. In: *Pharmaceutics* 12.11 (2020), pp. 1–19. DOI: 10.3390/pharmaceutics12111095.

[24] S. C. Semple et al. „Rational design of cationic lipids for siRNA delivery“. In: *Nature Biotechnology* 28.2 (2010), pp. 172–176. DOI: 10.1038/nbt.1602.

[25] K. T. Love et al. „Lipid-like materials for low-dose, in vivo gene silencing“. In: *Proceedings of the National Academy of Sciences of the United States of America* 107.5 (2010), pp. 1864–1869. DOI: 10.1073/pnas.0910603106.

[26] M. Jayaraman et al. „Maximizing the potency of siRNA lipid nanoparticles for hepatic gene silencing in vivo“. In: *Angewandte Chemie - International Edition* 51.34 (2012), pp. 8529–8533. DOI: 10.1002/anie.201203263.

[27] J. A. Kulkarni et al. „On the Formation and Morphology of Lipid Nanoparticles Containing Ionizable Cationic Lipids and siRNA“. In: *ACS Nano* 12.5 (2018), pp. 4787–4795. DOI: 10.1021/acsnano.8b01516.

[28] Y. Fan et al. „Automated high-throughput preparation and characterization of oligonucleotide-loaded lipid nanoparticles“. In: *International Journal of Pharmaceutics* 599 (2021). DOI: 10.1016/j.ijpharm.2021.120392.

[29] K. Okuda et al. „On the size-regulation of RNA-loaded lipid nanoparticles synthesized by microfluidic device“. In: *Journal of Controlled Release* 348 (2022), pp. 648–659. DOI: 10.1016/j.jconrel.2022.06.017.

[30] A. K. Leung, Y. Y. C. Tam, S. Chen, I. M. Hafez, and P. R. Cullis. „Microfluidic Mixing: A General Method for Encapsulating Macromolecules in Lipid Nanoparticle Systems“. In: *Journal of Physical Chemistry B* 119.28 (2015), pp. 8698–8706. DOI: 10.1021/acs.jpcb.5b02891.

[31] J. A. Kulkarni, D. Witzigmann, J. Leung, Y. Y. C. Tam, and P. R. Cullis. „On the role of helper lipids in lipid nanoparticle formulations of siRNA“. In: *Nanoscale* 11.45 (2019), pp. 21733–21739. DOI: 10.1039/c9nr09347h.

[32] J. A. Kulkarni et al. „Fusion-dependent formation of lipid nanoparticles containing macromolecular payloads“. In: *Nanoscale* 11.18 (2019), pp. 9023–9031. DOI: 10.1039/C9NR02004G.

[33] R. A. Petros and J. M. DeSimone. „Strategies in the design of nanoparticles for therapeutic applications“. In: *Nature Reviews Drug Discovery* 9.8 (2010), pp. 615–627. DOI: 10.1038/nrd2591.

[34] T. Terada et al. „Characterization of Lipid Nanoparticles Containing Ionizable Cationic Lipids Using Design-of-Experiments Approach“. In: *Langmuir* 37.3 (2021), pp. 1120–1128. DOI: 10.1021/acs.langmuir.0c03039.

[35] R. Vargas et al. „Dialysis is a key factor modulating interactions between critical process parameters during the microfluidic preparation of lipid nanoparticles“. In: *Colloids and Interface Science Communications* 54 (2023). DOI: 10.1016/j.colcom.2023.100709.

[36] R. van Reis and A. Zydney. „Bioprocess membrane technology“. In: *Journal of Membrane Science* 297.1-2 (2007), pp. 16–50. DOI: 10.1016/j.memsci.2007.02.045.

[37] C. Geng et al. „A preparation method for mRNA-LNPs with improved properties“. In: *Journal of Controlled Release* 364 (2023), pp. 632–643. DOI: 10.1016/j.jconrel.2023.11.017.

[38] W. Wu et al. „Process development of tangential flow filtration and sterile filtration for manufacturing of mRNA-lipid nanoparticles: A study on membrane performance and filtration modeling“. In: *International Journal of Pharmaceutics* 675 (2025). DOI: 10.1016/j.ijpharm.2025.125520.

[39] B. Chackerian. „Virus-like particles: Flexible platforms for vaccine development“. In: *Expert Review of Vaccines* 6.3 (2007), pp. 381–390. DOI: 10.1586/14760584.6.3.381.

[40] N. Kushnir, S. J. Streatfield, and V. Yusibov. „Virus-like particles as a highly efficient vaccine platform: Diversity of targets and production systems and advances in clinical development“. In: *Vaccine* 31.1 (2012), pp. 58–83. DOI: 10.1016/j.vaccine.2012.10.083.

[41] H. Tariq, S. Batool, S. Asif, M. Ali, and B. H. Abbasi. „Virus-Like Particles: Revolutionary Platforms for Developing Vaccines Against Emerging Infectious Diseases“. In: *Frontiers in Microbiology* 12 (2022). DOI: 10.3389/fmicb.2021.790121.

[42] Y. Liu, M. Pietzsch, and J. Ulrich. „Determination of the phase diagram for the crystallization of L-asparaginase II by a turbidity technique“. In: *Crystal Research and Technology* 49.4 (2014), pp. 262–268. DOI: 10.1002/crat.201300402.

[43] S. Nooraei et al. „Virus-like particles: preparation, immunogenicity and their roles as nanovaccines and drug nanocarriers“. In: *Journal of Nanobiotechnology* 19.1 (2021), p. 59. DOI: 10.1186/s12951-021-00806-7.

[44] B. E. Clarke et al. „Improved immunogenicity of a peptide epitope after fusion to hepatitis B core protein“. In: *Nature* 330.6146 (1987), pp. 381–384. DOI: 10.1038/330381a0.

[45] M. Peacey, S. Wilson, M. A. Baird, and V. K. Ward. „Versatile RHDV virus-like particles: Incorporation of antigens by genetic modification and chemical conjugation“. In: *Biotechnology and Bioengineering* 98.5 (2007), pp. 968–977. DOI: 10.1002/bit.21518.

[46] C. J. Burrell, P. Mackay, P. J. Greenaway, P. H. Hofschneider, and K. Murray. „Expression in Escherichia coli of hepatitis B virus DNA sequences cloned in plasmid pBR322“. In: *Nature* 279.5708 (1979), pp. 43–47. DOI: 10.1038/279043a0.

[47] S. Stahl, P. MacKay, M. Magazin, S. A. Bruce, and K. Murray. „Hepatitis B virus core antigen: Synthesis in Escherichia coli and application in diagnosis“. In: *Proceedings of the National Academy of Sciences of the United States of America* 79.5 (1982), pp. 1606–1610. DOI: 10.1073/pnas.79.5.1606.

[48] F. A. Crowther et al. „Three-Dimensional Structure of Hepatitis B Virus Core Particles Determined by Electron Cryomicroscopy“. In: *Cell* 77 (1994), pp. 943–950. DOI: 10.1016/0092-8674(94)90142-2.

[49] A. Zlotnick et al. „Dimorphism of Hepatitis B Virus Capsids Is Strongly Influenced by the C-Terminus of the Capsid Protein“. In: *Biochemistry* 35.23 (1996), pp. 7412–7421. DOI: 10.1021/bi9604800.

[50] R. McGonigle et al. „An N-terminal extension to the hepatitis B virus core protein forms a poorly ordered trimeric spike in assembled virus-like particles“. In: *Journal of Structural Biology* 189.2 (2015), pp. 73–80. DOI: 10.1016/j.jsb.2014.12.006.

[51] J. Schumacher et al. „Enhanced stability of a chimeric hepatitis B core antigen virus-like-particle (HBcAg-VLP) by a C-terminal linker-hexahistidine-peptide“. In: *Journal of Nanobiotechnology* 16.1 (2018), p. 39. DOI: 10.1186/s12951-018-0363-0.

[52] A. Valentic, J. Müller, and J. Hubbuch. „Effects of Different Lengths of a Nucleic Acid Binding Region and Bound Nucleic Acids on the Phase Behavior and Purification Process of HBcAg Virus-Like Particles“. In: *Frontiers in Bioengineering and Biotechnology* 10 (2022). DOI: 10.3389/fbioe.2022.929243.

[53] T. Klamp et al. „Highly Specific Auto-Antibodies against Claudin-18 Isoform 2 Induced by a Chimeric HBcAg Virus-Like Particle Vaccine Kill Tumor Cells and Inhibit the Growth of Lung Metastases“. In: *Cancer Research* 71.2 (2011), pp. 516–527. DOI: 10.1158/0008-5472.CAN-10-2292.

[54] M. Moradi Vahdat et al. „Hepatitis B core-based virus-like particles: A platform for vaccine development in plants“. In: *Biotechnology Reports* 29 (2021), e00605. DOI: 10.1016/j.btre.2021.e00605.

[55] A. M. Hassebroek et al. „A hepatitis B virus core antigen-based virus-like particle vaccine expressing SARS-CoV-2 B and T cell epitopes induces epitope-specific humoral and cell-mediated immune responses but confers limited protection against SARS-CoV-2 infection“. In: *Journal of Medical Virology* 95.2 (2023). DOI: 10.1002/jmv.28503.

[56] A. Zeltins. „Construction and Characterization of Virus-Like Particles: A Review“. In: *Molecular Biotechnology* 53.1 (2013), pp. 92–107. DOI: 10.1007/s12033-012-9598-4.

[57] M. G. Moleirinho, R. J. Silva, P. M. Alves, M. J. T. Carrondo, and C. Peixoto. „Current challenges in biotherapeutic particles manufacturing“. In: *Expert Opinion on Biological Therapy* 20.5 (2020), pp. 451–465. DOI: 10.1080/14712598.2020.1693541.

[58] L. K. Pattenden, A. P. Middelberg, M. Niebert, and D. I. Lipin. „Towards the preparative and large-scale precision manufacture of virus-like particles“. In: *Trends in Biotechnology* 23.10 (2005), pp. 523–529. DOI: 10.1016/j.tibtech.2005.07.011.

[59] M. W. Liew, Y. P. Chuan, and A. P. Middelberg. „Reactive diafiltration for assembly and formulation of virus-like particles“. In: *Biochemical Engineering Journal* 68 (2012), pp. 120–128. DOI: 10.1016/j.bej.2012.07.009.

[60] L. Gerstweiler, J. Billakanti, J. Bi, and A. Middelberg. „Comparative evaluation of integrated purification pathways for bacterial modular polyomavirus major capsid protein VP1 to produce virus-like particles using high throughput process technologies“. In: *Journal of Chromatography A* 1639 (2021), p. 461924. DOI: 10.1016/j.chroma.2021.461924.

[61] N. Hillebrandt, P. Vormittag, A. Dietrich, C. H. Wegner, and J. Hubbuch. „Process development for cross-flow diafiltration-based VLP disassembly: A novel high-throughput screening approach“. In: *Biotechnology and Bioengineering* 118.10 (2021), pp. 3926–3940. DOI: 10.1002/bit.27868.

[62] H. Mach et al. „Disassembly and reassembly of yeast-derived recombinant human papillomavirus virus-like particles (HPV VLPs)“. In: *Journal of Pharmaceutical Sciences* 95.10 (2006), pp. 2195–2206. DOI: 10.1002/jps.20696.

[63] Q. Zhao et al. „Disassembly and reassembly of human papillomavirus virus-like particles produces more virion-like antibody reactivity“. In: *Virology Journal* 9 (2012). DOI: 10.1186/1743-422X-9-52.

[64] A. Strods et al. „Preparation by alkaline treatment and detailed characterisation of empty hepatitis B virus core particles for vaccine and gene therapy applications“. In: *Scientific Reports* 5 (2015), pp. 1–16. DOI: 10.1038/srep11639.

[65] I. Petrovskis et al. „Production of the HBc Protein from Different HBV Genotypes in E. coli. Use of Reassociated HBc VLPs for Packaging of ss- and dsRNA“. In: *Microorganisms* 9.2 (2021), p. 283. DOI: 10.3390/microorganisms9020283.

[66] A. Valentic and J. Hubbuch. „Effective removal of host cell-derived nucleic acids bound to hepatitis B core antigen virus-like particles by heparin chromatography“. In: *Frontiers in Bioengineering and Biotechnology* 12 (2024), pp. 1–15. DOI: 10.3389/fbioe.2024.1475918.

[67] A. Cooper and Y. Shaul. „Recombinant viral capsids as an efficient vehicle of oligonucleotide delivery into cells“. In: *Biochemical and Biophysical Research Communications* 327.4 (2005), pp. 1094–1099. DOI: 10.1016/j.bbrc.2004.12.118.

[68] J. Z. Porterfield, M. S. Dhason, D. D. Loeb, M. Nassal, S. J. Stray, and A. Zlotnick. „Full-Length Hepatitis B Virus Core Protein Packages Viral and Heterologous RNA with Similarly High Levels of Cooperativity“. In: *Journal of Virology* 84.14 (2010), pp. 7174–7184. DOI: 10.1128/JVI.00586-10.

[69] S. D. Durbin and G. Feher. „Protein Crystallization“. In: *Annual Review of Physical Chemistry* 47.1 (1996), pp. 171–204. DOI: 10.1146/annurev.physchem.47.1.171.

[70] F. Rothstein. „Differential precipitation of proteins“. In: *Protein purification process engineering*. Ed. by R. G. Harrison. New York, 1994, pp. 115–208.

[71] E. Y. Chi, S. Krishnan, T. W. Randolph, and J. F. Carpenter. „Physical stability of proteins in aqueous solution: Mechanism and driving forces in nonnative protein aggregation“. In: *Pharmaceutical Research* 20.9 (2003), pp. 1325–1336. DOI: 10.1023/a:1025771421906.

[72] M. Boström, F. Tavares, S. Finet, F. Skouri-Panet, A. Tardieu, and B. Ninham. „Why forces between proteins follow different Hofmeister series for pH above and below pI“. In: *Biophysical Chemistry* 117.3 (2005), pp. 217–224. DOI: 10.1016/j.bpc.2005.05.010.

[73] E. O. Watanabe, E. Popova, E. A. Miranda, G. Maurer, and P. d. A. P. Filho. „Phase equilibria for salt-induced lysozyme precipitation: Effect of salt type and temperature“. In: *Fluid Phase Equilibria* 281.1 (2009), pp. 32–39. DOI: 10.1016/j.fluid.2009.03.021.

[74] H. Mahadevan and C. K. Hall. „Experimental analysis of protein precipitation by polyethylene glycol and comparison with theory“. In: *Fluid Phase Equilibria* 78.C (1992), pp. 297–321. DOI: 10.1016/0378-3812(92)87043-M.

[75] M. d. C. Pons Royo, J. L. Beulay, E. Valery, A. Jungbauer, and P. Satzer. „Mode and dosage time in polyethylene glycol precipitation process influences protein precipitate size and filterability“. In: *Process Biochemistry* 114 (2022), pp. 77–85. DOI: 10.1016/j.procbio.2022.01.017.

[76] Y.-C. Shih, J. M. Prausnitz, and H. W. Blanch. „Some characteristics of protein precipitation by salts“. In: *Biotechnology and Bioengineering* 40.10 (1992), pp. 1155–1164. DOI: 10.1002/bit.260401004.

[77] R. A. Curtis, J. M. Prausnitz, and H. W. Blanch. „Protein-protein and protein-salt interactions in aqueous protein solutions containing concentrated electrolytes“. In: *Biotechnology and Bioengineering* 57.1 (1998), pp. 11–21. DOI: 10.1002/(SICI)1097-0290(19980105)57:1<11::AID-BIT2>3.0.CO;2-Y.

[78] W. Kunz, J. Henle, and B. Ninham. „‘Zur Lehre von der Wirkung der Salze’ (about the science of the effect of salts): Franz Hofmeister’s historical papers“. In: *Current Opinion in Colloid & Interface Science* 9.1-2 (2004), pp. 19–37. DOI: 10.1016/j.cocis.2004.05.005.

[79] B. Kang, H. Tang, Z. Zhao, and S. Song. „Hofmeister Series: Insights of Ion Specificity from Amphiphilic Assembly and Interface Property“. In: *ACS Omega* 5.12 (2020), pp. 6229–6239. DOI: 10.1021/acsomega.0c00237.

[80] P. Wingfield. „Protein Precipitation Using Ammonium Sulfate“. In: *Current Protocols in Protein Science* 13.1 (1998), pp. 1–8. DOI: 10.1002/0471140864.psa03fs13.

[81] S. Tsoka, O. C. Ciniawskyj, O. R. T. Thomas, N. J. Titchener-Hooker, and M. Hoare. „Selective Flocculation and Precipitation for the Improvement of Virus-Like Particle Recovery from Yeast Homogenate“. In: *Biotechnology Progress* 16.4 (2000), pp. 661–667. DOI: 10.1021/bp0000407.

[82] T. Koho et al. „Purification of norovirus-like particles (VLPs) by ion exchange chromatography“. In: *Journal of Virological Methods* 181.1 (2012), pp. 6–11. DOI: 10.1016/j.jviromet.2012.01.003.

[83] H. J. Kim, S. Y. Kim, S. J. Lim, J. Y. Kim, S. J. Lee, and H. J. Kim. „One-step chromatographic purification of human papillomavirus type 16 L1 protein from Saccharomyces cerevisiae“. In: *Protein Expression and Purification* 70.1 (2010), pp. 68–74. DOI: 10.1016/j.pep.2009.08.005.

[84] M. Zahin et al. „Scalable production of HPV16 L1 protein and VLPs from tobacco leaves“. In: *PLoS ONE* 11.8 (2016), pp. 1–16. DOI: 10.1371/journal.pone.0160995.

[85] A. Kazaks et al. „Production and purification of chimeric HBc virus-like particles carrying influenza virus LAH domain as vaccine candidates“. In: *BMC Biotechnology* 17.1 (2017), pp. 1–11. DOI: 10.1186/s12896-017-0396-8.

[86] Y. Zhang et al. „In vitro preparation of uniform and nucleic acid free hepatitis B core particles through an optimized disassembly-purification-reassembly process“. In: *Protein Expression and Purification* 178 (2021). DOI: 10.1016/j.pep.2020.105747.

[87] J. Yang, L. Zhang, C. Zhang, and Y. Lu. „Exploration on the expression and assembly of virus-like particles“. In: *Biotechnology Notes* 2 (2021), pp. 51–58. DOI: 10.1016/j.biotno.2021.08.003.

[88] N. Hillebrandt, P. Vormittag, N. Bluthardt, A. Dietrich, and J. Hubbuch. „Integrated Process for Capture and Purification of Virus-Like Particles: Enhancing Process Performance by Cross-Flow Filtration“. In: *Frontiers in Bioengineering and Biotechnology* 8 (2020). DOI: 10.3389/fbioe.2020.00489.

[89] S. Großhans, S. Suhm, and J. Hubbuch. „Precipitation of complex antibody solutions: influence of contaminant composition and cell culture medium on the precipitation behavior“. In: *Bioprocess and Biosystems Engineering* (2019). DOI: 10.1007/s00449-019-02103-y.

[90] C. H. Wegner and J. Hubbuch. „Calibration-free PAT: Locating selective crystallization or precipitation sweet spot in screenings with multi-way PARAFAC models“. In: *Frontiers in Bioengineering and Biotechnology* 10 (2022), pp. 1–18. DOI: 10.3389/fbioe.2022.1051129.

[91] P. Vormittag, T. Klamp, and J. Hubbuch. „Ensembles of Hydrophobicity Scales as Potent Classifiers for Chimeric Virus-Like Particle Solubility – An Amino Acid Sequence-Based Machine Learning Approach“. In: *Frontiers in Bioengineering and Biotechnology* 8 (2020). DOI: 10.3389/fbioe.2020.00395.

[92] P. Vormittag, T. Klamp, and J. Hubbuch. „Optimization of a Soft Ensemble Vote Classifier for the Prediction of Chimeric Virus-Like Particle Solubility and Other Biophysical Properties“. In: *Frontiers in Bioengineering and Biotechnology* 8 (2020), pp. 1–17. DOI: 10.3389/fbioe.2020.00881.

[93] A.-S. Jönsson and G. Trägårdh. „Fundamental principles of ultrafiltration“. In: *Chemical Engineering and Processing: Process Intensification* 27.2 (1990), pp. 67–81. DOI: 10.1016/0255-2701(90)85011-R.

[94] R. Van Reis and S. Saksena. „Optimization diagram for membrane separations“. In: *Journal of Membrane Science* 129.1 (1997), pp. 19–29. DOI: 10.1016/S0376-7388(96)00319-5.

[95] J. E. Ladwig, X. X. Zhu, P. Rolandi, R. Hart, J. Robinson, and A. Rydholm. „Mechanistic model of pH and excipient concentration during ultrafiltration and diafiltration processes of therapeutic antibodies“. In: *Biotechnology Progress* 36.5 (2020), pp. 1–19. DOI: 10.1002/btpr.2993.

[96] R. Ambrožič, D. Arzenšek, and A. Podgornik. „Designing scalable ultrafiltration/diafiltration process of monoclonal antibodies via mathematical modeling by coupling mass balances and Poisson–Boltzmann equation“. In: *Biotechnology and Bioengineering* 118.2 (2021), pp. 633–646. DOI: 10.1002/bit.27598.

[97] T. Briskot et al. „Modeling the Gibbs-Donnan effect during ultrafiltration and diafiltration processes using the Poisson–Boltzmann theory in combination with a basic Stern model“. In: *Journal of Membrane Science* 648 (2022), p. 120333. DOI: 10.1016/j.memsci.2022.120333.

[98] A. D. Marshall, P. A. Munro, and G. Trägårdh. „The effect of protein fouling in microfiltration and ultrafiltration on permeate flux, protein retention and selectivity: A literature review“. In: *Desalination* 91.1 (1993), pp. 65–108. DOI: 10.1016/0011-9164(93)80047-Q.

[99] W. F. Blatt, A. Dravid, A. S. Michaels, and L. Nelsen. „Solute Polarization and Cake Formation in Membrane Ultrafiltration: Causes, Consequences, and Control Techniques“. In: *Membrane Science and Technology: Industrial, Biological, and Waste Treatment Processes*. Ed. by J. E. Flinn. Boston, MA: Springer US, 1970, pp. 47–97. DOI: 10.1007/978-1-4684-1851-4_4.

[100] C. Quezada, H. Estay, A. Cassano, E. Troncoso, and R. Ruby-Figueroa. „Prediction of permeate flux in ultrafiltration processes: A review of modeling approaches“. In: *Membranes* 11.5 (2021). DOI: 10.3390/membranes11050368.

[101] T. Vicente, S. Burri, S. Wellnitz, K. Walsh, S. Rothe, and J. Liderfelt. „Fully aseptic single-use cross flow filtration system for clarification and concentration of cytomegalovirus-like particles“. In: *Engineering in Life Sciences* 14.3 (2014), pp. 318–326. DOI: 10.1002/elsc.201300093.

[102] A. Venkiteshwaran, P. Heider, L. Teysseyre, and G. Belfort. „Selective precipitation-assisted recovery of immunoglobulins from bovine serum using controlled-fouling crossflow membrane microfiltration“. In: *Biotechnology and Bioengineering* 101.5 (2008), pp. 957–966. DOI: 10.1002/bit.21964.

[103] M. Kuczewski, E. Schirmer, B. Lain, and G. Zarbis-Papastoitsis. „A single-use purification process for the production of a monoclonal antibody produced in a PER.C6 human cell line“. In: *Biotechnology Journal* 6.1 (2011), pp. 56–65. DOI: 10.1002/biot.201000292.

[104] N. Hammerschmidt, S. Hobiger, and A. Jungbauer. „Continuous polyethylene glycol precipitation of recombinant antibodies: Sequential precipitation and resolubilization“. In: *Process Biochemistry* 51.2 (2016), pp. 325–332. DOI: 10.1016/j.procbio.2015.11.032.

[105] D. Burgstaller, A. Jungbauer, and P. Satzer. „Continuous integrated antibody precipitation with two-stage tangential flow microfiltration enables constant mass flow“. In: *Biotechnology and Bioengineering* 116.5 (2019), pp. 1053–1065. DOI: 10.1002/bit.26922.

[106] G. Recanati et al. „Integration of a perfusion reactor and continuous precipitation in an entirely membrane-based process for antibody capture“. In: *Engineering in Life Sciences* 23.10 (2023), pp. 1–14. DOI: 10.1002/elsc.202300219.

[107] Z. Li, Q. Gu, J. L. Coffman, T. Przybycien, and A. L. Zydney. „Continuous precipitation for monoclonal antibody capture using countercurrent washing by microfiltration“. In: *Biotechnology Progress* 35.6 (2019), pp. 1–8. DOI: 10.1002/btpr.2886.

[108] M. Minervini et al. „Continuous precipitation-filtration process for initial capture of a monoclonal antibody product using a four-stage countercurrent hollow fiber membrane washing step“. In: *Biotechnology and Bioengineering* 121.8 (2024), pp. 2258–2268. DOI: 10.1002/bit.28525.

[109] K. P. S. Piash, C. MacElroy, Z. Wang, and A. L. Zydney. „Vibration-Assisted Single-Pass tangential flow filtration for processing precipitated proteins“. In: *Separation and Purification Technology* 376.P3 (2025), p. 134136. DOI: 10.1016/j.seppur.2025.134136.

[110] R. T. Kurnik et al. „Buffer exchange using size exclusion chromatography, countercurrent dialysis, and tangential flow filtration: Models, development, and industrial application“. In: *Biotechnology and Bioengineering* 45.2 (1995), pp. 149–157. DOI: 10.1002/bit.260450209.

[111] S. B. Carvalho et al. „Membrane-Based Approach for the Downstream Processing of Influenza Virus-Like Particles“. In: *Biotechnology Journal* 14.8 (2019). DOI: 10.1002/biot.201800570.

[112] A. S. Rathore, R. Bhambure, and V. Ghare. „Process analytical technology (PAT) for biopharmaceutical products“. In: *Analytical and Bioanalytical Chemistry* 398.1 (2010), pp. 137–154. DOI: 10.1007/s00216-010-3781-x.

[113] J. Glassey et al. „Process analytical technology (PAT) for biopharmaceuticals“. In: *Biotechnology Journal* 6.4 (2011), pp. 369–377. DOI: 10.1002/biot.201000356.

[114] L. Rolinger, M. Rüdt, and J. Hubbuch. „A critical review of recent trends, and a future perspective of optical spectroscopy as PAT in biopharmaceutical downstream processing“. In: *Analytical and Bioanalytical Chemistry* 412.9 (2020), pp. 2047–2064. DOI: 10.1007/s00216-020-02407-z.

[115] M. S. H. Akash and K. Rehman. „Ultraviolet-Visible (UV-VIS) Spectroscopy“. In: *Essentials of Pharmaceutical Analysis*. Singapore: Springer Nature Singapore, 2020, pp. 1–222. DOI: 10.1007/978-981-15-1547-7.

[116] D. F. Swinehart. „The Beer-Lambert Law“. In: *Journal of Chemical Education* 39.7 (1962), p. 333. DOI: 10.1021/ed039p333.

[117] P. H. Gamache et al. „HPLC analysis of nonvolatile analytes using charged aerosol detection“. In: *LC-GC Europe* 18.6 (2005), pp. 345–354.

[118] P. H. Gamache and S. L. Kaufman. *Principles of Charged Aerosol Detection*. John Wiley & Sons, Ltd, 2017, pp. 1–65. DOI: 10.1002/9781119390725.ch1.

[119] R. A. Moreau. „The analysis of lipids via HPLC with a charged aerosol detector“. In: *Lipids* 41.7 (2006), pp. 727–734. DOI: 10.1007/s11745-006-5024-7.

[120] L. Li, J. P. Foley, and R. Helmy. „Simultaneous separation of small interfering RNA and lipids using ion-pair reversed-phase liquid chromatography“. In: *Journal of Chromatography A* 1601 (2019), pp. 145–154. DOI: 10.1016/j.chroma.2019.04.061.

[121] C. Kinsey et al. „Determination of lipid content and stability in lipid nanoparticles using ultra high-performance liquid chromatography in combination with a Corona Charged Aerosol Detector“. In: *Electrophoresis* 43.9-10 (2022), pp. 1091–1100. DOI: 10.1002/elps.202100244.

[122] K. H. Kim et al. „Optimization of HPLC–CAD method for simultaneous analysis of different lipids in lipid nanoparticles with analytical QbD“. In: *Journal of Chromatography A* 1709 (2023), p. 464375. DOI: 10.1016/j.chroma.2023.464375.

[123] V. Bender, L. Fuchs, and R. Süss. „RP-HPLC-CAD method for the rapid analysis of lipids used in lipid nanoparticles derived from dual centrifugation“. In: *International Journal of Pharmaceutics: X* 7 (2024), p. 100255. DOI: 10.1016/j.ijpx.2024.100255.

[124] X. Yu et al. „Validation of an HPLC-CAD Method for Determination of Lipid Content in LNP-Encapsulated COVID-19 mRNA Vaccines“. In: *Vaccines* 11.5 (2023). DOI: 10.3390/vaccines11050937.

[125] M. Hof and R. Macháň. „Basics of Optical Spectroscopy“. In: *Handbook of Spectroscopy*. Ed. by G. Gauglitz and D. Moore. John Wiley & Sons, Ltd, 2014, pp. 31–38. DOI: https://doi.org/10.1002/9783527654703.ch3.

[126] J. Stetefeld, S. A. McKenna, and T. R. Patel. „Dynamic light scattering: a practical guide and applications in biomedical sciences“. In: *Biophysical Reviews* 8.4 (2016), pp. 409–427. DOI: 10.1007/s12551-016-0218-6.

[127] A. Einstein. „Zur Theorie der Brownschen Bewegung“. In: *Annalen der Physik* 324.2 (1906), pp. 371–381. DOI: 10.1002/andp.19063240208.

[128] J. C. Thomas. „The determination of log normal particle size distributions by dynamic light scattering“. In: *Journal of Colloid and Interface Science* 117.1 (1987), pp. 187–192. DOI: 10.1016/0021-9797(87)90182-2.

[129] R. L. McCreery. *Raman Spectroscopy for Chemical Analysis*. New York: John Wiley & Sons, 2005.

[130] K. A. Bakeev. *Process Analytical Technology: Spectroscopic Tools and Implementation Strategies for the Chemical and Pharmaceutical Industries*. Ed. by K. A. Bakeev. John Wiley & Sons, 2010. DOI: 10.1002/9780470689592.

[131] N. C. Maiti, M. M. Apetri, M. G. Zagorski, P. R. Carey, and V. E. Anderson. „Raman Spectroscopic Characterization of Secondary Structure in Natively Unfolded Proteins: α-Synuclein“. In: *Journal of the American Chemical Society* 126.8 (2004), pp. 2399–2408. DOI: 10.1021/ja0356176.

[132] A. Rygula, K. Majzner, K. M. Marzec, A. Kaczor, M. Pilarczyk, and M. Baranska. „Raman spectroscopy of proteins: A review“. In: *Journal of Raman Spectroscopy* 44.8 (2013), pp. 1061–1076. DOI: 10.1002/jrs.4335.

[133] L. G. d. O. Guardalini et al. „Comparison of chemometric models using Raman spectroscopy for offline biochemical monitoring throughout the VLP-making upstream process“. In: *Biochemical Engineering Journal* 198 (2023), p. 109013. DOI: 10.1016/j.bej.2023.109013.

[134] L. G. d. O. Guardalini et al. „Biochemical monitoring throughout all stages of rabies virus-like particles production by Raman spectroscopy using global models“. In: *Journal of Biotechnology* 363 (2023), pp. 19–31. DOI: 10.1016/j.jbiotec.2022.12.009.

[135] L. G. d. O. Guardalini et al. „Monitoring by Raman spectroscopy of rabies virus-like particles production since the initial development stages“. In: *Journal of Chemical Technology & Biotechnology* 99 (2023), pp. 658–673. DOI: 10.1002/jctb.7571.

[136] C. H. Wegner, S. M. Eming, B. Walla, D. Bischoff, D. Weuster-Botz, and J. Hubbuch. „Spectroscopic insights into multi-phase protein crystallization in complex lysate using Raman spectroscopy and a particle-free bypass“. In: *Frontiers in Bioengineering and Biotechnology* 12 (2024), pp. 1–16. DOI: 10.3389/fbioe.2024.1397465.

[137] L. Rolinger, J. Hubbuch, and M. Rüdt. „Monitoring of ultra- and diafiltration processes by Kalman-filtered Raman measurements“. In: *Analytical and Bioanalytical Chemistry* 415.5 (2023), pp. 841–854. DOI: 10.1007/s00216-022-04477-7.

[138] D. Weber and J. Hubbuch. „Raman spectroscopy as a process analytical technology to investigate biopharmaceutical freeze concentration processes“. In: *Biotechnology and Bioengineering* 118.12 (2021), pp. 4708–4719. DOI: 10.1002/bit.27936.

[139] Å. Rinnan, L. Nørgaard, F. V. D. Berg, J. Thygesen, R. Bro, and S. B. Engelsen. „Data Pre-processing“. In: *Infrared Spectroscopy for Food Quality Analysis and Control*. Vol. 3. Academic Press, 2009. Chap. 2, pp. 29–50.

[140] R. Gautam, S. Vanga, F. Ariese, and S. Umapathy. „Review of multidimensional data processing approaches for Raman and infrared spectroscopy“. In: *EPJ Techniques and Instrumentation* 2.1 (2015). DOI: 10.1140/epjti/s40485-015-0018-6.

[141] T. Bocklitz, A. Walter, K. Hartmann, P. Rösch, and J. Popp. „How to pre-process Raman spectra for reliable and stable models?“ In: *Analytica Chimica Acta* 704.1-2 (2011), pp. 47–56. DOI: 10.1016/j.aca.2011.06.043.

[142] T. Mehmood, K. H. Liland, L. Snipen, and S. Sæbø. „A review of variable selection methods in Partial Least Squares Regression“. In: *Chemometrics and Intelligent Laboratory Systems* 118 (2012), pp. 62–69. DOI: 10.1016/j.chemolab.2012.07.010.

[143] W. Kessler. „Multivariate Regressionsmethoden“. In: *Multivariate Datenanalyse*. Wiley, 2006, pp. 89–152. DOI: 10.1002/9783527610037.ch3.

[144] S. Wold, M. Sjöström, and L. Eriksson. „PLS-regression: a basic tool of chemometrics“. In: *Chemometrics and Intelligent Laboratory Systems* 58.2 (2001), pp. 109–130. DOI: 10.1016/S0169-7439(01)00155-1.

[145] A. Hardianto, Z. S. Muscifa, W. Widayat, M. Yusuf, and T. Subroto. „The Effect of Ethanol on Lipid Nanoparticle Stabilization from a Molecular Dynamics Simulation Perspective“. In: *Molecules* 28.12 (2023). DOI: 10.3390/molecules28124836.

[146] S. Pfister et al. „Structural conservation of HBV-like capsid proteins over hundreds of millions of years despite the shift from non-enveloped to enveloped life-style“. In: *Nature Communications* 14.1 (2023), pp. 1–15. DOI: 10.1038/s41467-023-37068-w.

[147] A. Fire, S. Xu, M. K. Montgomery, S. A. Kostas, S. E. Driver, and C. C. Mello. „Potent and specific genetic interference by double-stranded RNA in Caenorhabditis elegans“. In: *Nature* 391.6669 (1998), pp. 806–811. DOI: 10.1038/35888.

[148] B. L. Mui et al. „Influence of Polyethylene Glycol Lipid Desorption Rates on Pharmacokinetics and Pharmacodynamics of siRNA Lipid Nanoparticles“. In: *Molecular Therapy - Nucleic Acids* 2 (2013), e139. DOI: https://doi.org/10.1038/mtna.2013.66.

[149] Y. Dong et al. „Lipopeptide nanoparticles for potent and selective siRNA delivery in rodents and nonhuman primates“. In: *Proceedings of the National Academy of Sciences of the United States of America* 111.11 (2014), pp. 3955–3960. DOI: 10.1073/pnas.1322937111.

[150] R. Ball, P. Bajaj, and K. Whitehead. „Achieving long-term stability of lipid nanoparticles: examining the effect of pH, temperature, and lyophilization“. In: *International Journal of Nanomedicine* Volume 12 (2016), pp. 305–315. DOI: 10.2147/IJN.S123062.

[151] R. L. Ball, K. A. Hajj, J. Vizelman, P. Bajaj, and K. A. Whitehead. „Lipid Nanoparticle Formulations for Enhanced Co-delivery of siRNA and mRNA“. In: *Nano Letters* 18.6 (2018), pp. 3814–3822. DOI: 10.1021/acs.nanolett.8b01101.

[152] R. Mildner et al. „Improved multidetector asymmetrical-flow field-flow fractionation method for particle sizing and concentration measurements of lipid-based nanocarriers for RNA delivery“. In: *European Journal of Pharmaceutics and Biopharmaceutics* 163 (2021), pp. 252–265. DOI: 10.1016/j.ejpb.2021.03.004.

[153] Y. Fan, M. Marioli, and K. Zhang. „Analytical characterization of liposomes and other lipid nanoparticles for drug delivery“. In: *Journal of Pharmaceutical and Biomedical Analysis* 192 (2021), p. 113642. DOI: 10.1016/j.jpba.2020.113642.

[154] T. Cajka and O. Fiehn. „Comprehensive analysis of lipids in biological systems by liquid chromatography-mass spectrometry“. In: *TrAC - Trends in Analytical Chemistry* 61 (2014), pp. 192–206. DOI: 10.1016/j.trac.2014.04.017.

[155] A. Soliven et al. „A simplified guide for charged aerosol detection of non-chromophoric compounds—Analytical method development and validation for the HPLC assay of aerosol particle size distribution for amikacin“. In: *Journal of Pharmaceutical and Biomedical Analysis* 143 (2017), pp. 68–76. DOI: 10.1016/j.jpba.2017.05.013.

[156] J. Tam, I. A. Ahmad, and A. Blasko. „A four parameter optimization and troubleshooting of a RPLC – charged aerosol detection stability indicating method for determination of S-lysophosphatidylcholines in a phospholipid formulation“. In: *Journal of Pharmaceutical and Biomedical Analysis* 155 (2018), pp. 288–297. DOI: 10.1016/j.jpba.2018.03.067.

[157] I. A. H. Ahmad et al. „Revealing the inner workings of the power function algorithm in Charged Aerosol Detection: A simple and effective approach to optimizing power function value for quantitative analysis“. In: *Journal of Chromatography A* 1603 (2019), pp. 1–7. DOI: 10.1016/j.chroma.2019.04.017.

[158] R. Pawellek, T. Muellner, P. Gamache, and U. Holzgrabe. „Power function setting in charged aerosol detection for the linearization of detector response – optimization strategies and their application“. In: *Journal of Chromatography A* 1637 (2021). DOI: 10.1016/j.chroma.2020.461844.

[159] R. Díaz-López, D. Libong, N. Tsapis, E. Fattal, and P. Chaminade. „Quantification of pegylated phospholipids decorating polymeric microcapsules of perfluorooctyl bromide by reverse phase HPLC with a charged aerosol detector“. In: *Journal of Pharmaceutical and Biomedical Analysis* 48.3 (2008), pp. 702–707. DOI: 10.1016/j.jpba.2008.06.027.

[160] M. Kurmi et al. „Development of HPLC-CAD stability indicating assay method for polyethylene glycol-conjugated phospholipid (DMPE-PEG 2000) and identification of its degradation products“. In: *Journal of Pharmaceutical and Biomedical Analysis* 198 (2021). DOI: 10.1016/j.jpba.2021.113967.

[161] F. Weber, L. Rahnfeld, and P. Luciani. „Analytical profiling and stability evaluation of liposomal drug delivery systems: A rapid UHPLC-CAD-based approach for phospholipids in research and quality control“. In: *Talanta* 220 (2020), p. 121320. DOI: 10.1016/j.talanta.2020.121320.

[162] ICH. *Q2(R2) Guideline on validation of analytical procedures*. 2022. URL: https://www.ema.europa.eu/en/documents/scientific-guideline/ich-q2r2-guideline-validation-analytical-procedures-step-5-revision-1%7B%5C_%7Den.pdf (visited on 07/08/2024).

[163] V. Murugaiah, W. Zedalis, G. Lavine, K. Charisse, and M. Manoharan. „Reversed-phase high-performance liquid chromatography method for simultaneous analysis of two liposome-formulated short interfering RNA duplexes“. In: *Analytical Biochemistry* 401.1 (2010), pp. 61–67. DOI: 10.1016/j.ab.2010.02.012.

[164] S. Studzińska, L. Pietrzak, and B. Buszewski. „The Effects of Stationary Phases on Retention and Selectivity of Oligonucleotides in IP-RP-HPLC“. In: *Chromatographia* 77.23-24 (2014), pp. 1589–1596. DOI: 10.1007/s10337-014-2766-x.

[165] L. R. Snyder, M. A. Quarry, and J. L. Glajch. „Solvent-strength selectivity in reversed-phase HPLC“. In: *Chromatographia* 24.1 (1987), pp. 33–44. DOI: 10.1007/BF02688465.

[166] A. D. Stroock, S. K. W. Dertinger, A. Ajdari, I. Mezić, H. A. Stone, and G. M. Whitesides. „Chaotic Mixer for Microchannels“. In: *Science* 295.5555 (2002), pp. 647–651. DOI: 10.1126/science.1066238.

[167] EMA. *Onpattro: Summary of Product Characteristics*. 2018. URL: https://www.ema.europa.eu/en/documents/product-information/onpattro-epar-product-information%7B%5C_%7Den.pdf (visited on 07/08/2024).

[168] Y. Suzuki, K. Hyodo, Y. Tanaka, and H. Ishihara. „SiRNA-lipid nanoparticles with long-term storage stability facilitate potent gene-silencing in vivo“. In: *Journal of Controlled Release* 220 (2015), pp. 44–50. DOI: 10.1016/j.jconrel.2015.10.024.

[169] Z. J. Jakubek, S. Chen, J. Zaifman, Y. Y. C. Tam, and S. Zou. „Lipid Nanoparticle and Liposome Reference Materials: Assessment of Size Homogeneity and Long-Term -70 °C and 4 °C Storage Stability“. In: *Langmuir* 39.7 (2022). DOI: 10.1021/acs.langmuir.2c02657.

[170] N. M. Belliveau et al. „Microfluidic synthesis of highly potent limit-size lipid nanoparticles for in vivo delivery of siRNA“. In: *Molecular Therapy - Nucleic Acids* 1.8 (2012), e37. DOI: 10.1038/mtna.2012.28.

[171] I. Urits et al. „A Review of Patisiran (ONPATTRO®) for the Treatment of Polyneuropathy in People with Hereditary Transthyretin Amyloidosis“. In: *Neurology and Therapy* 9.2 (2020), pp. 301–315. DOI: 10.1007/s40120-020-00208-1.

[172] L. B. Jeffs, L. R. Palmer, E. G. Ambegia, C. Giesbrecht, S. Ewanick, and I. MacLachlan. „A scalable, extrusion-free method for efficient liposomal encapsulation of plasmid DNA“. In: *Pharmaceutical Research* 22.3 (2005), pp. 362–372. DOI: 10.1007/s11095-004-1873-z.

[173] R. Mihaila et al. „Lipid nanoparticle purification by Spin Centrifugation-Dialysis (SCD): A facile and high-throughput approach for small scale preparation of siRNA-lipid complexes“. In: *International Journal of Pharmaceutics* 420.1 (2011), pp. 118–121. DOI: 10.1016/j.ijpharm.2011.08.017.

[174] N. Kimura et al. „Development of a Microfluidic-Based Post-Treatment Process for Size-Controlled Lipid Nanoparticles and Application to siRNA Delivery“. In: *ACS Applied Materials and Interfaces* 12.30 (2020), pp. 34011–34020. DOI: 10.1021/acsami.0c05489.

[175] S. Hirsjärvi, G. Bastiat, P. Saulnier, and J. P. Benoît. „Evaluation of surface deformability of lipid nanocapsules by drop tensiometer technique, and its experimental assessment by dialysis and tangential flow filtration“. In: *International Journal of Pharmaceutics* 434.1-2 (2012), pp. 460–467. DOI: 10.1016/j.ijpharm.2012.06.019.

[176] Y. Sakurai, T. Hada, and H. Harashima. „Scalable preparation of poly(ethylene glycol)-grafted siRNA-loaded lipid nanoparticles using a commercially available fluidic device and tangential flow filtration“. In: *Journal of Biomaterials Science, Polymer Edition* 28.10-12 (2017), pp. 1086–1096. DOI: 10.1080/09205063.2017.1291297.

[177] M. Sheybanifard et al. „Liposome manufacturing under continuous flow conditions: towards a fully integrated set-up with in-line control of critical quality attributes“. In: *Lab on a Chip* 23.1 (2022), pp. 182–194. DOI: 10.1039/d2lc00463a.

[178] N. Dimov, E. Kastner, M. Hussain, Y. Perrie, and N. Szita. „Formation and purification of tailored liposomes for drug delivery using a module-based micro continuous-flow system“. In: *Scientific Reports* 7.1 (2017). DOI: 10.1038/s41598-017-11533-1.

[179] R. D. Worsham, V. Thomas, and S. S. Farid. „Impact of ethanol on continuous inline diafiltration of liposomal drug products“. In: *Biotechnology Journal* 18.11 (2023), pp. 1–9. DOI: 10.1002/biot.202300194.

[180] N. Forbes et al. „Rapid and scale-independent microfluidic manufacture of liposomes entrapping protein incorporating in-line purification and at-line size monitoring“. In: *International Journal of Pharmaceutics* 556 (2019), pp. 68–81. DOI: 10.1016/j.ijpharm.2018.11.060.

[181] N. Beckert, A. Dietrich, and J. Hubbuch. „RP-CAD for Lipid Quantification: Systematic Method Development and Intensified LNP Process Characterization“. In: *Pharmaceuticals* 17.9 (2024). DOI: 10.3390/ph17091217.

[182] T. McIntosh, R. McDaniel, and S. Simon. „Induction of an interdigitated gel phase in fully hydrated phosphatidylcholine bilayers“. In: *Biochimica et Biophysica Acta (BBA) - Biomembranes* 731.1 (1983), pp. 109–114. DOI: 10.1016/0005-2736(83)90403-0.

[183] F. W. Stetter and T. Hugel. „The nanomechanical properties of lipid membranes are significantly influenced by the presence of ethanol“. In: *Biophysical Journal* 104.5 (2013), pp. 1049–1055. DOI: 10.1016/j.bpj.2013.01.021.

[184] J. Paxman, B. Hunt, D. Hallan, S. R. Zarbock, and D. J. Woodbury. „Drunken Membranes: Short-Chain Alcohols Alter Fusion of Liposomes to Planar Lipid Bilayers“. In: *Biophysical Journal* 112.1 (2017), pp. 121–132. DOI: 10.1016/j.bpj.2016.11.3205.

[185] K. J. Hassett et al. „Impact of lipid nanoparticle size on mRNA vaccine immunogenicity“. In: *Journal of Controlled Release* 335 (2021), pp. 237–246. DOI: 10.1016/j.jconrel.2021.05.021.

[186] A. Pittiu et al. „Production of liposomes by microfluidics: The impact of post-manufacturing dilution on drug encapsulation and lipid loss“. In: *International Journal of Pharmaceutics* 664 (2024), p. 124641. DOI: 10.1016/j.ijpharm.2024.124641.

[187] Y. Perrie et al. „The impact of solvent selection: Strategies to guide the manufacturing of liposomes using microfluidics“. In: *Pharmaceutics* 11.12 (2019). DOI: 10.3390/pharmaceutics11120653.

[188] C. Webb et al. „Using microfluidics for scalable manufacturing of nanomedicines from bench to GMP: A case study using protein-loaded liposomes“. In: *International Journal of Pharmaceutics* 582 (2020), p. 119266. DOI: 10.1016/j.ijpharm.2020.119266.

[189] C. B. Roces et al. „Rapid scale-up and production of active-loaded PEGylated liposomes“. In: *International Journal of Pharmaceutics* 586 (2020), p. 119566. DOI: 10.1016/j.ijpharm.2020.119566.

[190] R. Besseling, M. Damen, J. Wijgergangs, M. Hermes, G. Wynia, and A. Gerich. „New unique PAT method and instrument for real-time inline size characterization of concentrated, flowing nanosuspensions“. In: *European Journal of Pharmaceutical Sciences* 133 (2019), pp. 205–213. DOI: 10.1016/j.ejps.2019.03.024.

[191] K. O. Messerian, A. Zverev, J. F. Kramarczyk, and A. L. Zydney. „Pressure-dependent fouling behavior during sterile filtration of mRNA-containing lipid nanoparticles“. In: *Biotechnology and Bioengineering* 119.11 (2022), pp. 3221–3229. DOI: 10.1002/bit.28200.

[192] K. O. Messerian, A. Zverev, J. F. Kramarczyk, and A. L. Zydney. „Characterization and associated pressure-dependent behavior of deposits formed during sterile filtration of mRNA-Lipid nanoparticles“. In: *Journal of Membrane Science* 684 (2023), p. 121896. DOI: 10.1016/j.memsci.2023.121896.

[193] J. Wang et al. „Probing the interaction mechanisms of lipid nanoparticle-encapsulated mRNA with surfaces of diverse functional groups: Implication for mRNA transport“. In: *Chemical Engineering Science* 301 (2025), p. 120693. DOI: 10.1016/j.ces.2024.120693.

[194] S. A. Kim et al. „Protein-based nanocages for vaccine development“. In: *Journal of Controlled Release* 353 (2023), pp. 767–791. DOI: 10.1016/j.jconrel.2022.12.022.

[195] C. Qian et al. „Recent Progress on the Versatility of Virus-Like Particles“. In: *Vaccines* 8.1 (2020), p. 139. DOI: 10.3390/vaccines8010139.

[196] B. Cheang and A. L. Zydney. „A two-stage ultrafiltration process for fractionation of whey protein isolate“. In: *Journal of Membrane Science* 231.1-2 (2004), pp. 159–167. DOI: 10.1016/j.memsci.2003.11.014.

[197] M. Nor, L. Ramchandran, M. Duke, and T. Vasiljevic. „Separation of bromelain from crude pineapple waste mixture by a two-stage ceramic ultrafiltration process“. In: *Food and Bioproducts Processing* 98 (2016), pp. 142–150. DOI: 10.1016/j.fbp.2016.01.001.

[198] M. Z. Nor, L. Ramchandran, M. Duke, and T. Vasiljevic. „Integrated ultrafiltration process for the recovery of bromelain from pineapple waste mixture“. In: *Journal of Food Process Engineering* 40.3 (2017), pp. 1–9. DOI: 10.1111/jfpe.12492.

[199] M. Z. M. Nor, L. Ramchandran, M. Duke, and T. Vasiljevic. „Performance of a Two-Stage Membrane System for Bromelain Separation from Pineapple Waste Mixture as Impacted by Enzymatic Pre-Treatment and Diafiltration“. In: *Food Technology and Biotechnology* 56.2 (2018), pp. 218–227. DOI: 10.17113/ftb.56.02.18.5478.

[200] C. T. Cuddington et al. „Pilot scale production and characterization of next generation high molecular weight and tense quaternary state polymerized human hemoglobin“. In: *Biotechnology and Bioengineering* 119.12 (2022), pp. 3447–3461. DOI: 10.1002/bit.28233.

[201] A. Dietrich, R. Schiemer, J. Kurmann, S. Zhang, and J. Hubbuch. „Raman-based PAT for VLP precipitation: systematic data diversification and preprocessing pipeline identification“. In: *Frontiers in Bioengineering and Biotechnology* 12 (2024), pp. 1–20. DOI: 10.3389/fbioe.2024.1399938.

[202] F. Zhang et al. „Baseline correction for infrared spectra using adaptive smoothness parameter penalized least squares method“. In: *Spectroscopy Letters* 53.3 (2020), pp. 222–233. DOI: 10.1080/00387010.2020.1730908.

[203] A. Savitzky and M. J. E. Golay. „Smoothing and Differentiation of Data by Simplified Least Squares Procedures.“ In: *Analytical Chemistry* 36.8 (1964), pp. 1627–1639. DOI: 10.1021/ac60214a047.

[204] E. Gasteiger et al. „Protein Identification and Analysis Tools on the ExPASy Server“. In: *The Proteomics Protocols Handbook* (2005), pp. 571–607. DOI: 10.1385/1-59259-890-0:571.

[205] K. Baumgartner et al. „Determination of protein phase diagrams by microbatch experiments: Exploring the influence of precipitants and pH“. In: *International Journal of Pharmaceutics* 479.1 (2015), pp. 28–40. DOI: 10.1016/j.ijpharm.2014.12.027.

[206] H. Huettmann, S. Zich, M. Berkemeyer, W. Buchinger, and A. Jungbauer. „Design of industrial crystallization of interferon gamma: Phase diagrams and solubility curves“. In: *Chemical Engineering Science* 126 (2015), pp. 341–348. DOI: 10.1016/j.ces.2014.12.018.

[207] M. Barros Groß and M. Kind. „From microscale phase screening to bulk evaporative crystallization of proteins“. In: *Journal of Crystal Growth* 498 (2018), pp. 160–169. DOI: 10.1016/j.jcrysgro.2018.06.010.

[208] Q. Gu, Z. Li, J. L. Coffman, T. M. Przybycien, and A. L. Zydney. „High throughput solubility and redissolution screening for antibody purification via combined PEG and zinc chloride precipitation“. In: *Biotechnology Progress* 36.6 (2020), pp. 1–14. DOI: 10.1002/btpr.3041.

[209] C. H. Wegner, I. Zimmermann, and J. Hubbuch. „Rapid Analysis for Multicomponent High-Throughput Crystallization Screening: Combination of UV-Vis Spectroscopy and Chemometrics“. In: *Crystal Growth and Design* 22.2 (2022), pp. 1054–1065. DOI: 10.1021/acs.cgd.1c00907.

[210] M. Mittal, M. Banerjee, L. H. Lua, and A. S. Rathore. „Current status and future challenges in transitioning to continuous bioprocessing of virus-like particles“. In: *Journal of Chemical Technology and Biotechnology* 97.9 (2022), pp. 2376–2385. DOI: 10.1002/jctb.6821.

[211] L. Gerstweiler, J. Bi, and A. P. Middelberg. „Continuous downstream bioprocessing for intensified manufacture of biopharmaceuticals and antibodies“. In: *Chemical Engineering Science* 231 (2021), p. 116272. DOI: 10.1016/j.ces.2020.116272.

[212] L. Gerstweiler, J. Billakanti, J. Bi, and A. P. J. Middelberg. „An integrated and continuous downstream process for microbial virus-like particle vaccine biomanufacture“. In: *Biotechnology and Bioengineering* 119.8 (2022), pp. 2122–2133. DOI: 10.1002/bit.28118.

[213] P. Iverius and T. Laurent. „Precipitation of some plasma proteins by the addition of dextran or polyethylene glycol“. In: *Biochimica et Biophysica Acta (BBA) - Protein Structure* 133.2 (1967), pp. 371–373. DOI: 10.1016/0005-2795(67)90079-7.

[214] A. Poison. „A Theory for the Displacement of Proteins and Viruses with Polyethylene Glycol“. In: *Preparative Biochemistry* 7.2 (1977), pp. 129–154. DOI: 10.1080/00327487708061631.

[215] F. Hämmerling, C. Ladd Effio, S. Andris, J. Kittelmann, and J. Hubbuch. „Investigation and prediction of protein precipitation by polyethylene glycol using quantitative structure–activity relationship models“. In: *Journal of Biotechnology* 241 (2017), pp. 87–97. DOI: 10.1016/j.jbiotec.2016.11.014.

[216] S. Mobini, M. Chizari, L. Mafakher, E. Rismani, and E. Rismani. „Computational Design of a Novel VLP-Based Vaccine for Hepatitis B Virus“. In: *Frontiers in Immunology* 11 (2020). DOI: 10.3389/fimmu.2020.02074.

[217] B. Li, P. W. Ryan, B. H. Ray, K. J. Leister, N. M. Sirimuthu, and A. G. Ryder. „Rapid characterization and quality control of complex cell culture media solutions using Raman spectroscopy and chemometrics“. In: *Biotechnology and Bioengineering* 107.2 (2010), pp. 290–301. DOI: 10.1002/bit.22813.

[218] N. R. Abu-Absi et al. „Real time monitoring of multiple parameters in mammalian cell culture bioreactors using an in-line Raman spectroscopy probe“. In: *Biotechnology and Bioengineering* 108.5 (2011), pp. 1215–1221. DOI: 10.1002/bit.23023.

[219] B. Berry, J. Moretto, T. Matthews, J. Smelko, and K. Wiltberger. „Cross-scale predictive modeling of CHO cell culture growth and metabolites using Raman spectroscopy and multivariate analysis“. In: *Biotechnology Progress* 31.2 (2015), pp. 566–577. DOI: 10.1002/btpr.2035.

[220] A. Golabgir and C. Herwig. „Combining Mechanistic Modeling and Raman Spectroscopy for Real-Time Monitoring of Fed-Batch Penicillin Production“. In: *Chemie-Ingenieur-Technik* 88.6 (2016), pp. 764–776. DOI: 10.1002/cite.201500101.

[221] Feidl et al. „Combining Mechanistic Modeling and Raman Spectroscopy for Monitoring Antibody Chromatographic Purification“. In: *Processes* 7.10 (2019), p. 683. DOI: 10.3390/pr7100683.

[222] L. Rolinger, M. Rüdt, and J. Hubbuch. „Comparison of UV- and Raman-based monitoring of the Protein A load phase and evaluation of data fusion by PLS models and CNNs“. In: *Biotechnology and Bioengineering* 118.11 (2021), pp. 4255–4268. DOI: 10.1002/bit.27894.

[223] J. Wang, J. Chen, J. Studts, and G. Wang. „In-line product quality monitoring during biopharmaceutical manufacturing using computational Raman spectroscopy“. In: *mAbs* 15.1 (2023). DOI: 10.1080/19420862.2023.2220149.

[224] U. Roessl, S. Leitgeb, S. Pieters, T. De Beer, and B. Nidetzky. „In situ protein secondary structure determination in ice: Raman spectroscopy-based process analytical tool for frozen storage of biopharmaceuticals“. In: *Journal of Pharmaceutical Sciences* 103.8 (2014), pp. 2287–2295. DOI: 10.1002/jps.24072.

[225] B. Wei et al. „Multi-attribute Raman spectroscopy (MARS) for monitoring product quality attributes in formulated monoclonal antibody therapeutics“. In: *mAbs* 14.1 (2022). DOI: 10.1080/19420862.2021.2007564.

[226] Z. Sun et al. „Assessment of the human albumin in acid precipitation process using NIRS and multi-variable selection methods combined with SPA“. In: *Journal of Molecular Structure* 1199 (2020), p. 126942. DOI: 10.1016/j.molstruc.2019.126942.

[227] L. Li et al. „The relevance study of effective information between near infrared spectroscopy and chondroitin sulfate in ethanol precipitation process“. In: *Journal of Innovative Optical Health Sciences* 7.6 (2014), pp. 1–7. DOI: 10.1142/S1793545814500229.

[228] Z. Sun et al. „Calibration transfer of near infrared spectrometers for the assessment of plasma ethanol precipitation process“. In: *Chemometrics and Intelligent Laboratory Systems* 181 (2018), pp. 64–71. DOI: 10.1016/j.chemolab.2018.08.012.

[229] H. Huang and H. Qu. „In-situ monitoring of saccharides removal of alcohol precipitation using near-infrared spectroscopy“. In: *Journal of Innovative Optical Health Sciences* 11.5 (2018), pp. 1–12. DOI: 10.1142/S179354581850027X.

[230] J. Meyer-Kirschner et al. „In-line Monitoring of Monomer and Polymer Content during Microgel Synthesis Using Precipitation Polymerization via Raman Spectroscopy and Indirect Hard Modeling“. In: *Applied Spectroscopy* 70.3 (2016), pp. 416–426. DOI: 10.1177/0003702815626663.

[231] M. D. Van Brink, M. Pepers, and A. M. Van Herk. „Raman spectroscopy of polymer latexes“. In: *Journal of Raman Spectroscopy* 33.4 (2002), pp. 264–272. DOI: 10.1002/jrs.834.

[232] J. V. Sinfield and C. K. Monwuba. „Assessment and correction of turbidity effects on Raman observations of chemicals in aqueous solutions“. In: *Applied Spectroscopy* 68.12 (2014), pp. 1381–1392. DOI: 10.1366/13-07292.

[233] M. Zelger, S. Pan, A. Jungbauer, and R. Hahn. „Real-time monitoring of protein precipitation in a tubular reactor for continuous bioprocessing“. In: *Process Biochemistry* 51.10 (2016), pp. 1610–1621. DOI: 10.1016/j.procbio.2016.06.018.

[234] R. M. Santos, J. M. Kessler, P. Salou, J. C. Menezes, and A. Peinado. „Monitoring mAb cultivations with in-situ raman spectroscopy: The influence of spectral selectivity on calibration models and industrial use as reliable PAT tool“. In: *Biotechnology Progress* 34.3 (2018), pp. 659–670. DOI: 10.1002/btpr.2635.

[235] S. Goldrick et al. „High-Throughput Raman Spectroscopy Combined with Innovate Data Analysis Workflow to Enhance Biopharmaceutical Process Development“. In: *Processes* 8.9 (2020), p. 1179. DOI: 10.3390/pr8091179.

[236] M. Hassoun et al. „A droplet-based microfluidic chip as a platform for leukemia cell lysate identification using surface-enhanced Raman scattering“. In: *Analytical and Bioanalytical Chemistry* 410.3 (2018), pp. 999–1006. DOI: 10.1007/s00216-017-0609-y.

[237] E. Genova et al. „SERS of cells: What can we learn from cell lysates?“ In: *Analytica Chimica Acta* 1005 (2018), pp. 93–100. DOI: 10.1016/j.aca.2017.12.002.

[238] S. He et al. „Baseline correction for Raman spectra using an improved asymmetric least squares method“. In: *Anal. Methods* 6.12 (2014), pp. 4402–4407. DOI: 10.1039/C4AY00068D.

[239] S. Wold, H. Antti, F. Lindgren, and J. Öhman. „Orthogonal signal correction of near-infrared spectra“. In: *Chemometrics and Intelligent Laboratory Systems* 44.1-2 (1998), pp. 175–185. DOI: 10.1016/S0169-7439(98)00109-9.

[240] J. Trygg and S. Wold. „Orthogonal projections to latent structures (O-PLS)“. In: *Journal of Chemometrics* 16.3 (2002), pp. 119–128. DOI: 10.1002/cem.695.

[241] H. F. M. Boelens, R. J. Dijkstra, P. H. C. Eilers, F. Fitzpatrick, and J. A. Westerhuis. „New background correction method for liquid chromatography with diode array detection, infrared spectroscopic detection and Raman spectroscopic detection“. In: *Journal of Chromatography A* 1057.1-2 (2004), pp. 21–30. DOI: 10.1016/j.chroma.2004.09.035.

[242] H. Martens, J. P. Nielsen, and S. B. Engelsen. „Light scattering and light absorbance separated by extended multiplicative signal correction. Application to near-infrared transmission analysis of powder mixtures“. In: *Analytical Chemistry* 75.3 (2003), pp. 394–404. DOI: 10.1021/ac020194w.

[243] A. Kohler et al. „Estimating and Correcting Mie Scattering in Synchrotron-Based Microscopic Fourier Transform Infrared Spectra by Extended Multiplicative Signal Correction“. In: *Applied Spectroscopy* 62.3 (2008), pp. 259–266. DOI: 10.1366/000370208783759669.

[244] K. H. Liland, A. Kohler, and N. K. Afseth. „Model-based pre-processing in Raman spectroscopy of biological samples“. In: *Journal of Raman Spectroscopy* 47.6 (2016), pp. 643–650. DOI: 10.1002/jrs.4886.

[245] C. P. Passos, S. M. Cardoso, A. S. Barros, C. M. Silva, and M. A. Coimbra. „Application of Fourier transform infrared spectroscopy and orthogonal projections to latent structures/partial least squares regression for estimation of procyanidins average degree of polymerisation“. In: *Analytica Chimica Acta* 661.2 (2010), pp. 143–149. DOI: 10.1016/j.aca.2009.12.028.

[246] F. F. Abdallah, H. W. Darwish, I. A. Darwish, and I. A. Naguib. „Orthogonal projection to latent structures and first derivative for manipulation of PLSR and SVR chemometric models' prediction: A case study“. In: *PLoS ONE* 14.9 (2019), pp. 1–13. DOI: 10.1371/journal.pone.0222197.

[247] FDA. *Development and Submission of Near Infrared Analytical Procedures Guidance for Industry*. 2015.

[248] J. Z. Porterfield and A. Zlotnick. „A simple and general method for determining the protein and nucleic acid content of viruses by UV absorbance“. In: *Virology* 407.2 (2010), pp. 281–288. DOI: 10.1016/j.virol.2010.08.015.

[249] R. R. Wilcox. *Introduction to Robust Estimation and Hypothesis Testing*. Netherlands: Elsevier Science, 2005, p. 100.

[250] J. Soch and C. Allefeld. „MACS – a new SPM toolbox for model assessment, comparison and selection“. In: *Journal of Neuroscience Methods* 306 (2018), pp. 19–31. DOI: 10.1016/j.jneumeth.2018.05.017.

[251] E. Spinner. „Raman-spectral depolarisation ratios of ions in concentrated aqueous solution. The next-to-negligible effect of highly asymmetric ion surroundings on the symmetry properties of polarisability changes during vibrations of symmetric ions.“ In: *Spectrochimica Acta Part A: Molecular and Biomolecular Spectroscopy* 59.7 (2003), pp. 1441–1456. DOI: 10.1016/S1386-1425(02)00293-7.

[252] M. D. Fontana, K. Ben Mabrouk, and T. H. Kauffmann. „Raman spectroscopic sensors for inorganic salts“. In: *Spectroscopic Properties of Inorganic and Organometallic Compounds*. Ed. by J. Yarwood, R. Douthwaite, and S. Duckett. Vol. 44. RSC Publishing, 2013, pp. 40–67. DOI: 10.1039/9781849737791-00040.

[253] G. Socrates. *Infrared and Raman Characteristic Group Frequencies: Tables and Charts*. Wiley, 2004.

[254] G. H. Watson, W. B. Daniels, and C. S. Wang. „Measurements of Raman intensities and pressure dependence of phonon frequencies in sapphire“. In: *Journal of Applied Physics* 52.2 (1981), pp. 956–958. DOI: 10.1063/1.328785.

[255] A. Weber, S. P. S. Porto, L. E. Cheesman, and J. J. Barrett. „High-Resolution Raman Spectroscopy of Gases with cw-Laser Excitation*“. In: *JOSA* 57.1 (1967), pp. 19–28. DOI: 10.1364/JOSA.57.000019.

[256] W. L. Peticolas. „Raman spectroscopy of DNA and proteins“. In: *Methods in Enzymology*. Vol. 246. Elsevier Inc., 1995, pp. 389–416. DOI: 10.1016/0076-6879(95)46019-5.

[257] R. Schiemer, M. Rüdt, and J. Hubbuch. „Generative data augmentation and automated optimization of convolutional neural networks for process monitoring“. In: *Frontiers in Bioengineering and Biotechnology* 12 (2024), pp. 1–21. DOI: 10.3389/fbioe.2024.1228846.

[258] A. Moreno, J. Mas-Oliva, M. Soriano-García, C. Oliver Salvador, and V. Martín Bolaños-García. „Turbidity as a useful optical parameter to predict protein crystallization by dynamic light scattering“. In: *Journal of Molecular Structure* 519.1-3 (2000), pp. 243–256. DOI: 10.1016/S0022-2860(99)00318-X.

[259] H. Grön et al. „Dynamic in-process examination of particle size and crystallographic form under defined conditions of reactant supersaturation as associated with the batch crystallization of monosodium glutamate from aqueous solution“. In: *Industrial and Engineering Chemistry Research* 42.20 (2003), pp. 4888–4898. DOI: 10.1021/ie021037q.

[260] R. S. Harner, R. J. Ressler, R. L. Briggs, J. E. Hitt, P. A. Larsen, and T. C. Frank. „Use of a fiber-optic turbidity probe to monitor and control commercial-scale unseeded batch crystallizations“. In: *Organic Process Research and Development* 13.1 (2009), pp. 114–124. DOI: 10.1021/op8001504.

[261] F. Capito, R. Skudas, H. Kolmar, and C. Hunzinger. „At-line mid infrared spectroscopy for monitoring downstream processing unit operations“. In: *Process Biochemistry* 50.6 (2015), pp. 997–1005. DOI: 10.1016/j.procbio.2015.03.005.

[262] J. Chen, J. Wang, R. Hess, G. Wang, J. Studts, and M. Franzreb. „Application of Raman spectroscopy during pharmaceutical process development for determination of critical quality attributes in Protein A chromatography“. In: *Journal of Chromatography A* 1718 (2024), p. 464721. DOI: 10.1016/j.chroma.2024.464721.

[263] H. Falkenberg et al. „Mass spectrometric evaluation of upstream and downstream process influences on host cell protein patterns in biopharmaceutical products“. In: *Biotechnology Progress* 35.3 (2019). DOI: 10.1002/btpr.2788.

[264] F. Alsmeyer, H. J. Koß, and W. Marquardt. „Indirect spectral hard modeling for the analysis of reactive and interacting mixtures“. In: *Applied Spectroscopy* 58.8 (2004), pp. 975–985. DOI: 10.1366/0003702041655368.

[265] E. Kriesten, F. Alsmeyer, A. Bardow, and W. Marquardt. „Fully automated indirect hard modeling of mixture spectra“. In: *Chemometrics and Intelligent Laboratory Systems* 91.2 (2008), pp. 181–193. DOI: 10.1016/j.chemolab.2007.11.004.

[266] H. Martens and E. Stark. „Extended multiplicative signal correction and spectral interference subtraction: New preprocessing methods for near infrared spectroscopy“. In: *Journal of Pharmaceutical and Biomedical Analysis* 9.8 (1991), pp. 625–635. DOI: 10.1016/0731-7085(91)80188-F.

[267] S. Andris, M. Rüdt, J. Rogalla, M. Wendeler, and J. Hubbuch. „Monitoring of antibody-drug conjugation reactions with UV/Vis spectroscopy“. In: *Journal of Biotechnology* 288 (2018), pp. 15–22. DOI: 10.1016/j.jbiotec.2018.10.003.

[268] C. Zhou, W. Qi, E. N. Lewis, and J. F. Carpenter. „Concomitant Raman spectroscopy and dynamic light scattering for characterization of therapeutic proteins at high concentrations“. In: *Analytical Biochemistry* 472 (2015), pp. 7–20. DOI: 10.1016/j.ab.2014.11.016.

[269] V. V. Kuzmin, V. S. Novikov, L. Y. Ustynyuk, K. A. Prokhorov, E. A. Sagitova, and G. Y. Nikolaeva. „Raman spectra of polyethylene glycols: Comparative experimental and DFT study“. In: *Journal of Molecular Structure* 1217 (2020), p. 128331. DOI: 10.1016/j.molstruc.2020.128331.

[270] J. Gerretzen et al. „Simple and Effective Way for Data Preprocessing Selection Based on Design of Experiments“. In: *Analytical Chemistry* 87.24 (2015), pp. 12096–12103. DOI: 10.1021/acs.analchem.5b02832.

[271] B. Brunel, F. Alsamad, and O. Piot. „Toward automated machine learning in vibrational spectroscopy - use and settings of genetic algorithms for pre-processing and regression optimization“. In: *Chemometrics and Intelligent Laboratory Systems* 219.104444 (2021), pp. 1–10. DOI: https://doi.org/10.1016/j.chemolab.2021.104444.

[272] C. Cui and T. Fearn. „Modern practical convolutional neural networks for multivariate regression: Applications to NIR calibration“. In: *Chemometrics and Intelligent Laboratory Systems* 182 (2018), pp. 9–20. DOI: 10.1016/j.chemolab.2018.07.008.

[273] U. Thissen, M. Pepers, B. Üstün, W. J. Melssen, and L. M. C. Buydens. „Comparing support vector machines to PLS for spectral regression applications“. In: *Chemometrics and Intelligent Laboratory Systems* 73.2 (2004), pp. 169–179. DOI: 10.1016/j.chemolab.2004.01.002.

[274] I. Barman, C.-R. Kong, N. C. Dingari, R. R. Dasari, and M. S. Feld. „Development of Robust Calibration Models Using Support Vector Machines for Spectroscopic Monitoring of Blood Glucose“. In: *Analytical Chemistry* 82.23 (2010), pp. 9719–9726. DOI: 10.1021/ac101754n.

[275] D. A. Zavala-Ortiz et al. „Support Vector and Locally Weighted regressions to monitor monoclonal antibody glycosylation during CHO cell culture processes, an enhanced alternative to Partial Least Squares regression“. In: *Biochemical Engineering Journal* 154 (2020), p. 107457. DOI: 10.1016/j.bej.2019.107457.

[276] R. Schiemer, J. T. Weggen, K. M. Schmitt, and J. Hubbuch. „An adaptive soft-sensor for advanced real-time monitoring of an antibody-drug conjugation reaction“. In: *Biotechnology and Bioengineering* 120.7 (2023), pp. 1914–1928. DOI: 10.1002/bit.28428.

[277] A. Dietrich, L. Heim, and J. Hubbuch. „Dual-Stage Cross-Flow Filtration: Integrated Capture and Purification of Virus-Like Particles“. In: *Biotechnology and Bioengineering* 122.4 (2025), pp. 884–894. DOI: 10.1002/bit.28914.

[278] D. P. Wasalathanthri et al. „Real-time monitoring of quality attributes by in-line Fourier transform infrared spectroscopic sensors at ultrafiltration and diafiltration of bioprocess“. In: *Biotechnology and Bioengineering* 117.12 (2020), pp. 3766–3774. DOI: 10.1002/bit.27532.

[279] G. Thakur, S. Thori, and A. S. Rathore. „Implementing PAT for single-pass tangential flow ultrafiltration for continuous manufacturing of monoclonal antibodies“. In: *Journal of Membrane Science* 613 (2020), p. 118492. DOI: 10.1016/j.memsci.2020.118492.

[280] G. Thakur, V. Hebbi, and A. S. Rathore. „Near Infrared Spectroscopy as a PAT tool for monitoring and control of protein and excipient concentration in ultrafiltration of highly concentrated antibody formulations“. In: *International Journal of Pharmaceutics* 600 (2021), p. 120456. DOI: 10.1016/j.ijpharm.2021.120456.

[281] N. Brestich, M. Rüdt, D. Büchler, and J. Hubbuch. „Selective protein quantification for preparative chromatography using variable pathlength UV/Vis spectroscopy and partial least squares regression“. In: *Chemical Engineering Science* 176 (2018), pp. 157–164. DOI: 10.1016/j.ces.2017.10.030.

[282] C. M. Andersen and R. Bro. „Variable selection in regression—a tutorial“. In: *Journal of Chemometrics* 24.11-12 (2010), pp. 728–737. DOI: 10.1002/cem.1360.

[283] N. N. Zhang et al. „A Thermostable mRNA Vaccine against COVID-19“. In: *Cell* 182.5 (2020), 1271–1283.e16. DOI: 10.1016/j.cell.2020.07.024.

[284] F. J. Krug, J. Růžička, and E. H. Hansen. „Determination of ammonia in low concentrations with Nessler's reagent by flow injection analysis“. In: *The Analyst* 104.1234 (1979), pp. 47–54. DOI: 10.1039/an9790400047.

[285] C. J. Patton and S. R. Crouch. „Spectrophotometric and Kinetics Investigation of the Berthelot Reaction for the Determination of Ammonia“. In: *Analytical Chemistry* 49.3 (1977), pp. 464–469. DOI: 10.1021/ac50011a034.

[286] R. Saini and S. Kumar. „A fluorescent probe for the selective detection of sulfate ions in water“. In: *RSC Advances* 3.44 (2013), p. 21856. DOI: 10.1039/c3ra44220a.

[287] T. V. Plisko, A. V. Bildyukevich, V. V. Usosky, and V. V. Volkov. „Influence of the concentration and molecular weight of polyethylene glycol on the structure and permeability of polysulfone hollow fiber membranes“. In: *Petroleum Chemistry* 56.4 (2016), pp. 321–329. DOI: 10.1134/S096554411604006X.

[288] Z. Li and A. L. Zydney. „Effect of zinc chloride and PEG concentrations on the critical flux during tangential flow microfiltration of BSA precipitates“. In: *Biotechnology Progress* 33.6 (2017), pp. 1561–1567. DOI: 10.1002/btpr.2545.

[289] R. Prasad, S. H. Crouse, R. W. Rousseau, and M. A. Grover. „Quantifying Dense Multicomponent Slurries with In-Line ATR-FTIR and Raman Spectroscopies: A Hanford Case Study“. In: *Industrial and Engineering Chemistry Research* 62.39 (2023), pp. 15962–15973. DOI: 10.1021/acs.iecr.3c01249.

[290] Tornado. *Achieving Superior Raman Measurements: Understanding And Avoiding Detector Saturation.* 2021. URL: https://tornado-spectral.com/blog/achieving-superior-raman-measurements-understanding-and-avoiding-detector-saturation/ (visited on 05/19/2025).

[291] B. Bayer, M. von Stosch, M. Melcher, M. Duerkop, and G. Striedner. „Soft sensor based on 2D-fluorescence and process data enabling real-time estimation of biomass in Escherichia coli cultivations". In: *Engineering in Life Sciences* 20.1-2 (2020), pp. 26–35. DOI: 10.1002/elsc.201900076.

[292] J. Kuligowski, G. Quintás, C. Herwig, and B. Lendl. „A rapid method for the differentiation of yeast cells grown under carbon and nitrogen-limited conditions by means of partial least squares discriminant analysis employing infrared micro-spectroscopic data of entire yeast cells". In: *Talanta* 99 (2012), pp. 566–573. DOI: 10.1016/j.talanta.2012.06.036.

[293] D. H. Müller, C. Flake, T. Brands, and H.-J. Koß. „Bioprocess in-line monitoring using Raman spectroscopy and Indirect Hard Modeling (IHM): A simple calibration yields a robust model". In: *Biotechnology and Bioengineering* 120.7 (2023), pp. 1857–1868. DOI: 10.1002/bit.28424.

[294] D. H. Müller, M. Börger, J. Thien, and H. J. Koß. „Bioprocess in-line monitoring and control using Raman spectroscopy and Indirect Hard Modeling (IHM)". In: *Biotechnology and Bioengineering* 121.7 (2024), pp. 2225–2233. DOI: 10.1002/bit.28724.

List of Figures

List of Tables

Abbreviations

Acronym	Meaning
ACN	acetonitrile
AMS	ammonium sulfate
asPLS	adaptive smoothness penalized least squares
CAD	charged aerosol detection
CFF	cross-flow filtration
CL	cationic lipid
DF	diafiltration
DLS	dynamic light scattering
DMG-PEG	1,2-Dimyristoyl-rac-glycero-3-methoxypolyethylene glycol-2000
DMPE-PEG	1,2-Dimyristoyl-sn-glycero-3-phosphoethanolamine-N-[methoxy(polyethylene glycol)-2000] (ammonium salt)
DOBAQ	N-(4-carboxybenzyl)-N,N-dimethyl-2,3-bis(oleoyloxy)propan-1-aminium
DOTAP	1,2-Dioleoyl-3-trimethylammonium-propane (chloride salt)
dsCFF	dual-stage cross-flow filtration
DSP	downstream processing
DSPC	1,2-Dioctadecanoyl-sn-glycero-3-phosphocholin
DV	diafiltration volume
E. coli	*Escherichia coli*
EE	encapsulation efficiency
ELISA	enzyme-linked immunosorbent assay
ELS	electrophoretic light scattering
ELSD	evaporative light scattering detection
EMSC	extended multiplicative signal correction
FFR	flow rate ratio
HBcAg	Hepatitis B core Antigen
HCP	host-cell protein
HPLC	high performance liquid chromatography

Continued on next page

Acronym	Meaning
ICH	International Council for Harmonisation
IHM	indirect hard modeling
IR	infrared
LMWS	low-molecular weight species
LNP	lipid nanoparticle
MF	microfiltration
MIR	mid-infrared
MLR	multiple linear regression
mPES	modified polyethersulfone
mRC	modified regenerated cellulose
mRNA	messenger RNA
MWCO	molecular weight cut-off
NIR	near-infrared
OPLS	orthogonal projection to latent structures
PAT	process analytical technology
PCR	principal component regression
PDI	polydispersity index
PEG	polyethylene glycol
PEGL	polyethylene glycol lipid
PFV	power function value
Phe	phenylalanine
PL	phospholipid
PLS	partial least squares
RI	refractive index
RMSE	root mean squared error
RP	reversed-phase
SEC	size-exclusion chromatography
SGF	Savitzky-Golay filter
siRNA	small interfering RNA
SNR	signal-to-noise ratio
SNV	standard normal variate
SS	scaled subtraction
ssCFF	single-stage cross-flow filtration
TE	Tris-EDTA
TEM	transmission electron microscopy
TFA	trifluoroacetic acid
TFR	total flow rate
TMP	transmembrane pressure
Tris	tris(hydroxymethyl)aminomethane
Trp	tryptophan
Tyr	tyrosine
UF	ultrafiltration
UV	ultraviolet

Continued on next page

Acronym	Meaning
UV/Vis	ultraviolet-visible
VIP	variable importance in projection
VLP	virus-like particle

A3

Appendix Chapter 3

RP-CAD for Lipid Quantification: Systematic Method Development and Intensified LNP Process Characterization

Nicole Beckert[1,*], Annabelle Dietrich[1,*], and Jürgen Hubbuch[1]

[1] Institute of Process Engineering in Life Sciences, Section IV: Biomolecular Separation Engineering, Karlsruhe Institute of Technology (KIT), Karlsruhe, Germany

[*] Contributed equally.

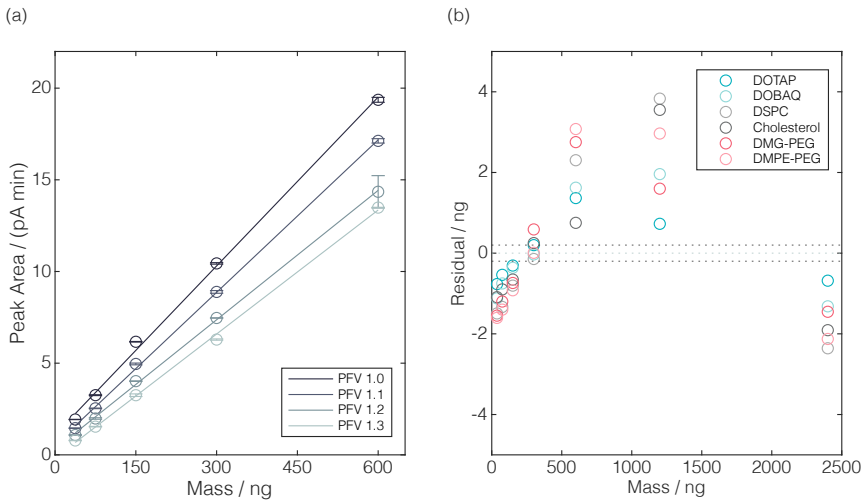

Figure A3.1 Variation of the power function value (PFV) and linearity range. The exploratory range I calibration curves (**a**) represent the peak area changes with lipid quantity for the varying PFVs (1.0, 1.1, 1.2, and 1.3) that are exemplarily visualized for 1,2-Dioctadecanoyl-sn-glycero-3-phosphocholin (DSPC). (**b**) Residual plots for exploratory range III calibration curves and PFV = 1.3 are displayed for the lipids 1,2-Dioleoyl-3-trimethylammonium-propane (chloride salt) (DOTAP), N-(4-carboxybenzyl)-N,N-dimethyl-2,3-bis(oleoyloxy)propan-1-aminium (DOBAQ), DSPC, cholesterol, 1,2-Dimyristoyl-rac-glycero-3-methoxypolyethylene glycol-2000 (DMG-PEG), and 1,2-Dimyristoyl-sn-glycero-3-phosphoethanolamine-N-[methoxy(polyethylene glycol)-2000] (ammonium salt) (DMPE-PEG). The target residual range of ±0.2 ng is displayed with dashed horizontal lines.

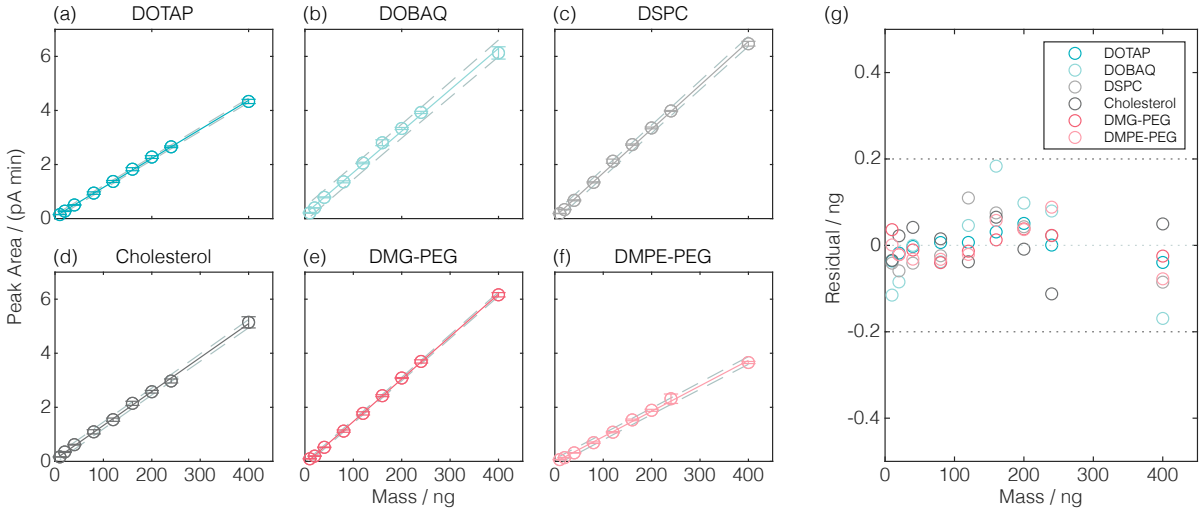

Figure A3.2 Method calibration—linearity. Changes in the peak area with lipid quantity at PFV = 1.3 are displayed as nine-point calibration curves with their standard deviation for DOTAP (**a**), DOBAQ (**b**), DSPC (**c**), cholesterol (**d**), DMG-PEG (**e**), and DMPE-PEG (**f**). The 95% confidence intervals are displayed as dashed lines. Linear regression equations and coefficients of determination (R^2) are provided in Table 3.1. The corresponding residuals (**g**) are within the target residual range of ±0.2 ng and are visualized by dashed horizontal lines.

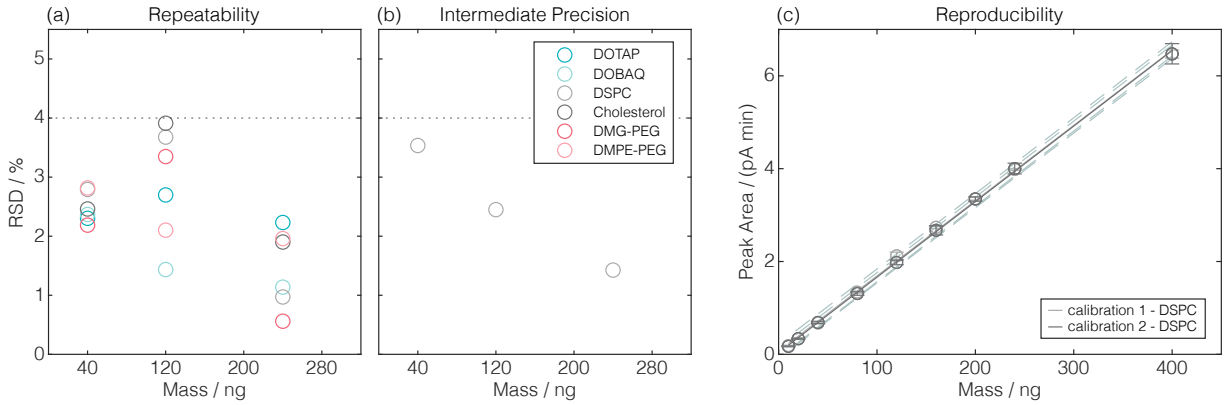

Figure A3.3 Method validation—precision. The percentage of the residual standard deviation versus lipid quantity is shown for repeatability (**a**) and intermediate precision for DSPC (**b**). The calibration curves for DSPC depicted in (**c**) show the reproducibility of the method.

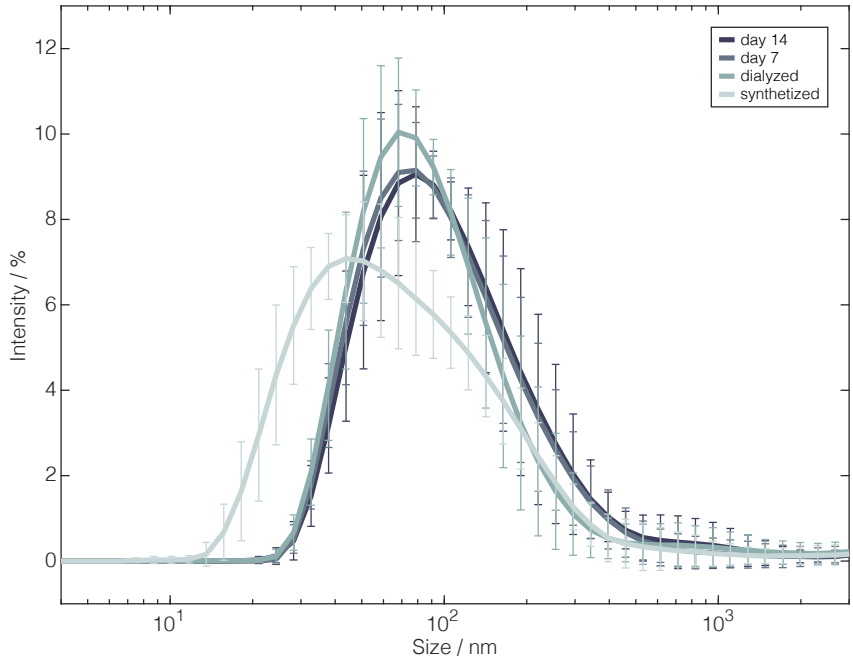

Figure A3.4 Intensity-weighted size distribution. The percentage intensity versus particle size is shown for the synthesized, dialyzed, and stored LNPs.

A4

Appendix Chapter 4

Time-Dependent Particle Size Increase during Lipid Nanoparticle Purification by Cross-Flow Filtration

Annabelle Dietrich[1,*], Nicole Beckert[1,*] and Jürgen Hubbuch[1]

[1] Institute of Process Engineering in Life Sciences, Section IV: Biomolecular Separation Engineering, Karlsruhe Institute of Technology (KIT), Karlsruhe, Germany

[*] Contributed equally.

Methods

Dialysis experiments

The workflow of the dialysis experiments is illustrated in Figure A4.1.

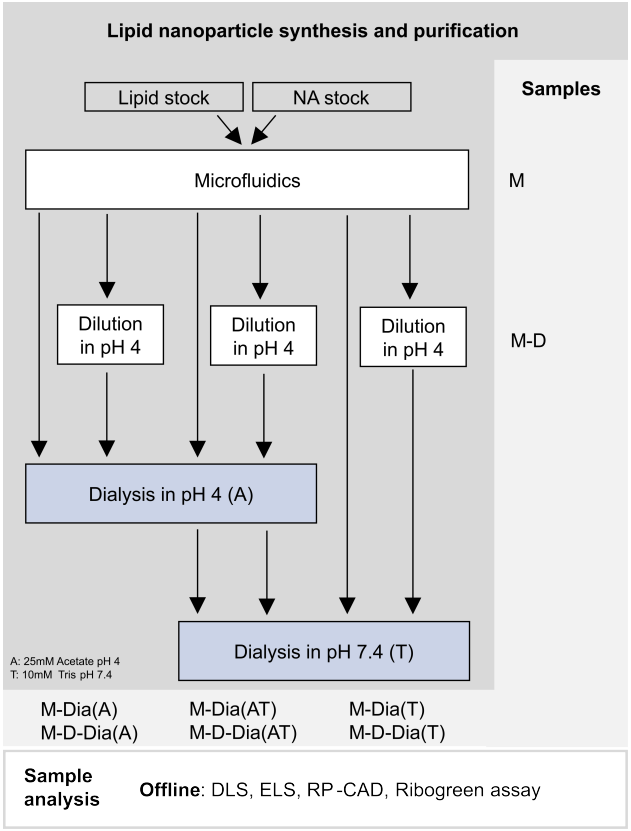

Figure A4.1 Workflow illustration of sequential process steps for LNP synthesis and purification by dialysis and sample analysis. Abbreviations: CAD: charged aerosol detection, D: dilution, Dia: dialysis, DLS: dynamic light scattering, ELS: electrophoretic light scattering, LNP: lipid nanoparticle, M: microfluidics, NA: nucleic acid, RP: reversed-phase.

LNP synthesis was performed as described in Section 4.2.2. LNPs synthesized by microfluidics (M) were either used directly or pre-diluted 1:4 (M-D) with pH 4 acetate buffer to reduce the ethanol content. Both undiluted and pre-diluted LNPs were dialyzed (M-Dia and M-D-Dia) using different buffer systems.

LNPs were dialyzed against 500 volumes of pH 4 acetate buffer (A) or pH 7.4 Tris(hydroxymethyl)aminomethane (Tris) buffer (T) at 2–8°C for 4 hours and overnight. Further, a two-step dialysis was conducted to lower the ethanol content before raising the buffer pH. Dialysis against pH 4 acetate buffer for two times 4 hours at 2–8°C was followed by dialysis against pH 7.4 Tris buffer for 4 hours and overnight (AT). Dialysis was conducted using 10 kDa Slide-A-Lyzer® dialysis cassettes (1–3 mL, Thermo Fisher Scientific Inc.). Sample analysis was performed after 1 and 7 days of storage at 2–8°C.

Results

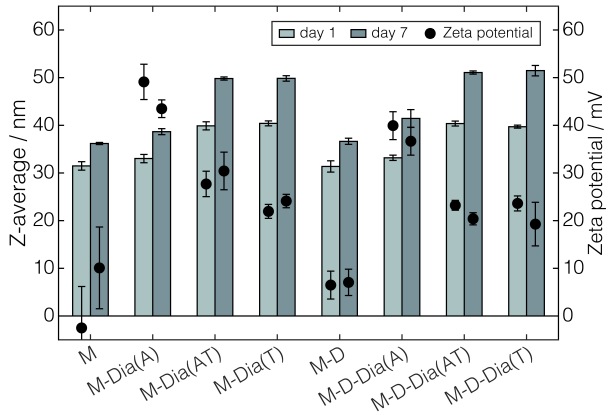

Figure A4.2 Effects of dialysis buffer on LNP Z-average and zeta potential. LNPs were dialyzed into different buffers or buffer combinations, stored at 2–8°C, and analyzed on day 1 and day 7. Abbreviations: A: sodium acetate buffer, D: dilution, Dia: dialysis, LNP: lipid nanoparticle, M: microfluidics, T: tris buffer.

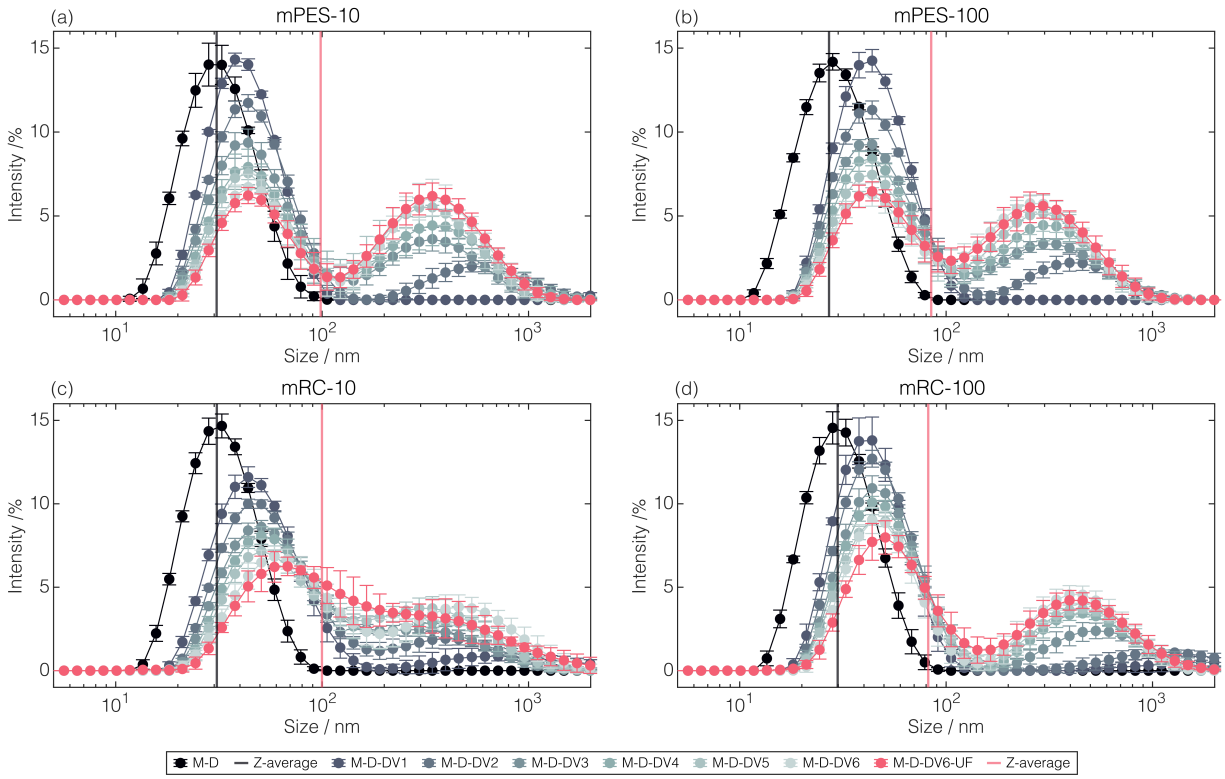

Figure A4.3 Intensity-weighted size distribution for CFF experiments. The intensity-weighted size distributions of LNPs are shown for the CFF runs with modified polyethersulfone (mPES)-10 (a), mPES-100 (b), modified regenerated cellulose (mRC)-10 (c), and mRC-100 (d) membranes. The Z-average values for the synthesized, diluted LNPs (M-D), which served as the starting material for the CFF, and the final CFF-purified LNPs (M-D-DV6-UF) are marked by vertical lines. Abbreviations: CFF: cross-flow filtration, D: dilution, Dia: dialysis, DV: diafiltration volume, LNP: lipid nanoparticle, M: microfluidics, mPES: modified polyethersulfone, mRC: modified regenerated cellulose, UF: ultrafiltration.

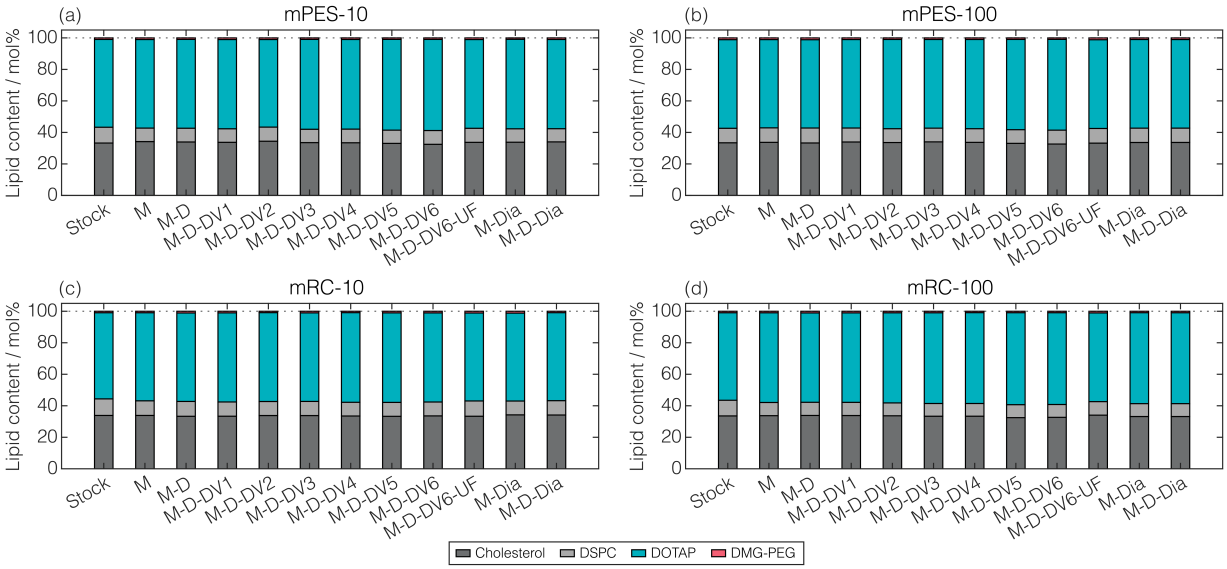

Figure A4.4 Lipid molar ratio of LNPs across processing. The lipid content of the lipid stock and the LNPs at every processing state is shown as a stacked vertical bar for the CFF runs with mPES-10 (a), mPES-100 (b), mRC-10 (c), and mRC-100 (d) membranes after one day of storage at 2–8 °C. Abbreviations: D: dilution, Dia: dialysis, DV: diafiltration volume, M: microfluidics, LNP: lipid nanoparticle, mPES: modified polyethersulfone, mRC: modified regenerated cellulose, UF: ultrafiltration.

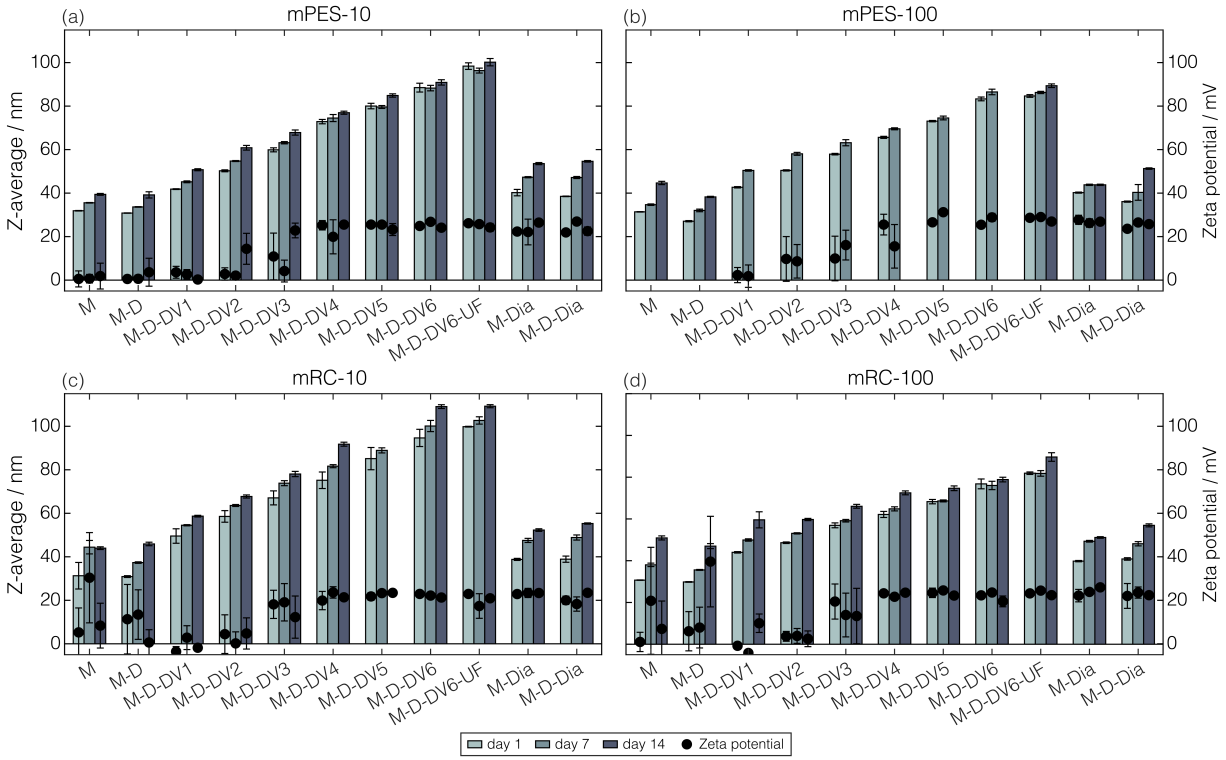

Figure A4.5 Changes in Z-average and zeta potential over storage. Over 14 days of storage at 2–8 °C, Z-average and zeta potential are shown for LNPs processed by dialysis or CFF using mPES-10 (a), mPES-100 (b), mRC-10 (c), and mRC-100 (d) membranes. Abbreviations: CFF: cross-flow filtration, D: dilution, Dia: dialysis, DV: diafiltration volume, LNP: lipid nanoparticle, M: microfluidics, mPES: modified polyethersulfone, mRC: modified regenerated cellulose, UF: ultrafiltration.

A5

Appendix Chapter 5

Dual-Stage Cross-Flow Filtration: Integrated Capture and Purification of Virus-Like Particles

Annabelle Dietrich[1], Luca Heim[1], and Jürgen Hubbuch[1]

[1] Institute of Process Engineering in Life Sciences, Section IV: Biomolecular Separation Engineering, Karlsruhe Institute of Technology (KIT), Karlsruhe, Germany

Erratum to “Dual-Stage Cross-Flow Filtration: Integrated Capture and Purification of Virus-Like Particles”

Dietrich, A., Heim, L. and Hubbuch, J. (2025), Dual-Stage Cross-Flow Filtration: Integrated Capture and Purification of Virus-Like Particles. Biotechnology and Bioengineering 122: 884–894. https://doi.org/10.1002/bit.28914

In the sections ”5 Abstract”, ”5.1 Introduction”, ”5.3 Results”, ”5.4 Discussion”, and ”5.5 Conclusion and Outlook”, as well as in the Graphical Abstract, Figure 5.1, the captions of Figures 5.1 and 5.2, and the ”Appendix A5”, the pore size of the microfiltration membrane was incorrectly reported as 2 µm. The correct pore size is 0.2 µm, as correctly stated in ”5.2 Materials and Methods” section. The corrected Graphical Abstract and Figure 5.1 are included below.

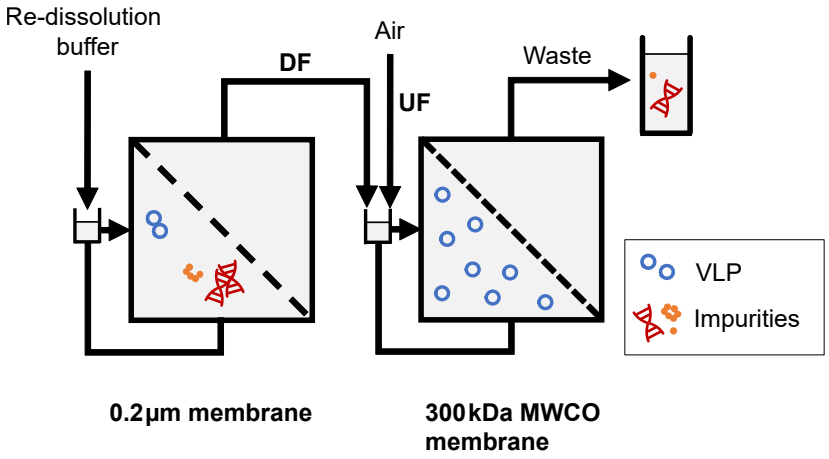

Figure A5.1 Graphical Abstract

In paragraph 5 of the section ”5.1 Introduction”, the text “Further, MF was combined with UF to isolate polymerized human hemoglobin from its product-related high or low-molecular weight species (LMWS) using an integrated 2 µm/500 kDa MWCO membrane configuration (Cuddington et al. 2022).” should read “Further, MF was combined with UF to isolate polymerized human hemoglobin from its product-related high- or low-molecular weight species (LMWS) using an integrated 0.2 µm/500 kDa MWCO membrane configuration (Cuddington et al. 2022).”

All other parts are unchanged.

We apologize for these errors.

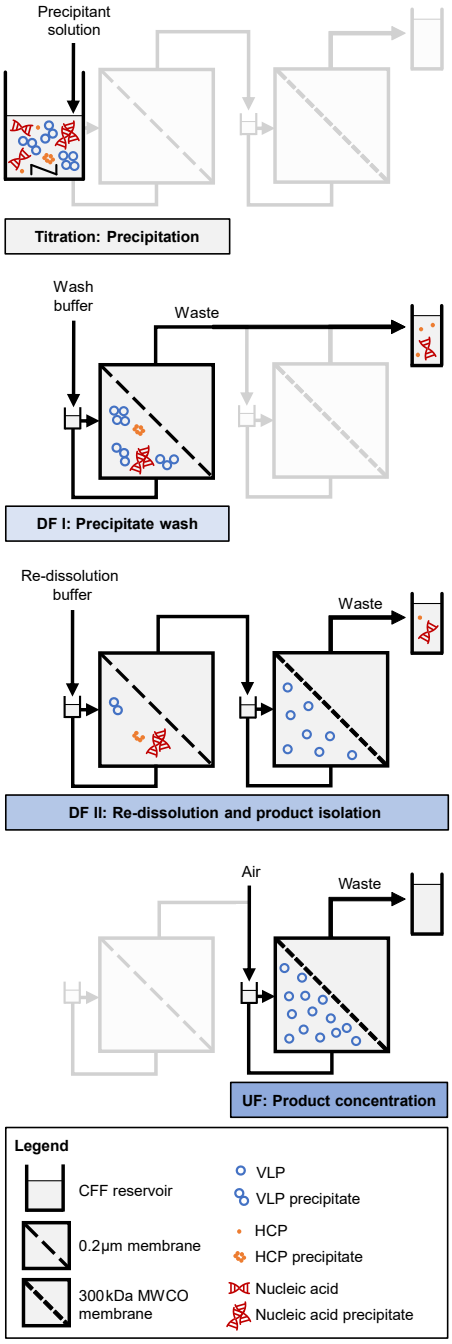

Figure A5.2 Schematic illustration of the integrated dual-stage CFF (*dsCFF*) process. Precipitation by titration in the CFF reservoir is followed by washing of the precipitate by constant-volume DF using a 0.2 µm membrane (DFI). Product re-dissolution by a consecutive DF using the dual-stage 0.2 µm/300 kDa MWCO membrane configuration (DFII) allows for integrated product isolation in the second membrane stage. Finally, the setup enables product concentration by subsequent UF. Adapted from Hillebrandt et al. [88].

Supporting Information

Supplementary Data

CFF-Based Wash Reproducibility

To recover precipitated VLPs after selective precipitation, the applicability of a CFF-based wash of the precipitate by a first DF step (DFI) has been assessed. The CFF-based wash aims for the integrated removal of dissolved species while the precipitate is still retained by the 0.2 µm MF membrane. In-line permeate data from a representative wash step are shown in Supporting Information: Figure A5.4 (A), since reproducible data were achieved across all conducted processes. In-line conductivity measurements showed a consistent conductivity value of approx. 56 mS cm^{-1} throughout the wash step, indicating the presence of AMS. Raman spectral analysis of the fractionated permeate enabled AMS quantification and underlined the constant AMS concentration of approx. 1.1 M (data not shown), as expected due to a 1.1 M AMS-containing wash buffer. Contaminant removal was monitored by in-line ultraviolet (UV) of the permeate (cf. Supporting Information: Figure A5.4 (A)) and after approx. six diafiltration volume (DV), the signal dropped below 60 mAU. Contaminant removal was further supported by SDS-PAGE of the permeate fractions (data not shown). Overall, VLP precipitation and the CFF-based wash could be reproducibly performed, allowing for efficient contaminant removal and providing a consistent basis for subsequent CFF-based re-dissolution processes.

CFF-Based Re-Dissolution Reproducibility

Considering the first membrane stage, residual turbidity of the retentate was visible after CFF-based re-dissolution, the second DF step (DFII), suggesting aggregated or irreversibly precipitated host-cell species. Mass balances derived from HPLC control runs of the retentate supernatants revealed $A260_C$ discrepancies, hence underlining this assumption (data not shown), which is in good agreement with findings from the re-dissolution screening. Analysing the retentate supernatants for soluble species, size-exclusion chromatography (SEC)-HPLC analysis revealed VLP concentrations between 0.23–0.26 g L^{-1}, similar A260/A280 ratios of 0.81, and purities between 88–89%, indicating reproducible process operations. However, the authors believe that extending the DF process for re-dissolution could have led to a greater proportion of VLPs passing through the MF membrane, thereby increasing overall VLP recoveries in both processes.

Supplementary Figures

Figures

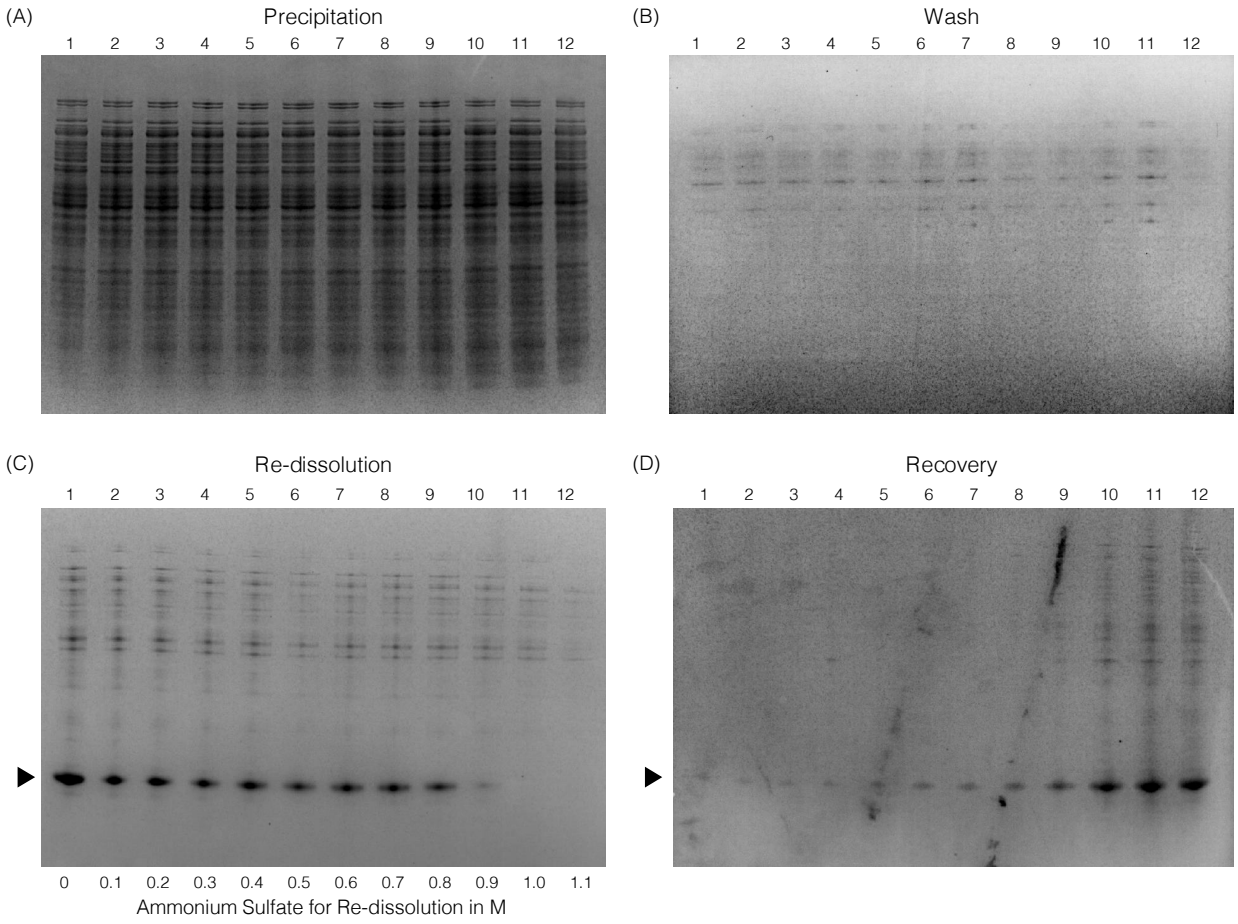

Figure A5.3 SDS-PAGE gel scans of the VLP re-dissolution screening. Supernatants after the steps precipitation (A), wash (B), re-dissolution (C), and recovery (d) are depicted. The lanes 1-12 correspond to the solutions, for which the AMS concentrations were varied during VLP re-dissolution (C). Note that 1.1 M AMS was consistently deployed for precipitation (A) and wash (B), while VLPs were finally recovered using a buffer without AMS (D). The protein band attributed to Cp149 is indicated by arrows.

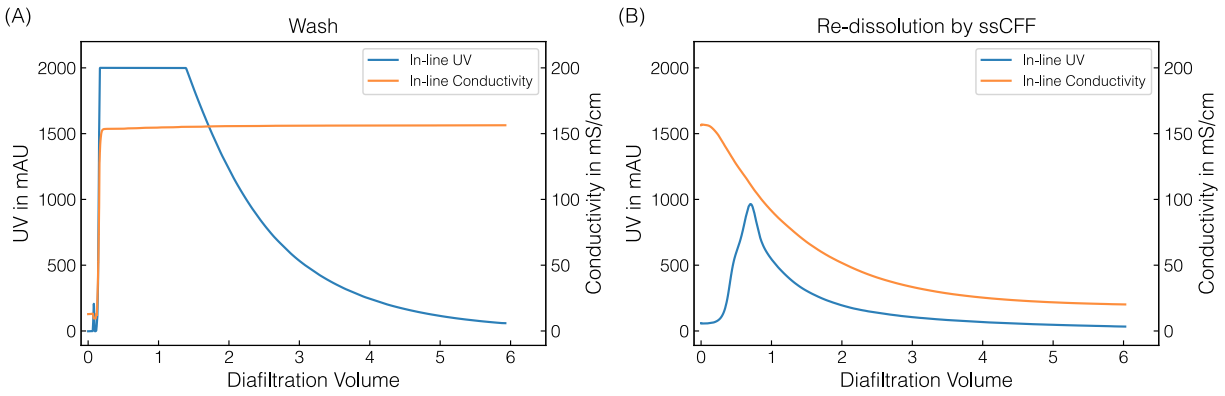

Figure A5.4 In-line conductivity and UV measurements of wash (A) and re-dissolution (B) by *ssCFF*.

A6

Appendix Chapter 6

Raman-Based PAT for VLP Precipitation: Systematic Data Diversification and Preprocessing Pipeline Identification

Annabelle Dietrich[1,*], Robin Schiemer[1,*], Jasper Kurmann, Shiqi Zhang, and Jürgen Hubbuch[1]

[1] Institute of Process Engineering in Life Sciences, Section IV: Biomolecular Separation Engineering, Karlsruhe Institute of Technology (KIT), Karlsruhe, Germany

[*] Contributed equally.

Supplementary Data

Buffers, Solutions, and Spiking Materials

If not otherwise stated, chemicals (Merck KGaA, Darmstadt, DE) and ultrapure water (PURELAB Ultra, ELGA LabWater, Lane End, High Wycombe, UK) were used for buffer and stock solution preparation. Buffers were pH-adjusted with 32 % HCl using a SenTix62 pH electrode (WTW, Weilheim, DE) coupled to a HI 3220 pH meter (Hanna Instruments, Woonsocket, US). Buffers and stock solutions were filtered through a 0.2 µm pore-size cellulose acetate filter (VWR International, Radnor, US). For all experiments, stock solutions used for polysorbate adjustment and precipitation experiments were 10% (v/v) polysorbate 20 and 4 M AMS, respectively. Lysis or high-salt lysis buffers consisted of 50 mM Tris, 100 mM or 1500 mM NaCl, 1 mM EDTA (AppliChem GmbH, Darmstadt, DE) at pH 8.0, respectively.

For the VLP-enriched spiking material, clarified lysate was further purified by precipitation and re-dissolution, diafiltration, and chromatography as described by Hillebrandt et al. [61]. The purified VLPs were further dialyzed into lysis buffer overnight using 10 kDa MWCO Slide-A-Lyzer G2 cassettes (Thermo Fisher Scientific Inc., Waltham, US) and concentrated by ultrafiltration with Vivaspin 20 centrifugal filters (Sartorius Stedim Biotech GmbH, Göttingen, DE) in a 5810R centrifuge (Eppendorf, Hamburg, DE). VLP concentration was determined using a NanoDrop 2000c UV/Vis spectrometer (Thermo Fisher Scientific Inc.) and the theoretical extinction coefficient at 280 nm of 1.764 $L\,g^{-1}\,cm^{-1}$ as provided by the ProtParam tool [204]. VLP-enriched spiking material concentrations were 6.95 $g\,L^{-1}$ for batch precipitation experiment B5 and 3.85 $g\,L^{-1}$ for batch and fed-batch precipitation experiments B6 and F2, respectively. For both VLP-enriched spiking materials, a A260/A280 ratio of 0.63 indicated almost pure protein.

For the host-cell protein (HCP)-enriched spiking material, clarified lysate was adjusted to 0.25% (v/v) polysorbate 20 and precipitation was conducted at 1.1 M AMS for 30 min under stirred conditions. Precipitate solution was centrifuged at 12000 G and 4 °C for 30 min. Supernatant was collected and a similar procedure of dialysis and concentration was performed as for the VLP-enriched spiking material, but using 2 kDa MWCO devices. HCP-enriched spiking material characteristics were a A280 value of 57.3 mAU and a A260/A280 ratio of 1.88, both indicating host-cell nucleic acids in the spike solution.

Supplementary Tables and Figures

Figures

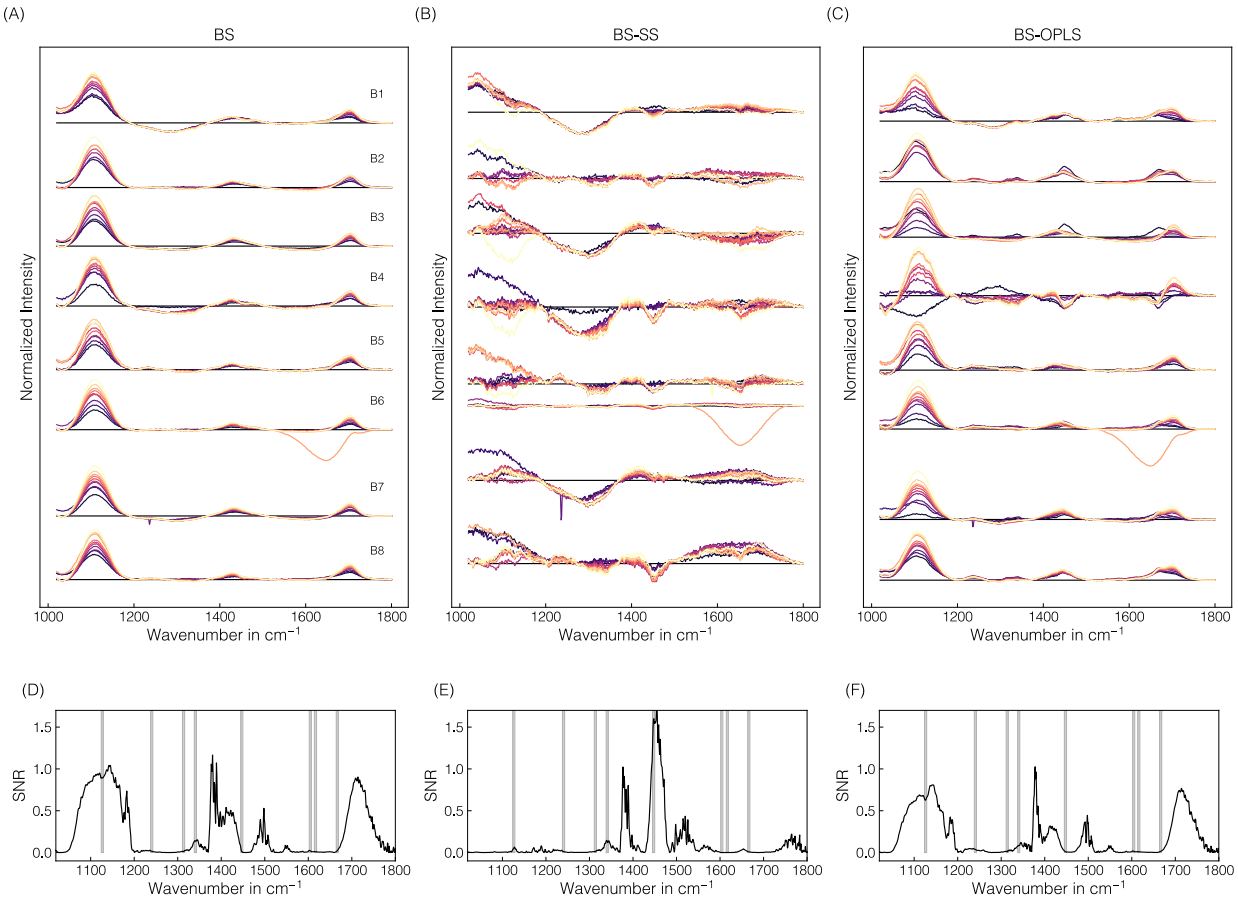

Figure A6.1 Comparison of the effects of preprocessing operations on Raman spectra in supernatant samples for the wavenumber region 1020-1800 cm^{-1}. In **(A)-(C)**, difference spectra are shown for all batch experiments B1-B8 after turbidity and baseline correction, with incorporated scaled subtraction (SS)-background correction, or with incorporated orthogonal projection to latent structures (OPLS)-background correction, respectively. The spectra are colored according to the AMS concentration with brighter colors denote higher concentrations. In **(D)-(F)**, the corresponding signal-to-noise ratio (SNR) are shown. Gray shaded areas indicate protein-related Raman regions according to literature [131, 132].

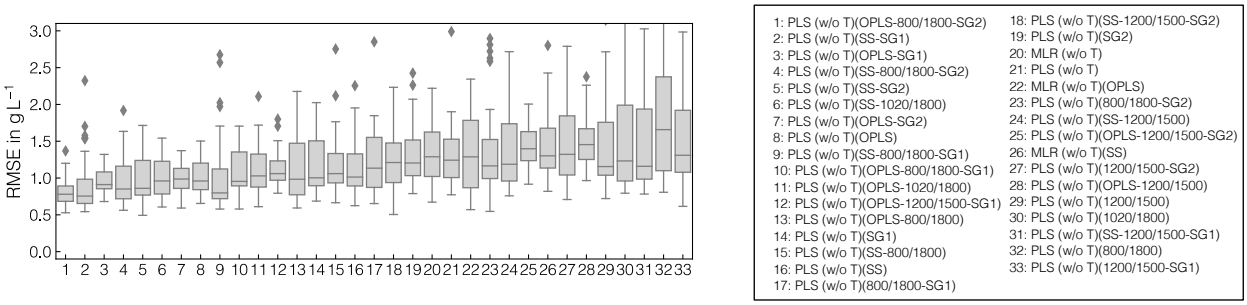

Figure A6.2 Comparison of model types and preprocessing pipelines without turbidity correction. The distributions of root mean squared error (RMSE) of the outer cross-validation are presented and ranked by the mean of the RMSEs for all tested model configurations. All tested model configurations comprised baseline correction and difference spectra. The solid lines within the boxes represent the median of the obtained performances.

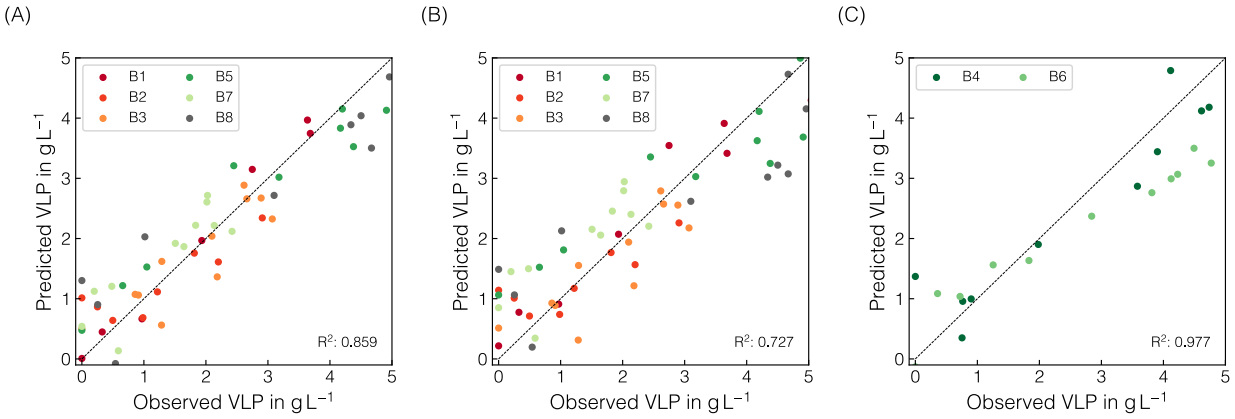

Figure A6.3 PLS model predictions with regard to precipitated VLP concentration for batch experiments. The predicted and observed VLP concentrations for calibration **(A)**, cross-validation **(B)** and test sets **(C)** are plotted against each other with the tie line indicating the optimal result.

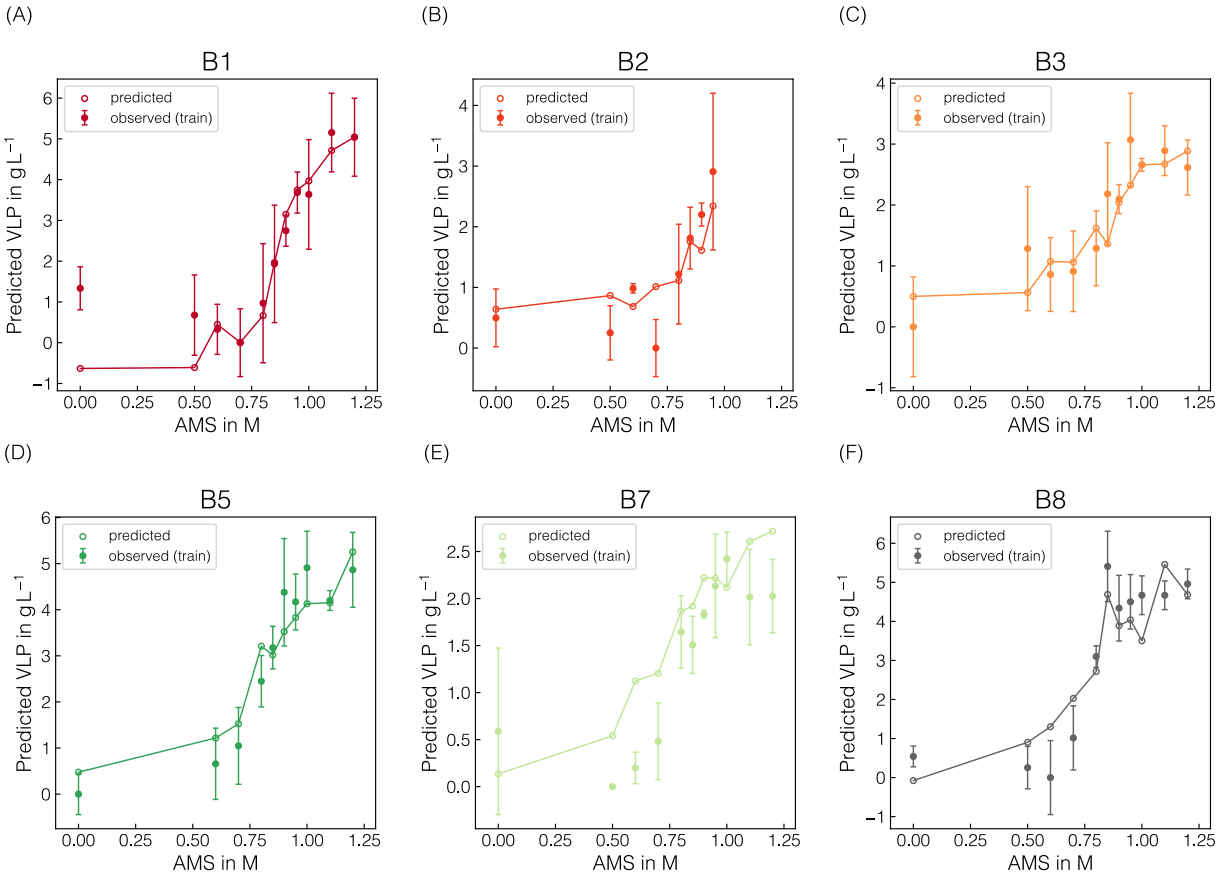

Figure A6.4 PLS model predictions with regard to the precipitated VLP concentration for batch experiments over AMS concentrations. Batch experiments assigned to the training set (B1, B2, B3, B5, B7, B8) are shown in **(A)-(F)**, respectively. The predicted and observed VLP concentrations for all calibration experiments are displayed as empty and full circles, respectively. For visual purposes, solid are shown to linearly connect the PLS model predictions. For batch experiment B2, the data points above 0.95 M were excluded due to defective Raman spectra.

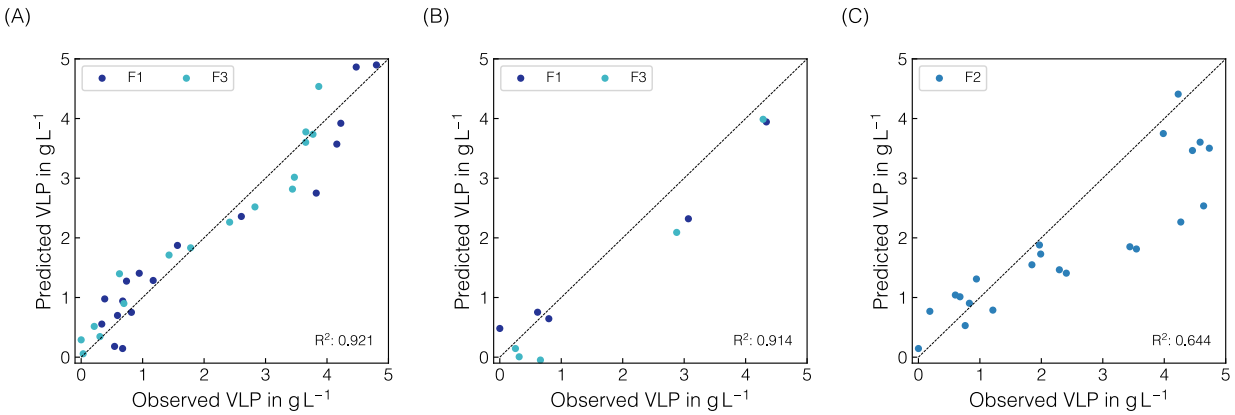

Figure A6.5 PLS model predictions with regard to precipitated VLP concentration for fed-batch experiments. The predicted and observed VLP concentrations for calibration **(A)**, validation **(B)** and test sets **(C)** are plotted against each other with the tie line indicating the optimal result.

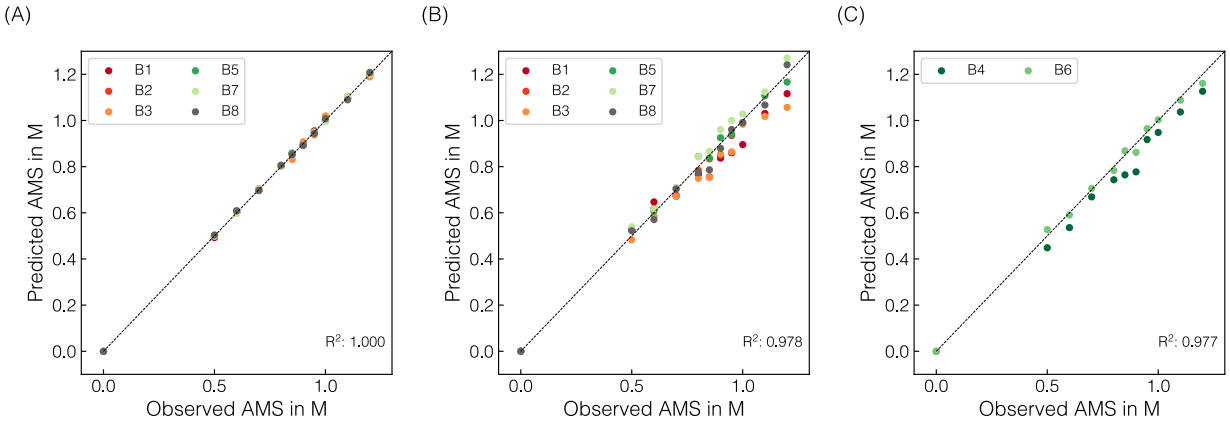

Figure A6.6 PLS model predictions with regard to AMS concentration for batch experiments. The predicted and observed AMS concentrations for training **(A)**, cross-validation **(B)** and test sets **(C)** are plotted against each other with the tie line indicating the optimal result.

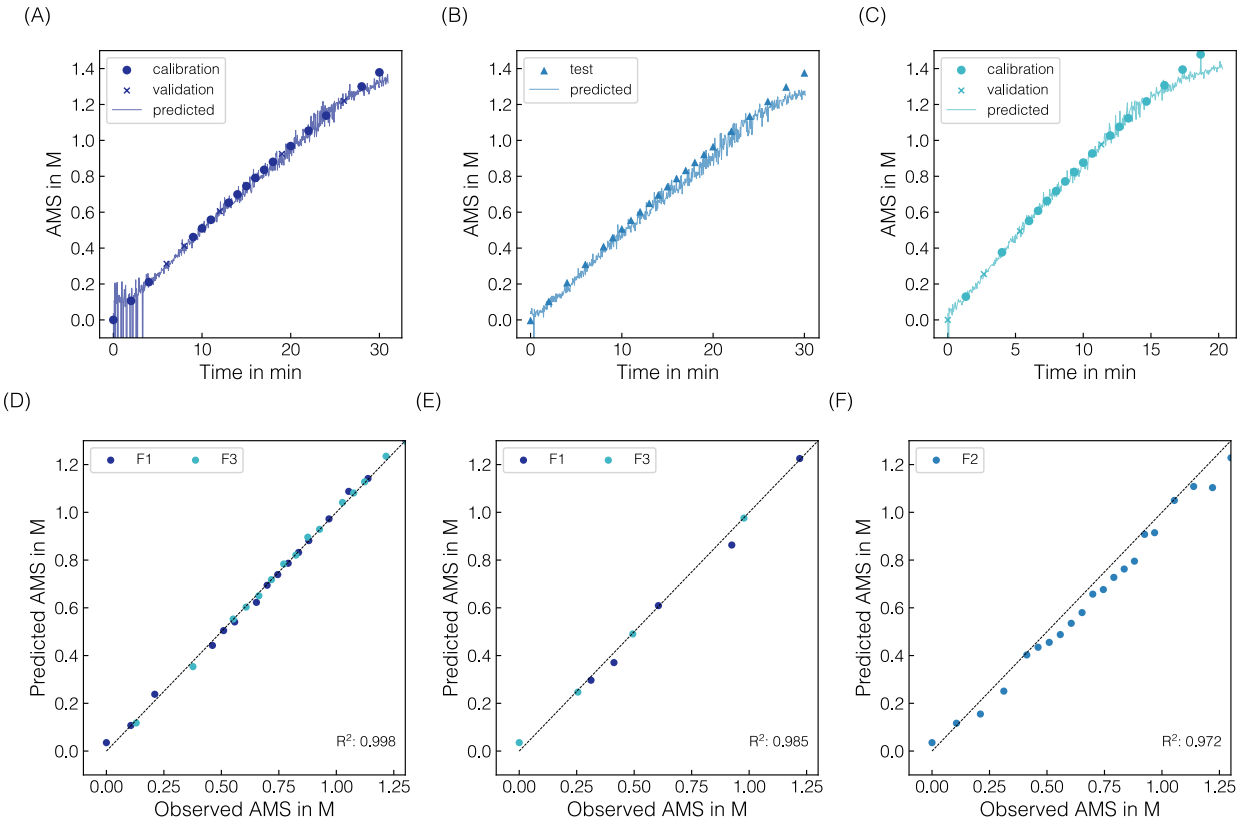

Figure A6.7 PLS model predictions with regard to AMS concentration for fed-batch experiments. In **(A)-(C)**, the timely predictions obtained from real-time Raman spectra are shown as solid lines and observed AMS concentrations are shown as scattered points. The data points belonging to the calibration, validation and test sets are marked with circles, crosses and triangles, respectively. The PLS predictions for the calibration, validation and test sets are plotted against the observed AMS concentrations in **(D)-(F)**, respectively.

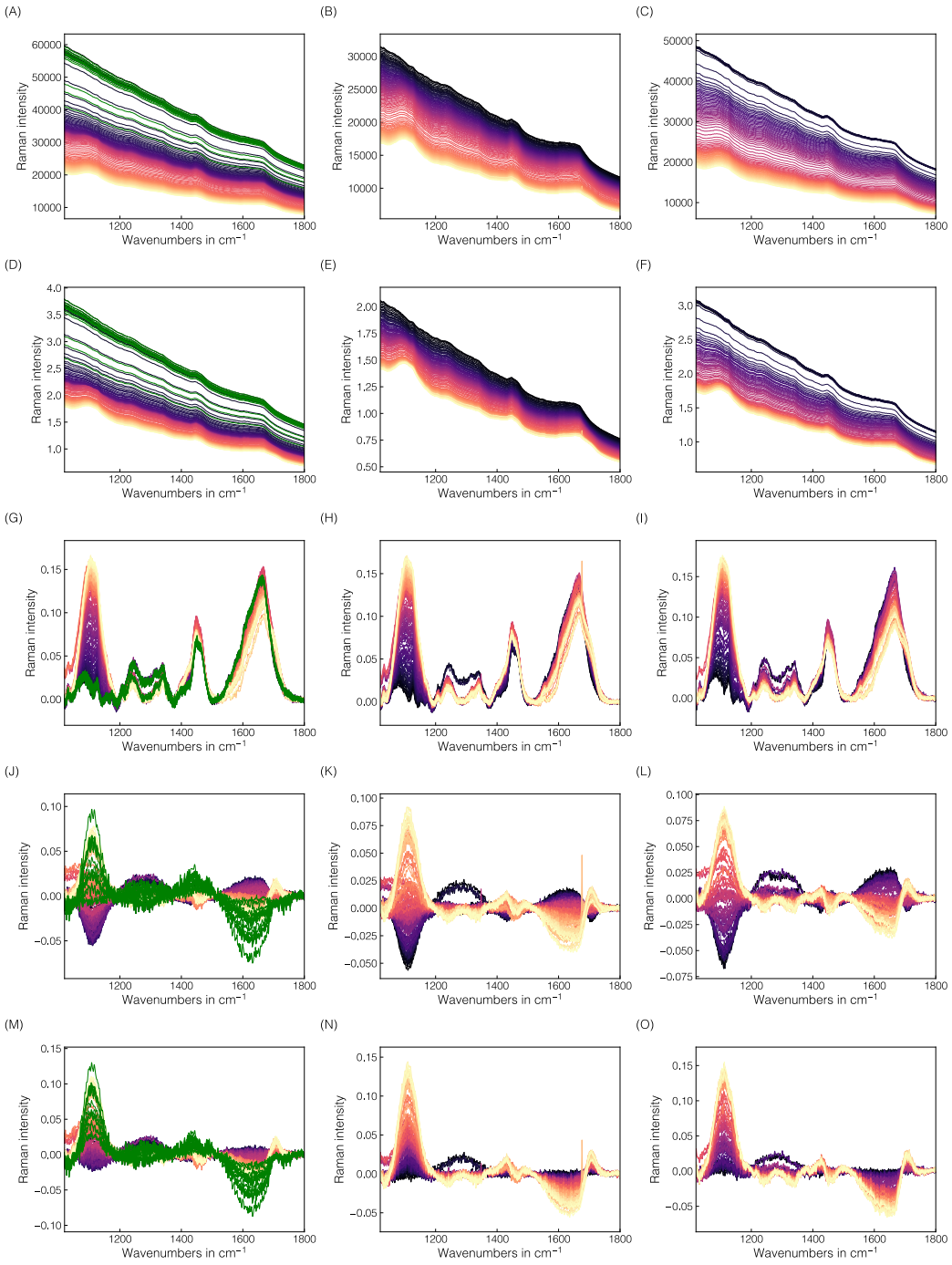

Figure A6.8 Visualization of preprocessing operations for fed-batch experiments F1-F3 from left to right. The individual rows depict the Raman spectra at different stages of the preprocessing pipeline: Raw **(A)-(C)**, turbidity correction **(D)-(F)**, baseline **(G)-(I)**, OPLS background **(J)-(L)** and difference spectra **(M)-(O)**. For visual purposes, only every 5th spectra from each fed-batch experiment is shown. The Raman spectra affected by scattering in the PLS predictions are marked in green. The Raman spectra are colored according to the theoretical AMS concentration in the system with brighter colors denoting higher concentrations.

A7

Appendix Chapter 7

Raman-Based PAT for Multi-Attribute Monitoring during VLP Recovery by Dual-Stage CFF: Attribute-Specific Spectral Preprocessing for Model Transfer

Annabelle Dietrich[1], Luca Heim[1], and Jürgen Hubbuch[1]

[1] Institute of Process Engineering in Life Sciences, Section IV: Biomolecular Separation Engineering, Karlsruhe Institute of Technology (KIT), Karlsruhe, Germany

Piping and Instrumentation Diagram of the Dual-Stage CFF Set-Up

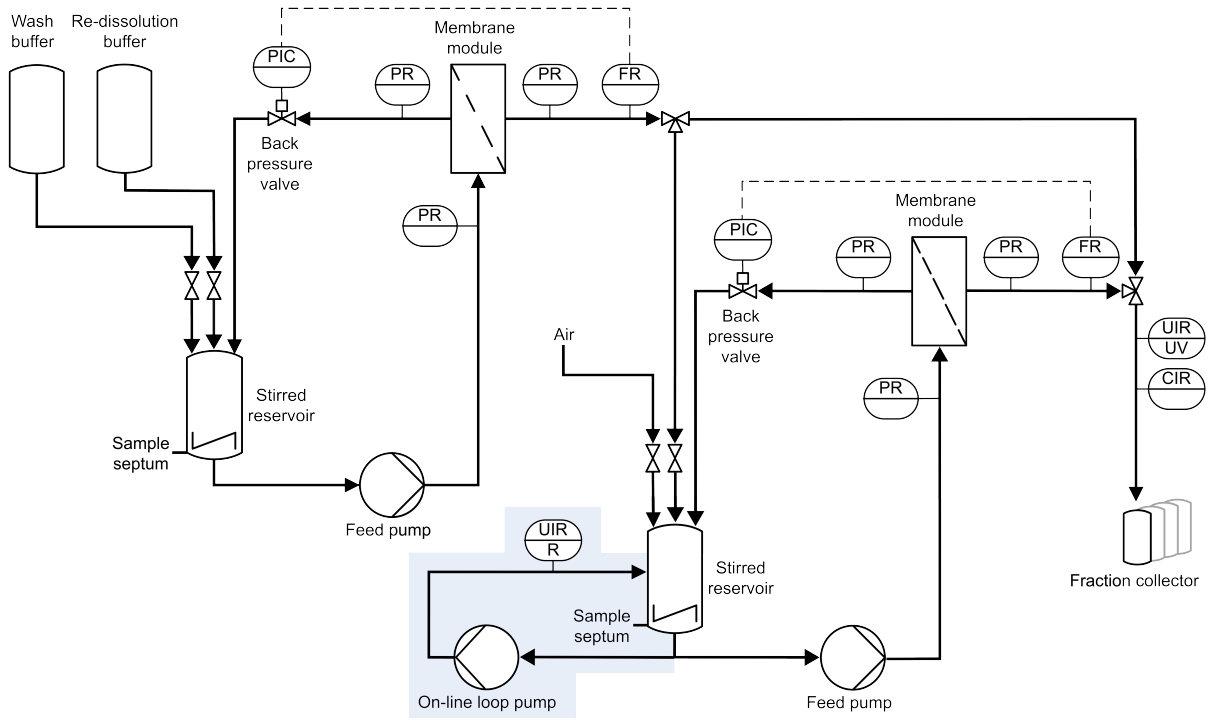

Figure A7.1 Piping and instrumentation diagram of the dual-stage cross-flow filtration (CFF) set-up. Two serially connected CFF units are equipped with 0.2 µm and 300 kDa MWCO membranes, respectively, and connected to a system for permeate stream fractionation. Starting from the CFF reservoir in the second membrane stage, an on-line monitoring loop was implemented using peek capillaries, a loop pump, and a flow cell for in-line measurements by Raman spectroscopy. The on-line loop is highlighted in blue. C, conductivity or control; F, flow rate; I, indicate; P, pressure; R, record or Raman; U, multivariate; UV, ultraviolet. Adapted from Dietrich et al. [277].

Spectral Data of Precipitant-Containing Stock Solutions

In general, the spectral appearance of ammonium sulfate (AMS)-containing solutions is due to several precipitant and buffer contributions, as presented in Supplementary Fig. A7.2. Next to the predominant Raman peak near 980 cm^{-1}, gradually increasing contributions at 450, 618, and 1106 cm^{-1} are also attributable to sulfate ions of AMS, while the bands at 1435 and 1693 cm^{-1} are indicative for ammonium ions [251, 252]. On the contrary, bands of buffer components and sapphire remained constant. The bands originating from Tris appear near 1249 and 1470 cm^{-1} [253]. A broad, water-related band is visible near 1650 cm^{-1} [251], while narrow bands at 379, 418, 430, 450, 577, and 750 cm^{-1} are caused by the sapphire [254]. Considering spectral interferences, all ammonium bands and the sulfate bands at 450 and 618 cm^{-1} are partially affected by interference from sapphire or buffer bands, while the sulfate band located at 980 cm^{-1} remained largely unaffected. Further, the contributions of AMS will by far exceed protein-associated contributions in process-derived spectra, mostly located in the wavenumber regions 600–880 cm^{-1}, 1004 cm^{-1}, and 1200–1800 cm^{-1} [131, 132].

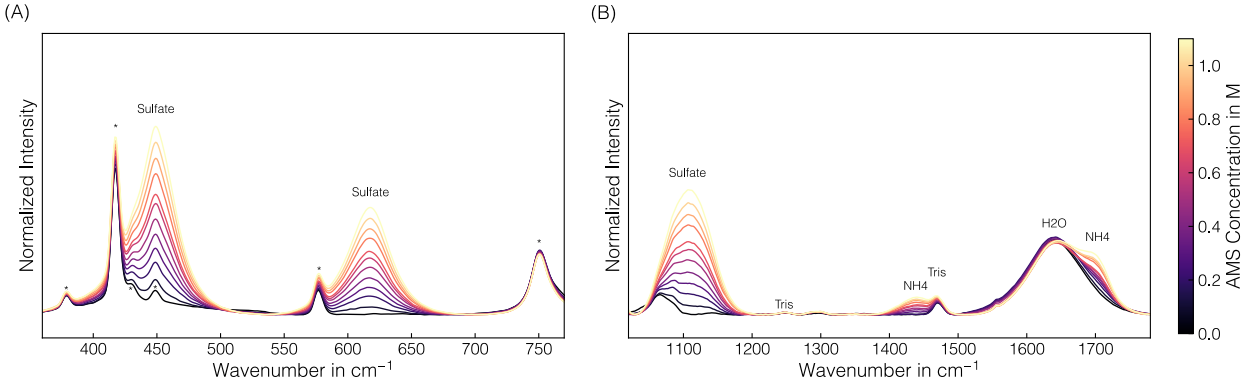

Figure A7.2 Spectral data comparison. Individual wavenumber intervals of preprocessed Raman spectra derived from a set of stock solutions with varying AMS concentrations are depicted in (A) and (B). Sapphire bands are marked with asterisks, and the other bands were assigned to sulfate ions, ammonium ions, or buffer components. All spectra are shown normalized and colored with brighter colors denoting higher AMS concentrations.

Defective Spectral Data

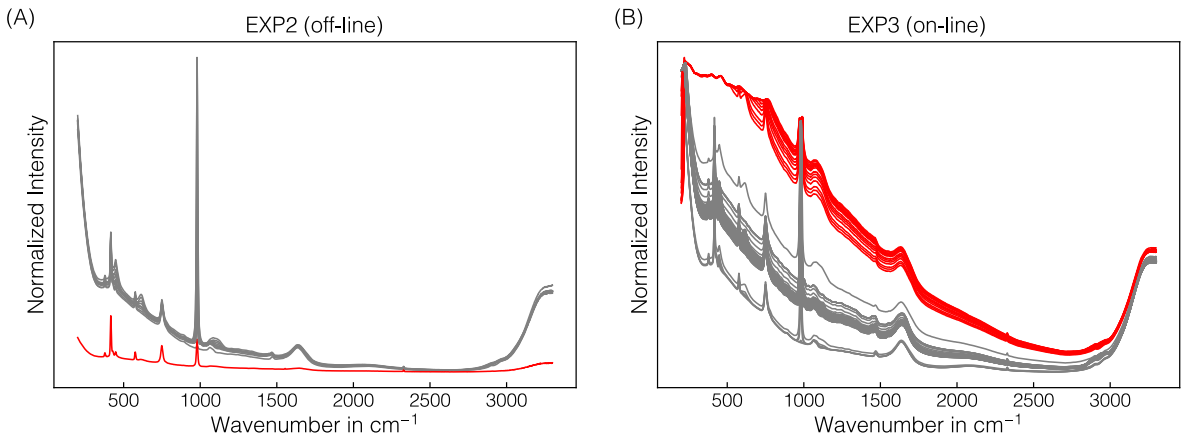

Figure A7.3 Defective spectra. Raw Raman spectra from EXP2 off-line Raman measurements (A) and EXP3 on-line Raman measurements (B) are shown. Defective spectra are colored in red.